U-Pb dating of brittle deformation

Klaus Martin Rittner

Royal Holloway

University of London

Thesis submitted for the degree of

Doctor of Philosophy

August 2012

Declaration of authorship

I, Martin Rittner, hereby declare that this thesis and the work presented in it is entirely my own. Where I have consulted the work of others, this is always clearly stated.

Signed: _____

Date: _____

Abstract

A new method for dating brittle deformation is presented, based on U-Pb dating of syndeformationally grown calcite fibres, or "tectonic carbonates", found e.g. on brittle slickensides and in tension fractures. Brittle structures from various areas in the Alps were sampled from outcrops where the deformation age is well constrained in the literature, to be able to test the results of the new method.

Laser ablation inductively-coupled plasma mass spectrometry (LA-ICPMS) is used for rapid screening of samples with respect to their U, Th, Pb and other trace and major element concentrations and spacial distribution. For data reduction of LA-ICPMS data, an add-on package for the open-source "R" environment was developed that in addition to one-dimensional single line scans allows two-dimensional trace and major elemental mapping of the samples.

Based on this spatial information, regions within the samples with high, yet variable U/Pb ratios are chosen for mechanical subsampling. For subsequent solution-based U-Th-Pb isotopic analysis, an optimized low-Pb blank methodology has been developed to facilitate work with very low-concentration (typ. ≤ 1 ppm U, as low as tens of ppb Pb) calcite samples.

High precision isotope-dilution U-Th-Pb isotope ratio measurements are conducted on a multi-collector (MC-) ICPMS. Alternatively, determination of isotopic ratios directly from LA-ICPMS analyses are conducted in situ, which yields results much faster, but with limited precision due to instrumental limitations.

Only a small fraction of screened samples yielded precise ages. The deformation ages fit respective published models of regional structural evolution. The ages obtained in situ correspond well with the data from solution chemistry, although with very large error margins. Where repeated measurement of the same structures was achieved, the respective ages lie within error of each other.

For faulting in the Swiss Jura, ages of 9.05 ± 0.94 Ma were obtained, constraining maximum age of later folding. Thrusting of the most external Digne Nappe (French

Alps) was dated to 9.59 ± 0.05` Ma, in accordance with literature. In the Austrian Gosau Basin, distinct deformation phases at 29 ± 2 and 23 ± 1 Ma could be observed, ages from the LA-ICPMS data of ~42 and ~27 Ma. confirm the first age and add an older observed deformation phase. This correlates with basin formation and Miocene tectonic overprinting in this area. Presumably hydrothermally grown calcite sealing fissures associated with the formation of the Miocene Fohnsdorf basin (Austria), could be dated to 13.44 ± 0.84 Ma. Other samples yielded less conclusive age results, mainly due to geological scatter, aggravated by the extremely low Pb concentrations and U/Pb ratios in some samples.

Table of Contents

Acknowledgements

I would like to thank the following people who through their respective contributions were all crucial for the success of this research and the completion of the present work:

My parents Ingrid and Klaus Rittner, for inspiring my interest in geology and the natural world, and for unconditionally encouraging and supporting me at all times.

My supervisor Dr. Wolfgang Müller, for his guidance in labwork and research practice, discussion of results, and for never losing his patience and taking the right steps of encouragement when needed.

My Co-supervisor Prof. Matthew Thirlwall, for guidance and help in the lab, and for discussion of methodology and results.

Prof. Robert Hall for acting as my PhD advisor and for providing additional sample material.

Staff at RHUL Department of Earth Sciences (DoES), especially Kevin D'Souza for organising anything that needed organising; Neil Holloway for sample preparation and discussion thereof; Frank Lehane for saving many a day and late night providing IT assistance; Julie Brown, Kathryn Hardy and Diane Serpant for keeping track of the administrative and financial aspects of my work at RHUL.

Dr. Nathalie Grassineau for guidance in analysis of organic carbon and in using the ICPMS at the DoES Geochemistry lab; Prof. Dave Mattey for guidance on abusing the Micromill for sample preparation in ways it was not intended for.

Ao. Univ-Prof. Dr. Hugo Ortner, University of Innsbruck, Austria, Univ-Prof. Dr. Michael Wagreich, University of Vienna, Austria, Prof. Dr. Neil Mancktelow, ETH Zürich, Switzerland, Univ-Prof. Dr. Franz Neubauer, University of Salzburg, Austria, Dr. Herfried Madritsch, NAGRA, Switzerland, Dr. Marion Campani, at the time PhD student at ETH Zürich, and Dr. Simon Craggs, at the time PhD student at RHUL, for field guidance, recommendation of field areas, discussion, and provision of additional sample material.

This work was funded by grants from NERC, the RHUL DoES Research Commitee and the UoL Central Research Fund. The PhD position was supported by a RHUL Thomas Holloway studentship.

Units and abbreviations

The following abbreviations and acronyms are used throughout the present work.

cps ..... counts per second

FEP ..... Tetrafluoroethylene-Perfluoropropylene

ICPMS ..... Inductively coupled plasma mass-spectrometry

LA-ICPMS ..... Laser ablation ICPMS

MC-ICPMS ..... Multi-collector ICPMS

PE, HDPE, LDPE ..... Polyethylene, high-density or low-density

PFA ..... Perfluoroalkoxy

PP ..... Polypropylene

ppb ..... parts per billion, factor 10^{-9}

ppm ..... parts per million, factor 10^{-6}

PS ..... Polystyrene

PTFE ..... Polytetrafluoroethylene

RHUL ..... Royal Holloway, University of London

Additionally, SI units and prefixes (e.g. ml, MΩ) are used. Non-Si units are avoided and their respective conversion to SI units used, where required.

Common derived non-SI units of time and their abbreviations are used in the text: min (minute), h (hour), d (day), a (year). As common in Earth Sciences, the non-SI symbol “a” for annum is combined with standard SI prefixes to form ka (thousands of years), Ma (millions of years) and Ga (“billions” of, i.e. 10^9 years). This work follows the recommendations in Holden et al., 2011, using “Ma” to indicate both “x million years before present” and “a duration of x million years” (see Christie-Blick, 2012 for a discussion and alternate notations).

Structural geological data like fault planes, fractures and slip directions on slickensides are given as azimuth of dip direction (clockwise from the north) and dip angle in "three digits / two digits" notation (e.g. 076/25 denotes a feature dipping down 25º from the horizontal towards the ENE). Abbreviations fp for fault planes, l for linears (usually, a slickenfibre, occasionally numbered l1, l2, and so forth to denote different movements on the same fault plane), j for joints and fractures, fa for fold axes, ss for sedimentary bedding, s for cleavage and so on are used to identify features, sense of movement is given as sn (sinistral), dx (dextral), up (up) or dn (down). Thus, an example of a fault plane with slickenfibres and sense of movement would be:

fp 328/76 l 237/05 sn

1. Introduction

1.1 Project aim

In this study, we evaluate and develop U-Pb dating of tectonic carbonates as a new method to directly determine the age of brittle deformation (see chapter 2.1 for a definition of "tectonic carbonates"). This method could yield unprecedented insight into not only tectonic processes on a plate-tectonic and regional scale, but potentially also into the faulting process. Applications could involve studies of regional tectonic evolution, fault zone and single fault evolution and fault kinematics (e.g. duration of activity and seismicity), but also commercial applications like fracture sealing ages in hydrocarbon reservoirs or ore deposits.

1.2 Approach

Together with local collaborators, we chose sampling areas in various regions of the Alps where the deformation ages are well established in the literature, to have a control on the results of our method (see chapters 2.2 and 6.4). All samples were screened by single-track profiling and occasionally 2D mapping with laser-ablation inductively coupled mass spectrometry (LA-ICPMS) for their major and trace element contents and distribution, in particular for an elevated U/Pb ratio (chapters 4.7 and 4.8). Samples with a favourably high U/Pb ratio and high enough concentrations in these elements were further subsampled, dissolved, mixed with an isotopic "spike", and U (and Th) and Pb were separated with extraction resins (see chapter 4.3 and 4.4). The wet-chemical workflow involved was optimised towards small sample sizes and minimal procedure blanks (see chapters 4.4.1 and 4.12.2). Isotopic ratios were determined with multi-collector (MC-) ICPMS (chapter 4.10). Alternatively, isotopic ratios were measured directly by LA-ICPMS, albeit with much lower precision (see chapter 4.9). From the isotopic ratios, crystallisation ages, assumed to be deformation ages, were calculated (chapters 3.2, 4.10 and 4.12.3).

1.3 Previous work

Isotopic dating of Tectonic deformation

To unravel the geodynamic evolution of an area, regional tectonic studies must involve the timing of the movements and deformation of geological units. Whereas the relative sequence of deformations can usually be deduced from direct observations on the map- to microscopic scale (see e.g. chapters 2.2.1 and 4.2), the absolute ages of the individual processes involved are determined with isotopic dating methods.

Depending on the specific geological setting, any dating technique might yield information that is relevant to the tectonic evolution of an area. Only the most commonly applied techniques are mentioned here in a short overview of applications to tectonics, without background information on the principles and methodology for each technique. An introduction to U-Pb dating, with focus on carbonates, is given in chapter 3.2, further information on the other techniques can be found in the relevant literature (see in e.g. Faure & Mensing, 2005; Zou, 2007; Gill, 1997; Banner, 2004).

In principle, a distinction can be made between indirect methods of determining deformation ages, based on reconstructing the respective movements of homogeneous areas/fault blocks (e.g. thermobarometry combined with dating of metamorphosis, thermochronology, exposure dating, paleomagnetism), and direct dating of fault activity as recorded in materials newly formed or geochronologically reset within fault zones (e.g. fault gouges, pseudotachylytes, syntectonic intrusions and the main topic of this study: slickenfibres and fracture fills).

Classical isotopic systems in use are based on the growth of a daughter nuclide from the radioactive decay of a parent (see chapter 3.2.1), e.g. K-Ar, $^{40}Ar/^{39}Ar$, Rb-Sr Sm-Nd, Lu-Hf, and U-Pb. This assumes the system (mineral of interest) to behave as a closed system since the dated event. Due to diffusion of parent-, daughter- or intermediate nucleides out of (or into) the crystal lattice, each mineral exhibits a certain *closure temperature* (T_c), below which no significant loss (or gain) occurs, and above which the isotopic system is reset. Thus, isotopic ages for many isotopic method/mineral combinations are not actually formation ages, but cooling ages below T_c. For different

isotopic systems (elements) within the same mineral, T_c differs due to different diffusion coefficients; so potentially, several cooling ages from different isotopic systems can be determined on the same mineral, allowing to reconstruct the cooling history (e.g Berger & Bousquet, 2008; Bousquet et al., 2008; Blanckenburg et al., 1989; Freeman et al., 1998; see also "Thermochronology", below).

Tectonic processes can be dated if they cause the growth of minerals which these methods are applicable to on structures associated with the deformation. Dating the metamorphosis within fault blocks (combined with P-T information from thermobarometry) and inferring the relative movements can indirectly date fault activity (e.g. Müller, 1998; Müller, 2003; Krohe, 1987; Essene, 1989; Bousquet et al., 2008; Blanckenburg et al., 1989; Cliff, 1985; Fossen & Dallmeyer, 1998; Mezger et al., 1991). More directly, the formation of mylonites on ductile and semi-brittle faults can be dated (e.g. Müller et al., 2000a; Costa & Maluski, 1988; Freeman et al., 1998; Dunlap et al., 1991; Kralik et al., 1992; Lips et al., 1998; Müller et al., 2000a; Rolland et al., 2009; Shaw et al., 2001; Shibata & Takagi, 1988; Sherlock et al., 2004; Wang & Lu, 2000; Leloup et al., 1993), as can the rarer cases of intrusion of igneous rocks into a fault zone (e.g. Ring & Collins, 2005; Pomella et al., 2010; Glodny & Hetzel, 2007). Müller et al., 2000b, dated growth increments of micas grown in the pressure shadow of porphyroclasts in a shear zone, obtaining not only the age of deformation, but also the duration. A combination of different techniques (including those mentioned below) yields a more comprehensive picture of the geodynamic evolution of an area (e.g. Mancktelow et al., 2001; Müller, 1998; Müller, 2003; Cliff, 1985; Bousquet et al., 2008; Essene, 1989; Csontos & Voros, 2004; Freeman et al., 1998; Berger & Bousquet, 2008).

The dating of clay minerals formed in fault gouges, and of pseudotachylytes, both formed on brittle faults, is widely applied, see "Dating brittle faults" below.

U series dating is based on the fact that due to the half lives of the daughter nucleides in the chain of radioactive decay, it takes a certain time (~1Ma) to establish secular equilibrium (see chapter 3.2.1) in a system. During that time, isotopic disequilibrium allows to determine the time since formation (or reset). This technique is the method of choice in age determinations for studies of relatively young samples

(younger than ~550 ka), e.g. in Quarternary research, palaeoclimate studies, archaeology and palaeontology.

Thermochronology is the combination of different temperature-sensitive geochronometers to reconstruct the cooling history of a sample. From this, exhumation ages and -rates, and thus fault activities can be inferred (e.g. Fillipone et al., 1995). Common methods in use are Rb-Sr and K-Ar mentioned earlier, (U-Th)/He and fission track dating. In fission track dating, T_c is the temperature above which the system contains enough energy to continuously heal the radiogenically induced defects in the crystal lattice (the "fissures"). For the (U-Th)/He method, T_c is the temperature below which the radiogenically produced He can not (significantly) escape the host mineral.

Exposure dating like the cosmogenic nucleides and OSL methods, determine the time since exposure or burial of a sample (respectively), which can yield information on tectonic processes, depending on the local geological situation (e.g. Ritz et al., 1995).

Paleomagnetism has been used to date pseudotachylytes on fault planes, and thus the tectonic process causing their formation (e.g. Eide et al., 1997; Torsvik et al., 1992). Indirectly, tectonic movements have been deduced from the relative movements of tectonic blocks, observed by palaeomagnetism of sediments or magmatic rocks in these blocks (e.g. Channell et al., 1992; Csontos & Voros, 2004; Marton & Fodor, 2003; Pomella et al., 2010; Thöny et al., 2006; Wortmann et al., 2001).

Direct dating brittle faults

Brittle deformation usually occurs in the uppermost crust, at relatively low temperatures. Thus, only few minerals grow syndeformationally that could record the faulting age. Various attempts have been made to directly date brittle deformation (see e.g. in van der Pluijm et al., 2001). The most common techniques are isotopic dating of syndeformationally grown clay minerals and micas in fault gouges by use of the *K-Ar*, $^{40}Ar/^{39}Ar$ and *Rb-Sr* method and combinations thereof (e.g. Lyons & Snellenburg, 1971; Kralik et al., 1987; Shibata & Takagi, 1988; Takagi et al., 1991; Tanaka et al., 1995; Kosaka & Chikashige, 2002; Tanaka et al., 1992; Wang et al., 2009; Kralik et al., 1992; Zwingmann et al., 2004; Choo & Chang, 2000; Kosaka & Chikashige, 2002van der

Pluijm et al., 2006; Och et al., 2009). Parry et al., 2001, combined $^{40}Ar/^{39}Ar$ with apatite fission track dating of the exhumation of the adjacent blocks. Bonhomme et al., 1987, dated clays from within (later) mineral-filled fractures by the K-Ar method. Different grain size fractions from fault gouges commonly give different ages, which is due to alteration and continued/new growth of clay minerals, and has to be interpreted in the respective geological framework (see the works listed above).

Masuda et al., 1995, studied the the behaviour of Pb isotopes in fault gouges and the implications for U(Th)-Pb dating of this material. Eyal et al., 1992, used U/Th dating of carnotite slickenfibres on brittle faults. Plan et al., 2010, use this dating technique on deformed carbonate speleothems to deduce fault activity on the fault cutting the investigated cave.

Bar et al., 1974, used fission track dating of epidotes from fault planes and correlated fractures to date fault activity. *Thermoluminescence* of fault gouges can also be used (Banerjee et al., 1999).

Dating of *pseudotachylytes* by isotopic methods (e.g. Kohút & Sherlock, 2003; Müller et al., 2002), fission track dating (e.g Murakami & Tagami, 2004) or palaeomagnetism (e.g. Eide et al., 1997; Torsvik et al., 1992) can very exactly determine the age of their formation.

Electron Spin Resonance (ESR) dating (Grün, 1989) has been used to determine the age of minerals grown on fault planes (e.g. Ikeya et al., 1982) and fault gouge (Buhay et al., 1988).

As mentioned earlier, a combination of methods will lead to a more comprehensive picture of tectonic evolution, as demonstrated in e.g. Zwingmann & Mancktelow, 2004, Siebel et al., 2010, Zwingmann et al., 2010, or Kralik et al., 1992.

Laser ablation

Laser ablation has been applied to analyse a wide range of samples for various applications (see e.g. in Durrant, 1999; Günther & Hattendorf, 2005; Fryer et al., 1995). LA-ICPMS combines the advantages of microsampling by laser ablation (easy sample preparation and rapid sample throughput, high resolution, in situ spatially resolved analysis) with those of analysis by ICPMS (ppb detection limits, wide elemental coverage and a linear dynamic range of up to 9 orders of magnitude ; Durrant, 1999; Fryer et al., 1995).

The method has been extensively used for the multi-elemental microanalysis of various geological materials (e.g. Günther et al., 1997; Jackson et al., 1992), single mineral grains (e.g. Jeffries et al., 1998) and the in situ determination of isotopic ratios – see e.g. "In situ LA-ICPMS U-Pb dating" below, but it has also been used for many other isotopic systems. Because the ablation process and the ICP ion source respond robustly to a wide range of different analytes (Durrant, 1999; Günther & Hattendorf, 2005), the method can also be applied to e.g. fluid inclusion studies (e.g. Günther et al., 1998), metallurgical studies (e.g. in Günther & Hattendorf, 2005; Arrowsmith, 1987), melt inclusions (e.g. Halter et al., 2004), and in material sciences, biological sciences and forensics (see e.g. in Günther & Hattendorf, 2005).

LA-ICPMS analysis of isotopic ratios has been used in archaeological studies, e.g. to classify glazings on ceramics with minimal sample damage (Resano et al., 2008).

Sinclair et al., 1998, used LA-ICPMS to reconstruct high-resolution seasonal patterns in the isotopic composition of corals. Hathorne et al., 2009, analysed trace element variations in foraminifera tests, to reveal variations in environmental factors and throughout ontogeny. Teeth are of special interest for high-resolution geochemical and isotopic studies, because of their continuous record over time of growth and their good preservation potential in the fossil record (e.g. Eggins et al., 2003; Müller et al., 2009a). Hoffmann et al., 2008, demonstrated the advantages of the high spatial resolution obtainable to aid in multi-method fission track, TIMS and ESR analyses of fossil equid teeth. Duval et al., 2011, also worked on fossil equid teeth, but used LA-ICPMS to map U and Th isotopic ratios in high resolution. The principle of using an

array of spot- or single-track LA-ICPMS analyses to construct two-dimensional trace- and major element maps has been utilised on geological and biological materials e.g. by Woodhead et al., 2007, and Ulrich et al., 2009. Dedicated software for this purpose greatly facilitates the data processing involved (e.g. Hellstrom et al., 2008; Rittner & Müller, 2012).

Current developments move towards shorter wavelengths, shorter pulse durations and the utilisation of alternative mass spectrometer designs (TOF, magnetic sector, ion trap), to further reduce problems of e.g. mass fractionation, analyse smaller samples and to open new areas of application.

In situ LA-ICPMS U-Pb and U-series dating

The benefits of LA-ICPMS (see above), offering potentially high-precision elemental and isotopic analysis at high spatial resolution/small sample size, make this method of analysis very attractive for in situ isotopic studies.

Early studies like Fryer et al., 1993, analysing pitchblende ores and zircons, established in situ U-Pb dating by LA-ICPMS.

Stirling et al., 2000, combined LA with a multi-collector magnetic sector ICPMS (LA-MC-ICPMS) to attain high-precision in situ measurements of ^{238}U-^{234}U-^{230}Th isotopic ratios. Eggins et al., 2003, analysed ^{238}U and ^{232}Th for U-series studies on fossil teeth, and Eggins et al., 2005, describe the possible merits of LA-MC-ICPMS U-series analyses in Quarternary geochronology.

Pickhardt et al., 2005, give an overview of various applications of in situ isotopic ratio studies on solid samples, comparing laser-ablation microsampling combined with quadrupole ICPMS (LA-ICP-QMS), with a double-focusing sector field ICPMS (LA-ICP-SFMS) and multi-collector magnetic sector mass spectrometer (LA-MC-ICPMS). Another overview of development and challenges of LA-ICPMS in various applications, especially for U(Th)-Pb dating, is given in Košler, 2007.

Woodhead et al., 2009, apply both LA-ICP-QMS and LA-MC-ICPMS to the problem of Pb-isotopic analysis of pyrite and compare strengths and limitations of the two approaches. Paton et al., 2010, address the problem of increasing fractionation effects during down-hole (single spot) analyses of zircons.

Fasset et al., 2011, present results from direct LA-MC-ICPMS U-Pb dating of Dinosaur bones and discuss possible further applications in vertebrate palaeontology.

U-Pb dating of carbonates

Previous studies have proven the feasibility of U-Pb dating of carbonates, laying the base on which the present study is based. Early works involve the whole-rock analyses of Moorbath et al., 1987, Smith & Farquhar, 1989, and Jahn et al., 1990. More detailed studies requiring higher resolution sampling followed, e.g. Smith et al., 1991, and Israelson et al., 1996.

The ongoing improvements in analytical methods aided in the further development of the method towards lower concentrations/smaller sample sizes, higher precision and new applications: Rasbury et al., 1997, and Rasbury et al., 1998, used the technique for dating of palaeosols, Wang et al., 1998, determined the age of calcretes and thus sedimentation age. Jones et al., 1995, studied the influence of diagenesis on U-Pb dating of marine biogenic sediments by combining various isotopic methods including trace element and Sr-isotopic analysis, pointing out the importance of testing for diagenetic alteration, but also demonstrating the potential of these rocks to retain a pristine formation composition. Richards et al., 1998, demonstrated the applicability of the method to speleothems, thus opening the age range for dating of speleothems beyond the limits of U-series dating. This was followed up by several authors, e.g. by Woodhead et al., 2006, pointing to applications in palaeoclimatology, or by Pickering et al., 2010; Pickering et al., 2011, to date archaeological sites of importance to early hominid evolution. Studies of sedimentation age of carbonate sediments benefited from the increasing precision of the method (e.g. Edwards et al., 2003) and applications to some less common sedimentary settings followed (e.g. Cole et al., 2005).

Overviews of techniques and applications of U-Pb dating of carbonates are given in Jahn & Cuvellier, 1994 and Rasbury & Cole, 2009, respectively. The latter mentions the possible application of U-Pb dating of carbonate slickenfibres for dating fault activity, an idea proposed earlier in Müller, 2003, but up to date, no studies on this use of the technique seem to exist in the literature.

2. Geological background

2.1 Tectonic carbonates

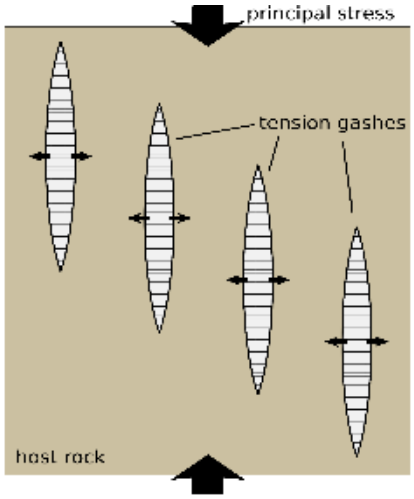

Fig. 1: Schematic tension fractures

In this study, the term *tectonic carbonates* is used as a summary term for fibrous carbonate mineral (mainly calcite) aggregates that grow syndeformationally on brittle fractures and faults. Common examples of these features are mineral fibres growing on slickensides (*slickenfibres)*, fibrous fracture fills (*veins* and *tension gashes*), fibrous aggregates growing in the pressure shadow of more competent components within a deformed matrix, and similar features. There are gradual transitions between these mentioned features, and it may sometimes not be possible to clearly classify a sample. All of these have in common, that mineral fibres grow keep growing during deformation and each new growth increment records the deformation direction at that time (Petit, 1987, Durney & Ramsay, 1973, Phillips, 1974, Wickham, 1973).

The exact mechanism forming these mineral fibres is still not fully understood and concurrent models have been developed from observations in different environments and experiments (see below). The basic principles are applicable to various minerals commonly found on faults and in fractures (e.g. quartz, calcite, chlorite), the individual behaviour of each of these minerals under a certain combination of pressure, temperature, pore fluid chemistry, host rock mineralogy and rheology, and deformation mechanism open a wide field of possible scenarios.

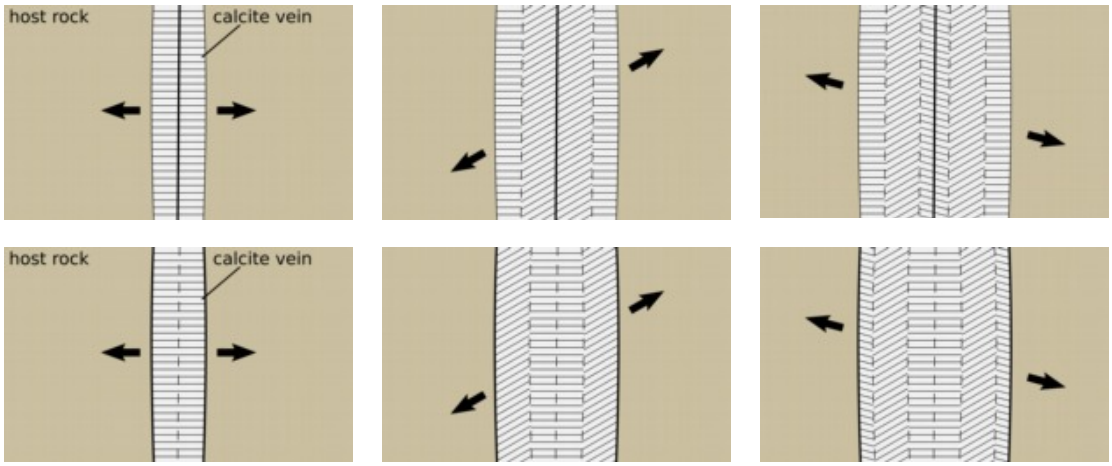

Fig. 2: Fibre growth in tension fracture
Multiphase mineral fibre growth in a syntaxial (top row, left to right) and an antitaxial tension fracture (bottom row, l to r). the same three deformation phases result in different growth patterns, depending on whether growth originates at the fracture walls (antitaxial) or on a central crack (syntaxial).

A widely accepted model is the *crack-seal mechanism* presented by Ramsay, 1980. To fill a fracture with mineral fibres, fluid must be present. Ramsay, 1980 suggest that this fluid might take part in the fracturing itself, by hydraulic fracturing. In each deformation increment, a small space would open antitaxially on one wall of the fracture, fluid would flow in from the pore space of the surrounding rock, and the relative drop in fluid pressure would facilitate precipitation from the pore fluid supersaturated by pressure solution in the surrounding host rock. In this model, the originally adjacent portions of the host rock can always be correlated exactly by following the direction of the mineral fibres.

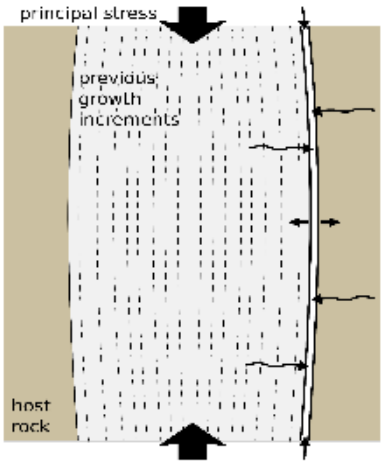

Fig. 3: Crack-seal mechanism
For each deformation increment, a crack opens (randomly either side of the fracture) and is healed by mineral fibres growing from the pore fluid.

Several authors (e.g. Urai et al., 1991; Cox, 1987) have presented natural case studies where the mineral fibres do not exactly trace the opposite margins, and Urai et al., 1991 present an expanded model involving recrystallisation and competitive crystal growth in the fracture. Hilgers et al., 2001 present a numerical model for this

mechanism. The more complicated case when portions of the host rock are (repeatedly) incorporated into the fracture fill is presented in Hilgers & Urai, 2002.

Renard et al., 2005 use the crack-seal patterns of large sets of fractures to reconstruct the continuous aseismic deformation of a rock body. Koehn & Passchier, 2000 define a classification for striped bedding-veins and determine the shear sense based on crack-seal pattern and inclusion tracks.

To elucidate the processes of vein formation and fibre growth during brittle deformation, analogue models have been built, utilising NaCl, KCl (e.g. Bons & Jessell, 1997) and other salts (e.g. Means & Li, 2001) to simulate naturally (slower) grown fibres of other minerals.

Bons & Jessell, 1997, and Means & Li, 2001, observed in their experiments antitaxial growth sustained by constant diffusional transport of solution from the host rock, not in a crack-seal mechanism. This explains much better the often observed perfect symmetry of fibrous fills around a central seam (the origin of growth in this model). They suggest the possibility that fibrous veins might in cases form due to crystallisation pressure and indeed not necessarily (only) during phases of tectonic deformation. Wiltschko & Morse, 2001, propose this as the main mechanism for fracture initiation in certain types of rock and see quartz-calcite banding as an expression of a fine kinetic interplay of solution concentration and pressure. In this view, fractures would originate at local inhomogeneities in the host rock or concentration maxima in the saturated pore fluid, and systematic arrangement of sets of fractures would follow a remote tectonic stress field, but would not entirely be caused by it. Elburg et al., 2002, support this view based on geochemical data from veins in an area in South Australia.

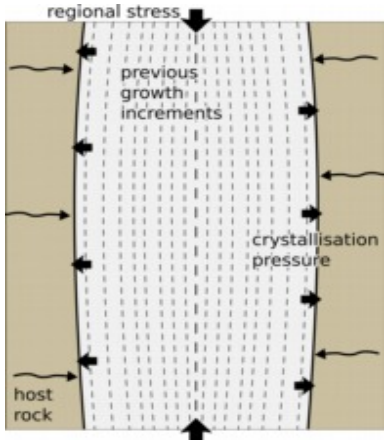

Fig. 4: Diffusion growth of mineral fibres
A constant supply of saturated solution from the host rock causes the mineral fibres to grow, crystallisation pressure widens the fracture.

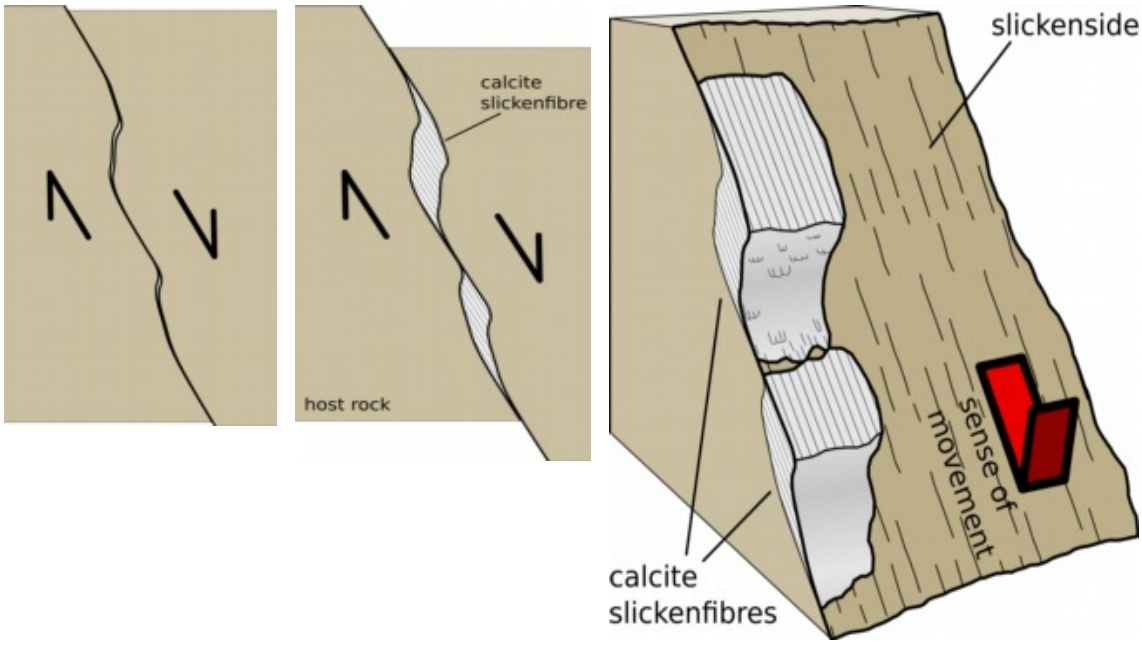

Fig. 5: Slickenfibre growth
Irregularities on the initial fracture will lead to opening of space (cf. pull-apart structures), small deformation increments will lead to fibrous mineral growth in a crack-seal mechanism (see above). Left: initial stage. Middle: with slickenfibres developed. Right: block diagram showing the faultplane.

However, there can be no doubt that the direction of slickenfibres on brittle faults, the main type of samples analysed in this study, records actual tectonic movements on this fault (Petit, 1987). Irregularities on the fault plane will, when the two opposing fault blocks are offset by tectonic movement, result in the opening of space where a protrusion from one block moves out of its indentation in the other. The resulting space is in many cases filled by slickenfibres (see Fig. 5), growing syndeformationally and at the same rate of movement. For slickenfibre growth, a crack-seal mechanism is most likely, the fibre growth will be controlled by the increments of tectonic movement (resulting in opening of cracks). Conceptually, the mineral-filled voids can be thought of as small pull-apart structures. Over time, protrusions on the fault plane may be broken off the host rock and ground into progressively finer fragments, forming fault breccias and fault gauge, resulting in an overall smoothing of the fault plane, but the slickenfibres, filling former indentations, are unlikely to be removed.

Fig. 6: Normal fault
Natural normal fault (left block down) with slickenfibres, fault plane superimposed. Near Kilve, Somerset.

Fig. 7: Slickenfibre
Detail of the fault plane on the previous page. Chisel for scale. Near Kilve, Somerset.

Fig. 8: Tension gashes
Several generations of en-echelon tension fractures in dark limestone. Chisel for scale. Valais, Switzerland.

2.2 Sampling areas, geological background and structural geology

Sampling areas were chosen along the Alpine orogen in diverse settings, so as to yield:

- a spectrum of various lithologies hosting the calcite samples
- different tectonic settings
- a range of deformation ages – ideally known independently through other geochronological or biostratigraphic dating methods

Together with local collaborators (Neil Manktelow, ETH Zürich, Switzerland; Michael Wagreich, University of Vienna, Austria; Hugo Ortner, University of Innsbruck, Austria; Franz Neubauer, University of Salzburg, Austria), sampling sites known to exhibit well developed tectonic carbonates were determined. Areas of relatively young age of deformation (mostly Tertiary) were preferred to minimise the potential of later alteration of the samples. The sampling area Digne (DGN) was chosen because of ease of visit during the annual RHUL 3rd-year mapping course, because it contains highly deformed carbonate units up to very young ages of deformation, and because from former years, calcite fibres were known to occur. Samples from the Swiss Jura mountains were provided by Herfried Madritsch, NAGRA, Switzerland.

Additional samples were taken during a field trip with Chris Elders, Royal Holloway, University of London, to the Bristol channel near Kilve, Somerset, UK.

The aim of sample collection was to provide material to develop the analytical method presented in this work. It was not intended to perform a detailed regional study of any of the sampling areas or the Alps as a whole. Thus, the following geological descriptions of the individual sampling areas were kept short and general, the overview maps are strongly simplified, and local open questions and ongoing discussions are omitted.

2.2.1 Tectonic overview of the Alps

The Alps are a complex orogen formed in at least two orogenic phases in the closure and subduction of several smaller oceanic branches linked to the evolution of the Tethys and the North Atlantic ocean, and subsequent continent-continent collision between the Apulian plate and continental Europe.

In alpine orogenic evolution, typically an earlier upper Cretaceous *Eoalpine* phase is distinguished from the main orogenic phase in the upper Eocene to Miocene (e.g. Neubauer et al., 2000; Schmid et al., 2004; Dal Piaz et al., 2003).

In the upper Jurassic, opening of the North Atlantic ocean causes divergence of Africa (and Apulia) and Europe, opening the Piemont-Liguria ocean (or Penninic ocean, also referred to as Alpine Tethys) north of Apulia (Stampfli, 2000; Stampfli et al., 2001a; Stampfli et al., 2001b). For a discussion of the pre-Alpine (Upper Jurassic) palaeogeographic and plate-tectonic evolution of the Adriatic plate and its surroundings, see also Wortmann et al., 2001.

In the upper Cretaceous Eoalpine phase, collision east of Apulia after closure of the Meliata-Hallstatt (or/and Vardar) ocean, a westernmost subbasin of the Tethys (Csontos & Voros, 2004; Channell & Kozur, 1997; Mandl, 2000; Stampfli et al., 2001a), forms the *Austroalpine* nappe stack in a generally top to the W motion (Dal Piaz et al., 2003; Schmid et al., 1996), possibly with locally more N-S and E-W trends due to strain partitioning (Ortner, 2001b). Subsequently, the Austroalpine is kinematically to be considered part of Apulia. North of the Apulian plate, subduction of the Piemont-Liguria ocean begins, but most other units of the future Alpine orogen (especially the Western Alps) are unaffected by the Cretaceous orogeny (Schmid et al., 1996).

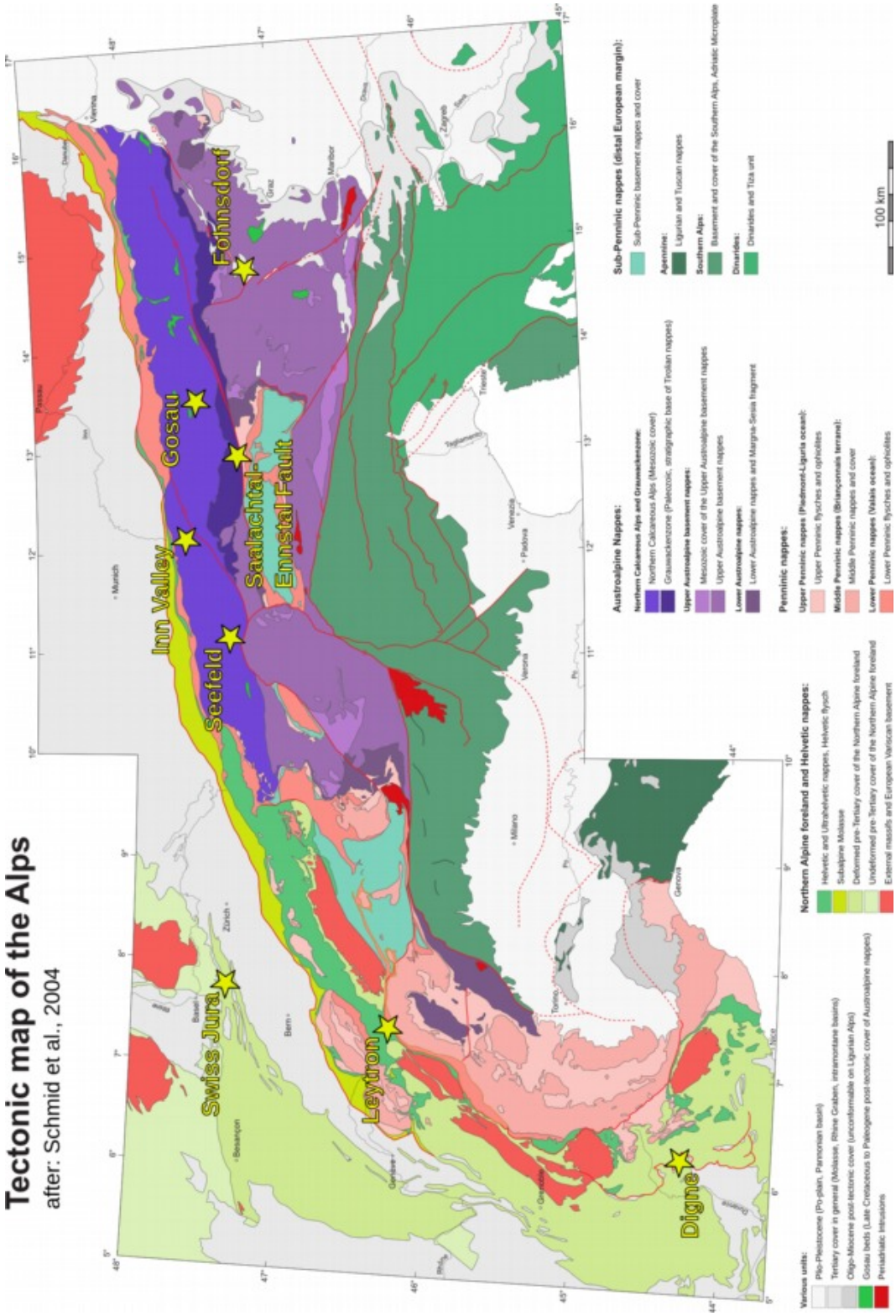

Fig. 9: Tectonic map of the Alps
Sampling areas are marked by a star. Simplified after Schmid2004.

During the following oblique subduction of the Piemont-Liguria (/Penninic) ocean, Apulia is in an upper tectonic position. The Eastern Alpine units (as part of Apulia) undergo subsidence and extension in a sinistral transpressional setting (Schmid & Kissling, 2000; Schmid et al., 2004). Pull-apart basins open, and the widespread sedimentation of the upper Cretaceous to Eocene *Gosau Group* fills the topography on top of the Austroalpine wedge (Willingshofer et al., 1999; Neubauer et al., 2000; Wagreich & Faupl, 1994; Ortner et al., 2008). Most Gosau successions show a distinct division into a Lower Gosau Subgroup of terrestrial to shallow marine sediments and an Upper Gosau Subgroup consisting of deep water hemipelagic and turbiditic sediments (Wagreich & Faupl, 1994). The two Subgroups are divided by a phase of deformation and erosion, followed by rapid subsidence (Wagreich & Faupl, 1994).

In the Late Eocene, the Ligurian (/Penninic) ocean is closed, Apulia collides with continental Europe commencing the main Alpine orogeny (Schmid et al., 2004). Due to flexural load of the upper plate, foreland basins begin to form on the European continental crust north of the orogen (Neubauer et al., 1995). The motion of Apulia relative to Europe during collision results in stress partitioning, with N-S convergence in the northern Alpine units, while central Alpine units experience sinistral wrenching and block rotations (Neubauer et al., 1995). Likely, a precursor to the later Periadriatic Fault (see below) formed at this time (Neubauer et al., 1995). Further shortening is consecutively conveyed by the *Southalpine Indenter* (or Adriatic Indenter), a protrusion of the Apulian plate that is driven into the central and Eastern Alps and by its shape significantly influences the further tectonic structuring of the orogen (e.g. Neubauer et al., 1995; Schmid et al., 2004; Schmid & Kissling, 2000; Linzer et al., 2002). The northern boundary of the Indenter is the *Periadriatic Fault*, a large-scale fault marking the boundary of the Northern and Central to the Southern Alps. At this line, vergence of structures and nappe stacking changes from generally northwards in the North, to southwards in the Southalpine units (Schmid et al., 2004; Neubauer et al., 1995). Anticlockwise rotation of the Southalpine Indenter and change in the relative movement of Europe and Africa caused major dextral movement on the Periadriatic Fault in the Oligo-Miocene (Müller et al., 2001), which at the western termination is transferred along the Rhone-Simplon-Line into contraction and transport in the Western Alpine

Arch, and even causes deformation in the Molasse basin and the Swiss Jura mountains (Schmid et al., 2004, see also below).

At around the Early/Late Oligocene boundary, the subducted Penninic oceanic crust detaches from the European plate (slab break-off), resulting in rapid growth of relief, as evidenced by the first occurrence of large conglomerate fans in the northern Molasse basins (Frisch et al., 2000; Kuhlemann & Kempf, 2002; Kuhlemann, 2007). The exact causes for orogen uplift in the different segments of the Alps (West, Central, East) differ and are still discussed, especially in respect of the relative influence of climatic conditions (erosion) and tectonic forces (see e.g. Rosenberg & Berger, 2009; Champagnac et al., 2009; Wölfler et al., 2011) Relief increase and weakening of the orogenic base by increased heat supply after slap break-off, together with the localised, wedge-shaped contraction due to the Southalpine Indenter (causing further mountain build-up), resulted in the Miocene *Lateral Orogenic Collapse* (or *Lateral Extrusion*) of the central Eastern Alps towards the East (Frisch et al., 2000; Linzer et al., 2002; Ratschbacher et al., 1991a; Ratschbacher et al., 1991b). Lateral orogenic flow was possible because rapid subduction rollback of the Carpathians had left the Pannonian basin filled with weak, thin crust (Neubauer et al., 2000; Ratschbacher et al., 1991a; Ratschbacher et al., 1991b; Neugebauer et al., 2001; Wölfler et al., 2011).

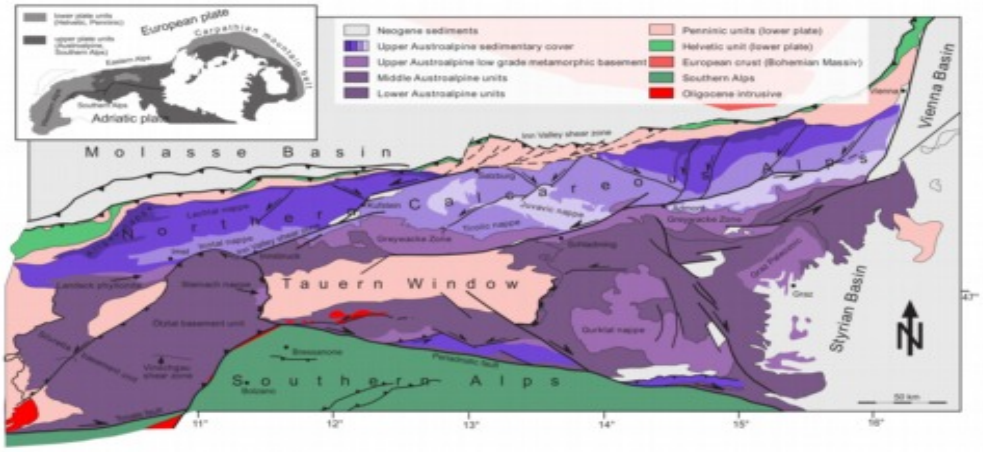

Fig. 10: Tectonic overview of the Eastern Alps. For location of sampling areas, see Error: Reference source not found (note different map extract).
After Ortner2001#587.

Lateral orogenic flow was largely a homogeneous, ductile flow in the lower, metamorphic Penninic units of the central Eastern Alps derived from the European continental margin, whereas the overlying Austroalpine units moved in rigid blocks delineated by ENE trending sinistral and SE trending dextral strike-slip faults (Neubauer et al., 2000; Schmid et al., 2004; Linzer et al., 2002). The southern boundary of the extruding Central Alpine units is the dextral Periadriatic Fault, the northern boundary was initially the sinistral Salzachtal-Ennstal-Mariazell-Puchberg fault (SEMP), but ENE-NE trending sinistral faults branch off this fault and cut through the Northern Calcareous Alps (NCA; e.g. Inntal fault, Königsee-Lammertal-Traunsee fault/KLT; see e.g. Linzer et al., 2002; Peresson & Decker, 1997). Large-scale, low-angle extensional shear zones (Brenner shear zone in the West, Katschberg shear zone in the East) delineate the exhumed and unroofed European units exposed in the Tauern Window as a result of the Lateral Extrusion (Frisch et al., 2000; Schmid et al., 2004). Lammerer & Weger, 1998, assumed a tectonic duplex structure to aid in explaining the rapid uplift of the Tauern Window of 20-30km since the Oligocene. Results from the TRANSALP deep seismic indicate a South-dipping ramp structure beneath the Tauern window, indicating an alternative/additional mechanism for the exhumation of the

Penninic units (Lüschen et al., 2006; Lüschen et al., 2004; Inntal shear zone Sub-Tauern ramp sensu Ortner et al., 2006).

Although mainly in a N-S compressional setting on a plate-tectonic scale, the mentioned changing stresses acting on the northern Eastern Alps throughout the Miocene have led to a complex sequence of deformation phases, mainly recorded in brittle fault movements (e.g. Decker et al., 1993; Ortner, 2003c; Peresson & Decker, 1997; Linzer et al., 2002) and in small intramontane sedimentary basins (e.g. Ortner & Stingl, 2001; Ortner, 2003b).

In the Late Cretaceous, the Valais and Piemont-Ligurian ocean dividing the Adriatic from the European plate were much wider in the West than in the East, thus more material was subducted in the Central and Western Alps than in the Eastern Alps, and onset of the oblique subduction and consequent tectonic phases resulting from the convergence tends to be earlier in the East than in the West (Bousquet et al., 2008; Schmid et al., 2004; Bousquet et al., 2002). However, on a smaller scale, fragmentation of units occurred, and a complex plate configuration (palaeogeography) can be assumed, resulting in a more complex distribution of the timing of metamorphic events along individual tectonic units (Berger & Bousquet, 2008; Bousquet et al., 2008).

The western Alpine arc started forming after the sinistral transpressional phase before 35Ma (Schmid & Kissling, 2000). After 35Ma, the Adriatic plate rotated anti-clockwise and movement of the Indenter changed to WNW, giving the western Alpine arc its bent shape (Schmid & Kissling, 2000). Kinematic decoupling from the Eastern Alps occurred along the Tonale-Simplon dextral shear zone (Schmid & Kissling, 2000). The Rhone-Simplon fault zone is suggested to act as a low-angle extensional shear zone similar to e.g. the Brenner shear zone, accommodating orogen-parallel flow similar to the Eastern Alps (Seward & Mancktelow, 1994; Hubbard & Mancktelow, 1992). From 12Ma onwards, stress transfer through the orogen to the foreland is responsible for deformation in the Swiss Jura mountains and in the Molasse basins (Schmid & Kissling, 2000). Flexural orogenic foreland basins (Molasse basins) are not well developed in the western Alps (Schmid et al., 2004). Neogene thick skinned thrusting in the European foreland resulted in exhumation of the external massifs (Schmid et al., 2004). Delacou

et al., 2004, determine the recent stress field in the western Alpine arc from earthquake focal mechanisms to be mainly due to gravitational flow of the thickest (highest) parts of the orogen perpendicular away from the crestline, resulting in a radial stress pattern along the arc (see also Delacou et al., 2005; Sue, 2003; Sue & Tricart, 2002). Eva et al., 1997, reach similar results from earthquake data of the internal and eastern parts of the south-western French Alps, and Champagnac et al., 2004, observe earlier orogen parallel escape and later orogen perpendicular collapse in palaeostress data from brittle faults. Selverstone, 2004, confirm the observation of the Western Alps being an area of active orogenic collapse today (the only recently active one in the Alps), and give a precise definition of gravitational orogenic collapse as opposed to other extensional features or tectonic extrusion in collisional mountain belts - only to suggest further to abandon the term and concept altogether, because in natural tectonic settings many different processes will be active and interact with each other at any given time.

2.2.2 Digne

The Digne nappe is the most external unit of the external fold-and-thrust belt (Ford et al., 2006) of the south-western Alps in Provence, France. Structural evolution involves early to mid-Oligocene stacking of thin skinned thrust sheets and Mio- to Pliocene reactivation of the frontal thrust of the Digne nappe (Lickorish & Ford, 1998). This younger reactivation is driven by the exhumation of the Argentera crystalline basement massif and associated out-of-sequence thrusts (Ford et al., 2006). Movement of the nappe front in the Pliocene is evidenced by thrusting over Pliocene Sections of the Valensole conglomerate in the foreland (Hippolyte, 2001; Hippolyte et al., 2011). Fournier et al., 2008, found evidence for bedding-parallel shortening due to NNE-SSW compression prior to folding late Miocene Valensole conglomerate at the front of the Digne nappe. Baroux et al., 2001, determined the recent stress field (and thus, potentially continuing thrust movements of the Digne nappe today) from inversion of earthquake focal mechanisms to be NE-SW contractional, which corresponds to GPS measurements by Jouanne et al., 2001, and the stress direction suggested by Hubbard & Mancktelow, 1992, to result from lateral orogenic extension SW of the Rhone-Simplon shear zone; Sanchez et al., 2010, suggest a more NNW-SSE stress field and associated dextral movements on the N-S oriented front of the Digne nappe.

Calcite slickenfibres were sampled from various small- and medium-scale fault planes and from bedding surfaces, as well as calcite tension gashes, from most stratigraphic units in the area (see Fig. 12). In the young Valensole conglomerate, slickenfibres occurred between larger clasts.

Only one outcrop (outcrop 300, see Fig. 11 and Fig. 15) yielded samples suitable for dating (KMR-DGN55, collected by the author, or D1W, provided courtesy of Dr. W. Müller, respectively), see chapter 5 Results. In this outcrop, massy Tithonian limestone is thrust onto marly limestone, in the lower parts of the outcrop "Green Molasse" (Miocene) and "Red Molasse" (Paleogene) occurs. The whole sequence is overturned, how much of the sedimentary succession between Thithonian and Paleogene was originally missing in a hiatus, and how much is due to tectonic processes, could not be determined. The overturned sequence likely represents the lower limb of the frontal

fault propagation fold on a medium-scale out-of-sequence thrust within the Digne Nappe.

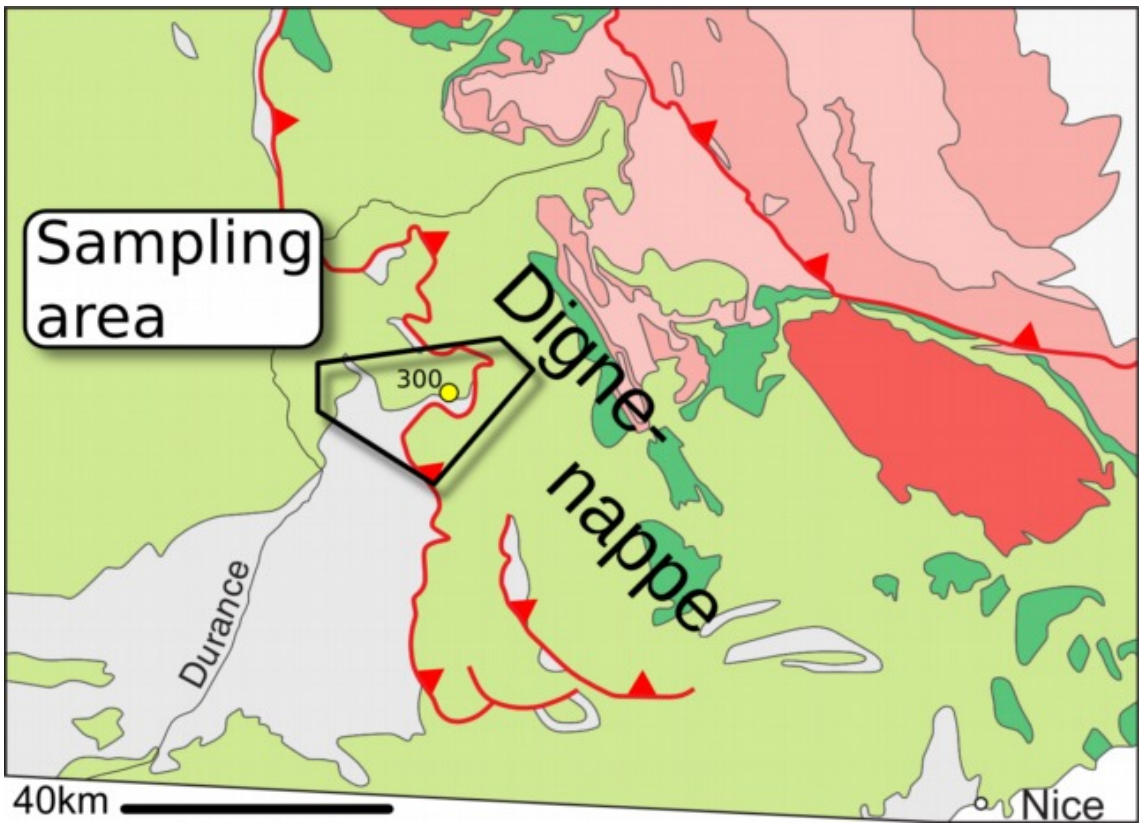

Fig. 11: Geological sketch map of the front of the Digne nappe complex
Sampling area simplified from 16 sampling sites. Outcrop 300 (see Fig. 15) for reference.
After Schmid2004, colour key see Fig. 9.

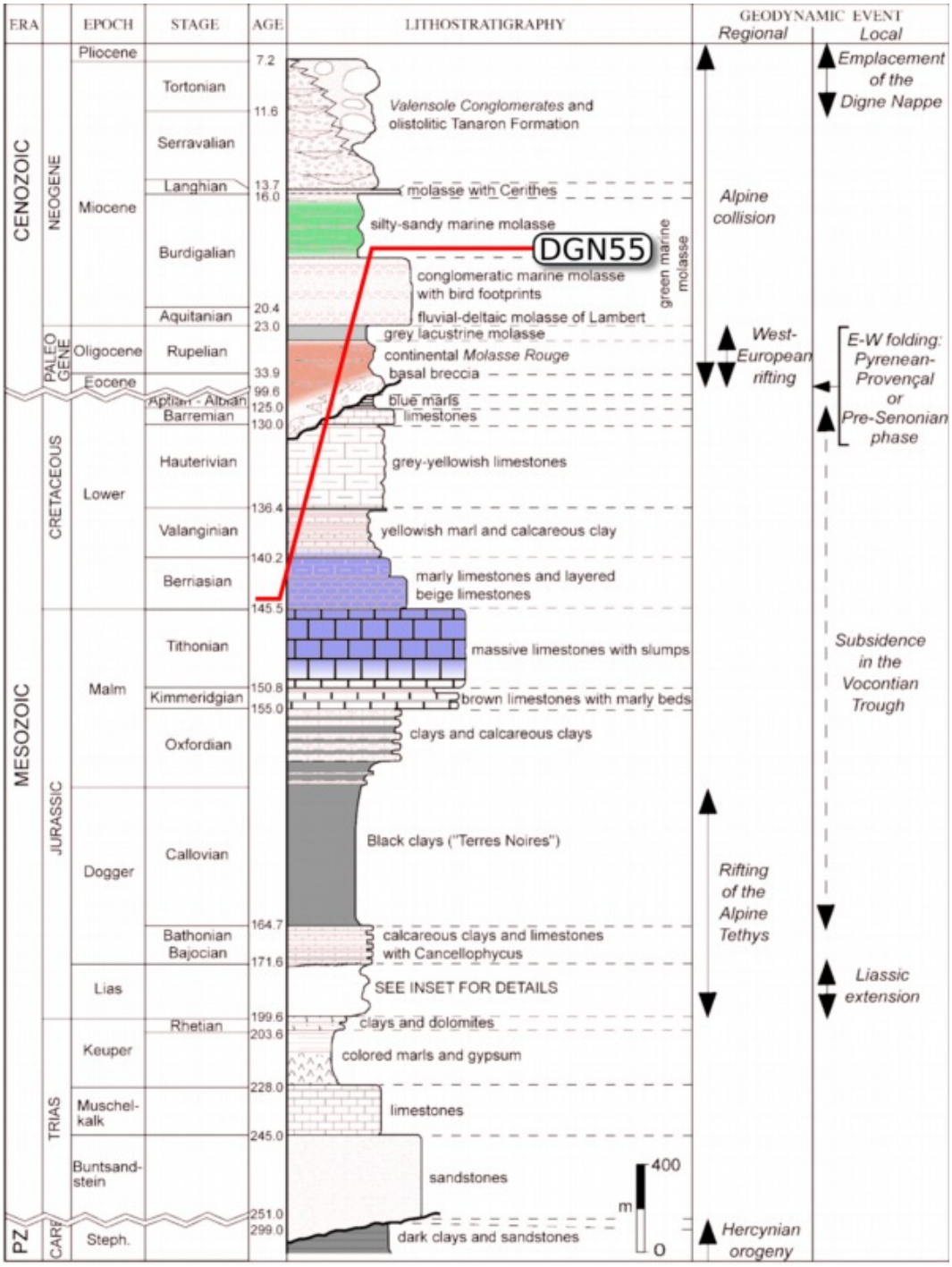

Fig. 12: Stratigraphic column for the Digne sampling area
Most stratigraphic units pictured were visited in the field, and tectonic structures from many were sampled. Only sample KMR-DGN55 proved date-able (see 5 Results). Coloured above are the stratigraphic units present at that locality (see Fig. 15, Fig. 16), albeit in the field the sequence is inverted. The faulted contact between Tithonian lime-stone and its overlying units, pictured above, was sampled. The position of the fault contact in the column does not represent faulting age, which was calculated as ~10-8 Ma.
Modified from Fournier2008.

Fig. 13: Right: Outcrop 159 Sampling location of KMR-DGN04. N-S striking, calcite-filled tension gashes up to 40 cm wide and several metres long in strongly deformed Lower Jurassic marly limestone.
Outcrop ~3 m high, chisel at middle-right for scale. View towards North.
Inset: stereonet of features, dashed: tension gashes, dotted: folded cleavage (possibly sedimentary bedding).

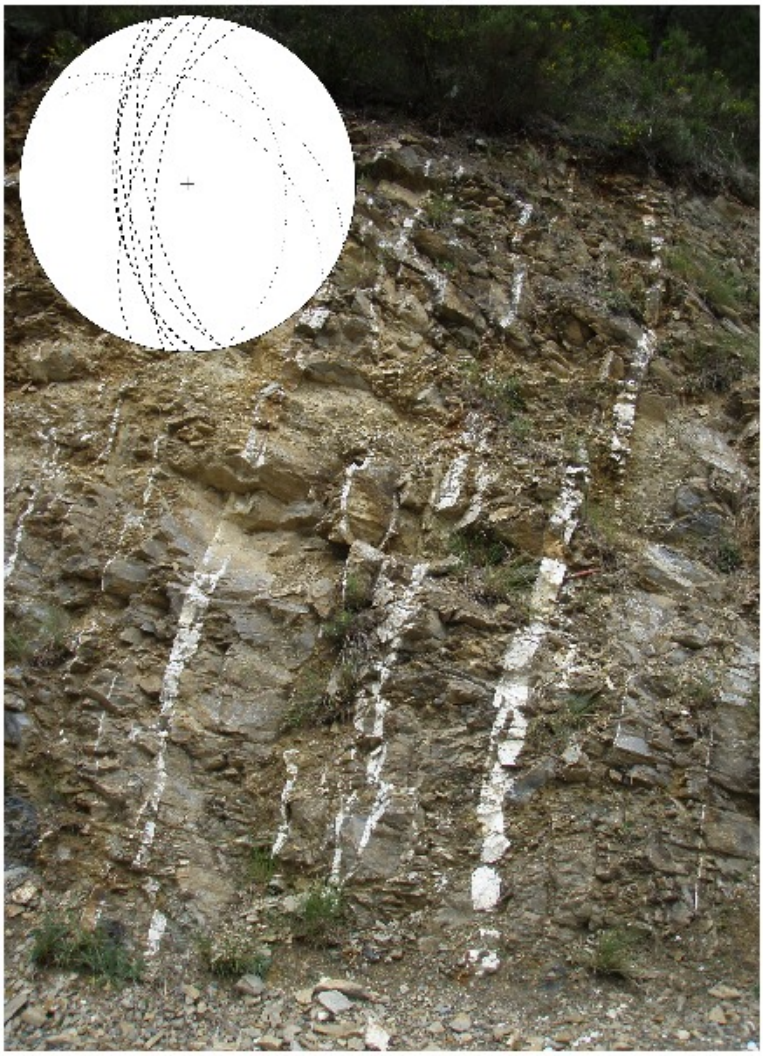

Fig. 14: Below: Outcrop 164 The Late Miocene Valensole Conglomerate shows slickenfibres between components and in fractures of cracked components. The photo shows sample KMR-DGN10A in situ before recovery. Bedding locally folded up to 084/53.

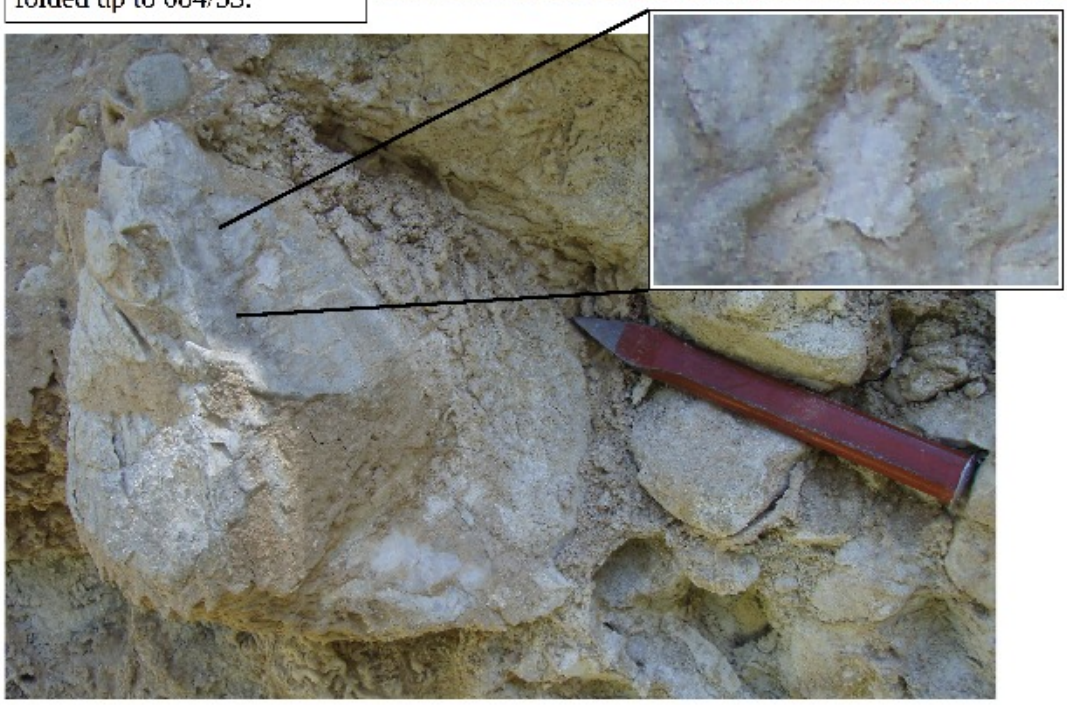

Fig. 15: Outcrop 300
Tithonian limestone thrust onto marly limestone of uncertain age, sequence inverted. Sampling location of KMR-DGN55e. View north, pictured outcrop height ~1.5 m.

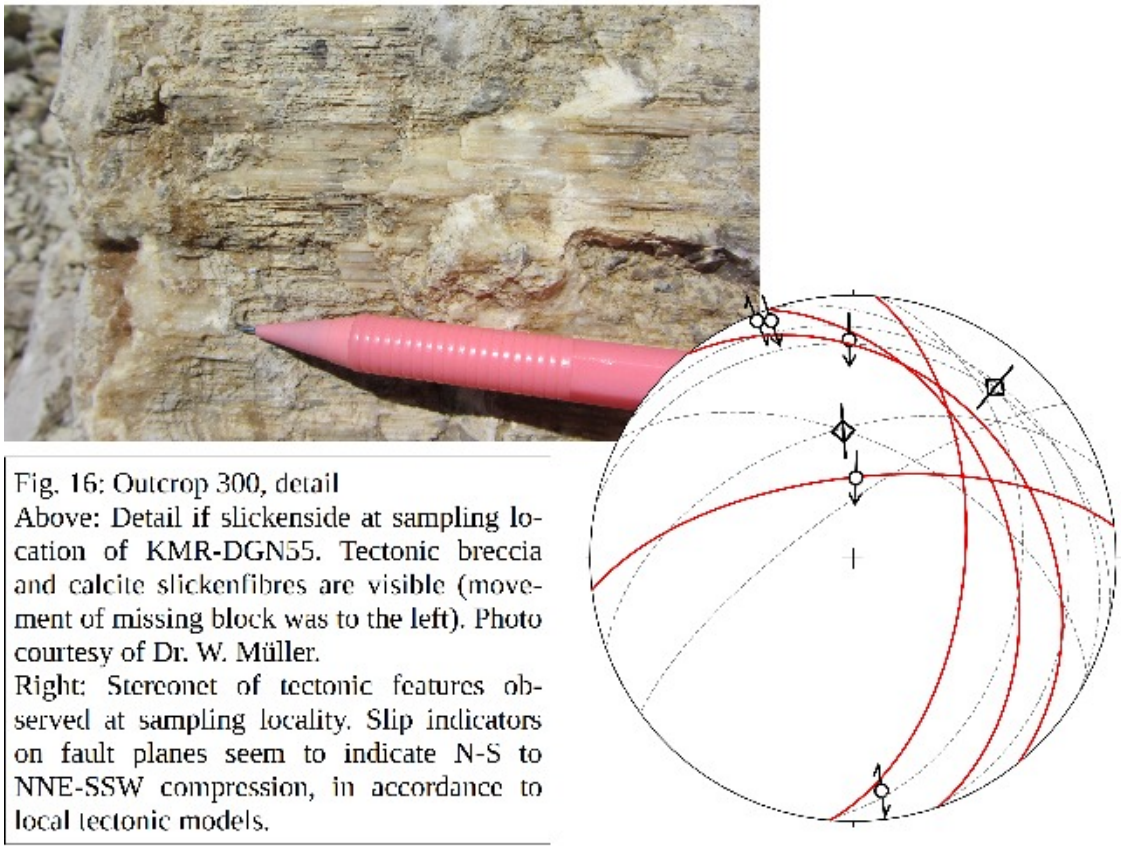

Fig. 16: Outcrop 300, detail
Above: Detail if slickenside at sampling location of KMR-DGN55. Tectonic breccia and calcite slickenfibres are visible (movement of missing block was to the left). Photo courtesy of Dr. W. Müller.
Right: Stereonet of tectonic features observed at sampling locality. Slip indicators on fault planes seem to indicate N-S to NNE-SSW compression, in accordance to local tectonic models.

2.2.3 Leytron

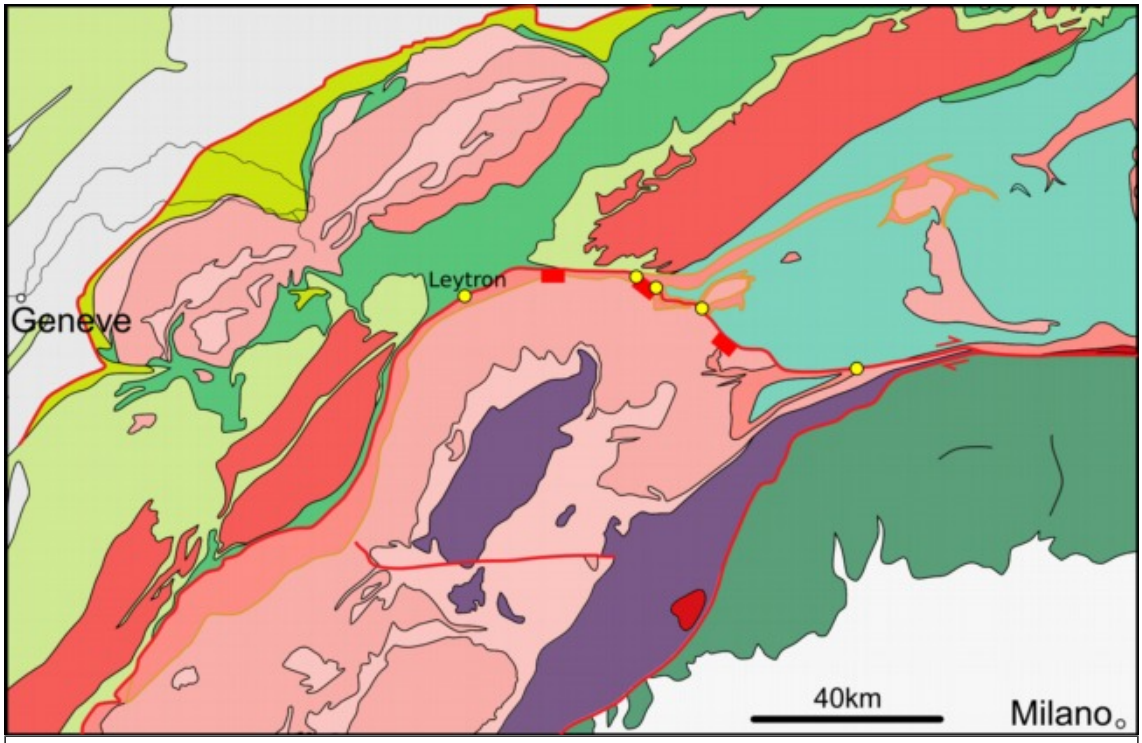

Fig. 17: Geological sketch map of the Valais sampling area
Yellow dots indicate sampling locations (simplified). After Schmid2004, key see Fig. 9.

Leytron is a small village in the "Valais", the upper Rhone valley. The Valais is the topographical expression of the contact of the Helvetic nappes in the SW to the Aar massif in the NE (part of the Rhone-Simplon shear zone). Although at approximately the same elevation today, the Helvetic units originally were in a higher tectonic position (thrust onto the European continental crust; Seward & Mancktelow, 1994; Hubbard & Mancktelow, 1992). The thrust contact is reactivated as a normal fault related to dextral strike-slip movement at the Simplon and Tonale fault further to the East (Schmid & Kissling, 2000; Hubbard & Mancktelow, 1992; see also 2.2.1 above).

Deformed sediments were sampled, containing harder clasts (fragmented belemnite fossils and pyrite crystals) in a homogeneously deformed fine-grained matrix, around which quartz and calcite crystallised in the pressure shadow of the clasts (Fig. 18). Other samples comprised calcite tension gashes in limestone (see Fig. 7 and Fig. 19).

Unfortunately, no samples from the Leytron area proved suitable for dating (see chapter 5 Results).

Fig. 18: Fractured Belemnite
Belemnite fossil (black), fractured during homogeneous deformation of the Lower Jurassic host rock. The voids between fossil fragments were filled with a fibrous calcite and quartz matrix that shows diffuse zoning of calcite dominating the margins, quartz dominating the central portions of the white infills. Outcrop 253, sampling location of KMR-LEY16. Coin for scale.

Fig. 19: Multiphase tension gashes
Valanginian limestone showing multiphase tension gashes (expected Oligocene or Miocene, pers. comm. N. Manktelow). Near outcrop 230, view down, North to the left, hammer for scale.

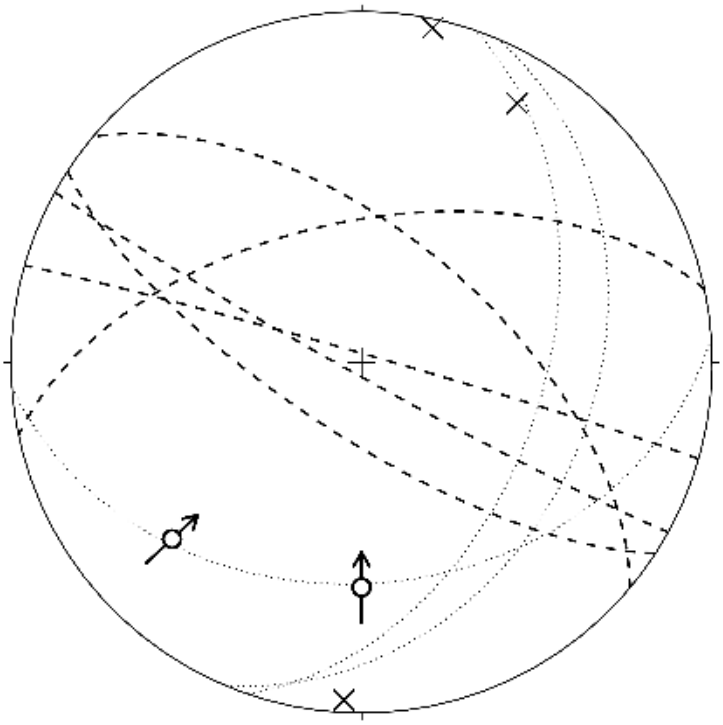

Fig. 20: Tectonic plot, Leytron area
Stereonet of tectonic features observed in the Leytron sampling area. Dotted lines: main cleavage, possibly overprinted sedimentary bedding planes. Crosses: stretching linears. Dashed: joints and tension gashes. All structures can be associated with a NNE-SSW stress field at the nappe contact of Helvetic units to the underlying Aar massif.

2.2.4 Gosau Basin

The sedimentary basin of Gosau formed as a pull-apart basin during upper Cretaceous to lowest Paleogene times (Wagreich, 1995; Wagreich & Decker, 2001). The Gosau group overlies the nappe stack of the Northern Calcareous Alps (NCA) unconformably, indicating an interval of erosion in the Middle Turonian (Wagreich & Decker, 2001). The Lower Gosau Group in the Gosau area comprises approximately 1000m of Upper Turonian to lower Campanian terrestrial and shallow water sediments, unconformably overlain by 1200m of Campanian to Paleogene deep-water sediments (Wagreich & Decker, 2001; Wagreich et al., 2010; Wagreich, 1988). Many faults in the area have been reactivated and overprinted in later (Miocene) phases of Alpine orogeny (see e.g. Peresson & Decker, 1997). Sampling comprised mainly slickenfibres from various faults in different kinematic settings within the basin.

The deformation phases established by Peresson & Decker, 1997, for the central Northern Calcareous Alps were used as the framework to put observed deformation structures into context. Peresson & Decker, 1997, established the relative sequence of six deformation phases from cross-cutting criteria observed in numerous outcrops along the NCA, and assigned absolute deformation ages from the stratigraphic ages of deformed units, especially in sediments of the Gosau Group and in younger (Miocene) sections in several sedimentary basins.

Sample KMR-GOB21 (outcrop 240, Fig. 25) yielded samples for some of the best age measurements in this study (see chapter 5 Results), two different directions of slickenfibres could be dated to distinct deformation ages (see Fig. 22 and Fig. 24). Sample KMR-GOB18 is not well constrained by structural field data, but the observations and obtained ages fit well into the regional structural model (see Fig. 24 and Fig. 26). At both locations deformation was expected to be associated with the Paleogene and Neogene kinematics on the Königsee-Lammertal-Traunsee fault line (pers. comm Wagreich, 2008) that passes by the Gosau Basin in a generally SW-NE direction to the North.

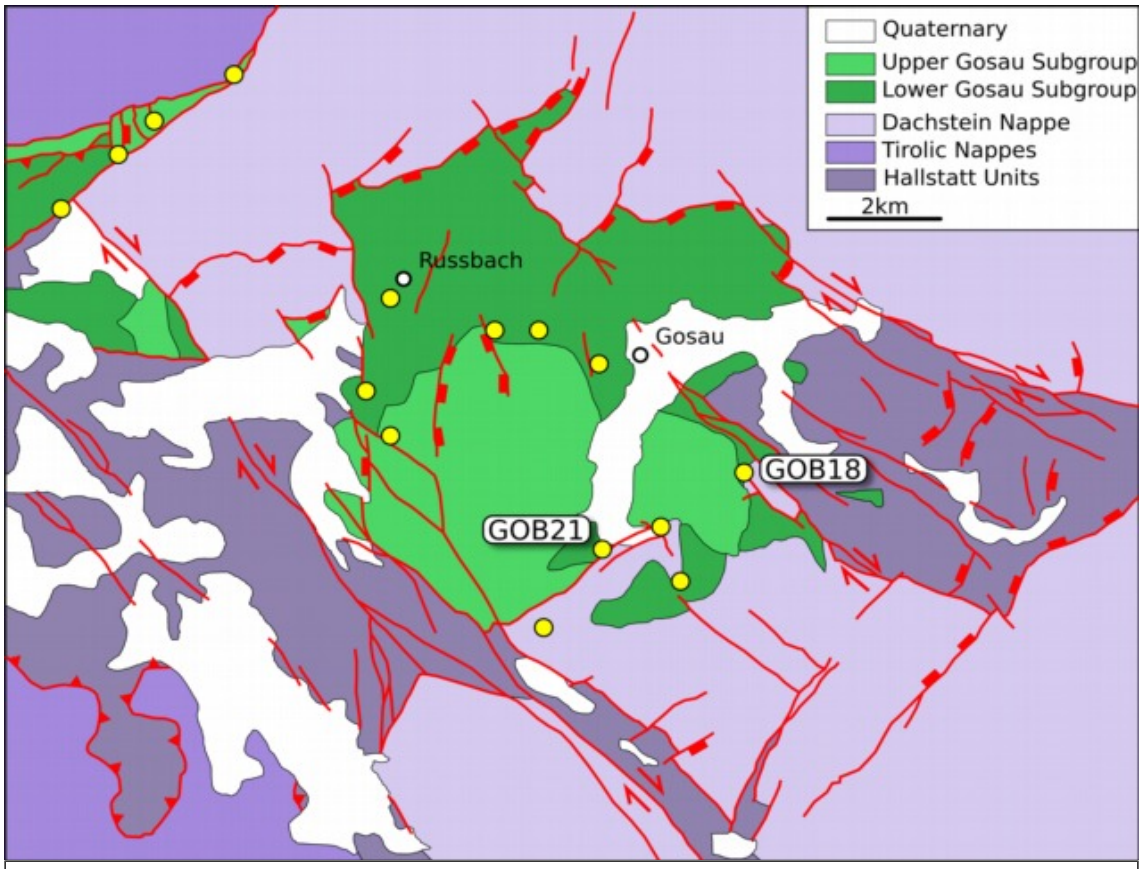

Fig. 21: Geological sketch map of the Gosau basin
Yellow dots: sampling locations (simplified). After Wagreich2001#282.

Fig. 22: Stereonet for Outcrop 240
Plot of tectonic features observed at sampling location. NE-SW trending sinistral strike-slip faults are dominant, the less steeply W-dipping dextral and reverse faults are secondary structures, one of which yielded sample KMR-GOB21.
Slickenfibres l2 were observed to be younger than the main calcite fibre package l1, although the stereonet illustrates that both could have originated in the same overall stress field. The observations indicate N-S to NNE-SSW compression, in accordance with deformation phase "T2" sensu Peresson1997#203 (Fig. 24).

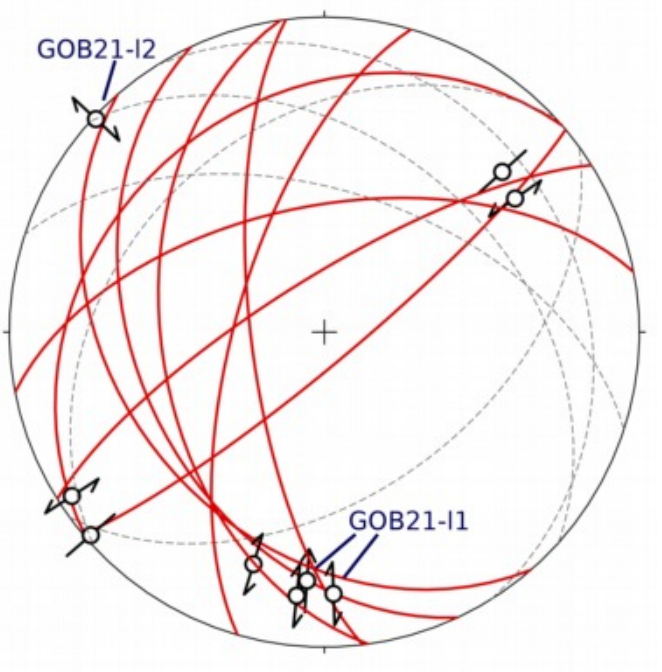

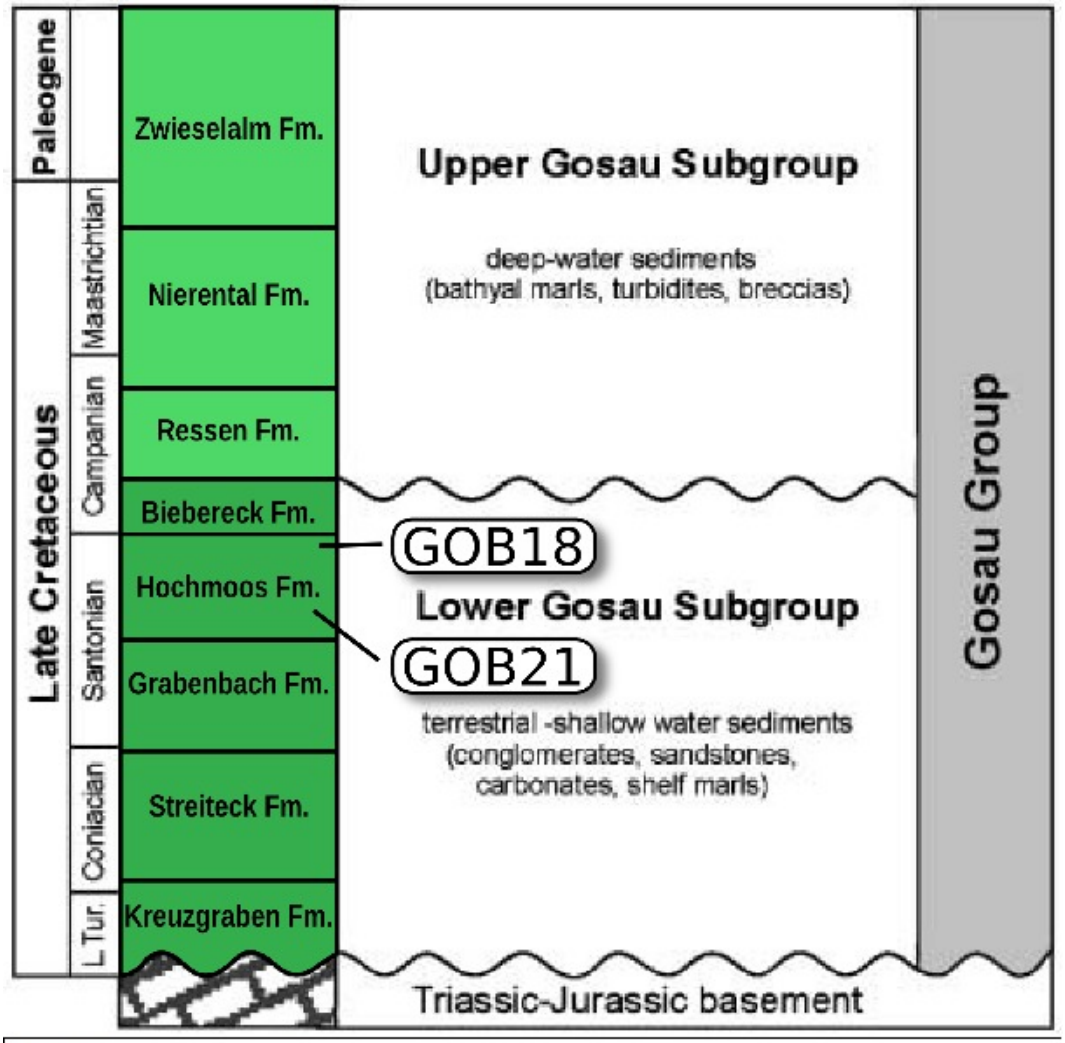

Fig. 23: Stratigraphic column of Gosau area
Main stratigraphic units in the Gosau basin. The two outcrops that yielded deformation ages (see 5 Results), KMR-GOB21 (Fig. 25) and KMR-GOB18 (Fig. 26) are both of the lacustrine sandy/marly Hochmoos Fm., but show differing deformation ages and are in different positions relative to the sedimentary basin.
Modified from Wagreich2001#282.

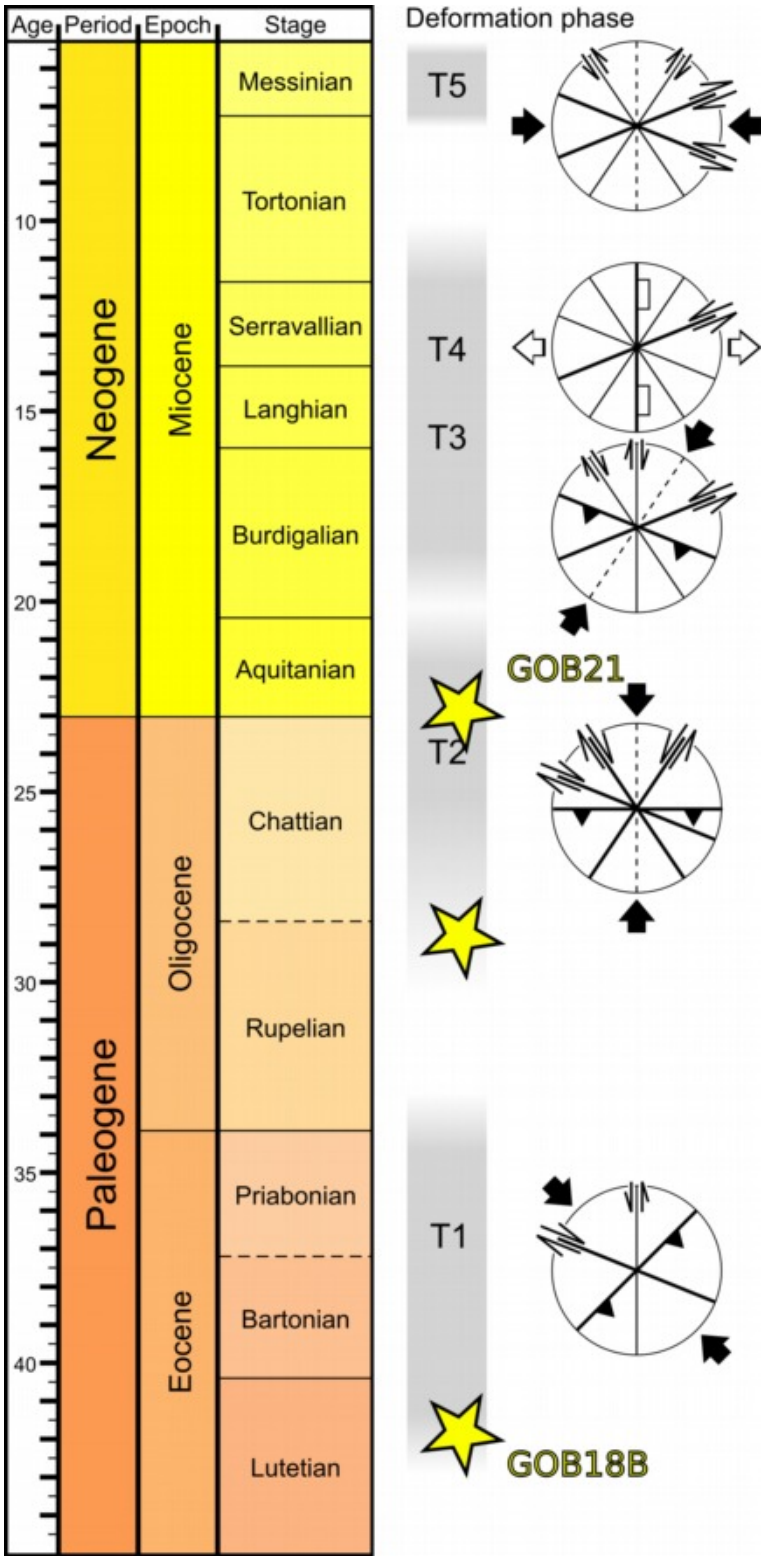

Fig. 24: Deformation phases of the NCA
Based on a large data set of brittle deformation structures, Peresson1997#203, established six main deformation phases (five pictured) for the central Northern Calcareous Alps (NCA) throughout the Eocene to Miocene. The calculated ages for samples GOB21 and GOB18 obtained from the Gosau basin are in good agreement with the age of deformation phases that are consistent with the structural settings observed at the sampling locations.

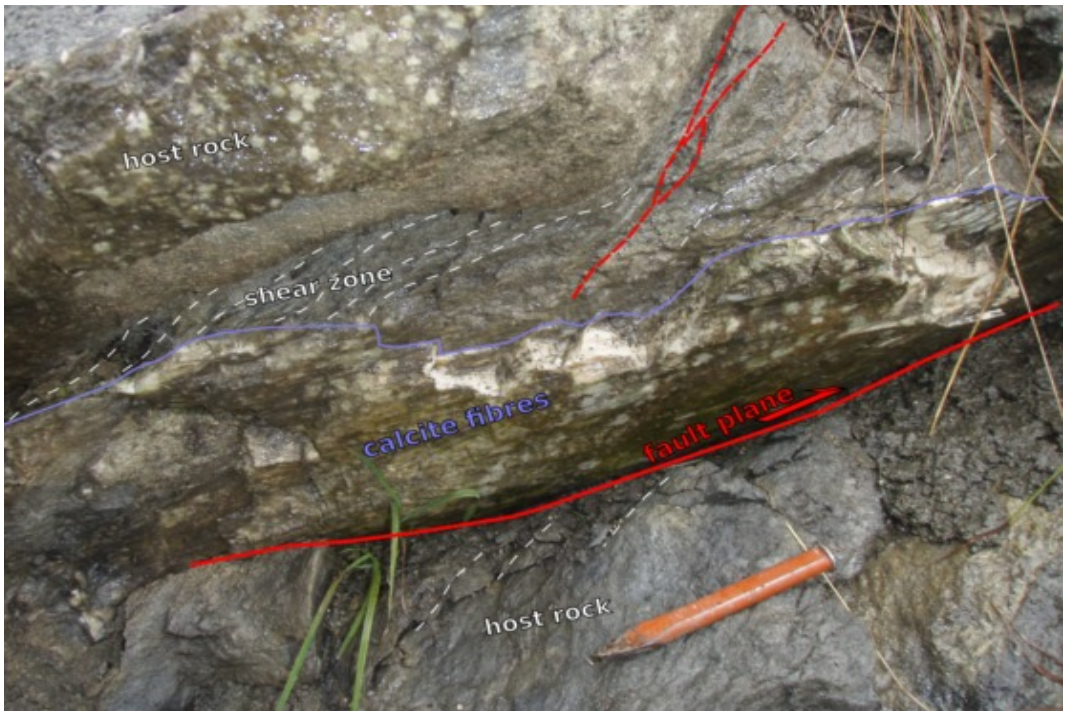

Fig. 25: Outcrop 240
Large, multiphase slickenfibre in Santonian, coarse, sandy marls (Hochmoos fm.); sample KMR-GOB21. The main calcite package fp 245/40 l1 184/22 up? showed reactivation and overgrowth at the margins, fp 229/35 l2 312/04 dx; see also Fig. 22.
View ~NW, fault slip top to the right, chisel for scale.

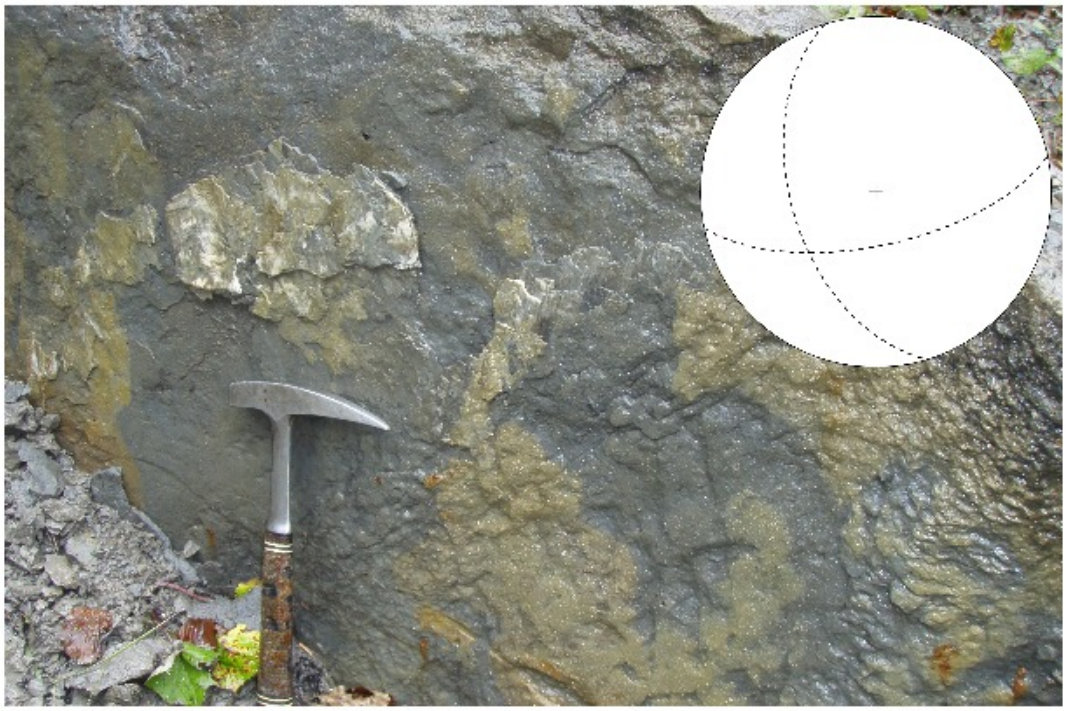

Fig. 26: Outcrop 236
Sample KMR-GOB18B in situ before recovery. Tension gash in Santonian marls of Hochmoos fm. Loose block, hammer for scale.
Inset: two tension gashes measured at the same location. Palaeostress can not be determined based on these data, but the observations are consistent with NW-SE compression during deformation phase "T1" (see Fig. 24), as indicated by LA-ICPMS dating, see chapter 5 Results.

2.2.5 Fohnsdorf Basin

The Fohnsdorf intramontane sedimentary basin formed in early to middle Miocene as a pull-apart half-graben in the Mur-Mürz fault system during lateral extensional movement of the central parts of the Eastern Alps (Wagreich & Strauss, 2005; Sachsenhofer et al., 2000). The basin is underlain by metamorphic rocks of the Austroalpine tectonic unit (Wagreich & Strauss, 2005). Tectonic development started with the northern Seckau subbasin and the southern Fohnsdorf subbasin as separate pull-apart basins along the ~E-W trending sinistral Mur-Mürz fault system (Strauss et al., 2001). In a second phase, the basin acted as a half-graben with the largest subsidence along normal faults in the South (Strauss et al., 2001). In the first two phases, the basin was filled with an up to 3400m thick sedimentary succession (see Wagreich & Strauss, 2005). In a third phase, the NW-SE trending dextral Pöls-Lavanttal fault formed a positive flower structure along the south-western basin margin (Strauss et al., 2001).

Slickenfibres from bounding faults of the basin and a layered travertine filling fissures close to the basin margin in the South (“Mariabucher Marmor”) were sampled. The latter yielded sample KMR-FOB28, which could be dated, see chapter 5 Results. The fissures transect the coarse polymikt conglomeratic host rock (equivalent of Fohnsdorf fm., ~Burdigalian/Langhian age, pers. comm. Prof. M. Wagreich, 2008) in an undulating, irregular fashion. They probably formed due to quick subsidence in the basin, while or shortly after the host rock was deposited.

The travertine was mined in older times for building and decoration. Thus, most samples from that locality were loose blocks from the old quarry, and no structural geological data could be collected.

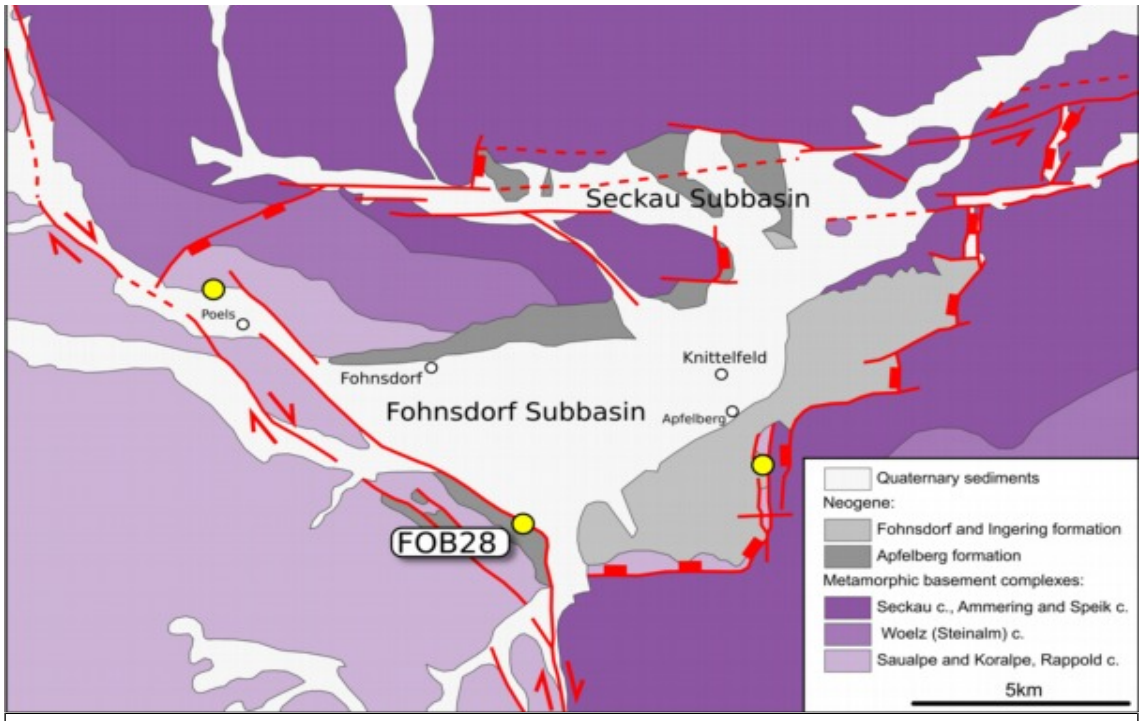

Fig. 27: Geological sketch map of the Fohnsdorf basin
Yellow dots: sampling locations. After Wagreich2005.

Fig. 28: Outcrop 248
Laminated calcitic fissure fills locally known and mined as "Mariabucher Marmor" in polymikt conglomeratic host rock. Sample KMR-FOB28C in situ before recovery, pencil for scale, view ~NW.

2.2.6 Lower Inn Valley

The Tertiary sedimentary succession of the lower Inn valley overlies the nappe stack of the Northern Calcareous Alps, and thus represents intramontane Molasse basins. They record the Oligocene tectonic development of the Alpine orogenic wedge in this area throughout several phases of tectonic activity (Ortner & Stingl, 2001; Ortner, 2003a; Kuhlemann & Kempf, 2002). The Molasse of the Lower Inn valley was deposited on a small-scale block-tilt topography, rapid thickness variations and facies transitions over short distances are common (Ortner, 2003b).

The sampling area is intensely overprinted by sinistral strike slip and thrust faults related to the Inntal shear zone and/or the "sub-Tauern ramp" (Ortner et al., 2006); the expected ages of the tectonic carbonates sampled are constrained by cross-cutting relationships and sedimentary ages of deformed units (Ortner, pers. comm., 2008).

Sample KMR-LIV34 is from a fault plane indicating NNW-SSE compression (Fig. 34), both consistent with the setting during formation of the Rupelian host rock (Bergpeterl mb. of the Häring fm., deformation phase D1 sensu Ortner, 2003b), and with a later deformation phase (D3, post-Chattian). See chapter 5 Results for age data from this sample and 6 Interpretation and Discussion for a discussion of the implications.

Sample KB2 (Fig. 33), provided by courtesy of Dr. H. Ortner, is a tectonic breccia with an interesting genetic history, including several distinct phases of cementation. These are discussed in detail in Ortner, 2003b, and briefly described in chapter 5 Results, including 2D element maps and age data. Yet, this sample could not be dated precisely.

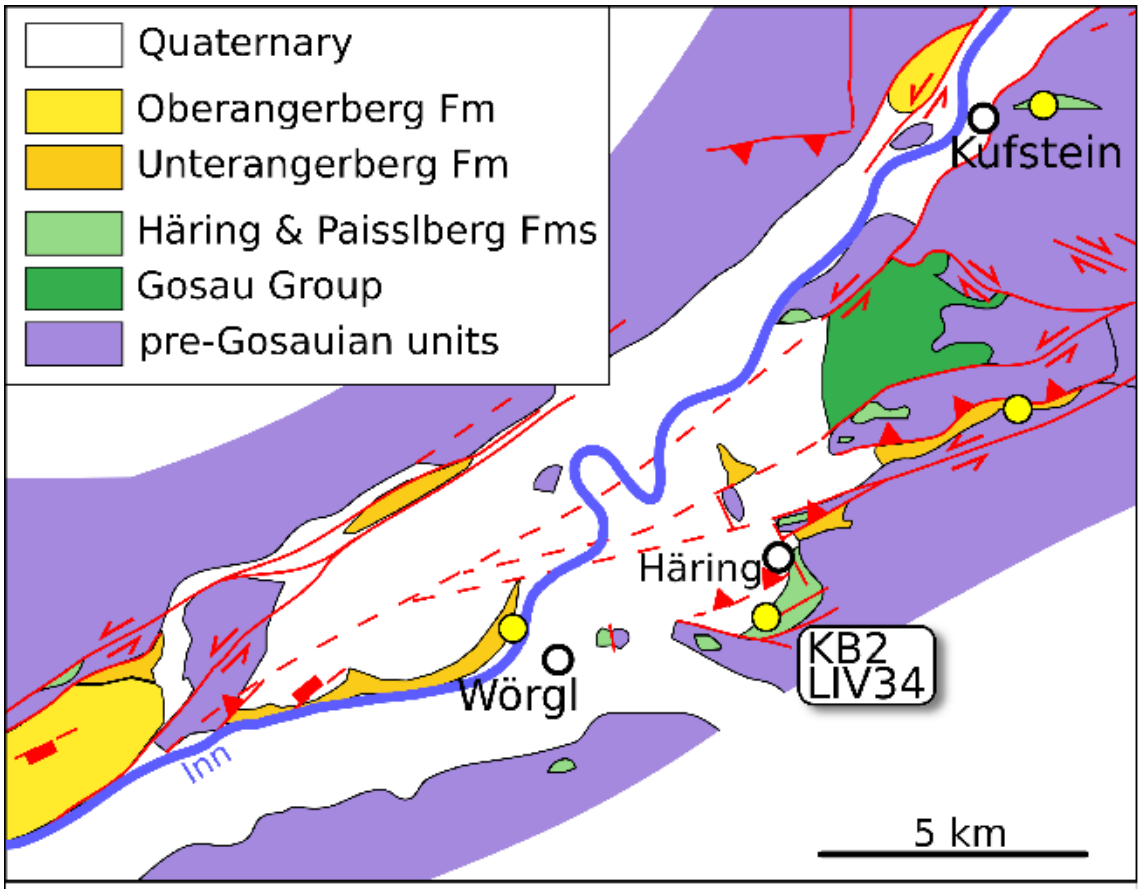

Fig. 29: Geological sketch map of the Lower Inn valley
After Ortner2003#479.

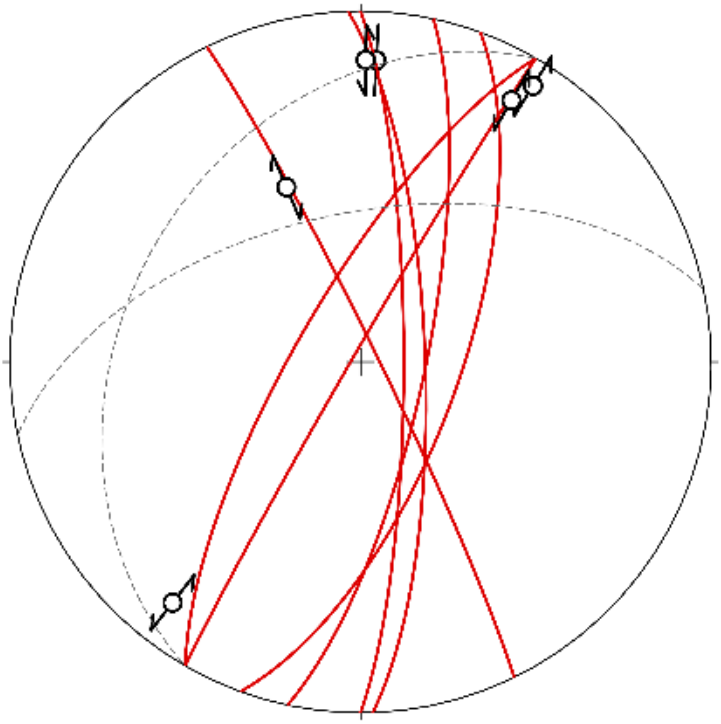

Fig. 30: Stereonet Lower Inn Valley
Tectonic features observed at sampling locations within the Rupelian Bergpeterl mb. in the Lower Inn Valley. Dashed lines: sedimentary bedding. The structures shown indicate NNW-SSE compression, both consistent with conditions during sedimentation, as during a later deformation phase in the area (deformation phases D1 or D3 sensu Ortner2003#479, respectively).

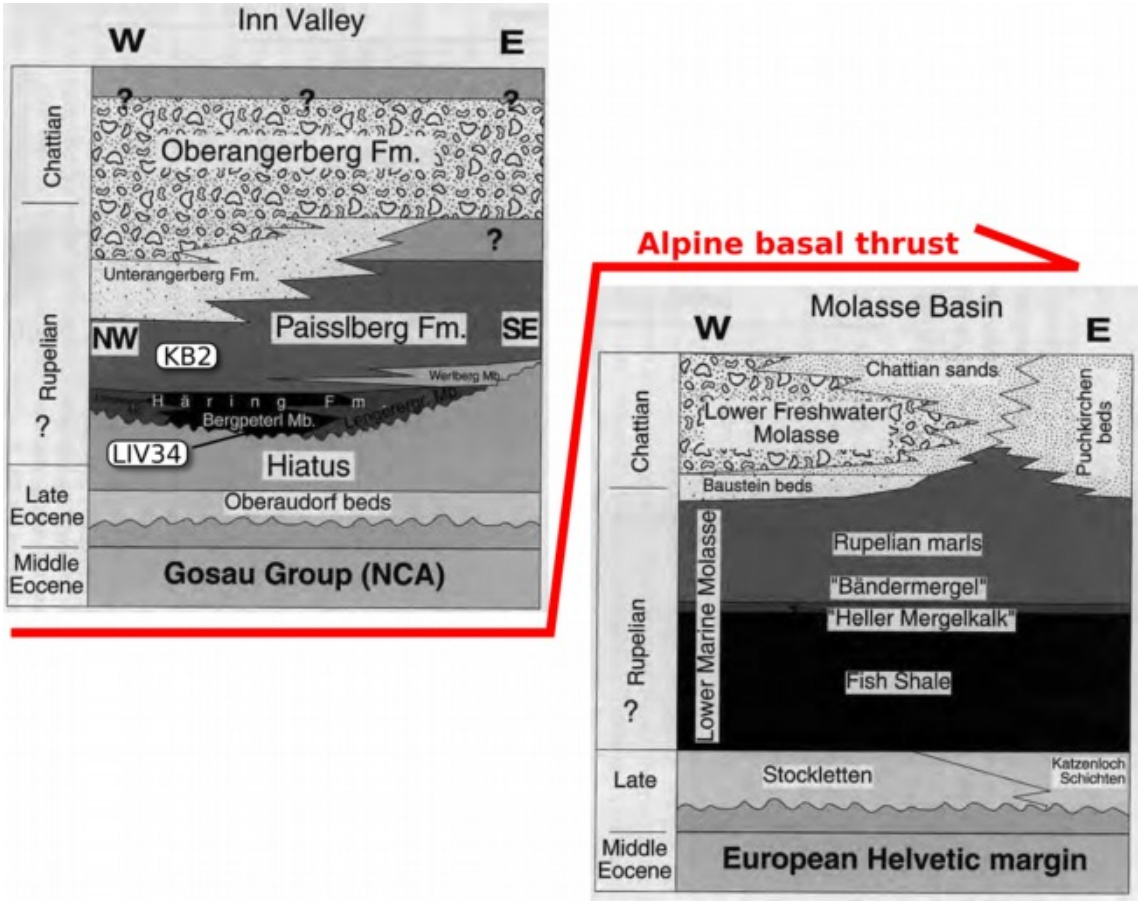

Fig. 31: Stratigraphy of the Lower Inntal Molasse
Comparison of the lithostratigraphic units of the Intramontane Molasse in the Lower Inn Valley to the Molasse sequence of the Alpine Foreland of Southern Germany. Samples KB2 and KMR-LIV34 are placed in their respective host rocks, deformation ages were expected to be Middle Miocene (pers. comm. Ortner, 2008). In case of KMR-LIV34, this could not be confirmed, see chapter 5 Results.
Modified from Ortner2001.

Fig. 32: Outcrop 269
Sample KMR-LIV34A in situ before recovery: slickenfibre on a fault plane of expected Miocene age (fp 300/88 l 032/08 sn) in early Oligocene bituminous marl (Bergpeterl mb. of the Häring fm., Ortner2003#479). View towards SE, hammer for scale.

Fig. 33: Sample KB2
Scanned thick section. Middle Miocene (pers. comm. Ortner, 2008) tectonic breccia with Triassic limestone components (dark grey, left) in a Rupelian bituminous marl host rock (Bergpeterl mb., brownish grey, right), cemented by several distinct generations of calcite (beige and white, middle). Closer description of this sample in chapter Error: Reference source not found Error: Reference source not found. Sample width ~91 mm.

2.2.7 Seefeld

The middle Norian Seefeld Fm (location see on overview map Error: Reference source not found) comprises of small-scale outcrops of kerogene, bituminous and to a variable degree calcareous and dolomitic finely laminated sediments of restricted intraplatform basins in the Upper Triassic Hauptdolomit/Dachstein limestone carbonate platform of the Northern Calcareous Alps (Donofrio et al., 2003). Earlier interpretations indicated gradual large-scale facies transitions over the whole Hauptdolomit platform (Fruth & Scherreiks, 1982; Fruth & Scherreiks, 1984), with euxinic basins forming locally by sedimentary processes (e.g. Schlager, 2005). Whereas the basins are now believed to have been initiated by tectonic processes compartmentalising the Hauptdolomit platform (e.g. Bechtel et al., 2007), sedimentation itself is believed to be mainly controlled climatically and by resulting sea-level fluctuations (Hopf et al., 2001; Berra et al., 2010).

Slumping in the fine-laminated sediments is common, indicating synsedimentary tectonic activity. Radial tension gashes from chaotic folds (slump folds, Fig. 34) and slickenfibres on bedding planes caused by flexural slip during folding were sampled. The fold geometries and orientations indicate that the slumping and sliding must have occurred in a (semi-)soft-sediment state, thus deformation ages are expected to be close to sedimentation age (Ortner, pers. Comm., 2008). The slickenfibres are orientated unsystematically and sometimes follow fold geometry, and the tension fractures are filled with pure, white calcite (not sediment infilled), thus, these structures are considered to have formed after burial, at the time of the slumping.

The Chaotic nature of slump folds does not allow easy interpretation of small data sets, thus structural data is not presented here. No samples from this area could be dated.

Fig. 34: Outcrop 274
Radial tension gashes (highlighted with blue dashed lines) in intensely folded bituminous black shales of the Upper Triassic Seefeld fm. Slickenfibres caused by bedding-parallel slip during folding also occur.
Sampling location of KMR-SEF39A-C. View ~N, hammer for scale.

2.2.8 Swiss Jura

The Swiss Jura Mountains represent an arcuate thrust-and-fold belt of deformed sediments of European-plate origin, that has been detached from its basement as a result of the advancement of the Alpine orogen towards the NW, in particular the exhumation of the external massifs (Rosenberg & Berger, 2009; Schmid & Kissling, 2000). Propagation of Alpine deformation to the foreland, thus formation of the Jura mountains, begins in the Mid-Miocene (Rosenberg & Berger, 2009 and references therein; Ziegler & Fraefel, 2009) and continues through Pliocene and Pleistocene, presumably to the present (Madritsch et al., 2010a; Ustaszewski & Schmid, 2007; Ustaszewski & Schmid, 2006; Madritsch et al., 2010b; Ziegler & Fraefel, 2009). After ~3 Ma, a transition occurred from the thin-skinned deformation of the main deformation phase to the ongoing thick-skinned deformation involving crystalline basement nappes (Ustaszewski & Schmid, 2007; Ustaszewski & Schmid, 2006; Ziegler & Fraefel, 2009). These latter movements are facilitated by and orientated along pre-existing structures of the European basement (Ustaszewski & Schmid, 2006; Ustaszewski & Schmid, 2007).

Dr. Herfried Madritsch (NAGRA, Switzerland) provided samples of slickenfibres from fault planes exposed in the North-Eastern Swiss Jura which have been deformed since fault slip, thus the age of the tectonic carbonates would determine the maximum possible age of the later folding event. Only one sample (MHH01) yielded convincing age information.

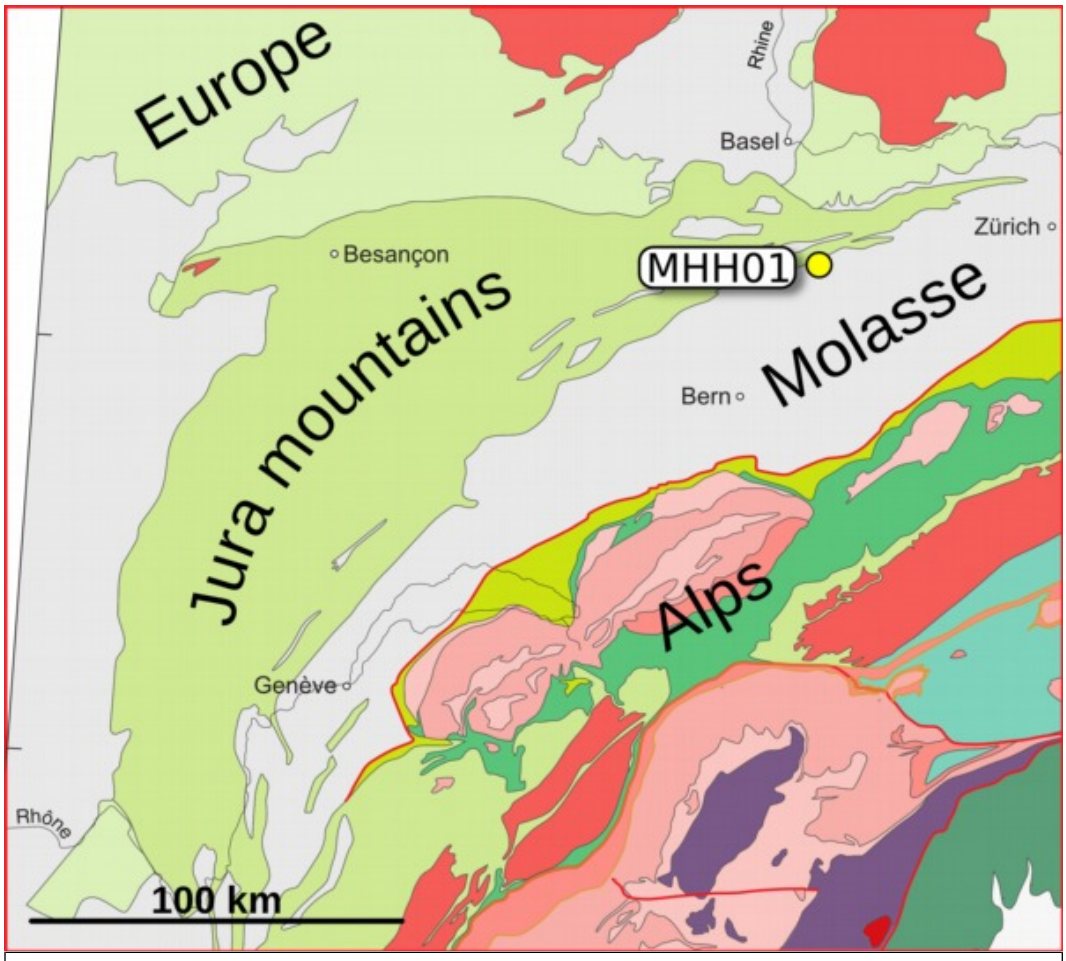

Fig. 35: Tectonic sketch map of the Swiss Jura Mountains and adjacent areas.
After Schmid2004, colour key see Fig. 9.

Fig. 36: Outcrop MHH01
Slickenside at sampling location for MHH01. Height of outcrop ~3 m.
Image by courtesy of Dr. H. Madritsch.

Fig. 37: Outcrop MHH06
Several 10s of metres high slickenside at sampling location for MHH06.
Image by courtesy of Dr. H. Madritsch.

2.2.9 Kilve

Kilve lies on the North Somerset coast of the Bristol Channel, UK. The Bristol Channel traces the Triassic-Jurassic Bristol Channel half-graben basin, which extends further offshore to the West (McGrath & Davison, 1995; Glen et al., 2005; Peacock & Sanderson, 1999). The Carboniferous – Devonian basement is generally dipping southwards, the Southern basin margin exhibits steep normal faults and more complex structures (Dart et al., 1995; McGrath & Davison, 1995; Davison, 1995). The structure was inverted and exhumed in Early Cretaceous and Tertiary times (Dart et al., 1995; Glen et al., 2005). Tertiary inversion was obliquely, resulting in strike-slip faulting and pull-apart basins (Dart et al., 1995; Glen et al., 2005; Davison, 1995).

The exceptional exposure of the structures along the coast, exposed both in vertical cliffs and a large horizontal wave-cut platform exposed at low tide, has attracted studies on many different aspects of the rock deformation, e.g. faulting mechanism (Davison, 1995), fault and vein macro- and microstructure (Belayneh & Cosgrove, 2010; McGrath & Davison, 1995), and basin inversion (Dart et al., 1995; Glen et al., 2005). During a RHUL field trip with Prof. Chris Elders, slickenfibres from fault planes in Jurassic mudstones and limestones were sampled along the coast.

For examples of outcrops near Kilve, see Fig. 6 and Fig. 8. Unfortunately, no samples from this area were suitable for dating.

2.2.10 Other samples

Samples were also collected from deformed carbonates and metasediments near the Salzachtal-Ennstal-Fault, close to the northern edge of the Tauern Window. Strong tectonic deformation in proximity to the large bodies of metamorphic rock in the Tauern window were assumed to possibly favour higher U/Pb ratios in the circulating solutions. Various small accumulations of ore minerals and pure metals are known in the Tauern Window.

In sample screening, none of these samples proved suitable for dating.

A few additional samples have been made available for evaluation by the following persons: Simon Craggs, at the time PhD student at RHUL, provided a slickenfibre from a fault in E Canada. Prof. Robert Hall from RHUL provided a massy crystalline aragonite fracture fill from Turkey. Marion Campani, at the time PhD student at ETH Zürich, Switzerland, provided some samples from her field area in the Simplon/Valais area.

These samples proved not suitable for dating.`

See Appendices for a list of samples and acquired data (where applicable).

3. Methodology I: theory

This is the first of two methodology chapters. In this section, theoretical background information to techniques utilised in this study is given. Details on the actual steps applied for sampling and analysis are found in the next chapter (4 Methodology II: application).

3.1 Geochemistry of Uranium and Lead in calcite

The main elements considered in this study are Uranium and Lead (and Thorium), see section 3.2 below. Due to the nature of the samples analysed, focus is given here on the behaviour of these elements in inorganically precipitated calcite, and in the solutions typically expected to form these samples.

Uranium and Thorium can occur in the tetravalent oxidation state (U^{4+}, Th^{4+}), which does not generally form water soluble compounds (Faure & Mensing, 2005). Some solubility exists in pH ranges <6.5, but in neutral and slightly alkaline conditions, these ions will be extracted from the water column by particulate sorbtion, mainly onto phyllosilicates, or colloidal and solid organic matter (e.g. Langmuir & Herman, 1980; Chappaz et al., 2010). Complexation with organic compounds like humic acids may provide mobility, where these ligands are available (e.g. Langmuir & Herman, 1980).

Under oxidising conditions, Uranium occurs in the hexavalent (U^{6+}) oxidation state, forming the *uranyl ion* (UO_2^{2+}), which is water soluble with naturally abundant inorganic ligands such as in carbonate complex ions (e.g. as $UO_2(CO_3)_2^{2-}$, $UO_2(CO_3)_3^{4-}$ and UO_2CO_3) and phosphate complex ions (e.g. $UO_2(HPO_4)_2^{2-}$; Jahn & Cuvellier, 1994; Faure & Mensing, 2005; Rasbury & Cole, 2009; Bruno, 1990). Typical concentrations of dissolved U are ~3.2ppb for seawater (Chen et al., 1986), and an average of ~0.3ppb for river water (Palmer & Edmond, 1993; Dunk et al., 2002). Concentrations in groundwater are highly variable, depending on local lithology, water chemistry and redox potential (Porcelli & Swarzenski, 2003).

The uranyl ion also shows sorbtion onto organic solids, which can accumulate high concentrations of several 1000ppm U in organic sediments and soils (Zielinski & Meier, 1988; Regenspurg et al., 2010; Arbuzov et al., 2011). Coprecipitation with metallic hydroxides (e.g. deep-sea Fe and Mn hydroxides, also in lakes and palaeosols) is also a proposed mechanism binding U to the sediment (Jahn & Cuvellier, 1994; Rasbury et al., 2000). In this environment, redox potential is believed to be a major controlling factor for U binding. However, Chappaz et al., 2010 have found no correlation of redox potential with U concentration in lake sediments and rather attribute U input predominantly to organic particulates. The presence of possible organic ligands, especially under acidic conditions, leads to formation of complexes with in the uranyl ion, which stimulates (re-)mobilisation and influences the sorbtion behaviour onto solid particles (Zielinski & Meier, 1988; Barger & Koretsky, 2011). Rasbury et al., 2000 suggest the presence of organic material and redox potential to be major factors driving U incorporation into calcite of caliche palaeosols, and point out the high concentrations of U and Pb in microscopic haematite particles in their samples. Weltje et al., 2002 studied the fate of lanthanides (also as an analogue for the behaviour of the actinides) in soil, water and biota of freshwater ecosystems and found sediment-water partition coefficients between 100000 and 3000000 l·kg-1 dry matter, relative to surface water.

Kelly et al., 2003 have shown the mechanism of U incorporation into calcite to be the linear uranyl ion taking the position of one Ca and two adjacent CO_3 groups within the calcite lattice. This configuration is stable in that the uranyl is incorporated at a well defined position within the lattice, and due to its size, can not diffuse out. The authors suggest the primary mineral in their sample to have been aragonite, which can incorporate much higher concentrations of U, and that the uranyl stayed in the crystal lattice during recrystallisation to calcite (Kelly et al., 2003). The study of Elzinga et al., 2004 indicates the presence of multiple species of uranyl complexes to be present on the surface of the calcite crystal during growth and complicated sorbtion/desorbtion processes likely to be acting, also depending on U concentration in the surrounding medium. Over longer times, the locally disturbed crystal lattice around the uranyl may resettle back to a more stable state (Kelly et al., 2006). As many studies successfully dating calcite by the U-Pb method prove (e.g. Israelson et al., 1996; Richards et al.,

1998; Rasbury et al., 1997; Moorbath et al., 1987; see also Jahn & Cuvellier, 1994 and Rasbury & Cole, 2009, and references therein), the radioactive intermediate daughter nuclides and final Pb isotopes seem to be equally well trapped and the U-Pb system in calcite can be considered closed over geological timescales.

Lead occurs as divalent Pb^{2+} and tetravalent Pb^{4+} in nature (Jahn & Cuvellier, 1994). Pb is generally more insoluble, with a high affinity to adsorb onto particle surfaces, resulting in typically very low concentrations of 0.003ppb in natural seawater (Jahn & Cuvellier, 1994; Chester, 1990). In river water and groundwater, contents are very variable, depending on local lithology and input from anthropogenic pollution (Jahn & Cuvellier, 1994; Morton-Bermea et al., Komárek et al., 2008). Solubility of Pb is given mainly as complexes with the carbonate ion CO_3^{2-} and with Cl^- in seawater (Bruno, 1990; Chester, 1990), reduction of Pb concentration is by adsorption onto organic particles and clay minerals, and by precipitation as hydroxides, phosphates and carbonates (Jahn & Cuvellier, 1994).

Pollution from industrial sources poses a special problem, because Pb isotopic ratios of the pollutants (mainly from the use of leaded gasoline) are not the ratios of natural "common lead" (e.g. Morton-Bermea et al., Komárek et al., 2008) and can thus distort isotopic analyses even if contamination is very small.

Thorium behaves geochemically similar to Pb, but it adsorbs even stronger onto particulate organic and inorganic matter and is thus quickly removed from solution (Jahn & Cuvellier, 1994). Concentration in seawater is typically ~0.0001ppb (Chen et al., 1986).

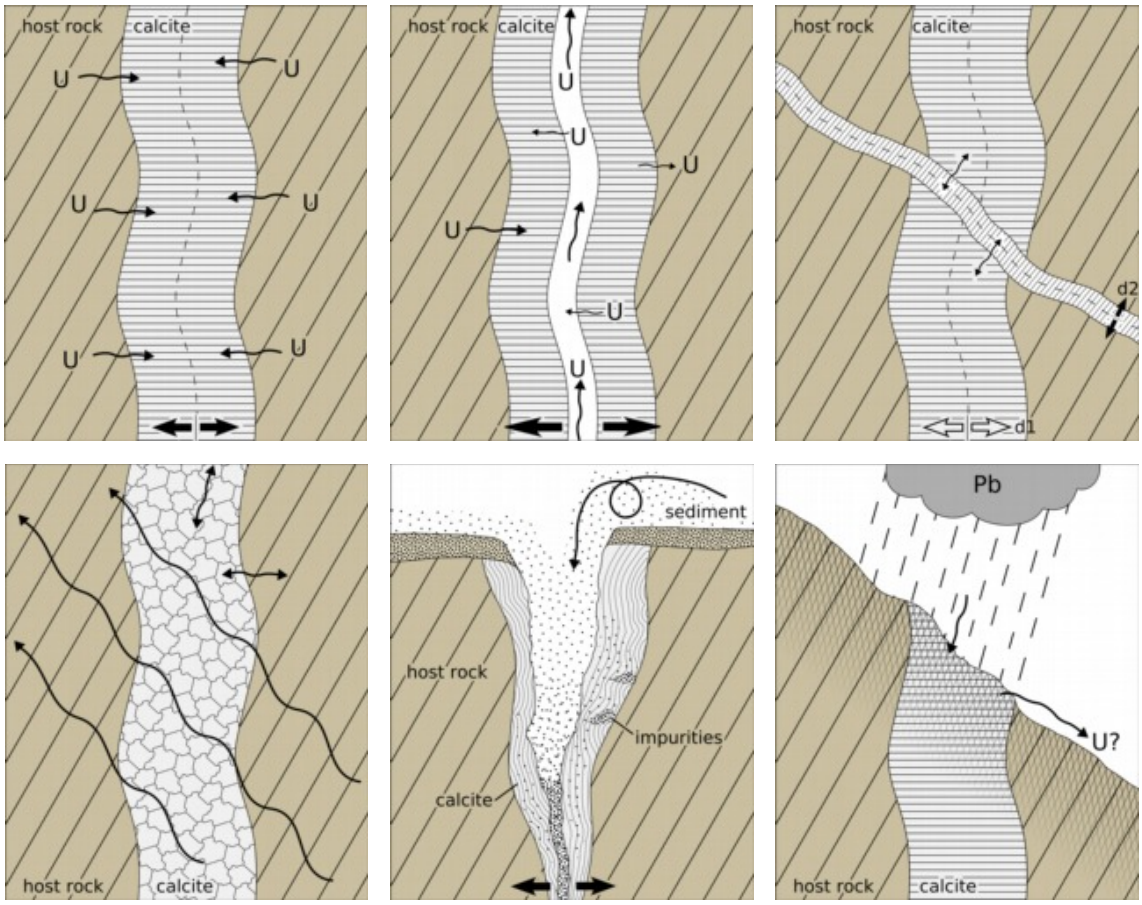

Fig. 38: Different possible secondary disturbances of the U-Pb system in calcite-filled veins. Top row, left to right: Diffusive fluid seepage along pore space from the host rock in a crack-seal scenario. Fluids circulating in an open fracture. Multiple fracture generations.
Bottom row: Pervasive diffusion, and recrystallisation e.g. during diagenesis. Sediment influx and fluid circulation in a fissure open to the surface. Weathering.

3.2 U-Pb dating

U-Pb dating is one of the best established methods in the Geosciences to determine the age of a rock or mineral. It is based on the radioactive decay of uranium (^{238}U, ^{235}U) and thorium (^{232}Th) via various daughter elements to different stable isotopes of lead (^{206}Pb, ^{207}Pb, ^{208}Pb, respectively; see "The U-Pb system" below). Because the halflives of ^{238}U, ^{235}U and ^{232}Th are much longer than those of their respective intermediate daughter nuclides, after sufficient time, a *secular equilibrium* (see "Radioactive decay" below) establishes in the (closed) system, i.e. the production rate of the Pb isotopes equals the decay rate of their respective parent (after Faure & Mensing, 2005). In general, high U concentration of a sample is desirable for measuring, but it is variations in the U/Pb ratio (μ), that actually allow for dating (see chapters 3.2.2 and 3.2.3). Elevated common Pb concentrations, as may be indicated by a lower U/Pb ratio, hinder the ability to measure radiogenic Pb (after Jahn & Cuvellier, 1994).

Preconditions for applicability of the methods described below are (after Cole et al., 2005, Faure & Mensing, 2005):

- Closed-system behaviour (as is the case for other dating methods like Rb-Sr, K-Ar, Sm-Nd, U-Pb on zircons; Jahn & Cuvellier, 1994).
- Initial homogeneity in the common (nonradiogenic) Pb isotopes.
- Establishment of secular equilibrium (after ~10^6 a; Richards et al., 1998).

3.2.1 Basic principles

Radioactive decay

The rate of radioactive decay of a radionuclide follows the *law of radioactivity*:

$$-\frac{dN}{dt} \propto \lambda N$$

where:
N … number of atoms
λ … decay constant

(all formulas after Faure & Mensing, 2005).

From that follows, that the number N of remaining radioactive parent atoms at time t equals:

$$N = N_0 e^{-\lambda t}$$

where:
N … number of radioactive parent atoms at time t
N_0 … number of atoms at time $t = 0$
λ … decay constant

The time required for half of the parent nuclides to decay is referred to as the *halflife* of this radionuclide, and is calculated from the above equation as:

$$T_{1/2} = \frac{\ln 2}{\lambda}$$

where:
$T_{1/2}$ … halflife
λ … decay constant

If a radionuclide decays to a daughter that is radioactive itself, a *decay chain* will form, continuing until a stable nuclide is formed. If the parent has a longer halflife than an unstable daughter, after a certain time, the rate of decay of the unstable daughter is only controlled by the resupply of daughter nuclides, thus by the halflife of the parent. Common examples are ^{235}U, ^{238}U and ^{232}Th decaying to ^{207}Pb, ^{206}Pb and ^{208}Pb, respectively. So in a decay chain, after an initial settling of equilibria of the supply and decay of daughters, the rate of decay of all daughters, and the growth in the stable end members will depend on the decay rate of the initial parents only. This state is called *secular equilibrium*. If established, the decay chain of intermediate daughters can be eliminated from consideration (in a closed system), and the system is treated as though the parent nuclide decayed directly to the stable radiogenic daughter. The number of stable radiogenic daughter nuclides D^* is equal to the number of parent atoms decayed:

$$D^* = N_0 - N$$

where:
D^* … number of stable radiogenig daughter atoms
N_0 … initial number of parent atoms
N … remaining parent atoms

Geochronometry

Substituting N_0 and N for the equation given for radioactive growth yields:

$$D = D_0 + N\left(e^{\lambda \cdot t} - 1\right)$$

where:
D … number of daughter atoms at time t
D_0 … initial number of daughter atoms
N … number of parent atoms
λ … decay constant

From this, the age t of the system can be calculated as:

$$t = \frac{1}{\lambda} \ln\left(\frac{D - D_0}{N} + 1\right)$$

where:
D … number of daughter atoms at time t
D_0 … initial number of daughter atoms
N … number of parent atoms
λ … decay constant

This forms the basis of age determinations by radioactive decay in natural samples. D and N are measured in the sample, the decay constant of the parent nuclide must be known. D_0 can often be assumed, or is obtained mathematically:

If a suite of cogenetic samples with the same D_0 exhibit different chemical composition, in a graph of number of daughter atoms versus parent atoms, they will plot on a straight line. This line is called an *isochron*. The age of the system is calculated from the slope of the isochron, the intercept (daughter atoms on the y-axis) equals D_0 (see chapter 3.2.2).

The U-Pb system

Measuring the concentrations of U, Th and Pb isotopes allows for calculation of the (closing) age of a system (e.g. the growth age of a calcite crystal). The accumulation of radiogenic isotopes of Pb by decay of their respective parents follows the form

$$\frac{^{206}Pb}{^{204}Pb} = \left(\frac{^{206}Pb}{^{204}Pb}\right)_i + \frac{^{238}U}{^{204}Pb}\left(e^{\lambda_{238} t} - 1\right)$$

$$\frac{^{207}Pb}{^{204}Pb} = \left(\frac{^{207}Pb}{^{204}Pb}\right)_i + \frac{^{235}U}{^{204}Pb}\left(e^{\lambda_{235} t} - 1\right)$$

$$\frac{^{208}Pb}{^{204}Pb} = \left(\frac{^{208}Pb}{^{204}Pb}\right)_i + \frac{^{232}Th}{^{204}Pb}\left(e^{\lambda_{232}t} - 1\right)$$

given as ratios respective to ^{204}Pb, the only stable naturally occurring isotope of Pb. The date can then be calculated from e.g. the ^{238}U → ^{206}Pb system as:

$$t = \frac{1}{\lambda_{238}} \ln\left(\frac{\frac{^{206}Pb}{^{204}Pb} - \left(\frac{^{206}Pb}{^{204}Pb}\right)_i}{\frac{^{238}U}{^{204}Pb}} + 1\right)$$

(index $_i$ denoting the initial isotope ratio at time of system closure; after Faure & Mensing, 2005). The ages for the other decay chains are calculated similarly. If all three calculations yield the same date, this is called a *concordant date* (or age). These equations require the determination/assumption of initial Pb isotopic ratios and are susceptible to errors by Pb loss from the system. The latter can be overcome by calculating an age from the ^{206}Pb/^{207}Pb ratio, resulting from the difference in the decay constants of ^{238}U and ^{235}U (after Faure & Mensing, 2005):

$$\frac{\frac{^{207}Pb}{^{204}Pb} - \left(\frac{^{207}Pb}{^{204}Pb}\right)_i}{\frac{^{206}Pb}{^{204}Pb} - \left(\frac{^{206}Pb}{^{204}Pb}\right)_i} = \frac{^{235}U}{^{238}U}\left(\frac{e^{\lambda_{235}t} - 1}{e^{\lambda_{238}t} - 1}\right) = \left(\frac{^{207}Pb}{^{206}Pb}\right)^*$$

(the asterisk identifies the radiogenic isotopes). This equation is solved for t by iteration or interpolation in a table.

3.2.2 Isochron diagrams

Cogenetic samples will plot on a straight line in coordinates of e.g. x=$^{206}Pb/^{204}Pb$, y=$^{207}Pb/^{204}Pb$, with slope m of:

$$m = \frac{^{235}U}{^{238}U}\left(\frac{e^{\lambda_{235}t}-1}{e^{\lambda_{238}t}-1}\right) = \left(\frac{^{207}Pb}{^{206}Pb}\right)^{*}$$

From the slope m of this *Pb-Pb isochron* the age of a suite of samples can be calculated. Because of the small difference in accumulation rates of ^{206}Pb and ^{207}Pb, only samples older than approximately 1Ga exhibit measurable $^{206}Pb/^{207}Pb$ ratios (thus, the method is not applicable in this study).

3.2.3 Concordia diagrams

Wetherill Concordia

Using the calculated ratios of radiogenic ^{206}Pb to ^{238}U and radiogenic ^{207}Pb to ^{235}U as the y- and x-coordinates, respectively, in a plot over time t yields the so-called *Wetherill Concordia* after Wetherill, 1963, Wetherill, 1956. Ratios that yield concordant ages plot on this curve (thus the name). If conformable Pb-loss has occurred on a set of samples, these will plot on a line (called “discordia”) that intersects the Concordia in two points. Interpretation of the ages obtained from these points depends on context. Each individual sample along the discordia would yield a discordant age. In typical applications, the upper ("older") intersection point will give

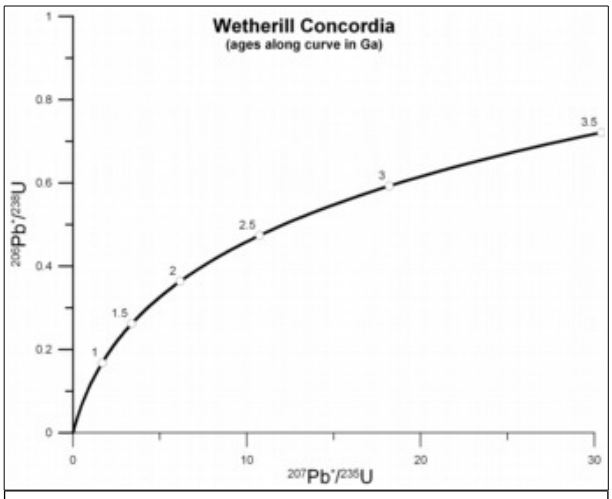

Fig. 39: Wetherill Concordia
Labelled points indicate age in Ga.

the crystallisation age of the suite of samples under investigation (Faure & Mensing, 2005).

Tera-Wasserburg Concordia

Tera & Wasserburg (Tera & Wasserburg, 1972) developed a concordia plot that does not require prior knowledge of the initial $^{206}Pb/^{204}Pb$ ratios. The $^{238}U/^{206}Pb$ and $^{207}Pb/^{206}Pb$ ratios are used as x- and y-coordinates, respectively, again given as parametric equations for time t (Tera & Wasserburg, 1972, Ludwig, 1998). Intersection of a discordia with this curve again will yield two ages t_1 and t_2.

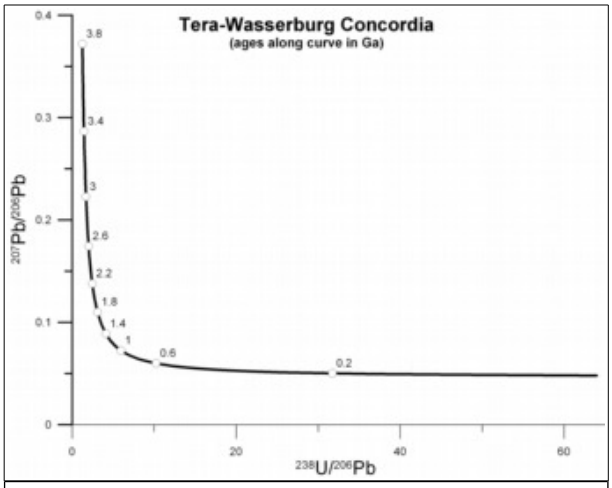

Fig. 40: Tera-Wasserburg Concordia
Labelled points indicate age in Ga.

For the samples considered in this study, this method has the great advantage of not being dependent on measurements of ^{204}Pb (difficult to attain, because of a high ^{204}Hg background typically inherent in ICPMS). The discordia results from mixing of two components of different isotopic composition in the samples at time of formation. One component has the isotopic composition of the intercept of the discordia, the other one the composition of the younger point of intersection with the concordia. The younger intersection age yields the age of crystallisation of the calcites under consideration, the older intersection has no geological significance.

Three-dimensional Concordia plots

Treating U/Pb data in a orthogonal three-dimensional space of coordinates $x=^{238}U/^{206}Pb$, $y=^{207}Pb/^{206}Pb$, $z=^{204}Pb/^{206}Pb$ allows for constructing “total” Pb/U-isochrons (Wendt, 1984; Wendt, 1989; Jahn & Cuvellier, 1994). The technique was further developed by Zheng, 1989; Zheng, 1990; Zheng, 1992.

Actual ages are calculated by interception of a linear (or planar) best-fit discordia in 3D space (isochrons) with the Tera-Wasserburg Concordia (in the xz-plane). The mathematics of data clustering, age calculation, error calculation and -propagation, as well as including error of decay constants are described in Ludwig, 1998; Ludwig, 2001. The latter describes the use of the total U-Pb isochron for eliminating mass-fractionation effects without double-spiking.

The method requires some basic assumptions to be fulfilled by all samples (in addition to the general ones mentioned before; after Jahn & Cuvellier, 1994):

- a single crystallisation age
- the same post-crystallisation disturbance of the U-Pb system
- identical common Pb isotopic composition

As with the Tera-Wasserburg Concordia method, the actual initial Pb isotopic composition needs not to be known. The advantage of this method over the (2D) Tera-Wasserburg diagram is a higher precision, a quantitative test of U-Pb concordance and recovery of both $^{206}Pb/^{204}Pb$ and $^{207}Pb/^{204}Pb$ initial ratios (Ludwig, 2001).

3.3 Mass spectrometry

3.3.1 Basic principles

Mass spectrometry allows to determine the proportions or relative ratios of constituents of a sample (molecules, elements, isotopes), based on their mass. Sample atoms/molecules are ionised and focussed to an ion beam, different masses are separated in a mass analyser, and the resulting ion beam intensities are measured electronically. Different types of mass spectrometers are distinguished by the means in which the basic steps of sample introduction & ionisation, mass separation and ion detection are performed.

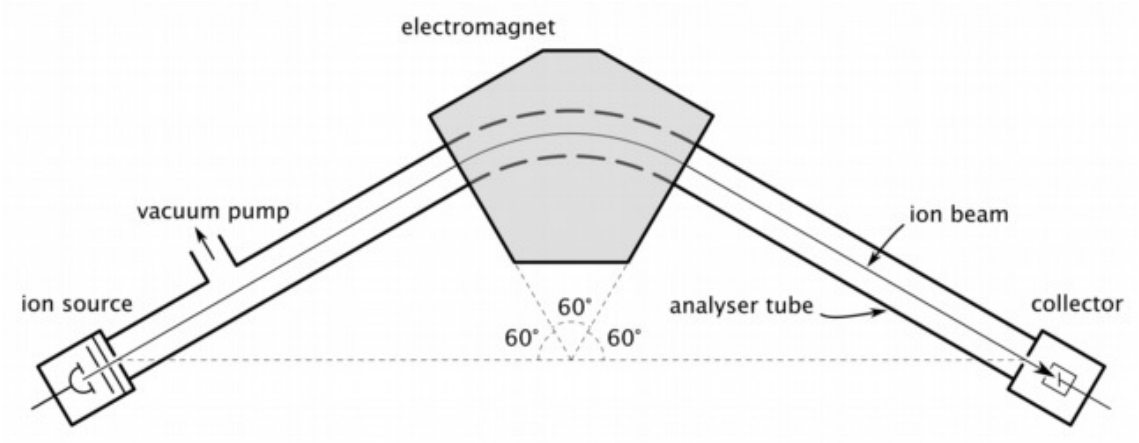

Fig. 41: The basic parts of a mass spectrometer: ion source, mass analyser, collector

3.3.2 Typical designs of the individual parts

Sample introduction

Many different strategies and designs for taking up solid, liquid or gaseous samples and introducing them in the ion source exist. Some common ones are:

Manual sample loading: the sample is loaded upon some sample carrier, which is put directly into (and forms part of) the ion source assembly (e.g. beads used in TIMS, see below).

A *nebuliser* creates a fine aerosol from a sample solution. Different geometries of the relative positioning and shapes of the sample introduction capillary and carrier gas supply are in use. Typically, argon is utilised as the carrier gas. The aerosol passes the *spray chamber*, in which larger droplets settle out and only homogeneously fine droplets pass on to the ion source (typically ICP, see below). This causes loss of sample solution of up to 99%.

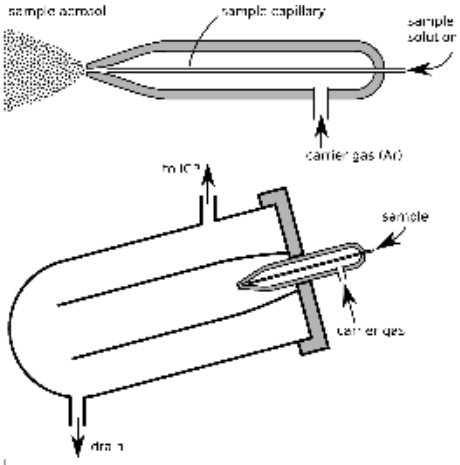

Fig. 42: Concentric nebuliser (Meinhard1976) and spray chamber.

The *desolvating nebuliser* uses a heated spray chamber and a countercurrent flow of Ar sweep gas along a porous heated membrane to remove solvent from the sample aerosol, resulting in an increased sensitivity (after CETAC Aridus II™ product brochure, www.cetac.com/pdfs/Brochure_Aridus_II.pdf, accessed May 2011).

Laser ablation (LA) utilises short, intense laser pulses to break the bondings between the surface atoms of a solid sample (e.g. Gray, 1985; Günther & Hattendorf, 2005; Fryer et al., 1995; Jeffries et al., 1998). The resulting mixture of ions, vapour, recondensed droplets and particulates broken off the surface is taken up from the ablation site by an inert gas flow (typically He) and subsequently introduced to the ion source (typically ICP, after mixing with an Ar carrier gas flow; Arrowsmith & Hughes, 1988; Hathorne et al., 2008; Eggins et al., 1998).

Ion Source

In the ion source, the analyte is ionised, ideally homogeneously for any masses (elements/isotopes) to be analysed and constantly over time. The resulting ions are accelerated by an electric potential and collimated by different geometries of charged electrodes (*ion lenses*) to form a thin ion beam.

For *thermal ionisation* (TI), the sample is loaded onto a thin filament of an inert metal with high work function and low volatility (typically W, Ta or Re), mounted on an isolating glass base (*bead*). The filament is then electrically heated (in high vacuum) to volatilise sample atoms, which are thermally ionised. For elements with a high first ionisation potential, additional ionisation filaments are placed alongside which can be heated to different (higher) temperatures than the heating filament.

An array of beads (the *turret*) can be prepared in advance and after introducing the whole turret in the vacuum chamber, samples are changed remotely.

An effective way of ionising a sample is in an *inductively coupled plasma* (ICP; Reed, 1961; Jarvis & Jarvis, 1992). The sample, carried in a constant noble gas flow (typically argon), is passed into an array of concentric quartz glass tubes, the plasma *torch*. A coil around the end part of the torch, the *load coil*, allows for inductive coupling of the plasma to a radiofrequency (RF), the plasma is sustained by ohmic heating within. The sample is injected in the centre of the plasma, where it readily volatilises, dissociates and ionises due to temperatures of about 10000° Centigrade.

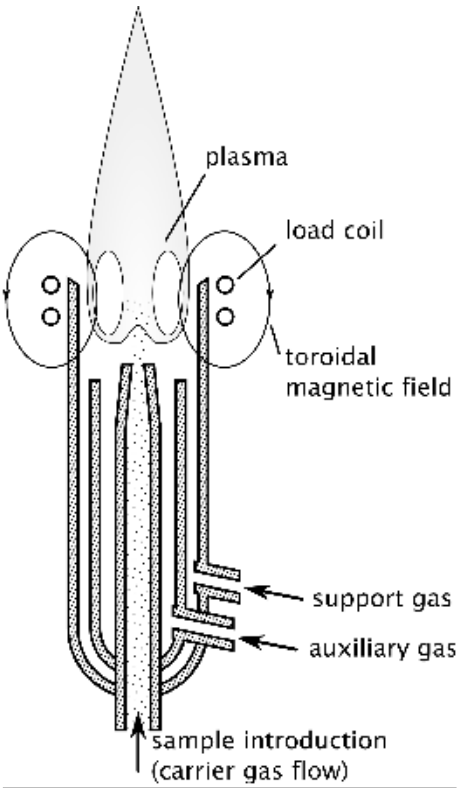

Fig. 43: Inductively coupled plasma torch.

The torch operates at (near) atmospheric pressure, and the resulting ion plume is guided through an differentially pumped interface consisting of two small nickel or platinum

apertures (the *sampling cone* and *skimmer cone*), which deflect a majority of uncharged molecules and atoms. Separation of positive ions from electrons is achieved by diffusion of the lighter electrons from the ion beam under high vacuum, inertia keeps the heavier ions on track. This principle results in strong mass fractionation, favouring heavier elements relative to lighter ones (because of higher inertia), and requires appropriate correction. Following lies an array of electrostatic lenses that further focus and accelerate the ion beam. Final focussing occurs in the high vacuum of the mass analyser.

ICP can ionise all elements with high efficiency, even those with high ionisation energies (up to 15.76eV, the ionisation energy of Ar, used to form the plasma). However, ion transmission from plasma to the mass spectrometer is inefficient, only about 2% of the sample are detected, due to the characteristics of the plasma-vacuum interface (the "cones", see above).

Other possible ion sources for mass spectrometry include:

- ionisation by *electron bombardment* of a gaseous sample
- *photoionisation* of sample molecules by laser
- *spark source ionisation* (SSMS) vaporises a (conductive) solid sample in a high-voltage RF spark
- *glow discharge* (GDMS) uses the (solid, conductive) sample as one electrode in a low-pressure, high-voltage discharge chamber
- *secondary ionisation* (SIMS) utilises a primary ion beam to ionise and release atoms from the sample (*sputtering*)
- the Ion MicroProbe is an integrated system for sample introduction of a solid sample and sputtering with a very narrow primary ion beam

A *collision cell* may be fitted between ion source and ion beam collimator. It consists (typically) of a *hexapole*, an array of six cylindrical electrodes, on which a radiofrequency potential is applied. The hexapole is housed in an evacuated cell, and a constant small flow of *collision gas* (typically Ar or He) is introduced. The ions collide

with the gas atoms, and the radiofrequency is chosen so that only ions in a narrow energy range emerge from the array. A collision cell can effectively remove many interferences.

Mass analyser

The mass analyser filters the ion beam based on its physical properties to let only ions of one specific mass-to-charge (m/z) ratio pass onto the collector.

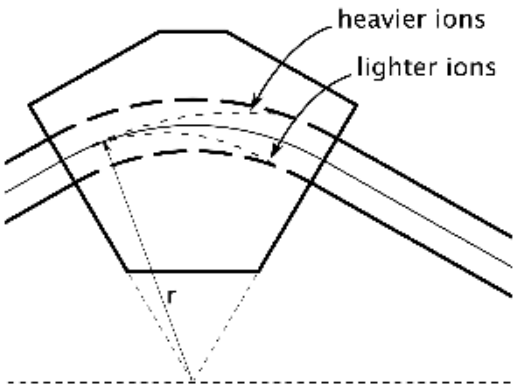

Fig. 44: 60° magnetic sector mass analyser

The most common design in mass spectrometers is the *magnetic sector mass analyser* (based on Nier, 1940). Mass separation is achieved by deflecting the ion beam in a magnetic field applied normal to the track of the ion beam. The ions will follow a circular path according to the formula:

$$\frac{m}{z} = \frac{B^2 r^2}{2U}$$

where:

m	…	ionic mass
z	…	charge of ion
B	…	magnetic flux density
r	…	radius of path of ion
U	…	accelerating voltage

Thus, ions of different mass or charge will follow paths of different radius (larger masses are less deflected than smaller ones). The ion beam is directed through the magnetic field for a certain radius of a circle (typically 60° or 90°), so ions of different m/z ratios will exit at different radii and with slightly different trajectory. Adjustment of either B or U allows for directing the beam of ions of exactly one m/z ratio onto the detector.

The *quadrupole mass analyser* achieves separation of different masses by electric fields. It consists of an array of four parallel cylindrical electrodes. Opposing electrodes are connected and to each pair a electrical potential, consisting of a DC- and an AC-

component, is applied. The AC component is a radiofrequency potential, the peak amplitude U_1 and frequency ν of which determine which masses pass the filter:

$$\frac{m}{z} = \frac{k U_1}{\nu^2 r_0^{\,2}}$$

where:

m	…	ionic mass
z	…	charge of ion
k	…	constant
U_1	…	peak amplitude of ac potential
ν	…	frequency of ac potential
r_0	…	radius of cylinder defined by inner surface of electrodes

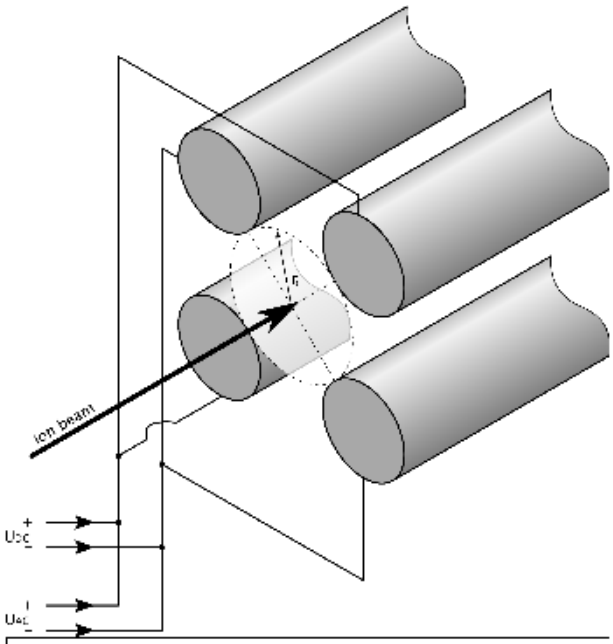

Fig. 45: Quadrupole mass analyser

It is noteworthy, that with the above mentioned techniques, only ions of differing m/z ratios can be distinguished, the actual elemental composition can not be determined. This leads to the problem of *mass interference*: Ions of isotopes of different elements, but (roughly) same mass and charge can not be distinguished. *Isobaric interference* is the interference of isotopes of the same mass, but different elements (e.g. ^{204}Hg and ^{204}Pb). *Polyatomic ions* form from gases present in the plasma (combinations of H, N, O and Ar; e.g. $^{44}Ca^{+}$ and $^{14}N_2{}^{16}O^{+}$ have both m/z=44). *Refractory oxide ions* result either from the sample matrix or the plasma tail flame (e.g. $^{44}Ca^{+}$ and $^{28}Si^{16}O_2{}^{+}$, both m/z=44). Ions of differing mass *and* charge might have the same m/z ratio as each other, thus being evenly indistinguishable (e.g. $^{172}Yb^{2+}$ and $^{86}Sr^{+}$, both m/z=86).

To overcome this and other interfering effects, separation of ion beams can also be achieved by filters based on other principles than electromagnetism. Acceleration in a defined electric potential will give all ions of same charge the same kinetic energy, which results in differing velocities of ions of different mass. The following two designs select ions based on their kinetic energy.

- An electrostatic energy filter (or electrostatic analyser, ESA) deflects the ion beam in an electrostatic field, forcing different masses into different trajectories. The design is similar to the magnetic sector mass analyser, with the electromagnet (above and below the ion beam) replaced by two electrodes, in the form of concentric cylindrical sectors (on the inner and the outer side of the bending analyser tube), between which the ion beam passes (see double focussing mass spectrometer, below).

- The time-of-flight mass analyser accelerates a short ion pulse in an electric potential and the travel time of the ions through a zero-field volume of known length is measured, thus the velocity of the ions determined.

Collector

Measuring of the ion beam intensity is typically performed with either one, or a combination of *Faraday Cup detectors or secondary electron multipliers*, a special design of which is the *Daly photomultiplier system*. The Faraday cup measures the electric charge accumulated by the ions hitting a collector electrode. Electron multipliers measure the cascading secondary electrons generated by the primary (sample) ions hitting an array of amplifier dynodes. The *channeltron* is another design of electron multiplier, using continuous semiconductor dynodes instead of an array of separate ones. In the Daly design, the ion beam is deflected by a high voltage cathode, from which secondary electrons are emitted upon impact of the ion beam. These electrons hit a scintillator and the signal is amplified by a photomultiplier. Daly detectors and Faraday cup detectors are often combined, the Daly cathode acts as a switch for which detector the ion beam hits.

Detection of the ion beam(s) may also be conducted by placing a *photographic plate* in the focal plane of the ion beam. Beam intensity is calculated from the (photometrically measured) grade of blackening of the plate. The Mattauch-Herzog geometry of a doubly focussing mass spectrometer (see below) is especially suited, because ion beams off all mass numbers (m/z) are focussed on one common focussing plane, so all ion beams are measured simultaneously on the same photographic plate.

3.3.3 Data acquisition and reduction (theory)

Principles (single-collector TIMS)

Measured ion beam intensities from a single collector analysis must be corrected for *beam instability*, *baseline contribution*, *isobaric interference*(s), and, if isotope ratios are to be obtained, *mass fractionation*.

The ion beam should ideally have a “flat-top profile”, meaning that along a traverse through the beam, the intensity should be constantly high, with steep fall-offs on either side. A profile of beam intensity can be measured by slightly increasing/decreasing either magnetic field strength or acceleration potential, thus slowly sweeping the ion beam over the fixed detector. Acquisition parameters are then chosen so that the beam is centered on the detector.

Different masses are measured by setting the magnetic field to the respective values to direct the ion beams of interest into the detector. Each mass is measured consecutively for an *integration time* long enough to obtain a sufficiently precise measurement, but short enough to allow for a series of repeated measurements of each mass before the sample on the filament is exhausted. Precision of the determined isotope ratios increases with the number of individual measurements (random error decreases, thus precision is a function of the square root of individual measurements).

Together with isotopes of the analyte of interest, additional, unique masses of elements contributing isobaric interference on the analyte, and intensity on a beam position in between mass peaks (to estimate baseline intensity) are acquired.

Even without altering instrument settings, ion beam intensity will change with time, both as a systematic, slow increase (*growth*), and as short, random fluctuations (*instability; Gill, 1997*).

The baseline intensity consists of electronic noise in the detector, and scattered ions of the analyte, caused by collisions of the ion beam with residual gas molecules in the analyser tube. The latter leads to a tail of increased background signal close to each peak (*tailing effect*). The effect is larger, the stronger the ion beam is, which can lead to

difficulties in precisely measuring small mass peaks close to large ones. The instrumental *abundance sensitivity* is a measure for tailing interference of adjacent mass peaks. It can be improved by fitting an electrostatic analyser between mass analyser and collector, and by maintaining a high vacuum.

Isobaric interference is monitored by measuring an interference-free isotope of the (or each of the) interfering element(s) together with the analyte isotopes. Interference correction is achieved by the formula:

$$A_{corr} = A_{meas} - B_{meas} \times \left(\frac{B_i}{B_m} \right)$$

where:

A_{corr}	…	corrected intensity of analyte isotope A
A_{meas}	…	measured intensity of analyte isotope A
B_{meas}	…	measured intensity of non-interfering isotope of element B
$\frac{B_i}{B_m}$	…	ratio of interfering isotope to non-interfering isotope of element B in the sample

Interference can be minimised by removal of the interfering isotope from the sample, e.g. by chemical separation, or by “burning off” of the interfering element prior to analysis, if it has a lower ionisation energy than the analyte.

Growth is corrected by an assumed linear interpolation of the measured intensities over time. Short-term instability of the ion beam can not be corrected and degrades precision of ratios obtained from the consecutive measurements.

Mass fractionation occurs because of preferential thermal ionisation of lighter masses from the sample on the filament. This leads to relative depletion of lighter masses in the residual sample and thus to changing isotopic ratios measured over the course of an analysis. The fractionation effect is greater for more volatile and for lighter elements (because of greater relative mass differences). Triple-filament loading shows less mass fractionation. For details, see "Mass fractionation" below.

Multi-collector ICPMS

In this setup, ICP is the ion source, with its associated advantages and disadvantages (see "Ion Source" above and "Mass fractionation" below).

Multiple detectors in one instrument allow for the simultaneous measurement of the intensities of several ion beams. Detectors are either set fixed for a particular element (fixed multi-collector), or adjustable (variable multi-collector). In the latter case, each detector must be centered separately on the respective ion beam to be measured.

In *static multi-collection*, additional to the actual mass peaks, baseline is measured at half-mass offset either side of the peak of interest. The magnetic field stays constant (static) during measurement. Simultaneous measurement of monitor isotopes for mass interference automatically corrects for beam instability. Isotope ratios are calculated directly from the ratios of (baseline corrected) measured intensities. Using a combination of electron multipliers and Faraday cups allows for the simultaneous measurement of very large ratios.

Precision of static multi-collector measurements is excellent, but accuracy and reproducibility is difficult to attain. Individual ion beams are measured on different detectors, which may exhibit differences in amplifier gain and in transmission efficiency. To determine amplifier gain differences, a constant electric current is regularly measured on each of the amplifiers. Transmission differences are determined by comparing the intensity of a stable ion beam measured on each of the detectors.

In *multi-dynamic analysis*, amplifier gain and transmission of the individual detectors is calibrated by successively measuring the same sample ion beam on all the of the detectors. This involves varying the magnetic field of the mass analyser, thus the term “dynamic”. Interference monitors are measured simultaneously. Reproducibility is much improved in this mode. It combines high precision, compared to single-collector analysis, with higher accuracy, compared to static multi-collector acquisition, but it is slower and requires larger sample sizes (Faure & Mensing, 2005; Gill, 1997).

Quadrupole ICPMS

This technique combines an ICP ion source with a quadrupole mass analyser (see above). Different masses of interest, or a whole mass spectrum, can be scanned very rapidly. Mass resolution on this type of analyser is relatively low; adjacent elemental mass numbers can easily be identified, but mass interferences from e.g. polyatomic ions can not be detected. A whole spectrum of blank signals, resulting from polyatomic ions or refractory oxides, is observed, mainly at m/z<80 (the argon dimer).

Ion beam intensity is typically measured with an electron multiplier, yielding very high sensitivity for most elements, and low detection limits. A wide dynamic range allows for (quasi-)simultaneous determination of elements of very different concentrations.

Quantification of signal intensities is usually achieved by external calibration to a standard material of known composition. This is the only possibility if the method is used in conjunction with sample introduction by laser ablation. If sample is introduced in solution, isotope dilution may be applied.

Mass fractionation

Ionisation effectiveness is mass dependent, because lighter isotopes will be more readily freed from their molecular bonds (Zou, 2007). In TIMS, this leads to a constant change in measured isotopic ratios towards heavier isotopes throughout the analysis of a sample (growth). Diffusion from the ion beam of an ICP ion source will cause a constant *mass bias* preferring heavier masses. Mass fractionation can be constant in time, or change systematically, both towards or away from heavier masses. Fractionation of the different isotopes of an element will be proportional to mass.

If three or more isotopes of an analyte element can be measured, any two isotope ratios plotted against each other for the data of one analysis will show near-linear correlation (Gill, 1997). Assuming a standard value for one of the ratios fixes the value for the other(s). This standard value may be obtained by integrating the whole signal of a sample until exhaustion from the filament (TIMS). If one isotope pair is non-radiogenic and non-radioactive, and isotope fractionation in the sample can be excluded,

an established standard value for its “natural” ratio can be used (*internal normalisation; Gill, 1997*).

When only two isotopes are present, or if there is no non-radiogenic isotope pair, a standard of known isotopic composition is run with the samples (*external normalisation*). Mass fractionation is determined in the external standard and assumed to be equal for the samples. Thus, it is important that the samples and the standard are prepared and handled in a way so they behave similarly.

For mass bias correction, a different element than the analyte, but with similar isotopic masses, can be mixed with the sample and measured simultaneously.

For the correction, the mass fractionation relative to mass difference of the isotopes of interest must be known. Linear, exponential or power fractionation laws (Wasserburg et al., 1981) are commonly applied. The formulas are:

Linear law:

$$\left(\frac{A}{B}\right)_{corr} = \left(\frac{A}{B}\right)_{meas} \times \left[1 + \frac{M_A - M_B}{M_B - M_C} \times \left(\frac{\left(\frac{B}{C}\right)_{true}}{\left(\frac{B}{C}\right)_{meas}} - 1\right)\right]$$

where:

A, B, C	…	isotopes A, B and C of the analyte
corr	…	indicates corrected (assumed true) value
meas	…	indicates measured values
$M_{A,B,C}$	…	masses of isotopes A, B and C
$\left(\frac{B}{C}\right)_{true}$	…	assumed natural ratio of isotopes B and C

Power law:

$$\left(\frac{A}{B}\right)_{corr} = \frac{\left(\frac{A}{B}\right)_{meas}}{\left(\frac{M_A}{M_B}\right)^{\beta}} \quad \text{with} \quad \beta = \frac{\ln\left[\frac{\left(\frac{B}{C}\right)_{meas}}{\left(\frac{B}{C}\right)_{true}}\right]}{\ln\left(\frac{M_B}{M_C}\right)}$$

where:

A, B, C	…	isotopes A, B and C of the analyte
corr	…	indicates corrected (assumed true) value
meas	…	indicates measured values
$M_{A,B,C}$	…	masses of isotopes A, B and C
$\left(\frac{B}{C}\right)_{true}$	…	assumed natural ratio of isotopes B and C

Exponential law:

$$\left[\frac{\left(\frac{A}{B}\right)_{meas}}{\left(\frac{A}{B}\right)_{true}}\right]^{\ln\left(\frac{M_B}{M_C}\right)} = \left[\frac{\left(\frac{B}{C}\right)_{meas}}{\left(\frac{B}{C}\right)_{true}}\right]^{\ln\left(\frac{M_A}{M_B}\right)}$$

where:

A, B, C	…	isotopes A, B and C of the analyte
meas, true	…	indicate measured and true values, respectively
$M_{A,B,C}$	…	masses of isotopes A, B and C

For small corrections (measured values close to assumed natural or CRM values), the differences between the three formulas are negligible. For very high precision measurements, the exponential law might be the better approximation of natural behaviour, see Thirlwall, 1991.

Quantification with internal and external standardisation

Calculating the concentrations of elements of interest in a sample from laser ablation data requires analysis of an *external standard* (a CRM, e.g. NIST SRM612, Reed, 1992) containing known concentrations of the elements of interest. The concentration of one

element in the sample must be known, either from analysis with another method or stoichiometric considerations. This element is called the *internal standard*. For the actual calculations applied in this study, see chapters 4.6 and 4.12.3.

Isotope dilution

Isotope dilution is based on the determination of the isotopic composition of an element in a mixture of a known quantity of a "spike" with an unknown quantity of the normal element. The spike is a solution containing a known concentration of a particular element artificially enriched in one of its isotopes. The sample contains an unknown concentration of the element whose isotopic composition is known (measured). Mixing a known amount of sample with a known amount of spike, and measuring the resulting isotopic composition, allows for calculation of the amount of the element in the sample (after Faure & Mensing, 2005).

After mixing, the ratio R_m of abundances of two isotopes A and B is:

$$R_m = \frac{Ab_N^A N + Ab_S^A S}{Ab_N^B N + Ab_S^B S}$$

where:

R_m	…	measured ratio of isotopes A and B
N, S	…	number of atoms of the normal element and the spike
Ab_N^A	…	abundance of isotope A in the normal element (and so forth)

A is the isotope which is enriched in the spike, B is a nonradiogenic isotope of the same element. The number of atoms of the analyte in the sample (N) can be calculated by:

$$N_w = S_w \left(\frac{W_N}{W_S} \right) \left[\frac{Ab_S^A - R_m Ab_S^B}{R_m Ab_N^B - Ab_N^A} \right]$$

where:

N_W, S_W	…	no. of atoms in normal element and spike, resp.
W_n, W_s	…	atomic weight of analyte in the sample and spike, resp.
Ab_N^A, Ab_S^A	…	abundance of isotope A in normal element and spike, resp.
Ab_N^B, Ab_S^B	…	abundance of isotope B in normal element and spike, resp.
R_m	…	ratio of isotopes A and B in the mixture (measured)

where W_N and W_S are the atomic weights of the analyte in the sample and in the spike, respectively, and N and S are in terms of numbers of atoms. Using concentrations rather than number of atoms, concentration of the analyte in the sample can be calculated as:

$$C_N = C_S \frac{M_S}{M_N} \frac{W_N}{W_S} \left[\frac{Ab_S^A - R_m Ab_S^B}{R_m Ab_N^B - Ab_N^A} \right]$$

where:

C_N, C_S	…	concentration of analyte in the sample and spike, resp.
M_N, M_S	…	weight of the sample and the spike, resp.
W_n, W_s	…	atomic weight of analyte in the sample and spike, resp.
Ab_N^A, Ab_S^A	…	abundance of isotope A in normal element and spike, resp.
Ab_N^B, Ab_S^B	…	abundance of isotope B in normal element and spike, resp.
R_m	…	ratio of isotopes A and B in the mixture (measured)

where M_N and M_S are the weights of the sample and the spike in the mixture, respectively, in units of weight (after Zou, 2007).

This method allows for very low concentrations being measured with high accuracy on small amounts of sample. For spikes, often artificial radioisotopes are used. The accuracy of results greatly depends on background contamination minimisation, calibration of spike solution, correction for fractionation effects during sample introduction (preferential ionisation,...), and avoidance of other sources of error, like change of spike concentration by evaporation (Gill, 1997).

3.3.4 Design combinations at RHUL

TIMS

The TIMS lab houses a VG 354 Thermal Ionisation Mass Spectrometer. Sample introduction is by beads on a 16 place turret. Mass separation is achieved with a 90° magnetic sector mass analyser. Measurement occurs on an array of four adjustable Faraday cups and one fixed axial Faraday cup/Daly detector combination.

IsoProbe

The GVI (MicroMass) IsoProbe uses an ICP ion source and a magnetic sector mass analyser. Sample introduction is achieved by either a Micromist glass nebuliser (Meinhard type) or a CETAC Aridus II™ desolvating micronebuliser. The IsoProbe is fitted with a hexapole collision cell. Multi-collector measurement occurs in an (adjustable) array of 9 Faraday detectors and three ion-counting detectors (two low-mass channeltrons; one axial Daly detector to be used alternatively to one of the nine Faraday cups).

LA-ICPMS

A RESOlution M-50 laser ablation system (Resonetics Inc.) with a 193nm ArF excimer laser (COMPexPro110, Coherent Inc.) allows for sample analysis of a wide range of solid samples. The ablation cell (Laurin Technic, AUS) has a two-volume geometry with a small effective ablation volume and invariant gas flow at the ablation site, enabling constant elemental/isotopic fractionation during sample stage movement (for a thorough description, see Müller et al., 2009b). The sample aerosol is transported by He and, mixed with Ar carrier gas, gets analysed by an Agilent Inc. 7500ce ICP quadrupole mass spectrometer. Carrier gas flow of the ablated sample may alternatively be directed to the IsoProbe (see above).

Comparison of techniques applied at RHUL

Comparison: TI vs. ICP

Thermal Ionisation (TI)	Inductively Coupled Plasma (ICP)
ionisation efficiency limits sensitivity	ion transmission from plasma inefficient (~2%) → large sample sizes
not all elements readily ionised	introduction of elements with high ionisation energy possible (most elements suitable)
mass fractionation relatively small	mass fractionation relatively large
preferential thermal ionisation of lighter masses, residuum depleted in lighter isotope → measured ratios change over time of analysis	measured ratios constant (precise), but inaccurate; heavy masses preferred (due to ion extraction in the plasma-vacuum interface)
mass fractionation greater for lighter elements (greater relative mass differences), and dependent on loading method (triple filaments showing less fractionation), but different elements behave differently	mass fractionation largely mass dependent, elements of similar atomic mass show similar fractionation
sample preparation takes long (filament loading)	allows easy and rapid sample introduction in different states (fluid, gaseous, to a limited extend particulate)

Comparison: Faraday Cup vs. electron multiplier (and Daly multiplier)

Faraday Cup	Electron multiplier and Daly photomultiplier
electronic noise limits sensitivity	very low electronic noise, high sensitivity
mass-independent, linear response → more precise ratios	signal may be mass and intensity dependent
slow signal decay (memory effect)	

Comparison: single collector vs. multi-collector

Single collector mass spectrometry	Multi-Collector Mass Spectrometry (MC-MS)
masses measured sequentially → longer analysis time → more sample needed	reduced analysis time, smaller sample sizes

one mass measured at any given time → ratios only obtained consecutively, short-term instabilities in ionisation intensity increase error	simultaneous acquisition of all masses of interest, direct measurement of ratios - short-term instabilities in source ionisation are overcome
signal growth → values need to be interpolated over time	no time interpolation required
	very large ratios can be measured by combinations of Faraday Cups and electron multipliers

3.3.5 Alternative designs

In a *double focussing mass spectrometer*, a combination of an electrostatic energy filter and a magnetic sector mass analyser allows for filtering of ions both based on electromagnetism and kinetic energy. Very high mass resolution is achieved this way.

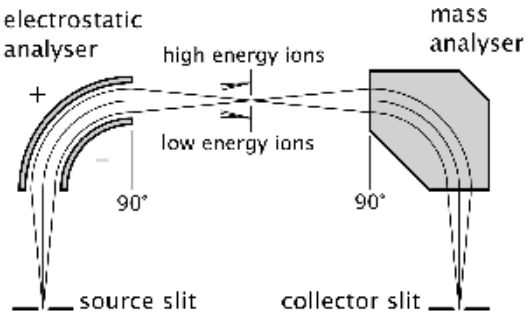

Nier–Johnson geometry

Two general geometries are in use: in the Nier-Johnson geometry, the electrostatic analyser works energy-selecting, whereas in the Mattauch-Herzog geometry, the electrostatic analyser works energy-focussing, cancelling out energy dispersion in the magnetic analyser.

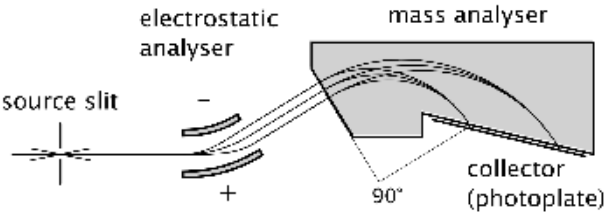

Mattauch–Herzog geometry

Fig. 46: Nier-Johnson and Mattauch-Herzog geometries of double focussing mass spectrometers

Secondary Ion mass spectrometry (*SIMS*) uses a highly focussed primary ion beam to *sputter* particles out of the surface of a solid sample. Some of these released particles are (mono- and multi-atomic) ions, which can be accelerated and filtered in a mass filter. For an overview and comparison of this technique with SHRIMP (see below), see e.g. Compston, 1999; Williams, 1985.

The Sensitive High-Resolution Ion MicroProbe (*SHRIMP*; e.g. Compston et al., 1984; Compston, 1996; Compston & Clement, 2006) uses secondary ionisation and a very large (high resolution) double focussing multi-collector mass spectrometer to achieve very high mass resolution on small samples. This allows for analysis of small, complex solid samples, like e.g. zoned, multiphase Zircons (e.g. Froude et al., 1983; Compston & Pidgeon, 1986).

In an *accelerator mass spectrometer*, negative ions are produced by sputtering the sample with a caesium beam. The ions are filtered by a first magnetic sector mass analyser, the selected beam is introduced in a linear particle accelerator. Within the accelerator, the negative ions hit a gas filled chamber or thin foil, which strips off all electrons and breaks any molecular bonds. The resulting positive ions are further accelerated and separated in a second magnetic sector mass analyser before measurement. This technique allows analysis of extremely low concentrations of e.g. cosmogenic nuclides (Gill, 1997).

3.4 Data quality (theory)

3.4.1 Precision and accuracy (theory)

The *mean* value $\bar{x}$ of a series of measurements x_i is defined as

$$\bar{x} = \frac{\sum_{1}^{N} x_i}{N}$$ (after Zou, 2007), where N is the number of observations.

The *standard deviation* of a data set is calculated as

$$\sigma_x = \sqrt{\frac{1}{N-1}\sum_{1}^{N}(x_i - \bar{x})^2} \quad .$$

The *standard error*, or standard deviation of the mean, is defined as

$$\sigma_{\bar{x}} = \frac{\sigma_x}{\sqrt{N}} \quad .$$

From this follows that in contrast to σ_x, the standard error will decrease with an increase in number of observations. The standard error is often denoted as se instead of $\sigma_{\bar{x}}$.

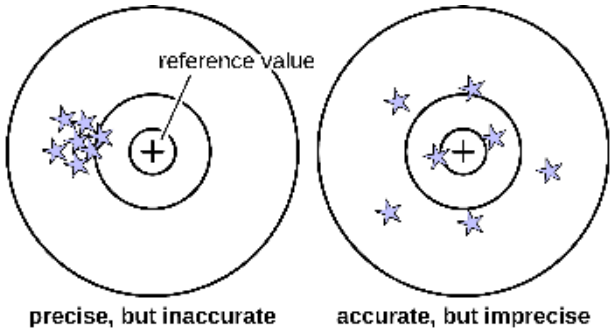

Illustration of data precision vs. accuracy. Stars indicate individual measurements of the true value at the centre.

Precision of a set of measurements is a measure for the *random error* of the data set. Assuming the individual measurements scatter around a mean value with normal distribution, the standard deviation σ of that distribution can be used to quantify precision. Commonly, a measured value is given as the mean value $\bar{x} \pm 2s$. In this notation, s stands for the calculated standard deviation of the data from their mean value $\bar{x}$ (after Gill, 1997), which is only an approximation for the true standard deviation σ around the true mean. It can be shown that in a set of values obeying a normal distribution, 95% of values will fall within 2σ of the mean. *Relative Precision* is expressed in percent of the mean value.

Data *accuracy* is a measure for *systematic error* in a set of measurements. It is usually calculated from comparison of measurements on a certified reference material (CRM; Gill, 1997) with the certified or preferred values for that material. From measurements of CRMs, correction factors can be calculated to be included in data processing, counteracting systematic bias.

Data *reproducibility* is a measure for the ability to obtain the same value in repeated measurements of a sample. It is normally calculated from a longer-time series of measurements of CRMs.

3.4.2 Error sources and uncertainties

Every measured value for a natural phenomenon can only be determined with a certain amount of certainty. The exact reasons for uncertainty are manifold. Sources of statistical error (causing imprecision) have to be distinguished from sources of bias (causing inaccuracy).

In this study, main sources of bias are mass fractionation during sample introduction and analysis in the mass spectrometer, instrumental bias e.g. in the detectors of the mass

spectrometer, and sample contamination during sample preparation. Generally, a constant bias in measurements (*systematic error*) can be determined with appropriate tests and corrected for mathematically or in instrument tuning (see e.g. chapter 4.5.4, 4.6.4 for mass fractionation correction and data quality assurance by measurements of CRMs), or attempted to be reduced in the analysis workflow (see 4.5, 4.6.3 for information on workflow optimisation to reduce blank). Another source of bias, potentially with a randomly fluctuating component to it, is isobaric interference, which can be minimised in instrument tuning.

Instabilities in the measurement process itself, like fluctuations in sample uptake, gas flows, in the plasma torch, sample ionisation, ion beam, magnetic field, detector response,... and electronic noise (in detectors and amplifiers) cause *random error*. These can be reduced trying to run an analysis under as stable conditions as possible, but can not be completely eliminated. Repeated measurements can alleviate this fact partially, because the standard error (se) decreases with increasing number of measurements.

There also exist uncertainties in values that go into the calculations during data reduction (chapter 4.6), namely the assumed concentrations of elements and isotopic ratios in CRMs, uncertainties on the values of the isotopic abundances and masses of elements under consideration and on the halflives of the radioactive nuclides in each of the decay chains. These errors should be propagated through all calculations (see e.g. Ludwig, 2003; Zou, 2007).

However, the greatest source for random error in this study is geological *scatter*, slight deviations of the isotopic compositions of analysed subsamples from one sample, caused either by initial sample inhomogeneity, or by (inhomogeneous) secondary disturbances of the sample (multiple deformation generations, weathering, diagenesis,...). Geological scatter results in the data points in an isochron or concordia plot not exactly lying on one line, and the resulting uncertainty in the linear regression will lead to an increased error on the calculated age. This error in most cases is much larger than the other error sources (for a fairly precise measurement), especially uncertainties in the values for atomic weights and decay constants are comparably insignificant.

4. Methodology II: application

4.1 Sampling and field techniques

Sample collection was by standard field geological methods, with a hammer and chisel. Only apparently fresh, unweathered samples, or samples big enough to contain an unweathered core after extensive cleaning, were collected. Outcrops with current or obvious past water flow were only sampled if fresh samples from a zone deeper within the host material could be extracted. Samples were collected in standard food-grade plastic zip bags. Structural data were measured using a CLAR-type geologist's compass. GPS coordinates for each outcrop were recorded.

4.2 Palaeo-Stress analysis

Palaeo-stress analysis from brittle deformation structures is a well established method for obtaining an estimate of local and potentially regional principal stress orientations during time of deformation (e.g. Angelier, 1979; Sperner & Zweigel, 2010). Relative motion of two blocks separated by a fault or fracture is inferred from indentations, grooves and scratch marks, secondary structures, and most commonly and reliably, from mineral fibres grown at the time of and in direction of movement, or "slickenfibres" (see e.g. Petit, 1987; Means, 1987 for a description of sense-of-movement indicators, and chapter "2.1 Tectonic carbonates", with references therein).

The aim of this study was not to conduct new palaeostress analyses in the visited areas. Where they could be acquired during sampling, measurements of brittle deformation structures were recorded, to be able to place the sample in a framework of published deformation phases for the respective area. Where sampling sites were visited together with local collaborators, often this correlation with a deformation event was based on personal communication.

For large enough data sets, a best fit orientation of palaeo-stress principal axes can be calculated (see e.g. Angelier, 1979; Will & Powell, 1991; Will & Powell, 1992; Fry, 1992; Mostafa, 2005; Phan-Trong, 1993). Because the deformation and the forces leading to it can not be observed directly, certain assumptions have to be made based on the resulting structures. For a discussion of validity and applicability of these assumptions that goes beyond the scope of this study, see e.g. Sperner & Zweigel, 2010 or Kaven et al., 2011.

The method has been applied successfully in many areas worldwide, e.g. Decker et al., 1993; Ortner, 2003c; Peresson & Decker, 1997 define the six phases of Miocene deformation in the northern and central Eastern Alps that form the tectonic framework in which samples from the areas Lower Inn Valley (LIV), Tauernwindow Northern Fault (TNF), Gosau Basin (GOB) and Fohnsdorf Basin (FOB) are to be seen. See chapter "2.2 Sampling areas, geological background and structural geology" for further references for the respective areas.

The program TectonicsFP (Ortner et al., 2002) was used for calculation of principal stress (PT-) axes.

4.3 Mechanical sample preparation

4.3.1 Thin sections, thick sections and polished blocks

Samples were cut with a rotating diamond coated rock cutting saw into slabs of few mm thickness. For laser ablation, one surface of the slabs was ground plain on rotating diamond coated grinding discs, and manually lapped with successively finer grained carborundum powder to P600 or P1000 grit size.

Before analysis, the slabs were ultrasonicated for 10-15 min, each: twice in acetone, once in isopropanol or methanol, and at least thrice in "triple red" (18.2 MΩ) deionised water, or until water stayed clear (see also chapter "4.12 Summary: detailed workflow for U-Pb dating of calcite"). The slabs were then air dried in a clean air hood.

Thin and thick sections were prepared by the thin sections lab in house at RHUL, using Crystalbond™ adhesive. If sections were analysed by laser ablation, cleaning was with methanol (shortly) and deionised water only.

Samples too small for stand-alone mounting in the laser ablation sample holder were embedded in epoxy resin, before grinding and lapping as described above. These samples also were not cleaned with acetone.

4.3.2 Microsampling

From samples determined to be suitable for high-precision MC-ICPMS analysis, subsamples of ~250 mg each were cut with a diamond-coated dental cutting wheel on a hand-held drill. The individual subsamples were chosen based on the spatial information about U/Pb ratio and element concentrations gained from laser ablation single tracks and maps (see chapters "4.7 1D LA-ICPMS screening" and "4.8 2D LA-ICPMS element mapping" below). Usually, subsamples were cut from the hand specimens the LA slabs were cut from, to preserve the latter for potential further LA analyses. The rock saw removes ~2-3 mm of material between the LA slab and the remaining sample, and cutting direction was usually perpendicular to fibre growth. This allowed for good correlation of the LA results to the hand specimen. Where more exact choice was necessary, the subsamples were cut from the LA slab, destroying it in the process.

Each subsample was mechanically cleaned under the binocular with a rotating diamond-coated abrasive tool. Any discolourations and visible foreign minerals were removed from the usually plain white calcite samples.

The resulting subsamples were degreased and cleaned with acetone and isopropanol/methanol as described for the laser ablation slabs above, and air dried in a clean air hood.

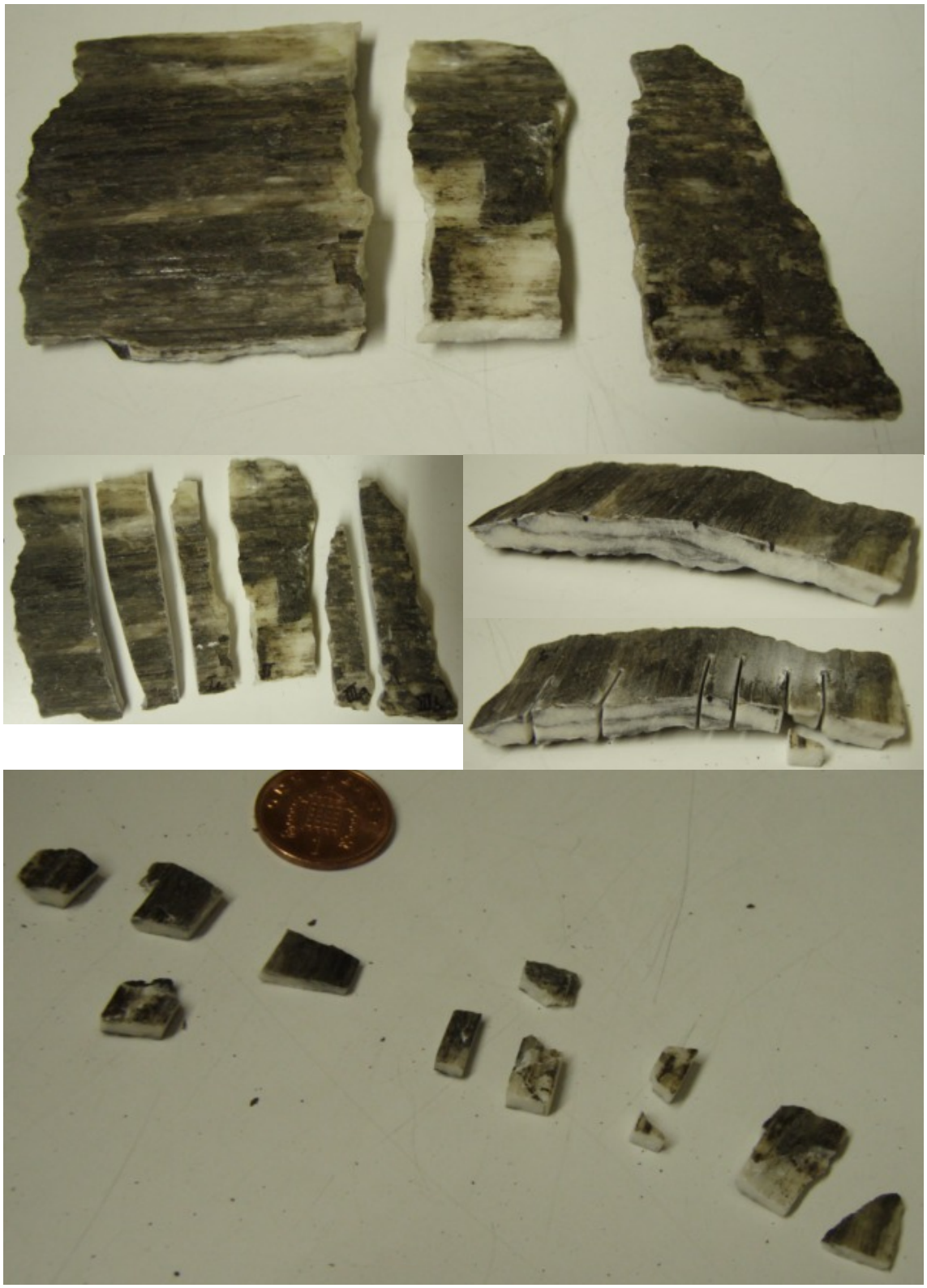

Fig. 47: Microsampling of KMR-GOB21B_A
Top: As sampled, broken in three pieces (I, II, III). Middle, left: pieces cut, one side will be prepared for LA, the other remains for microsampling (middle, right). Bottom: subsamples cut, before mechanical cleaning.

4.4 Chemical sample preparation

For all further chemical procedures, high-purity acids sub-boiling distilled in PTFA and FEP stills (abbreviated "TD." for 1 × "teflon distilled", "h.p.", standing for "high purity", for twice distilled), and high-purity deionised H_2O ("triple red", 18.2 MΩ, abbreviated "h.p.") were used. Distilled HNO_3 had a concentration of ~15M, distilled HCl ~8M. Lower concentration acids were produced by dilution with H_2O h.p.

All wet-chemical work for subsequent isotopic analyses was conducted in PFA vials cleaned by long-time leaching in alternating baths of hot, dilute (reagent grade, not h.p.) HNO_3 and HCl, followed by refluxing with h.p. HNO_3 on a hot plate. H.p. reagents were stored in FEP bottles cleaned in the same manner.

As a final cleaning step before dissolution, the surface of the subsamples was etched off in 1M HCl h.p. for 25-30 s, before rinsing with H_2O h.p. three times.

Samples were then dissolved with an amount of HNO_3 h.p. corresponding approximately to the stoichiometric equivalent of the amount of calcite in the sample. The resulting solution was diluted to 2M HNO_3.

The sample solution was aliquoted in a 20:80 ratio for isotope dilution (see below) and natural isotopic ratio analysis, respectively.

For a detailed step-by-step description of the whole wet-chemical workflow, see chapter "4.12.2 Detailed clean lab/column chemistry workflow".

4.4.1 Extraction chromatography

From the sample aliquots, Pb and U (with Th) were separated by extraction chromatography (Horwitz et al., 1992), following and adapting work by e.g. Woodhead et al., 2006 and Luo et al., 1997. In a first step, Pb was separated from the solution utilising Eichrom Sr resin. This resin, although developed for separation of Sr, has an even higher retention potential for Pb, as shown in Fig. 48 (from Horwitz et al., 1992).

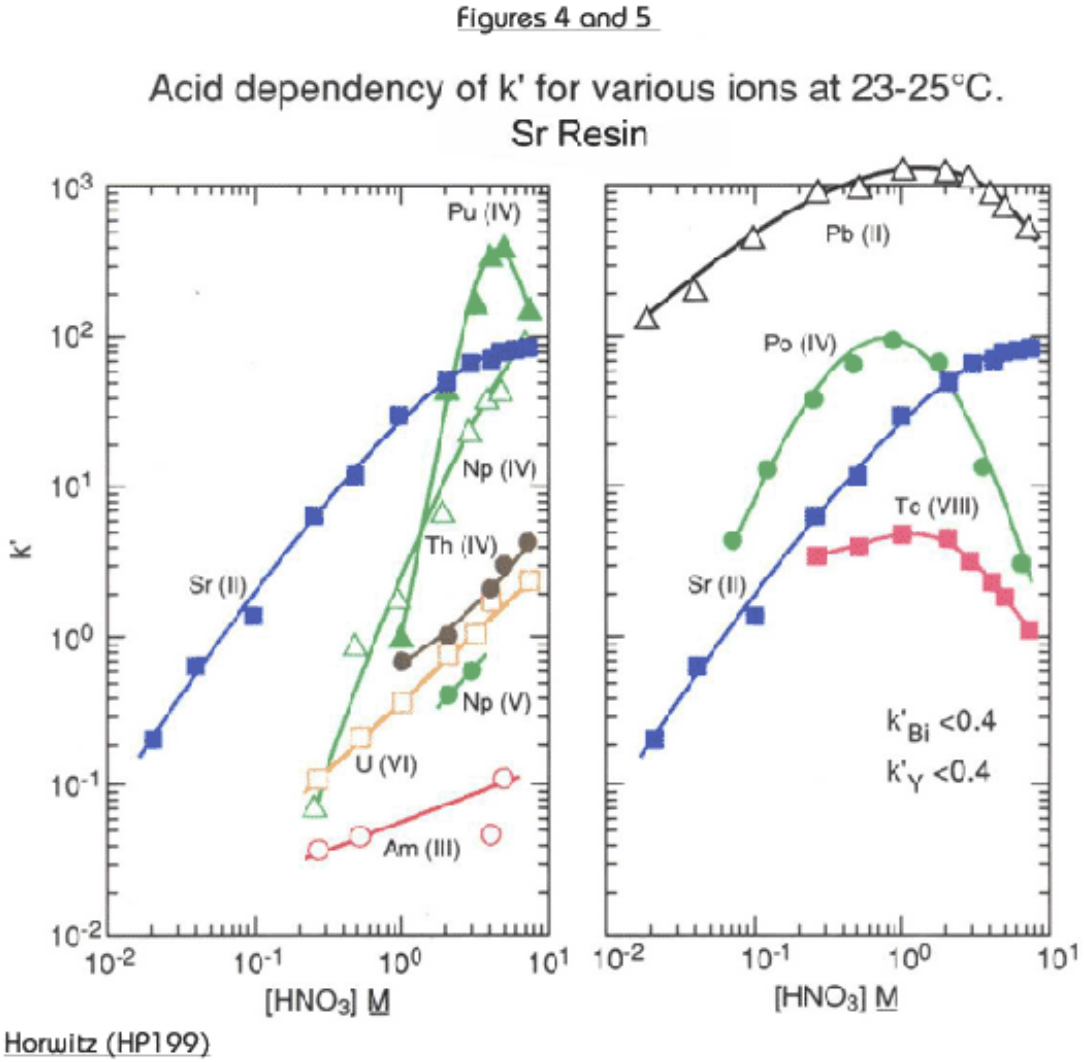

Fig. 48: Acid dependency of the uptake of selected metal ions
Acid dependency of the uptake of selected metal ions by Sr resin at temperature 23-25° C (from Horwitz1992). In the present study, samples were loaded in 2M HNO_3, to achieve maximum Pb retention.

100 µl Sr resin were loaded onto 100 µl prefilter resin (the same inert substrate the extraction resin is applied on in manufacture). The dissolved samples, diluted to 2M HNO_3 concentration, were loaded onto the cleaned and conditioned resin. The solution passing the columns was collected for subsequent separation of U and Th. 8M HCl h.p. was used for Pb elution off the resin and was collected for a second pass through the same columns.

The process was calibrated by collecting the passing solutions in small fractions and analysing these separately for their elemental concentrations, as shown in Fig. 49 and Fig. 50.

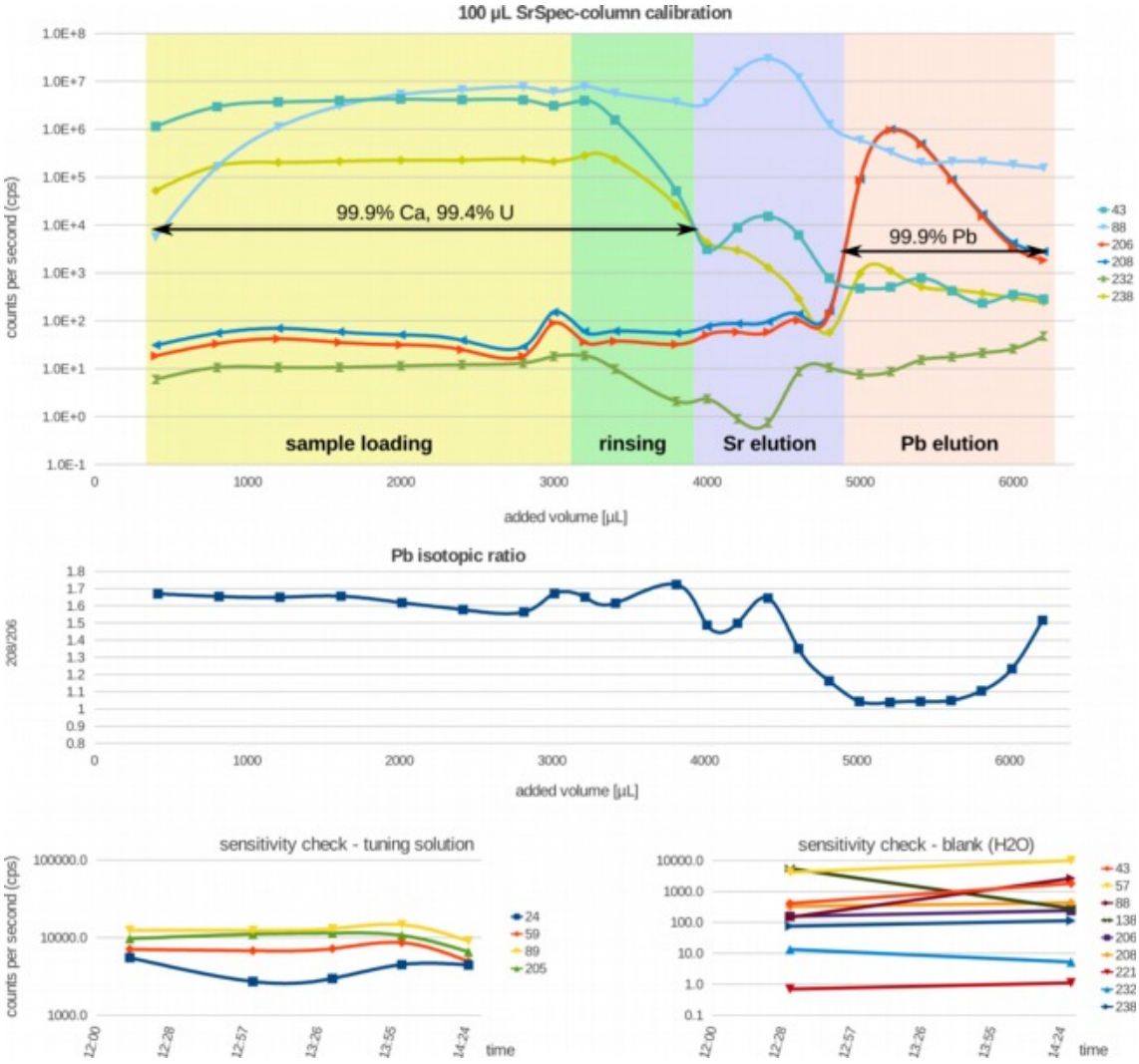

Fig. 49: Calibration curves for Sr resin column chemistry.
Most elements simply pass the column during sample loading, Ca and U are plotted as examples. The exponential rise followed by constantly high values for Sr might indicate that the loading capacity was exceeded. In this study, Sr was not considered, and the much higher affinity of the resin for Pb still assures an efficient separation. Pb signals remain low throughout sample loading (full retention), and Pb is readily stripped off the resin during elution.
For calibration, a tracer solution enriched in ^{206}Pb was used. The $^{208}Pb/^{206}Pb$ ratio curve (middle plot) shows values close to the natural background of ~1.6–1.7 throughout sample loading and Sr elution, and drops to the ratio of the artificial solution of ~1–1.1 during Pb elution. A rise in the ratio at the end indicates return to background values, thus complete elution.
Elements were measured by one representative m/z ratio each, signals are plotted in raw counts per second. For calibration, qualitative information was sufficient and values were not converted to concentrations.

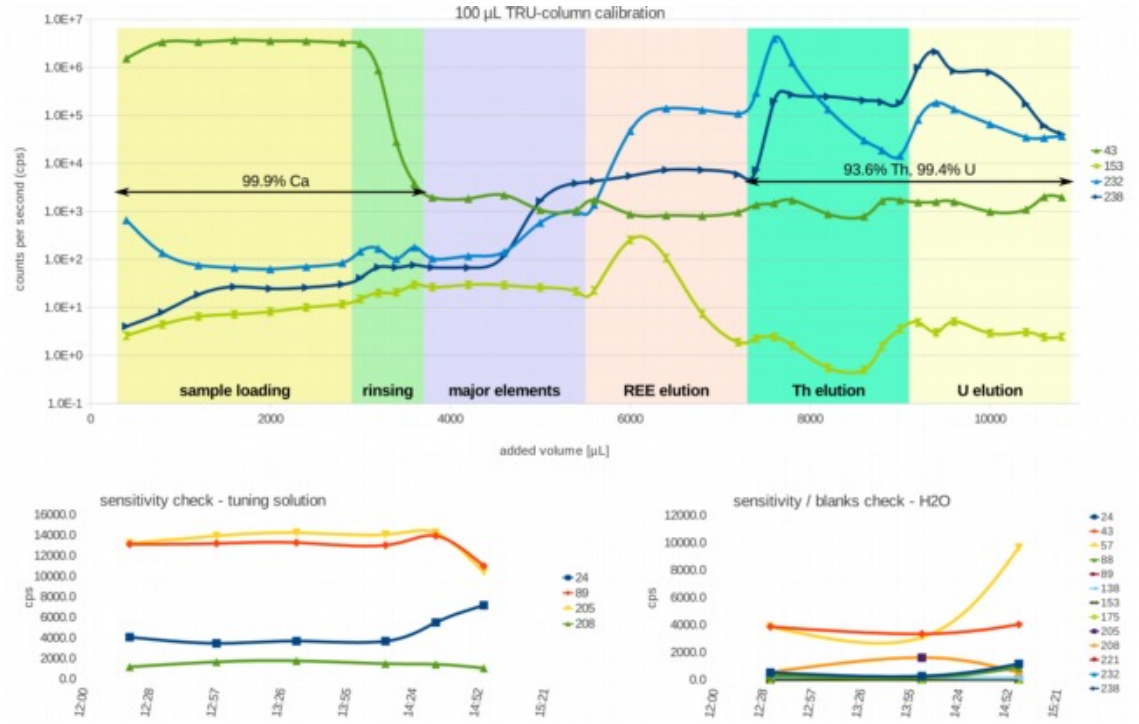

Fig. 50: Calibration curves for TRU resin column chemistry
Major elements (represented by Ca here) are rinsed off after sample loading. The last two fractions, yielding Th and U respectively, were collected together for analysis.

The U fraction was loaded on 100 µl Eichrom TRU resin (with 100 µl prefilter resin) in 2M HNO_3 solution, Th was eluded with 0.2M HCl h.p., U with a 0.1M HCl / 0.3M HF solution (HF was reagent grade, not distilled, as no significant U contamination occurred as a background to the process).

After column passes, the samples (both Pb and U) were dried down, 200 µl HNO_3 h.p. were added to break down organic residue of mobilised resin, and dried down again.

4.4.2 Isotope Dilution

For isotope dilution measurements (see chapter "3.3.3 Data acquisition and reduction (theory)"), a combined solution ("spike") enriched in ^{208}Pb, ^{229}Th and ^{236}U was mixed with the 20% aliquot of samples before column chemistry.

4.5 Error sources and avoidance strategies, quality assurance

Some potential problems arise from the specific nature of the samples considered in this study.

- A detrital clay or carbonate phase or late diagenesis processes may distort the isotope ratios (Cole et al., 2005). All optically visible foreign particles in the samples were either removed or the respective regions avoided in subsampling. LA-ICPMS trace element data also gave a good indication of homogeneity on samples and best suited subsamples.

- As the samples for this study are taken at the earth's surface and fractures and faults in general are prone to weathering, open-system behaviour may lead to fractionation by physical and/or chemical processes (leaching, expulsion, Rn-loss by diffusion). Concordance of $^{238}U/^{206}Pb$ and $^{235}U/^{207}Pb$ ages would indicate no major disturbances to have occurred (Cole et al., 2005).

- In very young samples, departure from initial secular equilibrium of the U-series decay chain at the time of precipitation may lead to an apparent offset (Wendt & Carl, 1985, Richards et al., 1998). This again can be argued to have had no major effect, if the $^{238}U/^{206}Pb$ and $^{235}U/^{207}Pb$ ages are concordant (Cole et al., 2005). The samples analysed in this study are all expected to be much older than the threshold of $\sim 10^6$ a given in Richards et al., 1998 and Gascoyne, 1992 for establishment of secular equilibrium.

Assuming undisturbed samples, and that a lot of the above mentioned natural disturbances can be avoided by careful sample selection, the main problem during sample preparation for analysis is Pb contamination from the (laboratory) environment. One main aspect of this study was to establish a workflow that allows reliably reproducible low-blank analyses of Pb and U isotopic ratios on as small sample sizes as technically possible.

Prerequisites for low-blank wet chemistry are thoroughly clean labware and reagents, careful handling in a controlled environment and constant blank monitoring,

as described below. Detailed step-by-step instructions for the applied lab procedures are given in chapter "4.12 Summary: detailed workflow for U-Pb dating of calcite".

4.5.1 Labware cleaning, reagents, handling

For all further chemical procedures, high-purity acids sub-boiling distilled in PTFA and FEP stills (abbreviated "TD." for 1 × "teflon distilled"; "h.p.", standing for "high purity", for twice distilled), and high-purity deionised H_2O ("triple red", 18.2 MΩ, abbreviated "h.p.") were used. Distilled HNO_3 had a concentration of ~15M, distilled HCl ~8M. Lower concentration acids were produced by dilution with H_2O h.p.

All wet-chemical work for isotopic analyses was conducted in PFA vials cleaned by long-time (1-3 weeks) leaching in alternating baths of hot, dilute (reagent grade, not h.p.) HNO_3 and HCl, followed by refluxing with HNO_3 h.p. on a hot plate. TD and h.p. reagents were stored in FEP bottles cleaned in the same manner.

FEP columns for extraction chromatography were ultrasonicated in reverse position after use, to remove resin particles possibly clinging to the frit material, and then leached in HCl h.p. on the hotplate in designated large PFA vials for several hours, before storage in 1M HCl h.p. in individually allocated and previously leached PS centrifuge tubes.

Wet chemical work was conducted in ISO class 10 designated clean air hoods, providing laminar air flow of filtered air with a slight overpressure towards the surrounding. Most measurement and handling of reagents was conducted by pipetting with PS pipette tips leached for cleaning (see "4.12.2 Detailed clean lab/column chemistry workflow" below), only spike solution was added from a FEP dropper bottle and resins were loaded with dedicated PP pipettes previously leached in dilute HNO_3.

All containers were opened only the absolute minimum time necessary, lids were placed back on loosely whenever possible, all movements within the clean air hood were made with great care to not reach over any open containers or risk any other particulate contamination. One dedicated cleaned pipette tip was used for handling of all "h.p." chemicals and was rinsed at each change of reagent and before and after putting

into storage container. This pipette tip was replaced whenever any possibility of contamination was suspected.

A special, antistatic hooded lab coat (SNDI Switzerland "Everest Clean 3000") with elastic cuffs made of a material not shedding particulates was worn for chemical work in clean labs. WRP Dermagrip powder-free latex examination gloves were worn and changed frequently.

4.5.2 Blanks

Blanks were run with every batch of samples processed in the column chemistry workflow – usually two blanks per batch, to potentially distinguish random, single-particle contamination from a systematic e.g. reagent contamination. Every step of the workflow was conducted in the same manner as with samples, and at the same time as samples, each time in different columns previously used for samples. This not only allows for a realistic estimation of amount and likelihood of contamination, but inherently also tests cleaning procedures applied between sample runs.

Reagent blanks were determined each time new distilled "h.p." acids were used. Cleaning procedures were tested by refluxing cleaned vials for several hours on the hotplate with HNO_3 h.p. and measuring the blank on the leachate. Besides particle counting (see next section below), particle contamination was also tested with long-time exposure blanks collected in open PFA vials. Occasionally, column blanks were determined by running HCl h.p. through columns with and without resin bed, without loading a sample.

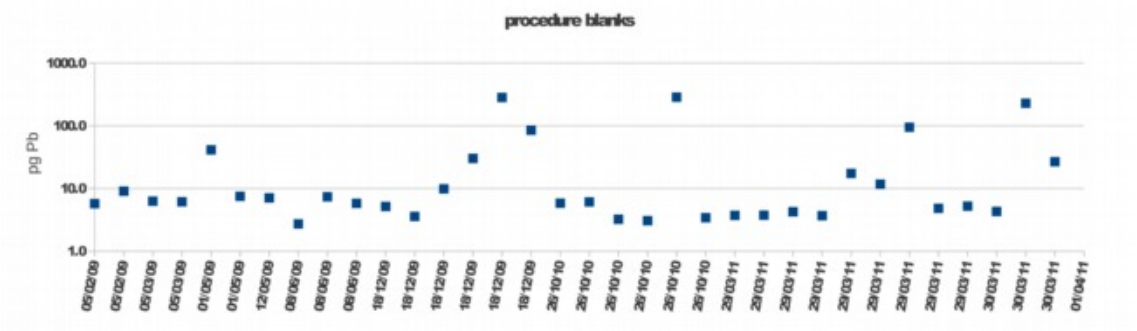

Fig. 51: All procedure blanks measured after the final adaptation of the presented workflow. Most outlying values can be explained by handling errors noticed during sample processing. The average of the remaining values is 11.4 pg Pb. Assuming a low value is generally achievable, and assuming elevated values result from particulate or other contamination not intrinsic to the workflow, and thus omitting all values > 20 pg, yields an average of 5.3 pg Pb assumed to be the lowest achievable value, calculated from 24 individual procedure blanks.

sample	date	pg Pb	2se pg Pb
procedure blank	05/03/09	6.3	0.5
procedure blank	05/03/09	6.1	0.4
procedure blank	12/05/09	7.1	0.4
procedure blank	18/12/09	5.1	0.7
procedure blank	18/12/09	3.6	0.4
procedure blank	18/12/09	9.9	0.8
procedure blank	18/12/09	30.1	0.4
procedure blank	18/12/09	282.2	0.7
procedure blank	18/12/09	85.1	0.5
procedure blank	05/02/09	5.7	0.6
procedure blank	05/02/09	9.0	0.9
procedure blank	01/05/09	41.3	0.6
procedure blank	01/05/09	7.5	2.9
procedure blank	08/06/09	2.7	1.4
procedure blank	08/06/09	7.4	0.7
procedure blank	08/06/09	5.8	3.2
procedure blank	26/10/10	5.8	0.9
procedure blank	26/10/10	6.1	0.9
procedure blank	26/10/10	3.2	0.4
procedure blank	26/10/10	3.1	0.8
procedure blank	26/10/10	286.7	0.5
procedure blank	26/10/10	3.4	1.6
procedure blank	29/03/11	3.7	0.7
procedure blank	29/03/11	3.7	0.5
procedure blank	29/03/11	4.2	0.6
procedure blank	29/03/11	3.7	0.8
procedure blank	29/03/11	17.3	1.2
procedure blank	29/03/11	11.7	1.1
procedure blank	29/03/11	94.7	0.6
procedure blank	29/03/11	4.8	0.5
procedure blank	29/03/11	5.2	0.8
procedure blank	30/03/11	4.3	0.4
procedure blank	30/03/11	228.3	0.7
procedure blank	30/03/11	26.6	0.6

sample	date	pg Pb	2se pg Pb
column blank	16/12/08	7.0	
column blank	16/12/08	8.7	
column blank	16/12/08	2.0	
exposure blank	16/12/08	1.3	
exposure blank	26/10/10	309.7	0.8
exposure blank	26/10/10	17.0	0.7
+4			
reagent blank HCl hp	10/12/08	8.4	
reagent blank HCl hp	16/12/08	4.2	
reagent blank HCl hp	26/10/10	6.5	0.6
reagent blank HCl hp	30/03/11	4.3	0.6
reagent blank HCl hp	01/05/09	1.5	2.7
reagent blank HCl TD	01/05/09	2.2	0.7
+1			
reagent blank HNO3 hp	10/12/08	2.9	
reagent blank HNO3 hp	16/12/08	5.8	
reagent blank HNO3 hp	26/10/10	15.9	0.5
reagent blank HNO3 hp	30/03/11	5.8	0.6
reagent blank HNO3 hp	01/05/09	3.0	1.4
+1			
reagent blank H2O	16/12/08	2.5	
reagent blank H2O	30/03/11	181.8	6.0
reagent blank H2O	01/05/09	2.6	5.3
+2			
vial blank	30/03/11	4.6	0.8
vial blank	30/03/11	2.1	0.7
vial blank	30/03/11	1.2	0.3
vial blank	30/03/11	1.8	0.6
+8			
+empty column blanks (~7)			

no handling issues recorded
long time storage before analysis
recorded handling error

Tab. 1 (above): Pb blanks.
Of the procedure blanks, those with handling issues noticed during work were not considered further. Of the remaining blanks (green), those over 20 pg were considered outliers, most likely due to particulate contamination, and were also not included in the final average procedure blank.

Tab. 2 (right): U blanks.
Contamination with U was considered a far less likely risk, thus fewer blank measurements were conducted.

sample	date	pg U	2se pg U
exposure blank	02/11/10	1.42	0.03
exposure blank	02/11/10	0.88	0.03
reagent blank HCl hp	02/11/10	0.82	0.03
reagent blank HNO3 hp	02/11/10	0.71	0.03
procedure blank	02/11/10	0.92	0.10
procedure blank	02/11/10	1.23	0.02
procedure blank	02/11/10	3.32	0.09
procedure blank	02/11/10	0.90	0.04
procedure blank	02/11/10	1.22	0.03
procedure blank	02/11/10	1.23	0.02

4.5.3 Particle counting

In order to assess and monitor air quality in the clean air hoods and to optimise air flow, a HandiLaz® Mini 3-channel, handheld airborne particle counter was used to count airborne particles. A pump draws a constant air stream through the detection chamber, at a flow rate of 2.83 l/min, while particles are detected optically.

Usually, counting time was 10 – 20 min, the minimum time to yield statistically meaningful results under the given situation according to the counter's user manual. Although stated to be ISO class 10 clean air hoods by the producer, our particle counts would not justify classification better than class 100 according to the strict ISO guidelines. This result varies between different locations in the air hood, the centre coming up to class 10 air quality, and an attempt was made to concentrate the work in these "good" zones. It must be stressed that the applied counting times are not sufficient to validate the calculated ISO clean air classes in an ISO-conform testing protocol, for which purpose this model of particle counter may not be suited at all. The model was chosen for it's ease of use and manageability, enabling quick, hand-held measurements. For the intent of setup optimisation, formal ISO certification was not deemed necessary and thus not pursued.

4.5.4 Standards

Throughout analyses, standard materials of known composition were measured intermittently with samples. NIST SRM 612 glass (Reed, 1992), USGS MACS-3 carbonate powder pellets were utilised, and a cross-check with MPI-DING GOR 128-G glass (Jochum et al., 2000; Jochum et al., 2006) was conducted (1 analysis).

In laser ablation work, the NIST SRM 612 glass standard was used for external standardisation, measured usually once before and after single track ablation, or several times throughout a mapping. The standard was mounted on the sample holder with the sample, and the geometry of the ablation cell (see "LA-ICPMS" in chapter "3.3.4 Design combinations at RHUL") assures constant sample aerosol transport at any position within the cell.

However, because the standard and samples are not matix-matched, i.e. the one being a silicate glass, the others carbonate, a differing ablation efficiency might be expected. With a 193nm excimer laser, the differences are insignificantly small. See also chapter "6 Interpretation and Discussion" for discussion.

Eggins & Shelley, 2002 point out the possibility of compositional heterogeneities in the NIST glass standards. Some indication for this could be observed, but because standards were measured as (short) tracks, not as point analyses, inhomogeneities could be easily recognised and the affected data were not used.

In solution work for MC-ICPMS, solutions of NIST SRM 981, 982 (Catanzaro et al., 1968; Thirlwall, 2002) and the NU-C standard were used, diluted to concentrations comparable to the samples. Thallium solution for mass fractionation correction was based on NIST SRM 997 with an assumed natural $^{205}Tl/^{203}Tl$ ratio of 2.3889 (Dunstan et al., 1980; Thirlwall, 2002).

	$^{208}Pb/^{206}Pb$	$^{207}Pb/^{206}Pb$	$^{204}Pb/^{206}Pb$
SRM 981	2.1677 ± 2 [b]	0.91488 ± 08 [b]	0.059026 ± 11 [b]
SRM 982	1.00016 ± 36 [a]	0.467080 ± 10 [c]	0.027212 ± 2 [c]

Tab. 4: NIST SRM 981 and SRM 982
Lead isotopic ratios after (a) Catanzaro1968, (b) Thirlwall2002 and (c) Doucelance2001.

Tab. 3 (following page): NIST SRM 612 concentration values.
GeoReM preferred concentration values as used in this study, and new values (Jochum2011). There are no changes for the elements most relevant in this study (U, Pb, Th, Ca).

NIST NISTSRM612: GeoReM preferred Values
Jochum and Nehring 11/2006

Item	Value	Uncertainty	Uncertainty Type	Unit
Ag	22	0.3	95%CL	micro_g/g
Al	11167	18	SD	micro_g/g
As	37	7	SD	micro_g/g
Au	5.1	0.1	SD	micro_g/g
B	35	3	SD	micro_g/g
Ba	39.7	0.4	SD	micro_g/g
Be	38	3	SD	micro_g/g
Bi	30	6	SD	micro_g/g
Ca	85048	176	SD	micro_g/g
Cd	28.3	0.7	SD	micro_g/g
Ce	38.7	0.4	SD	micro_g/g
Cl	131	13	SD	micro_g/g
Co	35	2	SD	micro_g/g
Cr	36	3	SD	micro_g/g
Cs	42	3	SD	micro_g/g
Cu	37	3		micro_g/g
Dy	36	0.4	SD	micro_g/g
Er	38	0.9	SD	micro_g/g
Eu	35	1	SD	micro_g/g
F	62	6	SD	micro_g/g
Fe	51	2	95%CL	micro_g/g
Ga	36	2	SD	micro_g/g
Gd	36.7	0.4	SD	micro_g/g
Ge	35	3	SD	micro_g/g
Hf	35	4	SD	micro_g/g
Ho	38	1	SD	micro_g/g
In	43	4	SD	micro_g/g
K	66.3	0.4	SD	micro_g/g
La	35.8	0.4	SD	micro_g/g
Li	42	3	SD	micro_g/g
Lu	36.9	0.4	SD	micro_g/g
Mg	77	30	SD	micro_g/g
Mn	38	1	SD	micro_g/g
Mo	38	2	SD	micro_g/g
Na2O	51930	2226	SD	%m/m
Nb	40	3	SD	micro_g/g
Nd	35.9	0.4	SD	micro_g/g
Ni	38.8	0.2	95%CL	micro_g/g
P	51	6	SD	micro_g/g
Pb	38.57	0.2	95%CL	micro_g/g
Pd	1.1			micro_g/g
Pr	37.2	0.9	SD	micro_g/g
Pt	2.6			micro_g/g
Rb	31.4	0.4	95%CL	micro_g/g
Re	6.6			micro_g/g
Rh	0.9			micro_g/g
Sb	38	2	SD	micro_g/g
Sc	41	4	SD	micro_g/g
Si	336085	3360	SD	micro_g/g
Sm	38.1	0.4	SD	micro_g/g
Sn	38	2	SD	micro_g/g
Sr	78.4	0.2	95%CL	micro_g/g
Ta	40	2	SD	micro_g/g
Tb	36	3	SD	micro_g/g
Th	37.79	0.08	95%CL	micro_g/g
Ti	44	5	SD	micro_g/g
Tl	15.1	0.7	SD	micro_g/g
Tm	38	1	SD	micro_g/g
U	37.38	0.08	95%CL	micro_g/g
V	39	4	SD	micro_g/g
W	40	1	SD	micro_g/g
Y	38	2	SD	micro_g/g
Yb	39.2	0.4	SD	micro_g/g
Zn	38	4	SD	micro_g/g
Zr	38	2	SD	micro_g/g

Jochum et al 2011

Item	Value	Unit	Difference
Ag	22	µg/g	0
Al	10744	µg/g	-423
As	35.7	µg/g	-1.3
Au	4.77	µg/g	-0.33
B	34.3	µg/g	-0.7
Ba	39.3	µg/g	-0.4
Be	37.5	µg/g	-0.5
Bi	30.2	µg/g	0.2
Ca	85048	µg/g	0
Cd	28.1	µg/g	-0.2
Ce	38.4	µg/g	-0.3
Cl	142	µg/g	11
Co	35.5	µg/g	0.5
Cr	36.4	µg/g	0.4
Cs	42.7	µg/g	0.7
Cu	37.8	µg/g	0.8
Dy	35.5	µg/g	-0.5
Er	38	µg/g	0
Eu	35.6	µg/g	0.6
F	80	µg/g	18
Fe	51	µg/g	0
Ga	36.9	µg/g	0.9
Gd	37.3	µg/g	0.6
Ge	36.1	µg/g	1.1
H2O	0.021	%m/m	
Hf	36.7	µg/g	1.7
Ho	38.3	µg/g	0.3
In	38.9	µg/g	-4.1
Ir	0.0045	µg/g	
K	62.3	µg/g	-4
La	36	µg/g	0.2
Li	40.2	µg/g	-1.8
Lu	37	µg/g	0.1
Mg	68	µg/g	-9
Mn	38.7	µg/g	0.7
Mo	37.4	µg/g	-0.6
Na	50817	µg/g	-1113
Nb	38.9	µg/g	-1.1
Nd	35.5	µg/g	-0.4
Ni	38.8	µg/g	0
P	46.6	µg/g	-4.4
Pb	38.57	µg/g	0
Pd	1.05	µg/g	-0.05
Pr	37.9	µg/g	0.7
Pt	2.51	µg/g	-0.09
Rb	31.4	µg/g	0
Re	6.63	µg/g	0.03
Rh	0.91	µg/g	0.01
S	377	µg/g	
Sb	34.7	µg/g	-3.3
Sc	39.9	µg/g	-1.1
Se	16.3	µg/g	
Si	337021	µg/g	936
Sm	37.7	µg/g	-0.4
Sn	38.6	µg/g	0.6
Sr	78.4	µg/g	0
Ta	37.6	µg/g	-2.4
Tb	37.6	µg/g	1.6
Th	37.79	µg/g	0
Ti	44	µg/g	0
Tl	14.9	µg/g	-0.2
Tm	36.8	µg/g	-1.2
U	37.38	µg/g	0
V	38.8	µg/g	-0.2
W	38	µg/g	-2
Y	38.3	µg/g	0.3
Yb	39.2	µg/g	0
Zn	39.1	µg/g	1.1
Zr	37.9	µg/g	-0.1

Tab. 5: GOR128-G concentration values.
GeoReM preferred concentration and isotopic composition values for glass standard MPI-DING GOR128-G. These values follow Jochum2006.

MPI-DING GOR128-G: GeoReM preferred Values
Jochum (Max-Planck-Institut fuer Chemie)
(3/2011)

Item	Value	Uncertainty	Uncertainty Type	Unit	
Ag	0.5			µg/g	information value
Al2O3	9.91	0.17	95%CL	%m/m	information value
As	0.1			µg/g	information value
Au	0.024			µg/g	information value
B	23.5	2.8	95%CL	µg/g	certified value
Ba	1.06	0.03	95%CL	µg/g	certified value
Be	0.034	0.007	95%CL	µg/g	information value
Bi	0.0009			µg/g	information value
Br	0.3			µg/g	information value
CaO	6.24	0.12	95%CL	%m/m	certified value
Cd	0.072			µg/g	information value
Ce	0.45	0.016	95%CL	µg/g	certified value
Cl	12			µg/g	information value
Co	92.4	6.2	95%CL	µg/g	certified value
CO2	0.00044			%m/m	information value
Cr	2272	171	95%CL	µg/g	certified value
Cs	0.24	0.025	95%CL	µg/g	certified value
Cu	63.8	12.5	95%CL	µg/g	certified value
Dy	1.98	0.07	95%CL	µg/g	certified value
Er	1.4	0.06	95%CL	µg/g	certified value
Eu	0.264	0.008	95%CL	µg/g	certified value
F	25			µg/g	information value
FeO(t)	9.81	0.12	95%CL	%m/m	certified value
Ga	8.67	1.07	95%CL	µg/g	certified value
Gd	1.17	0.04	95%CL	µg/g	certified value
Ge	0.96			µg/g	information value
H2O	0.026			%m/m	information value
Hf	0.349	0.017	95%CL	µg/g	certified value
Hg	0.2			µg/g	information value
Ho	0.443	0.019	95%CL	µg/g	certified value
In	0.067			µg/g	information value
Ir	0.063			µg/g	information value
K2O	0.036	0.005	95%CL	%m/m	certified value
La	0.121	0.004	95%CL	µg/g	certified value
Li	10.4	1.7	95%CL	µg/g	certified value
Lu	0.206	0.009	95%CL	µg/g	certified value
MgO	26	0.3	95%CL	%m/m	certified value
MnO	0.176	0.009	95%CL	%m/m	certified value
Mo	0.71	0.26	95%CL	µg/g	information value
Na2O	0.574	0.026	95%CL	%m/m	certified value
Nb	0.099	0.007	95%CL	µg/g	certified value
Nd	0.784	0.047	95%CL	µg/g	certified value
Ni	1074	61	95%CL	µg/g	certified value
O	444000			µg/g	information value
P2O5	0.025	0.005	95%CL	%m/m	certified value
Pb	0.345	0.043	95%CL	µg/g	certified value
Pr	0.1	0.004	95%CL	µg/g	certified value
Pt	11.1			µg/g	information value
Rb	0.406	0.025	95%CL	µg/g	certified value
Re	0.0006			µg/g	information value
S	4.3			µg/g	information value
Sb	0.01	0.021	95%CL	µg/g	information value
Sc	32.1	1.4	95%CL	µg/g	certified value
Se	0.03			µg/g	information value
SiO2	46.1	0.4	95%CL	%m/m	certified value
Sm	0.525	0.02	95%CL	µg/g	certified value
Sn	0.224	0.092	95%CL	µg/g	information value
Sr	30	1	95%CL	µg/g	certified value
Ta	0.019	0.001	95%CL	µg/g	certified value
Tb	0.248	0.012	95%CL	µg/g	certified value
Th	0.008	0.001	95%CL	µg/g	certified value
TiO2	0.288	0.012	95%CL	%m/m	certified value
Tl	0.003			µg/g	information value
Tm	0.204	0.009	95%CL	µg/g	certified value
U	0.0121	0.0012	95%CL	µg/g	certified value
V	189	13	95%CL	µg/g	certified value
W	15.5	2.4	95%CL	µg/g	information value
Y	11.8	0.5	95%CL	µg/g	certified value
Yb	1.41	0.06	95%CL	µg/g	certified value
Zn	74.7	6.7	95%CL	µg/g	certified value
Zr	10	0.5	95%CL	µg/g	certified value
143Nd/144Nd	0.513241				information value
206Pb/204Pb	18.518				information value
207Pb/204Pb	15.629				information value
207Pb/206Pb	0.845	0.0034	95%CL		reference value
208Pb/204Pb	38.286				information value
208Pb/206Pb	2.069	0.014	95%CL		reference value
87Sr/86Sr	0.706932				information value
d11B	13.7	0.6	95%CL	‰NIST951	reference value
d17O	4.83			‰VSMOW	information value
d18O	9.43			‰VSMOW	information value
d29Si	-0.21			‰NIST8546	information value
d30Si	-0.46			‰NIST8546	information value
d44/40Ca	0.77			‰NIST915a	information value
d7Li	14.4			‰LSVEC	information value

element	ppm	sd	element	ppm	sd
Ag	53.3	1.8	Lu	10.8	0.3
As	44.2	1.4	Mg	1756	136
Au	7.12		Mn	536	28
Ba	58.7	2	Mo	1.21	0.14
Be	56.4	1.7	Na	5900	400
Bi	19.9	1.6	Nb	35.2	3.1
Br	0.44		Nd	11	0.41
C	115000	600	Ni	57.4	4.9
Ca	376900	5200	Pb	56.5	1.8
Cd	54.6	2.2	Pd	3.4	
Ce	11.2	0.33	Pr	12.1	0.23
Cl	61	2	Pt	17.8	
Co	57.1	2	Ru	20.1	
Cr	117	5	Sb	20.6	1.1
Cu	120	5	Sc	21	0.8
Dy	10.7	0.5	Sm	11	0.27
Er	11.2	0.22	Sn	58.1	8.8
Eu	11.8	0.13	Sr	6760	350
Fe	11200	300	Ta	20.5	5.3
Ga	16.1	1.1	Th	55.4	1.1
Gd	10.8	0.3	Ti	54.9	0.18
Ge	56.9	4	Tl	14.2	1.7
Hf	4.73	0.21	U	1.52	0.04
Hg	10.2	0.4	V	46.3	1.13
Ho	11.3	0.14	W	2.16	0.19
I	20.3		Zn	111	5.7
La	10.4	0.5	Zr	8.67	0.63
Li	62.2	4.2			
		1 σ			
$^{87}Sr/^{86}Sr$	0.70759	2.5e-5			
		2 σ			
$^{208}Pb/^{204}Pb$	38.181	0.002			
$^{207}Pb/^{204}Pb$	15.619	0.002			
$^{206}Pb/^{204}Pb$	18.39	0.01			

Tab. 6: Preliminary concentration values for USGS standard MACS-3.

4.5.5 Comparison with published values

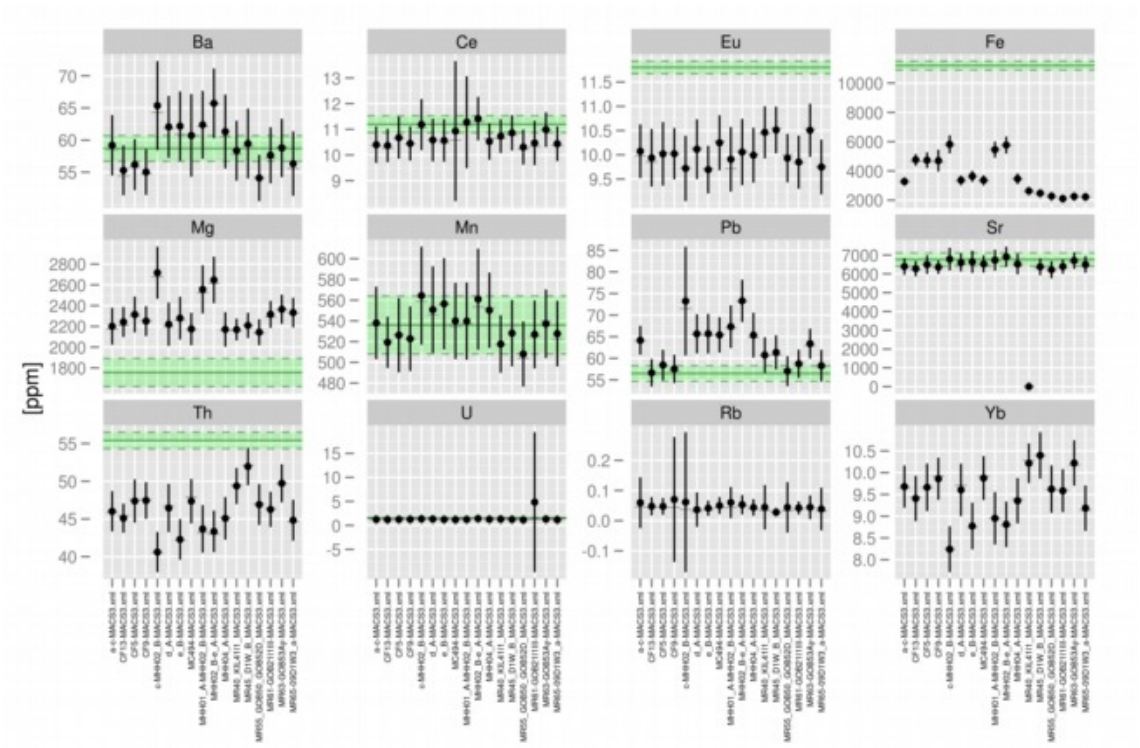

Fig. 52: Comparison of MACS-3 analyses to preliminary standard values
Black dots denote mean values, grey crosses denote median values, error bars are 1 sd. See Fig. 53 for plots of Sr and U omitting the large single outliers.

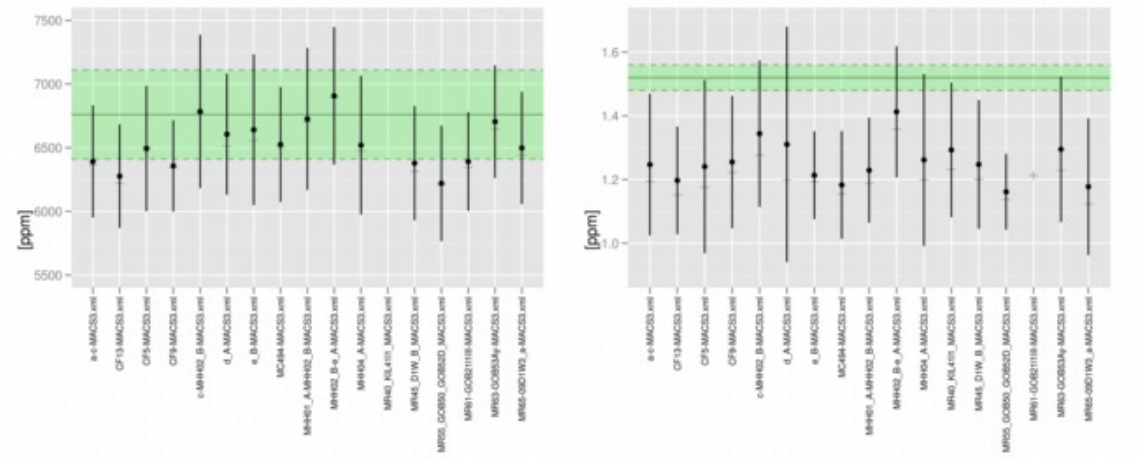

Fig. 53: Detailed view at U and Sr measurements
Left: U values, omitting the large outlier in analysis MR61. Please not that the median value (grey cross symbol) still lies within the range of the other values – see Fig. 54.
Right: Sr analyses, omitting erroneous value for analysis MR40.

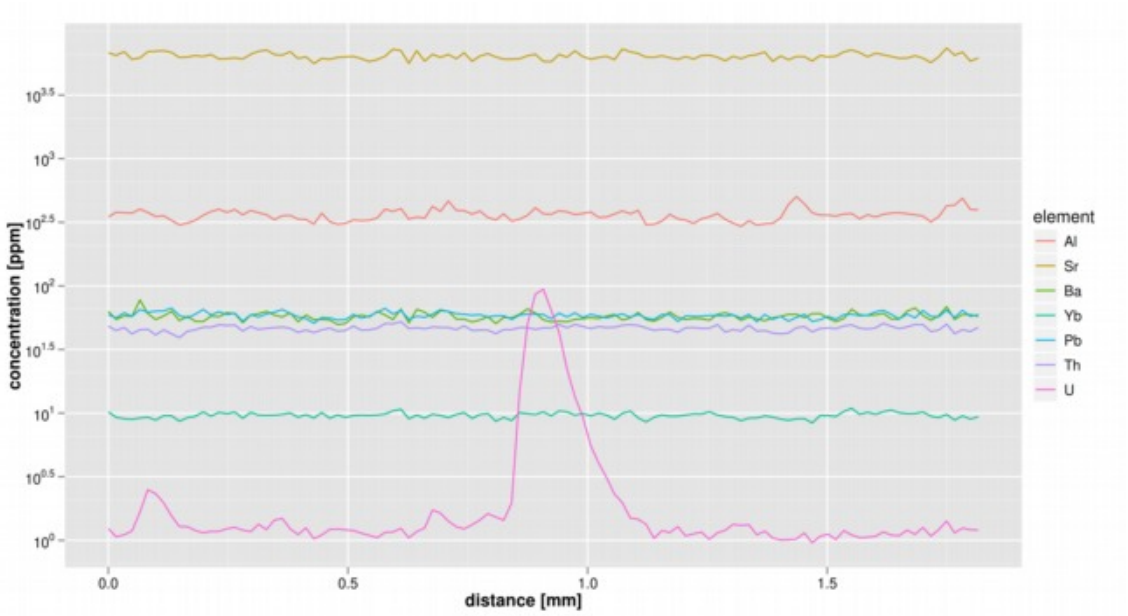

Fig. 54: Detailed view at MACS-3 analysis MR61.
Element concentration plot of the data acquired on MACS-3 in this analysis shows a constant signal for all elements except U, indicating element-specific inhomogeneities, most likely as a result of the manufacturing process. The U anomaly features up to 2 orders of magnitude higher values than the surrounding material. The anomaly spans several data points, thus is not a signal "spike" (e.g. a larger particle transported with the gas flow), but is a feature in the standard material.

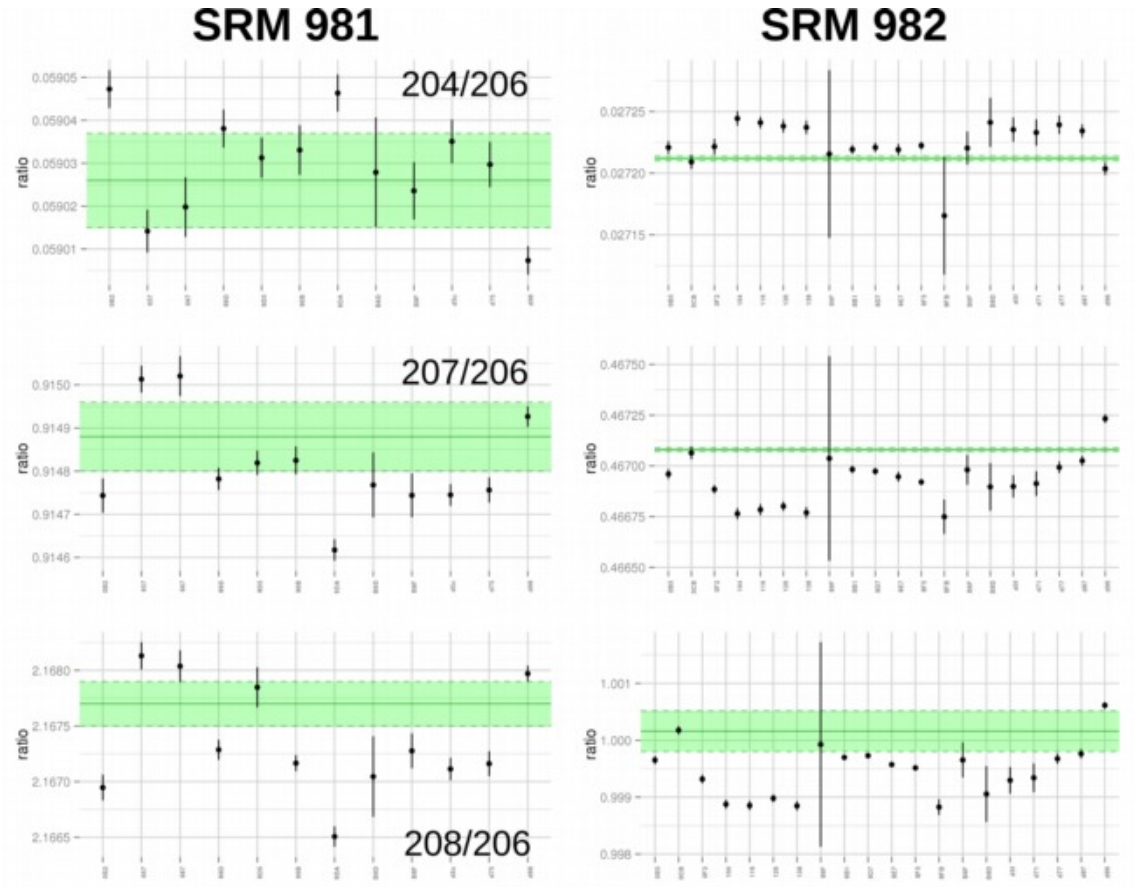

Fig. 55: Comparison of SRM 981 and 982 measurements to reference values
Measured Pb isotopic ratios acquired on the IsoProbe. From the measured values, correction factors for the further data processing were calculated.

	analysis 1	1 se	analysis 2	1 se	certified	95% CL
$^{207}Pb/^{206}Pb$	0.855	0.020	0.835	0.020	0.845	0.0034
$^{208}Pb/^{206}Pb$	2.099	0.020	2.063	0.019	2.069	0.014

	analysis 1	2 sd	analysis 2	2 sd	certified	95% CL
Al	54178	4431	55033	4647	52449	900
Pb	0.289	0.054	0.283	0.053	0.345	0.043
Th	0.008	0.018	0.007	0.016	0.008	0.001
U	0.014	0.019	0.0118	0.0054	0.0121	0.0012

Tab. 7: Comparison of MPI-DING GOR128-G measurements to certified values
In situ acquired data, ^{204}Pb not measurable on a quadrupole ICPMS. Lead isotopic ratios were estimated utilising the standard $^{206}Pb/^{204}Pb$ ratio of 18.518. Element concentrations in ppm, calculated based on 4.4597% w/w Ca as internal standard.

	analysis 1	1 se	analysis 2	1 se	preliminary	2 σ
$^{207}Pb/^{206}Pb$	0.853	0.009	0.848	0.009	0.849	0.002
$^{208}Pb/^{206}Pb$	2.062	0.009	2.059	0.009	2.076	0.002

	analysis 1	2 sd	analysis 2	2 sd	preliminary	95% CL
Pb	58.7	6.9	56.6	4.7	56.5	1.8
Th	51.2	6.3	50.9	4.9	55.4	1.1
U	1.39	0.53	1.37	0.63	1.52	0.04

Tab. 8: Comparison of USGS MACS-3 standard measurements to preliminary reported values
In situ acquired isotopic data, ^{204}Pb not measurable on a quadrupole ICPMS. Lead isotopic ratios were estimated utilising the standard $^{206}Pb/^{204}Pb$ ratio of 18.390. Element concentrations in ppm, calculated based on 37.69% w/w Ca as internal standard.

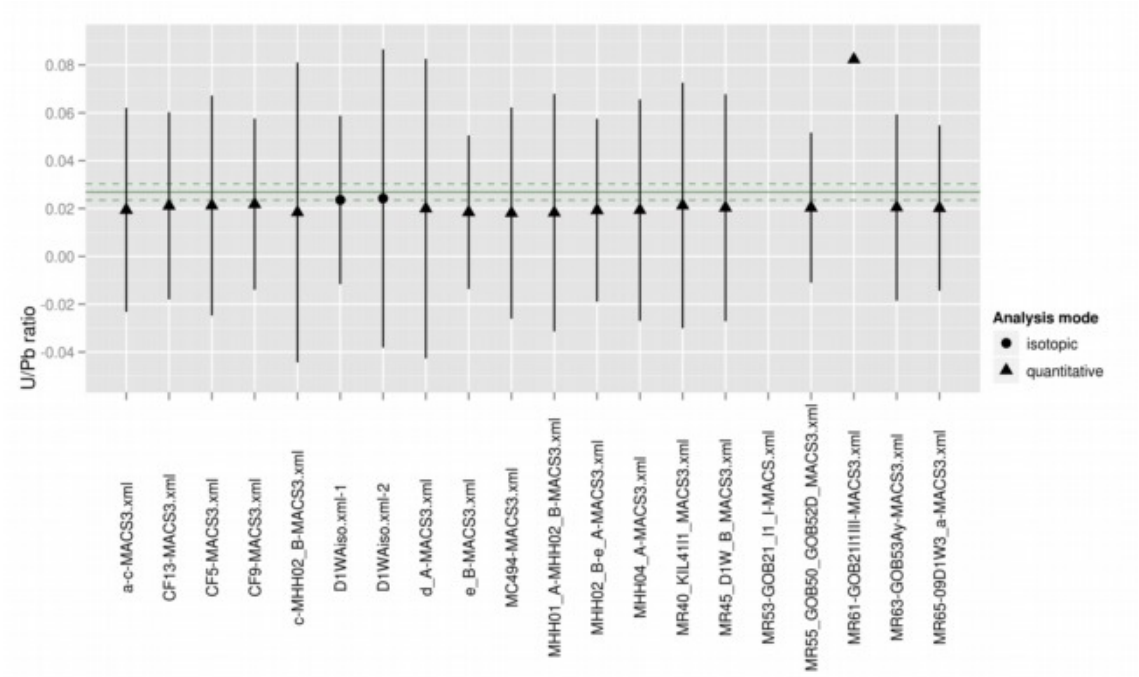

Fig. 56: Comparison of U/Pb ratios measured on USGS MACS-3
U/Pb elemental ratios measured on MACS-3. Error bars are 2 se. In green: U/Pb ratio calculated from preliminary information values, ± 2 sd. Most values are calculated means of data acquired with the standard settings for quantitative analysis, only 2 analyses were conducted with the settings used for in situ isotopic analyses – these lie closer to the proposed standard values. Analysis MR53 is erroneous and does not plot within the shown range of values. Mean value of analysis MR61 is too high due to an U anomaly, see Fig. 54. Error bars for this analysis are too large to plot on this scale.

4.6 ICPMS data reduction

Some basic principles are common to bot LA-(quadrupole) and MC-ICPMS. These are only shortly mentioned in this section, details will be found in the following chapters 4.7 – 4.10 and 4.12 for the respective methods.

4.6.1 Data conversion, handling and storage

Several programs controlling laser ablation, the quadrupole ICPMS and the IsoProbe produce various files containing information about a particular sample. These different data files have to be processed independently, and the information merged, to gain the most comprehensive view on the context of the analyses.

Laser ablation parameters are controlled by Resonetics' GeoStar software. The set parameters are stored in an .xml file, while the actual achieved ablation conditions, including some additional status information, gets saved in two log files during ablation (.csv and .log). Additionally, the samples are scanned on a flatbed scanner prior to analysis, and the image is reprojected to sample stage coordinates for a scaled display in GeoStar. The reprojected image (.png) and a small xml file containing coordination information (.coord) can be saved and facilitate exact scaled display of the scan and ablation tracks later.

The data from the Agilent 7500 quadrupole ICPMS are stored in a proprietary binary format (two files with extension .icp). The raw counts per second (CPS) data is exported as time-resolved .csv files.

The add-on package *LAICPMS* for the R Language for Statistical Computing (R Development Core Team, 2010), developed during this project for processing of the analyses data (see Rittner & Müller, 2012 in Appendix XXX), links these individual files by means of parameter files (.xml), which additionally include processing parameters and information about data structure. This information is loaded into one combined data structure containing all parameters, which is given to calculation functions as a single parameter, making handling easy. The data necessary for

calculations is read from the respective files automatically. In this approach, the original data files remain unaltered, calculations are usually performed on-the-fly as needed. The resulting data can be exported and plotted into various file formats.

Numerical or graphical analyses of the results from a sample are then saved as short script files, which include the calculations in few lines of code, and usually some graphical adaptations for the respective task (e.g. a figure in a publication).

Data from the GVI IsoProbe is stored in a structured text file (extension .dat), which in the workflow usually followed at RHUL is converted into a Microsoft Excel file, but saved under the same file name and extension (.dat). Main calculations are performed after copying the appropriate values from the source files into MS Excel masterfiles (.xls) previously set up for the task, which also serve as data repository for the results.

4.6.2 Quantification

In this study, the samples were assumed to be nearly pure calcite, thus a stoichiometric concentration of 40.04% w/w Ca was used as internal standard. Domains of host rock and contaminations (most often clay minerals in fault gauge) can not be quantified this way, but could easily be identified by elevated Al and Si counts, and were not considered in further calculations.

NIST SRM 612 glass was utilised as external standard. Concentration values for elements in NIST SRM 612 were obtained from GeoReM (as downloaded from georem.mpch-mainz.gwdg.de on 11.12.2007) and NIST (“Atomic Weights and Isotopic Compositions for All Elements”, as downloaded from physics.nist.gov/PhysRefData/Compositions/index.html on 11.12.2007).

For an explanation of the R commands called for data processing, see chapter 4.12.3 Data reduction.

After most data analysis was performed, new preferred values for element concentrations in NIST SRM 612 were published (Jochum et al., 2011), but the expected differences in results presented in this study would be negligible, thus calculations were not repeated.

4.6.3 Blank correction

In LA analyses, background signal was collected before and between individual ablations (standards, sample tracks), and usually the average raw CPS signal of the closest (in time) bracketing backgrounds was subtracted from the raw CPS measured for a sample/standard.

On the IsoProbe, machine background signals were measured before an analysis session, the blank signal of the clean (usually 2% HNO_3 h.p.) acid the sample was redissolved in was acquired before each individual measurement. The averaged background values for each analysis were subtracted from the individual raw data acquired.

Procedure blanks for the wet chemical (column) workflow were quantified from repeated blank runs. An average procedure blank of 5.3 pg Pb was determined. Blank isotopic composition was determined as the average of 10 unspiked blank column runs, and used in data reduction for correction of Pb concentrations and Pb isotopic ratios. See also chapter "4.5.2 Blanks" and individual data reduction in chapters 4.7 – 4.10 and 4.12.

4.6.4 Mass fractionation correction

In laser ablation analysis, a linear law mass fractionation correction is calculated from the measured isotopic ratios in the standards and the GeoReM preferred values – see chapter "4.12 Summary: detailed workflow for U-Pb dating of calcite" for details.

4.7 1D LA-ICPMS screening

For single track (1D) LA-ICPMS screening of samples, the polished and cleaned blocks (see chapter 4.3.1 Thin sections, thick sections and polished blocks) were mounted on sample holders provided with the HelEX ablation cell. Sample holders are machined from anodised aluminium. Different geometries are available, specialised for 4 × 1 inch epoxy blocks, 2 × 1 inch epoxy plus 1 × thin section, multiple thin sections (different widths), or free sample configurations. Standards were mounted together with the sample(s), to be analysed in the same analysis session. (usually acquired all together in one data file, including intermittent background signals).

Prior to analysis, the sample mounted in the holder is scanned on a flatbed scanner and the resulting image is later calibrated in GeoStar to sample stage coordinates, to serve as a guide for easy navigation and ablation location selection.

All sample handling was performed with powder free latex gloves to avoid contamination. Standard materials were occasionally surface-wiped with sub-boiling distilled methanol on soft laboratory wipes, to remove condensate from previous ablations. Loose dust particles were removed from the mounted sample array with an Ar hand blower connected to the ICPMS Ar supply line.

Typically, analysis laser settings were: 20 Hz pulse repetition rate, 74 µm spot size, 67 µm/s stage speed. Laser pulses last 20 ns, energy density was set to ~4 J/cm^2.

Standard, sample and intermittent background signals were usually acquired together in one continuous data file. Occasionally, standards and sample were recorded in separate files (with their respective bracketing backgrounds), which only requires a different setup of the parameter files for the utilised software, all calculations then follow the same steps described below.

The software automatically recognises data ranges containing background, standard and sample data, or they can be set and changed manually. The following refers to the typical calculations conducted to yield the presented results only, the data can be used

very flexibly for any other numerical analysis once loaded into R. Further information on the software can be found in Rittner & Müller, 2012, attached in Appendix XXX. The actual calculations are described in more detail in chapter "4.12.3 Data reduction" below.

Background was calculated as the average of background data intervals. The two background intervals recorded closest before and after a signal (both sample or standard) were usually averaged to obtain the signals to be subtracted from the signals of interest for background correction (bracketing backgrounds). Due to the great temporal as well as spacial signal stability in the utilised setup, statistical error within each background data interval was larger than the difference between averages of consecutive background measurements, thus no further interpolation of background signals over time was necessary.

From the background signals, the Limits of Determination (LoD) were calculated as average of background signals + 6 * standard deviation (after Gill, 1997), values below LoD are usually not shown in the final output.

Element concentrations are calculated by determining the signal response for each element (in cps/ppm) from the standard signal, and from that converting the signal intensities for the sample relative to the internal standard element (in this study Ca, assumed to be 40.04 % w/w) to concentrations.

To retrieve spatial information on the calculated concentrations, both the logfiles from the laser ablation software (containing track geometries in sample stage coordinates) and the data files from the ICPMS software (containing timestamps) are necessary. The sample stage moves at a constant velocity during ablation. This allows to calculate the distance along the ablation path from the timestamps in the data file. At the beginning and end of the data signal, an empirically determined time interval is cut off, to allow for signal stabilisation in the beginning and to disregard the interval of signal fall-off at the end.

After calculation, element concentration are stored internally in a hierarchical data structure containing metadata (analysis parameters) and the calculated data tables. The data can be stored to files externally if desired, but this is usually not necessary (all

calculations repeated from the original source data). See chapter "4.12.3 Data reduction" below for the function calls used in R and explanations.

4.8 2D LA-ICPMS element mapping

Two-dimensional element mapping of a sample area expands on the single track screening, by measuring an array of single tracks and interpolating a raster map of concentration values in between.

In this study, all data for a mapping, including backgrounds, several intermittent standard measurements and all tracks were usually recorded in one data file. Initial processing is thus the same as for single tracks, which yields concentration data for each individual track.

From the geometrical information about ablation area and tracks contained in the GeoStar analysis file and the logfiles written during analysis, coordinates for each data point in each track are calculated. These data points are then combined and kriging (e.g. Kravchenko & Bullock, 1999; Mueller et al., 2004) is utilised to interpolate a new raster over the whole area of interest.

Before kriging, smoothing of the individual data tracks can optionally be applied, and the results can be downsampled to a lower spatial resolution than initially acquired, to speed up interpolation and yield less noisy maps (see Fig. 57 for an illustration of terms). Downsampling into local averages does not involve a great loss of information, as the distance between individual tracks is usually much larger than data spacing along tracks, thus, in the interpolation the data will always be partially smoothed out, depending on the chosen cell size of the output raster.

To be able to optically distinguish the most features in the resulting element maps, a custom colouring algorithm based on the empirical cumulative density function (ecdf) was applied to give the maps the optimal colour scale.

A discussion and comparison of techniques applied to produce 2D element maps and further explanations can be found in Rittner & Müller, 2012 in Appendix A.

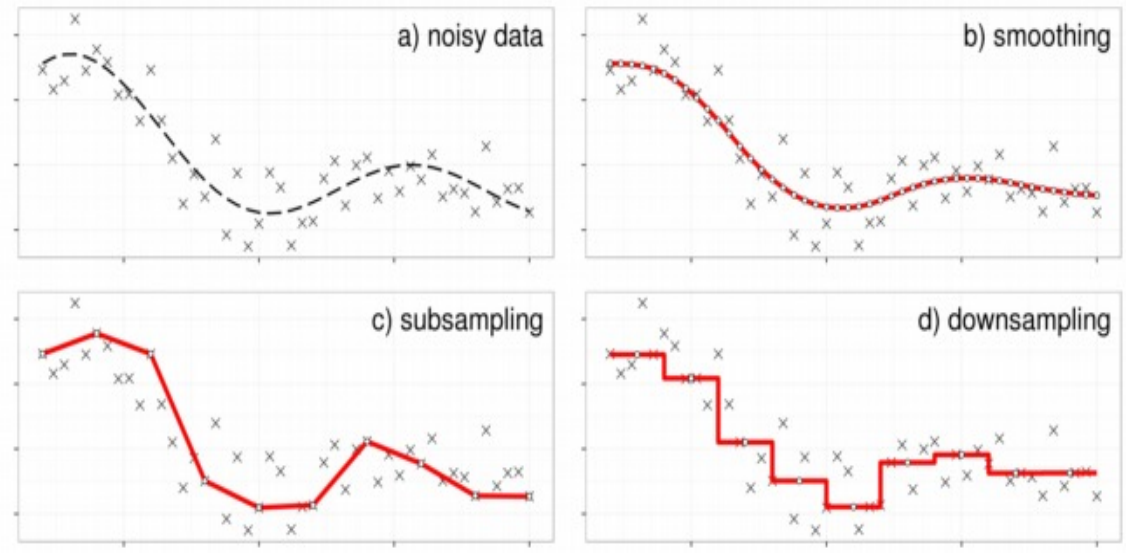

Fig. 57: Smoothing, subsampling and downsampling.
Comparison of: a) Original signal, dashed line, and recorded data containing random noise. b) Smoothing (algorithm “smoothn()”, see Rittner2012) fits a continuous function to best represent the given data, and then samples this function at the original x positions. c) Subsampling selects a subset of the given data, e.g. every n-th data point, at its measured position. This might sample outliers. d) Downsampling calculates the average of values in a given data window (e.g. 5-point running median), and assigns this value to the whole window – or a new data point representing the respective window, which does not necessarily need to lie at an original x position.

4.9 In situ isotope ratio measurements (LA-ICPMS)

The possibility to measure U and Pb isotopes in situ by laser ablation, on the quadrupole ICPMS, was evaluated. Different ablation geometries and settings were tested. High mass interference of ^{204}Hg makes direct measurement of ^{204}Pb impossible in the current setup, and lead isotope ratios can only be estimated based on an assumed ^{206}Pb/^{204}Pb ratio. See chapter “4.12.3 Data reduction“ for details.

To minimise the fractionation effects of more conventional spot analyses, where the stationary laser progressively drills into the sample, and thus also to more closely guarantee the ablated material is the same as analysed in previous screenings, the data was acquired in small tracks or small areas (arrays of tracks, see Fig. 58). Laser settings for these analyses were typically 20 Hz repetition rate, 0.5 mm/min stage speed and 96 µm spot size. A preablation was run on the same geometry before actual analysis.

From the acquired signals, the most homogeneous ranges of data were selected for averaging.

Mass fractionation correction was calculated based on the respective bracketing standards (NIST SRM 612).

For calculation of the ^{238}U/^{206}Pb ratio, U and Pb concentrations had to be quantified. Background correction was calculated as described for 1D and 2D screening, from bracketing backgrounds. Quantification was as described for 1D and 2D screening. For calculation of lead isotopic ratios for each sample, a ^{206}Pb/^{204}Pb ratio of 200 was estimated (assuming reasonably radiogenic samples).

Fig. 58: In situ analysis sites of sample KMR-FOB28C_A.
Scan of sample KMR-FOB28C_A before in situ isotopic analysis, as reprojected to sample stage coordinates by GeoStar, with individual short tracks filling sampled localities overlain. For further analysis, results from homogeneous domains within the small ablated areas were averaged. See chapter 5 Results for an enlarged view and resulting data.

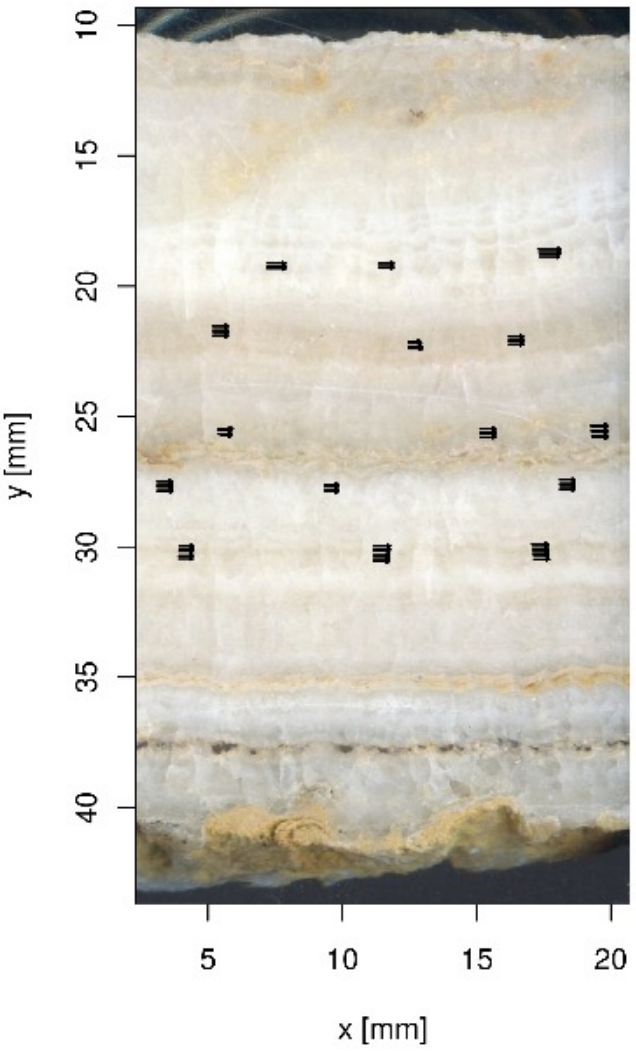

4.10 MC-ICPMS (solution samples)

Careful chemical sample preparation for multi-collector ICPMS analyses, avoiding (Pb) contamination, is described in chapter 4.4 Chemical sample preparation. Samples dried down after column chemistry are redissolved in 2% HNO_3 h.p. with added thallium solution, in a known (natural) $^{205}Tl/^{203}Tl$ ratio, for Pb isotopic analyses. For U/Th analyses, samples were redissolved in a 2% HNO_3 + 0.5% HF mixture (without thallium).

The sample vials are opened at the time of analysis only, the feeder probe from the nebuliser is put into the sample solution manually. Data acquisition is started manually. After analysis, various cleaning steps are performed, until signals have returned to background. Blanks are measured on the same 2% HNO_3 h.p. used for redissolution. All sample handling is performed with powder-free latex gloves.

The data reduction workflow for data from the GVI IsoProbe is well established at RHUL, and was therefore not altered. Data is stored as structured text files with extension ".dat", which are converted into MS Excel files of the same file name. Some initial calculations are performed in the data files (by copy-pasting the respective formulas in), the obtained summary information is then copied into MS Excel masterfiles, which also need sample and spike solution weight as input parameters.

The $^{206}Pb/^{204}Pb$ ratio is corrected for ^{204}Hg interference, calculated from measured ^{201}Hg (or ^{202}Hg) signals.

Based on the measured $^{205}Tl/^{203}Tl$ ratio, mass fractionation correction based on a power law (see chapter Mass fractionation) is applied.

From the measured Pb isotopic ratios of spiked aliquots, concentration, and thus amount, of Pb in the sample can be calculated. The natural isotopic ratios are measured independently, on the unspiked aliquot. Blank correction is applied to the concentrations, and blank-corrected Pb isotopic ratios calculated.

4.11 Other methods

4.11.1 C_{org}

Mobility of U in aqueous conditions is greatly affected by the presence of organic ligands, see chapter "3.1 Methodology II: application". To test whether the content of organically derived carbon (C_{org}) in the host rock of tectonic carbonates correlates with U concentrations, samples of host rock from different sampling areas were analysed for their C_{org} and U/Pb contents.

The samples were powdered, dried, and ashed in a furnace at a temperature below the dissociation temperature(s) of carbonates. The ashing weight loss was measured. See chapter "5.2 Organic Carbon (Corg)" for results.

4.11.2 Optical microscopy

A standard optical microscope with a fitted digital camera was used to take microphotographs of selected sample sections and polished blocks. Samples were examined in reflected light. Because of the small area visible, several pictures had to be taken of each sample, and stitched together. The freeware program Hugin (hugin.sourceforge.net) was used for reprojection and stitching of individual photos. See chapter 5.3 Imaging results and individual sample documentation in Appendix C for examples.

4.11.3 SEM

BSE and elemental concentration maps of selected samples were acquired on a Hitachi S3000 SEM with an associated Link Isis energy-dispersive X-ray detection system for chemical analysis. See chapter 5.3 Imaging results for examples. Elements of interest in this study typically occur in too low concentrations to be detected, whereas the LA-ICPMS 2D mapping technique (chapter 4.8 2D LA-ICPMS element mapping)

can produce trace element maps down to very low concentrations. Therefore, SEM imaging was not further pursued.

4.12 Summary: detailed workflow for U-Pb dating of calcite

4.12.1 Summary

In the following sections, detailed step-by step instructions for the developed workflow for U-Pb isotopic analysis of tectonic carbonates are given, in theory enabling the operator to reproduce the stated data quality. Under best circumstances, the individual stages of the process take about these amounts of time:

- sample preparation – 1 day
- LA-slab preparation and cleaning – 1 day
- laser ablation work – 1-2 days
- LA data reduction – 2 days
- subsampling, sample cleaning – 2-3 days
- aliquoting, column preparation – 1 day
- Pb / Sr resin column chemistry – 1-2 days × 2 (IC and ID fraction)
- TRU resin column chemistry – 1 day
- isotope ratio analysis Pb – 1 day
- isotope ratio analysis U – 1 day
- data processing – 1-2 d

This sums up to 21 days / 4 weeks per sample, assuming all labs and machines are available at the required time and without interruptions. This estimate excludes at least two to four weeks labware cleaning in between sample batches and assumes immediate availability of "high purity" distilled reagents.

4.12.2 Detailed clean lab/column chemistry workflow

Listed below, are the individual steps for different preparations and main parts of the workflow. The main factors influencing contamination are careful cleaning of labware and reagents and cautious handling in every step of the workflow.

Cleaning procedure for calcite samples for LA-ICPMS and subsamples before dissolution

- ultrasonicate in acetone, 15 min
- rinse in H_2O h.p., ultrasonicate in acetone, 15 min
- rinse in H_2O h.p., ultrasonicate in isopropanol or methanol, 15 min
- rinse and ultrasonicate in H_2O h.p., 15 min
- repeat H_2O cleaning at least twice, until water stays clear (and no more particles collect at bottom)

Cleaning procedure for PS pipette tips

To be conducted in 125 ml HDPE bottles:

- wash in acetone, shake, then tap until no more air bubbles cling to pipette tips, let stand ~½ – 1 h
- rinse in H_2O h.p., at least 4 ×
- handling pipette tips with PTFA tweezers, transfer individually via H_2O rinse (fill and empty) into HCl (reagent grade) mixed 1:1 with H_2O, leave several days or longer
- transfer via H_2O h.p. rinse (fill and empty) into HNO_3 (reagent grade), mixed 1:1 with H_2O, leave several hours
- transfer via H_2O h.p. rinse (fill and empty) into ~1M HNO_3 h.p. for storage

Cleaning procedure for new Fluoropolymer labware

- degrease with weak decon 90-solution (1 h – 1 d)
- rinse repeatedly with H_2O h.p.
- wash with acetone (let stand ~1 h)
- rinse with H_2O h.p.
- leach in warm HCl (conc., reagent grade) mixed 1:1 with H_2O h.p., on hotplate in fume cupboard, 1 d – 1+ week
- rinse with H_2O h.p.
- leach in warm HNO_3 (conc., reagent grade) mixed 1:1 with H_2O h.p., on hotplate in fume cupboard, 1 d – 1+ week
- rinse with H_2O h.p.
- repeat HCl- and HNO_3-steps at least twice
- [match numbered vials and lids, label]
- "reflux" with ~200-300 µl HNO_3 h.p., tightly closed, on hotplate for 1+ h
- check for irregularities (wetting) by collecting droplets, use H_2O h.p. or 5% HNO_3 h.p. to aid in droplet collection if needed

The refluxing step can be performed (or repeated) shortly before usage of vial, to minimise untreated storage time of labware.

After use in column chemistry, rinse all (closed!) vials with acetone to remove labelling, open and empty vials, optionally mechanically wipe each vial with a soft plastic disposable pipette to remove "sticky" resin residue (very careful not to scratch the vial, avoid sharp protruding seam from the production process of the pipette), reflux vials with HNO_3 conc. (reagent grade, 1 h – 1 d) on hotplate, discard leachate, rinse, and start long-time leaching at HCl step above.

Cleaning Sr and prefilter resin

Mix resin with H_2O h.p. in PFA beaker: close lid, shake well, potentially ultrasonicate. Decant any floating particles. Repeat at least 2 ×, until very few particles remain floating.

- load full resin bed of Sr and prefilter resin in respective dedicated FEP columns
- wash resins with 1 RV (~10 ml) 0.05M HNO_3 h.p.
- wash resins with 1 RV (~10 ml) 0.1M H_2SO_4 (analytically clean)
- wash resins with 1 RV H_2O h.p.
- repeat washing 10 ×, omitting the H_2O after ~the third time
- backwash resins in storage containers (e.g. 7 ml PFA vials or dropper bottles)

Preparation for column chemistry workflow

All reagents are measured by pipetting the stated amounts.

SR-resin (Pb) workflow:

- weigh empty, clean PFA vials: 3 × 7 ml and 2 × 3 ml per sample and blank
- put samples in 7 ml vials for dissolution, weigh again (dry)
- etch sample surface for ~30 s in 1M HCl, amount roughly adapted to sample size (~1 ml per 250 mg calcite), pipet solution off and rinse the sample with 3 × 1 ml H_2O h.p. (pipetted off each time), use one pipette tip dedicated to each sample
- put on hotplate shortly to dry – weigh again
- cover sample in 1500 µl H_2O h.p. and dissolve by adding HNO_3 h.p., roughly adapted to sample size (in 250 µl or smaller steps, stoichiometrically calculated according to amount calcite, new acid added only after reaction has finished). Put lid on immediately after adding acid, to collect all droplets produced by bubbling and avoid contamination of workspace and other samples by droplets. Screw on, but do

not tighten lid, to allow gas to escape. After adding HNO_3 h.p., be very careful to wash all droplets off the reagent (h.p.) handling pipette tip.

– after complete dissolution, dilute to 2M HNO_3 with H_2O h.p., weigh again, put on hotplate (~½ h, closed tight) and/or shake

– for ID fraction: add spike to one empty 7 ml vial per sample, weigh to obtain exact spike weight (plus weighing of spike bottle if using dropper bottle – use designated pipette tip if pipetting spike)

– pipette 20% of sample solution into vials with spike, use separate pipette tips for each sample

– unspiked rest (80%) of solution will be IC fraction.

– for blanks: add spike to empty vial after simulated sample dissolution, weigh, add H_2O, same amount of HNO_3 as for samples, dilute to 2M HNO_3 and put on hotplate and/or shake. Pipette off 20% aliquot into empty 7ml vial.

– weigh IC and ID fractions to obtain exact final aliquot amounts

– put on hotplate (closed tight) for ~1 h at 90°, shake again after cooling

Sr resin column chemistry workflow

Workflow forms have been devised aiding in keeping the correct sequence of working steps and correlation of source and collection vials, with boxes to tick off every step for every sample. The forms are added in the appendices and provided as PDF files on the enclosed CD-ROM. The basic steps are listed below, where each change from one reagent to another is performed by adding 0.1 ml at first and then gradually larger amounts of the new reagent, waiting for the reagents to have passed the column before adding the next increment. The workflow is typically performed on six to twelve columns simultaneously. Separation of ID and IC fractions requires two workflows per 1 sample. Blanks are treated in exactly the same way and at the same time with samples; different columns, having been used for samples previously, should be used for blanks in consecutive analyses.

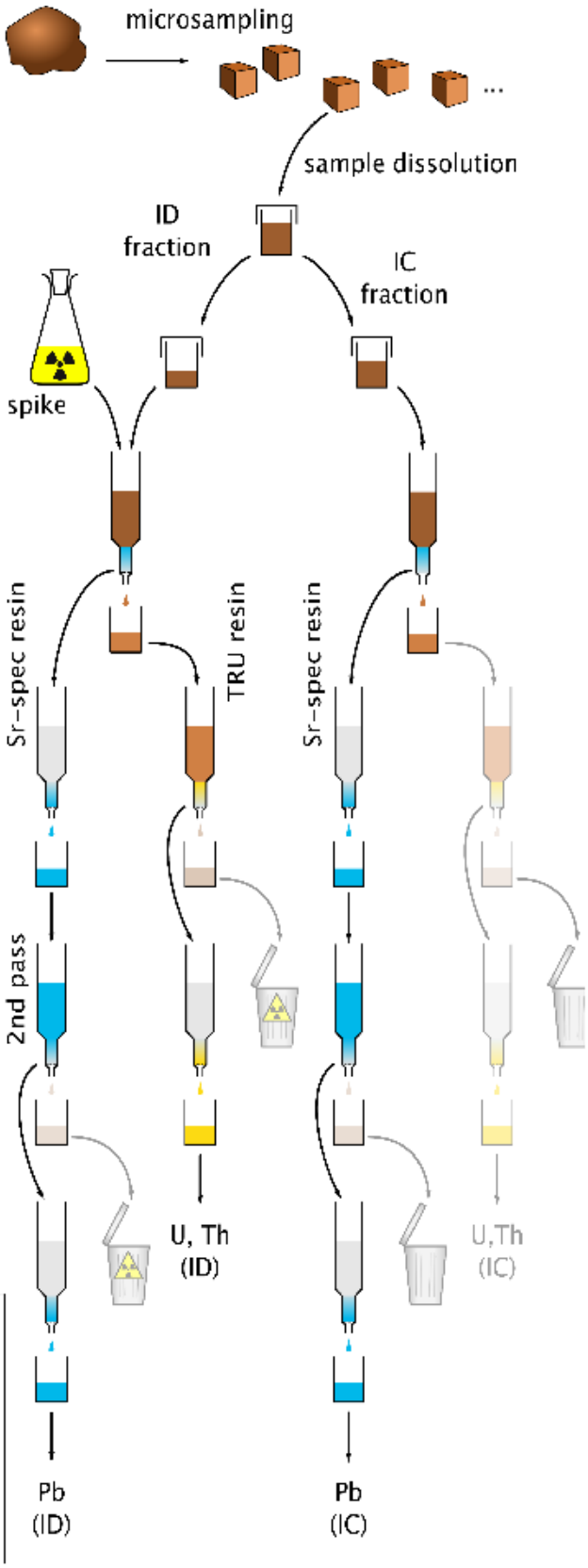

Fig. 59: Schematic column chemistry workflow. Each subsample is divided in two aliquots, one of which is mixed with "spike" (ID fraction), the other one is used to measure natural isotopic composition (IC fraction). The amount of U is determined on the ID fraction, no U-IC fraction is analysed.

The workflow, schematically pictured in Fig. 59, follows these steps see also prepared workflow monitoring forms for tick-off, in Appendix C):

- clean empty columns with 1 RV HCl TD
- load prefilter and Sr resin, 100 µl each
- clean resin with 1 RV HCl TD, repeat
- clean resin with 1 RV HCl h.p.
- condition resin with 0.5 ml 2M HNO_3 h.p.
- put 7 ml PFA vial under column to collect for TRU resin workflow
- load sample
- rinse resin with 0.8 ml 2M HNO_3 h.p.
- close collecting vial, put away for later use in TRU workflow
- elude Sr off resin with 1 ml H_2O h.p.
- place 3 ml vial (refluxed with ~0.3 ml HNO_3 h.p.) under column for collection
- elude Pb off resin with 1.2 ml HCl h.p.
- dry down Pb fraction on hotplate in clean air hood
- add 200 µl HNO_3 h.p., dry down
- redissolve in 0.5 ml 2M HNO_3 (briefly on hotplate)
- with same columns and resin beds used before: clean resin with 1 RV HCl h.p.
- condition resin with 0.5 ml 2M HNO_3 h.p.
- load sample
- add 250 µl HNO_3 h.p. to sample vial, close tight, put on hotplate for refluxing
- rinse resin with 1 ml 2M HNO_3 h.p.

- perform Sr elution step with 1 ml H_2O h.p. (sample should contain no Sr any more at this stage; if Sr analysis is required, collect Sr together with Pb in first column pass, and separate Sr here, additional vial required for collection)
- place refluxed vial under column for Pb collection
- elude Pb with 1.2 ml HCl h.p.
- dry down on hotplate
- add 200 µl HNO_3 h.p., dry down again
- store dried and closed tightly until redissolution for analysis

TRU resin column chemistry workflow

The TRU resin workflow to separate U and Th from the solution collected in the Pb workflow is generally less critical in terms of contamination, as no significant U pollution is expected in a typical environment. Nonetheless, the work was performed in the same clean air hoods, and great care has to be taken to avoid particulate and cross-contamination of samples. Usually, no separate IC fraction was processed for U, as the isotopic composition of U was assumed to be the natural average. The individual steps (see also workflow sheets in the appendix) are as follows:

- clean empty column with 0.1M HCl – 0.3M HF mix
- load prefilter and TRU resins, 100µl each
- clean resin with ~6 ml 0.2M HCl h.p.
- clean resin with ~6 ml 0.1M HCl – 0.3M HF mix
- condition resin with 0.5 ml 2M HNO_3 h.p.
- load sample
- add ~0.3 ml HNO_3 h.p., to emptied sample vial, close tightly, put on hotplate for refluxing
- rinse resin and wash out major elements with 1.8 ml 2M HNO_3 h.p.

- elude rare earth elements with 1.4 ml 3M HCl h.p.
- put (refluxed, empty) vial under column for collection
- elude Th with 1.8 ml 0.2M HCl h.p.
- elude U with 1.8 ml 0.1M HCl – 0.3M HF mix
- dry down collected samples on hotplate
- add 200 µl HNO_3 h.p., dry down again
- store dried and closed tightly until redissolution for analysis

4.12.3 Data reduction

Single track LA-ICPMS data

Agilent *ChemStation* on the ICPMS computer outputs signal intensities for the selected elements (m/z ratios) as data files containing one time-stamped entry per element of counts per second (cps) in the respective sweep interval. On request, these data are stored as comma separated value (.csv) files. Resonetics *GeoStar* saves ablation parameters and some information about ablation track geometry in the main analysis files (XML files), but more detailed geometric information is contained in the two logfiles written during analysis (one being a time-stamped protocol of status messages with the ending .log, the other a time-resolved table of every machine status change in a .csv file).

The R add-on package *LAICPMS* (Rittner & Müller, 2012), developed for data processing in this study, reads all these files and combines them to calculate spatially resolved element concentration information. The same principles apply for one-dimensional single ablation tracks and for two-dimensional element maps, calculated from an array of tracks (see next section below).

In the following, it is assumed that standard and sample signals, including background signals before, after and in between the former, are recorded in one data file. If standards and sample are recorded in separate files (with respective bracketing backgrounds), the setup of the parameter file for calculation changes to point to the respective files, all other calculation steps are then performed in the same manner. The R commands below are illustrating the most common workflow applied for the data presented in chapter "5 Results", a more exhaustive documentation of all functions and parameters can be found in the helpfiles for *LAICPMS*.

- The add-on package is loaded into the R environment with the command:

```
library("LAICPMS")
```

- The raw data file is read with the R command

```
raw_data <- readDataFile(filename="path_to_datafile")
```

where "path_to_datafile" specifies the (relative or absolute) path to the data file, including filename. Data files from Agilent *ChemStation* and from the GVI IsoProbe software are automatically recognised; data can also be read from a SQLite relational database (adding the parameter `tabname="table_name"` to specify the data table to load). If the type of data file is not recognised, an attempt to read it is still made (if a text or Microsoft Excel file), and if a block of tabulated numerical values is found, these are read ignoring any leading and tailing lines not part of the data.

The data table is now loaded into the variable `raw_data` in the current R environment.

– The function

```
parameters <- suggestRanges(data=raw_data)
```

detects the data ranges (backgrounds, standards and samples) in the data and sets up default calculation parameters in the variable `parameters`.

Range start and end are recognised by a rise or fall, respectively, in more than 90 % of the measured signals, that is greater than 3 times the 45-point running average of the 1st derivative of the respective signal. An empirically determined time window around start and end of each data range is cut out to retain only stabilised signals. Assuming standards and backgrounds to be the most stable signals, data ranges which show standard deviations lesser than 2 times the minimal standard deviation observed amongst all data ranges (for the respective mass) and containing signals greater than 10000 cps for over 90 % of observed masses, are considered to be standards. Ranges containing stable low signals are considered to be backgrounds, the remainder samples. The type of each data range, as well as start and end, can be changed and fine-tuned by the user, as well as ranges added or deleted.

– `parameters <- fillMissingValues(parameters)`

finds the bracketing backgrounds for each data range (or the ones recorded closest before and after) , and the bracketing standards for each sample, and stores them in the `parameters` variable.

– `parameters <- setLasingSpeed(parameters, 4, "mm/min")`

sets the lasing speed to the desired value.

– The `parameters` variable now contains all information necessary for single track data processing. The function call

```
ppms <-  getPPM(parameters)
```

will calculate element concentrations from the raw data and store the results in the variable `ppms`. By default, this function will not cut out values below LoD (this can be done by providing the additional parameter `cut=TRUE`), and assumes the standard material to be NIST SRM 612 and the internal standard to be Ca in a concentration of 40.04 wt% (calcite). Without listing all internal functions called in the process, the calculation steps are:

First, net i*sotope signals are calculated by subtracting the mean of the bracketing backgrounds from each data range.*

Dividing the measured signals by the isotopic abundance of the measured isotopes yields net e*lement signals.*

Sensitivities (cps/ppm) are calculated by dividing the mean signals of standards by the GeoReM "preferred values" for the standard material.

Sensitivity of each element divided by the sensitivity for the internal standard gives *relative fractionation ratios*.

In the final calculation step, *element concentrations (ppm)* are obtained by dividing net element signals by the signals of the internal standard, multiplying by the concentration of the internal standard times 1000000, and dividing by the relative fractionation ratios.

By means of the "lasing speed", the movement speed of the sample stage during ablation, the time stamps of individual data points are converted into distance from the start along track in mm.

If desired (parameter `cut=TRUE`), concentrations below the LoD are deleted from the final result.

– The final result is a list of tables of element concentrations along the ablation tracks, stored in the variable `ppms`. These can be stored as plain text (e.g. ".csv") or Microsoft Excel files for further analysis or plotted graphically. For example, to obtain a single track plot as shown in chapter "5 Results", the names of the individual ablation tracks stored in `ppms` are retrieved with `names(ppms)`, and assuming the track of interest is called "track1",

```
plotElements(data=ppms[["track1"]], filename="track1.png")
```

will save the track plot in a ".png" file called "track1.png".

Resonetics *GeoStar* allows to save the scanned image of the sample remapped to sample stage coordinates (in µm), and saves track geometry in the analysis file. This allows to produce an exact plot of the ablation track on the sample image, which greatly facilitates correlation of the calculated concentrations along track length with actual sample features (see e.g. Fig. 58 for an example).

2D LA-ICPMS mapping

To create a two-dimensional element concentration map of a sample, an array of tracks is analysed, and from this data the 2D map is interpolated. The initial steps, assuming the whole mapping, including intermittent standard measurements, is recorded in one data file, are the same as for single tracks to obtain the variables `parameters` and `ppm` containing all single tracks (see above).

– A call to

```
parameters2 <- getMetaDataFromGeoStar(parameters,
GSfile="file_path")
```

will read area and individual track geometry from the *GeoStar* analysis file at "file_path" and store it in the variable `parameters2` together with the original calculation parameters. The logfiles created by GeoStar during the ablation process must be present in the same folder (default behaviour of GeoStar), since not all geometrical information about the individual ablation tracks is stored in the main file (in the current version 5.8 of the software).

– `ppms2 <- getPPMXY(parameters2, ppm=ppms, correlation=corr)`

calculates a similar data object to `ppms` described before (see above), containing one data table per ablation track, but additionally to element concentrations and distance from start, x and y coordinates (in sample stage coordinates) are provided. The variable corr is an additional table necessary to describe which track, referenced by their track name in `ppms`, corresponds to which "sequence" and "subpoint" from the *GeoStar* logfile.

– `ppms2 <- smoothAndSubsample(ppms2, alg="runmed", sspace=40, spars=c(7))`

applies some smoothing to the data tracks, and then downsamples them to points in the spacing specified by `sspace` (in µm). The default smoothing algorithm is a running median followed by running mean (chosen with parameter `alg="runmed"`), with a running window width specified in `spars`. This step is not strictly necessary, but speeds up consecutive calculations.

– `newdata <- reshapeForMapping(ppms2)`

restructures the data of all tracks in one combined table (variable `newdata`) necessary by the following functions.

– The function `interpolateRaster()` creates an R image object for one element from `newdata`, with settable resolution, cropping data outside the ablated area, and optionally discarding values below LoD.

The 2D raster is interpolated utilising kriging functions from the R package *spatial* (Venables & Ripley, 2002). Kriging is an distance-weighted spatial interpolation method established in many Earth- and other sciences (e.g. Kravchenko & Bullock, 1999; Mueller et al., 2004).

– A custom colouring algorithm based on the empirical cumulative density function (ecdf) is applied to give the element maps optimum colour scale.

For a discussion of smoothing and colouring algorithms, please see Rittner & Müller, 2012 in Appendix A.

In situ isotope data

Data acquisition and resulting files are identical to 1D and 2D screening, see above. Further calculations for these analyses were performed in a spreadsheet calculation program (OpenOffice Calc, later LibreOffice Calc).

- Masses (m/z) 43, 201, 202, 204, 206, 207, 208, 232 and 238 were acquired. From the track or area, a homogeneous data range for each targeted spot on the sample is selected.

- Individual mass ratios 208/206, 207/206 and 238/206 are calculated. A very simple despiking, filtering out outliers greater than +/- 3 sd from the mean values, is applied, and the remaining values averaged.

- From each acquired standard, lead mass fractionation correction values per amu are calculated for ^{208}Pb and ^{207}Pb as:

$f_{cor} = ((R_{std} / R_m) - 1) / \Delta m$

where R_{std} is the ratio of the respective isotope to ^{206}Pb in the standard, R_m is the average measured ratio, and Δm is the mass difference between the respective isotope and ^{206}Pb. The two calculated correction factors are averaged.

- Lead isotopic ratios for each measured sample spot are then corrected as:

$R_{cor} = R_m * (1 + f_{cor} * \Delta m)$

- ^{204}Pb has too large interferences from ^{204}Hg to be directly measured on the quadrupole ICPMS. Therefore, to obtain an estimate of lead isotopic abundances in the samples, they were calculated from the measured ^{207}Pb/^{206}Pb and ^{208}Pb/^{206}Pb ratios and an assumed ^{206}Pb/^{204}Pb ratio of 200.

- Elemental concentrations of Pb and U (in ppm) are calculated from the acquired signals.

- The ^{238}U/^{206}Pb ratio is calculated as:

$c_U / c_{Pb} * ab_{238U} / ab_{206Pb} * w_{Pb} / w_U$,

where c_U and c_{Pb} are the concentrations (in ppm), ab_{238U} and ab_{206Pb} are the natural abundance of ^{238}U and the estimated ^{206}Pb abundance for the sample, and w_{Pb} and w_U are the estimated atomic weight of lead in the sample and the natural atomic weight of uranium, respectively.

- These $^{238}U/^{206}Pb$ are outlier-corrected and averaged, like the lead ratios above.
- Errors for all calculation steps are propagated.

MC-ICPMS data

Analysis data from the GVI IsoProbe are contained in tabulated plain text files with data columns separated by spaces, preceded and followed by additional analysis data and statistical summaries, saved with the file ending ".dat". In the workflow commonly applied at RHUL, these files undergo some preprocessing and conversion into Microsoft Excel files, before results from the individual data files are copied into one master file (MS Excel) set up to yield the final results of isotopic ratios and Pb or U and Th concentrations (separate master files for Pb and U/Th processing).

For each sample measurement, one measurement of blank solution is made and used for blank correction of the respective sample. For Pb isotopic analyses, the masses (m/z) 193.5, 194.5, 198, 201, 202, 203, 204, 205, 206, 207, 208, and the signal ratios of 208/206 and 204/206 were measured. For U/Th isotopic analyses, the masses (m/z) 229, 232, 233, 234, 235, 236, 238 and the signal ratios of 235/238 and 234/235 were measured.

The calculation steps for Pb data are:

- Machine baseline signals for the set masses and ratios are measured repeatedly, means and 2 standard errors are calculated.

- From the individual data in the blank file, means and 2 standard errors are calculated.

- The signals of the individual masses measured are blank corrected with the values from the blank file.

- From these, measured isotope ratios 205/203, 201/206, 204/206, 205/206, 207/206, 208/206, 198/201 and 201/202 are calculated, as well as ^{201}Hg corrected ^{204}Pb/^{206}Pb, ^{202}Hg-corrected ^{204}Pb/^{206}Pb as a control of the latter, and XXX 4/6N, 7/6N 5/3N ??. These values and their 2se errors are copied to the master spreadsheet as input parameters for the further calculations.

- measured lead isotopic ratios are corrected for mass bias by a power law (see chapter Mass fractionation), based on the measured ^{205}Tl/^{203}Tl ratio and machine-

and run-specific correction factors for $^{206}Pb/^{204}Pb$ and $^{207}Pb/^{206}Pb$ ("a" below). The following are the calculations for the $^{206}Pb/^{204}Pb$ ratio, the other ratios are calculated similarly:

a = 0.059033 / 0.059024 = 1.000152

$b = \ln(ram_{206} / ram_{204}) / \ln(ram_{205} / ram_{203})$

$c = (R_{Tl,n} / R_{Tl,m})$ ^ b

$R_{6/4N} = 1 / R_{4/6Hg\ corr} * a * c$

where ram is the relative atomic mass of the respective isotope, $R_{Tl,n}$ is the assumed real $^{205}Tl/^{203}Tl$ ratio of 2.3889, $R_{Tl,m}$ is the measured Tl isotope ratio, and $R_{4/6Hg\ corr}$ is the ^{201}Hg corrected $^{204}Pb/^{206}Pb$ ratio.

– After input of sample weight and spike weight into the master file, and combining the measurements of natural isotopic ratios (from the unspiked sample aliquots) and isotopic ratios in the spiked aliquots, the exact concentrations of measured Pb, and thus the exact amount of Pb, are calculated (see also Isotope dilution for details).

$d = ram_{204} / R_{6/4nat} + ram_{206} + ram_{207} * R_{7/4nat} / R_{6/4nat} + ram_{208} * R_{8/4nat} / R_{6/4nat}$

$ppm_{Pb} = d * spkwt * spkcon / smplwt * (R_{6/4N} / R_{8/4N} - 0.000895) / (1 - R_{6/4N} * R_{8/4nat} / R_{8/4N} * R_{6/4nat})$

$pg_{Pb} = ppm_{Pb} * smplwt * 1000000$

– Based on an assumed procedure blank (5.3 pg Pb in this study), blank-corrected concentration, $^{206}Pb/^{204}Pb$ and $^{206}Pb/^{204}Pb$ ratio are calculated.

– 2 se errors are propagated throughout the workflow.

5. Results

In this chapter, an overview of results for each methodology applied is given. Where a technique gave very similar results for all samples of an area, or no illustrative results, only few representative examples are shown. A full listing of resulting data can be found in the Appendices.

5.1 Sample overview

Overall, ~150 samples were collected from 56 outcrops in 8 sampling areas, another 24 samples were provided from collaborators from five different areas (see Tab. 9).

After choosing at least one representative sample from each outcrop, a total of ~80 single track LA-ICPMS screenings were conducted, yielding information helping in the selection of samples for the further methods to apply on.

2D LA-ICPMS element maps were acquired of only five samples because the 2D element mapping method (4.8 2D LA-ICPMS element mapping) was developed later in the course of this study. Samples that promised to be interesting examples for the mapping technique were chosen by optical examination. The presented maps are a feasibility study and test of the acquisition and data processing approach, the technique was not considered a routine screening method necessarily applied to all samples in this study.

Similarly, the attempt to date 13 samples in situ by quadrupole-LA-ICPMS was, in the scope of this study, a proof of concept and test of achievable measurement precision. The samples were chosen taking the data acquired in 1D and 2D LA-ICPMS screening as a guideline, especially U/Pb ratio, U and Pb concentrations and indications for contamination. The observed large measurement errors were anticipated beforehand.

For high precision measurements, 13 samples were chosen based on above mentioned screening information and processed following the workflow for ID MC-ICPMSdescribed in chapter 4 Methodology II: application.

The photographs on the following pages are examples of sample types encountered in this study. Slickenfibres and tension gashes are the prevalent features sampled.

sampled area	abbreviation	# outcrops	# samples	host rock lithologies
Digne	DGN	14	22	sandstone, limestone, marly limestone, polymict conglomerate
Fohnsdorf	FOB	3	9	various metamorphics, polymict conglomerate
Gosau	GOB	13	22	sandstone, limestone, marly limestone, sandy marl
Kilve	KIL	4	7	limestone, black shale, sandy marl, sandstone
Leytron	LEY	4	9	limestone, low-grade metamorphic sediments
Lower Inn Valley	LIV	7	8	limestone, marly limestone, marl
Seefeld	SEF	2	5	black shale, dolomite, limestone
Tauern Window North	TNF	8	15	mica shists, metamorphic sediments, limestone
contributed samples				
Lower Inn Valley		2	2	sandstone, limestone breccia
Swiss Jura		3	6	limestone
Simplon fault		2	2	mica-shist
Other		14	14	low-grade metamorphic limestone

Tab. 9: Sample overview
Number of samples is the individual sample numbers, often several pieces of a sample were collected or the sample was later split during preparation. Thus, ~150 samples were processed in total.

Fig. 60: Typical outcrop of a slickenside with calcite slickenfibres
Pen indicates movement direction of the missing block. Outcrop 267, sample KMR-LIV32 in situ before recovery. View towards W.

Fig. 61: Typical tension gash, hand specimen
Sample KMR-GOB22. Host rock is a biogenic limestone. Tension gash ~22 mm wide.

Fig. 62: Streched and fractured belemnite
Outcrop KMR-LEY16. The low-grade metamorphic sediment matrix has been homogeneously stretched, while the fossil acted as a porphyroclast and was fractured in the process. The voids opening between the black fossil fragments were filled by an intergrowth of calcite and quartz fibres (white).

Fig. 63: Cracked component of a conglomerate
From outcrop KMR-DGN10, sandstone component from the Valensole conglomerate, ca 18 cm long. Slickenfibres grown between and on components were sampled.

5.2 Organic Carbon (C_{org})

As seen in chapter 3.1 Geochemistry of Uranium and Lead in calcite, organic ligants play an important role in mobilising uranium in aqueous solutions. At the beginning of this project, the organic matter content in the host rock of a tectonic carbonate (C_{org}) was assumed to be an important factor influencing, and thus a proxy for, the uranium concentration in the sampled calcites (as indicated e.g. in Shpirt et al., 2007; Israelson et al., 1996).

To test this assumption, C_{org} in the host rock of 16 samples from various sampling areas and host rock lithologies was determined by ashing the powdered rock in a furnace at 400-450º C, below the dissociation temperature of calcium carbonate (significant ~800-900º C, Stern, 2000). Weight loss ranges from 0.1 to 1.4 % w/w (see Tab. 10). Comparison of the U (and Pb) concentration of the respective calcite samples to the weight loss due to ashing in their host rocks shows no clear correlation (Fig. 65). This corresponds to the observation that samples from areas of lithologies with high C_{org} content (e.g. Kilve, Seefeld) did not have high concentrations of U, and that the best suited samples do not all come from high-C_{org} host rocks. Overall, no clear correlation between any one host rock lithology and a sample's suitability for U/Pb dating could be observed, and samples from the same lithology in the same area can show great variability in U and Pb concentrations; see e.g. the 2D element maps of sample KMR-GOB21B in chapter 5.4.4 Gosau basin, showing two distinct domains with U concentrations of ~30 and ~400 ppb, respectively.

sample	avg U	avg Pb	% loss (Corg)
DGN03	0.01	0.73	0.14
DGN11	0.07	0.07	0.34
LEY15	0.17	0.10	0.19
LEY16D	0.19	0.75	0.24
GOB18A	0.61	0.01	0.41
GOB18B	0.90	0.17	1.20
GOB23B	0.10	0.05	0.13
GOB26	0.32	0.27	0.65
LIV31	0.80	0.03	0.29
LIV32	0.11	0.05	0.36
LIV33	0.07	0.03	0.68
LIV34	0.05	0.08	1.44
LIV36	0.02	0.03	1.37
SEF39A	0.64	0.03	1.27
SEF39D	<LOD	<LOD	1.01
UAS3	<LOD	<LOD	1.04

Tab. 10: Comparison of U and Pb concentration and ashing weight loss.
U and Pb concentrations (in ppm) measured on samples by laser ablation and weight loss due to ashing (C_{org}) of corresponding host rocks. See Fig. 64 and Fig. 65.

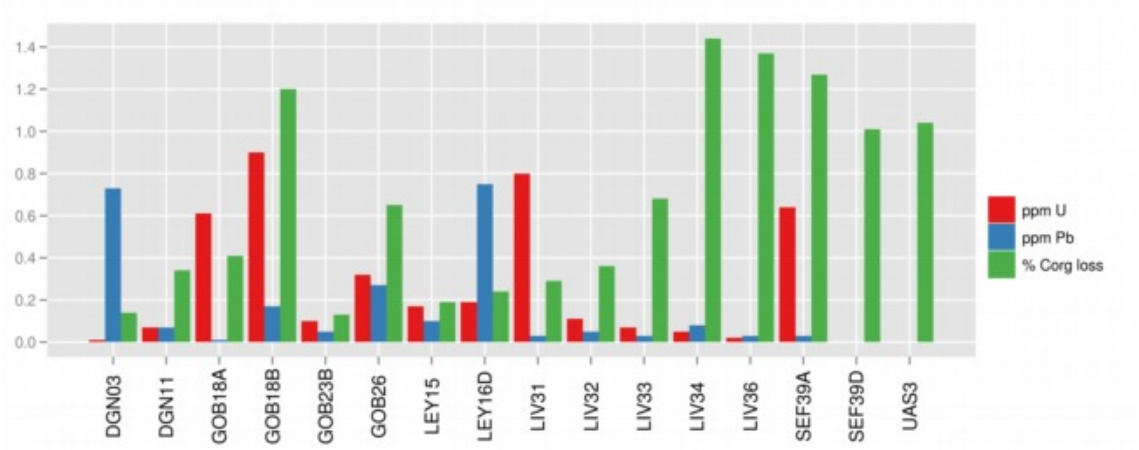

Fig. 64: Comparison of U and Pb concentration and ashing weight loss.
Selected samples were analysed for U and Pb concentrations and ashing weight loss of corresponding host rock. See Tab. 10 for data. Note differing units of scale (ppm and %, but similar numerical magnitude).

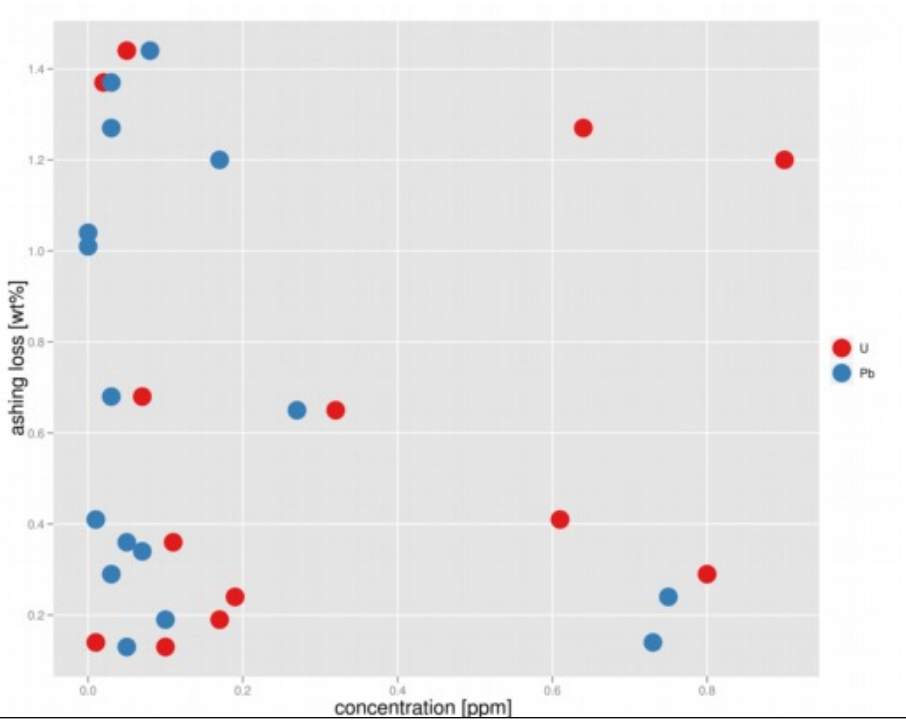

Fig. 65: Concentrations vs. C_{org}.
Host rock weight loss due to ashing plotted against U and Pb concentrations of corresponding tectonic carbonate samples. No correlation is observed.

5.3 Imaging results

Optical microscopy

Thin sections of selected samples were imaged in transmitted light using a petrographic microscope equipped with a digital camera. Some LA samples were imaged in the same instrument under reflected light settings (see figures below in this section). Due to the limitations in minimal magnification, several partial pictures of one sample had to be stitched together later to obtain an overview of a whole LA track and its surrounding. Since pure calcite of the analysed samples appears largely featureless in optical microscopy, and samples are routinely scanned on a flatbed scanner in high resolution before laser ablation, additionally yielding images aligned and coordinated to sample stage coordinates after analysis, optical microscopy was omitted in later analyses. Only some examples of microphotographs and scans of LA samples are given here. Further sample images can be found accompanying analysis results in the next section (chapter 5.4 Sample screening & dating) and in the Appendices.

Fig. 66: Sample KMR-FOB28A_A.
Composite microphotograph (reflected light) of analysed tracks (one horizontal, two vertical – dashed lines) and surrounding area of sample KMR-FOB28A_A from the Fohnsdorf Basin, Austria. The growth strata of the "Mariabucher Marmor" are clearly visible, from hand specimen, growth was determined from right to left. Image width ~55 mm.

Fig. 67: Sample KMR-GOB19A_A.
Composite microphotograph (reflected light) of sample KMR-GOB19A_A from the Gosau Basin, Austria. Multiphase cementation of a tectonic fissure in the reddish-brown host rock is discernible, both cut by younger fractures filled with white calcite. Image width ~60 mm.

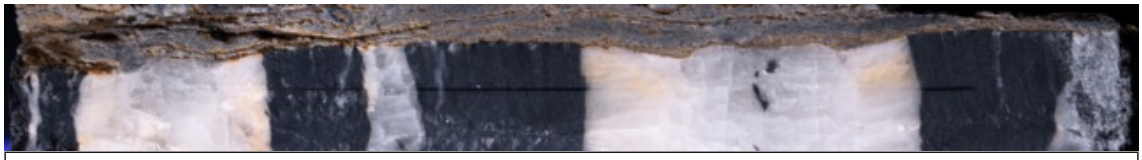

Fig. 68: Sample KMR-LEY16A_A.
Composite microphotograph (reflected light) of sample KMR-LEY16A_A from Leytron, Switzerland. In a homogeneously stretched fine-grained matrix (grey, top), the fossil of a belemnite (black portions) acted as relatively competent clast, fractured, and the voids opening between fragments as the host rock was further deformed were filled by fibrous calcite and quartz crystals (white). Image width ~50 mm.

SEM

Scanning electron microscopy (SEM) was used to image major element distribution by backscattered electron microscopy(Fig. 71), and to evaluate the quality of LA ablation track morphology (Fig. 69 and Fig. 70). Analyses were conducted on a Hitachi S3000 SEM fitted with a Link Isis energy-dispersive X-ray detection system.

Where the boundary of host rock to calcite fibre is present in a sample, the differences in the two phases are clearly visible in Ca, Al, and Si maps (Fig. 71 and Fig. 72). In limestones with biogenic components, high-Mg and low-Mg calcite in the host rock are distinguishable in the Ca and Mg maps (Fig. 71). The detection limits on the instrument used do not allow for mapping of minor and trace elements of interest in this study. The method proved to be of little value for characterising tectonic carbonates of "clean" calcite, while preparation and analysis are more time-consuming than for LA-ICPMS; thus, the method was not further utilised as a standard screening technique in this study.

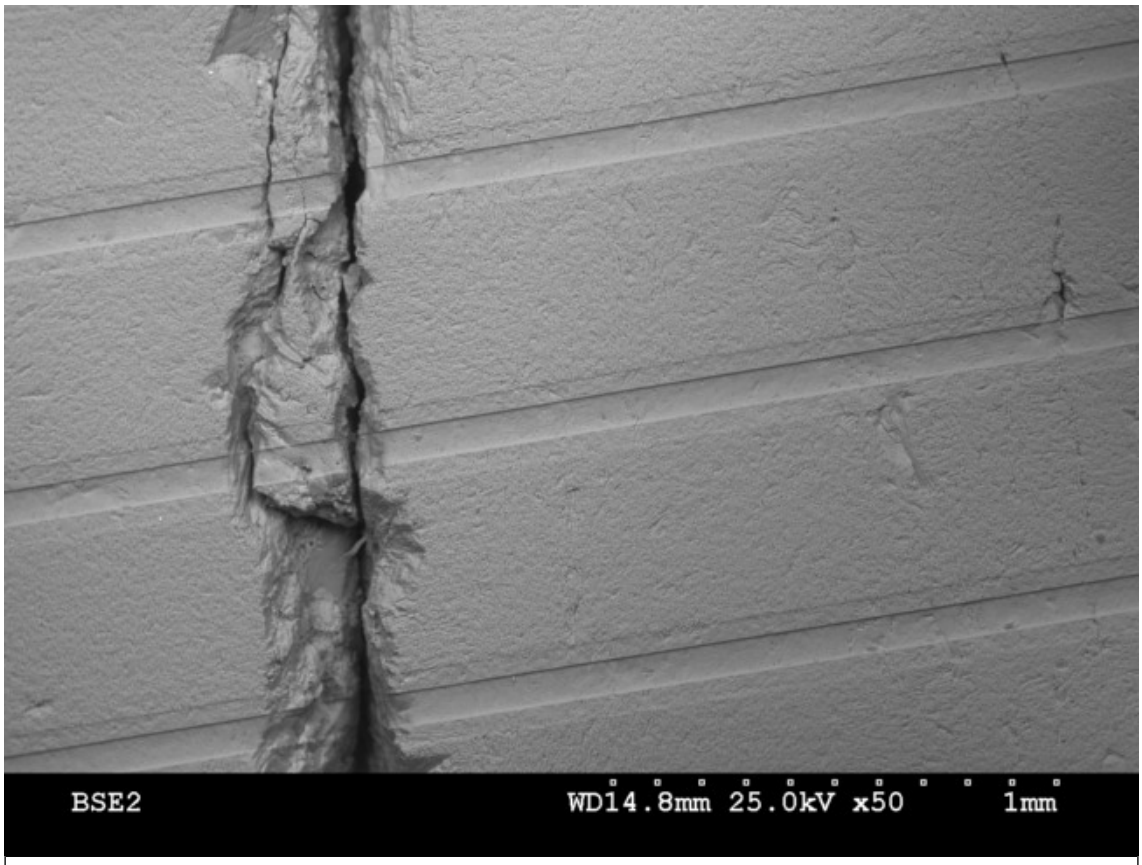

Fig. 69: Ablation tracks, SEM image.
SEM image of part of the sample surface of KMR-GOB21B_A. Three tracks of the array analysed for 2D mapping (see 5.4.4 Gosau basin) are visible with wider preablation trace and thinner, deeper, analysed ablation trace. Track spacing is ~600 µm.

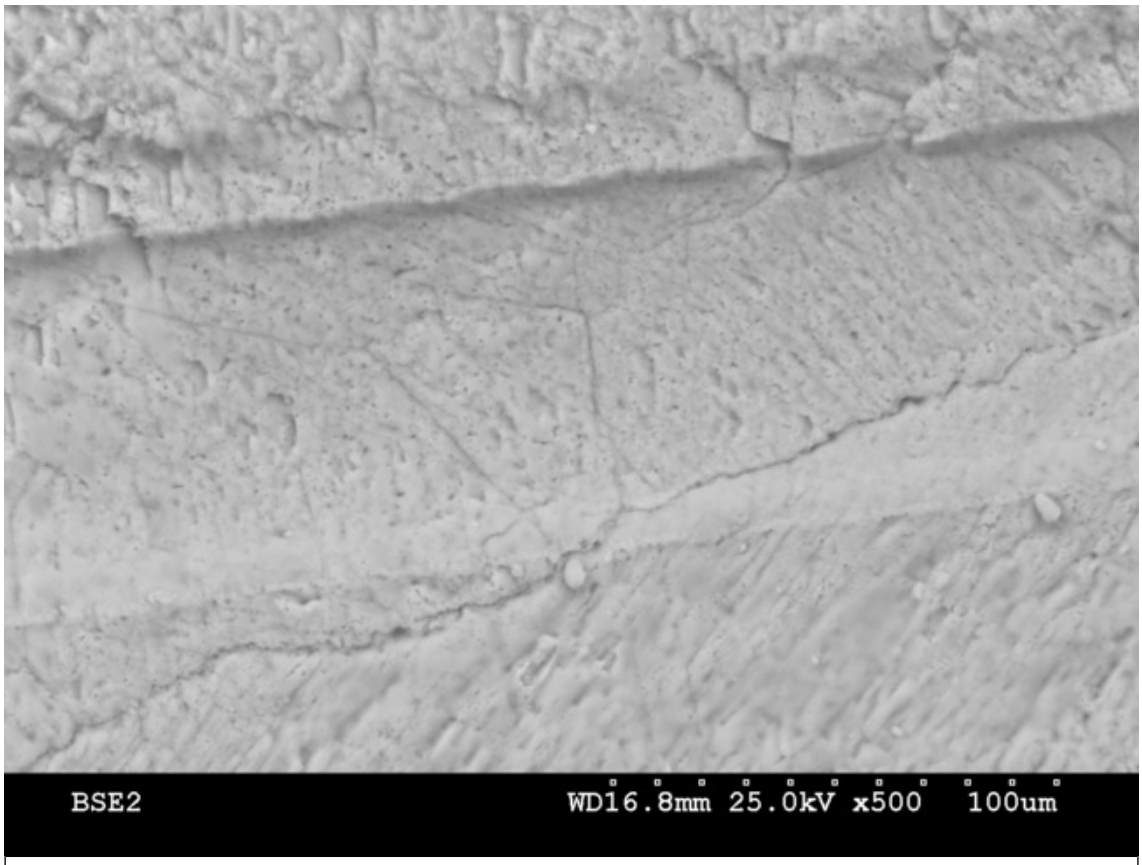

Fig. 70: SEM image of ablation track, detail.
SEM image of an ablation track on sample KMR-GOB18B_A (detail; see 5.4.4 Gosau basin). The wider preablation track and the narrower, deeper ablation track are visible. Note smooth surface and sharp margins of the ablated track. Main ablation track width is 74 µm, image width ~260 µm.

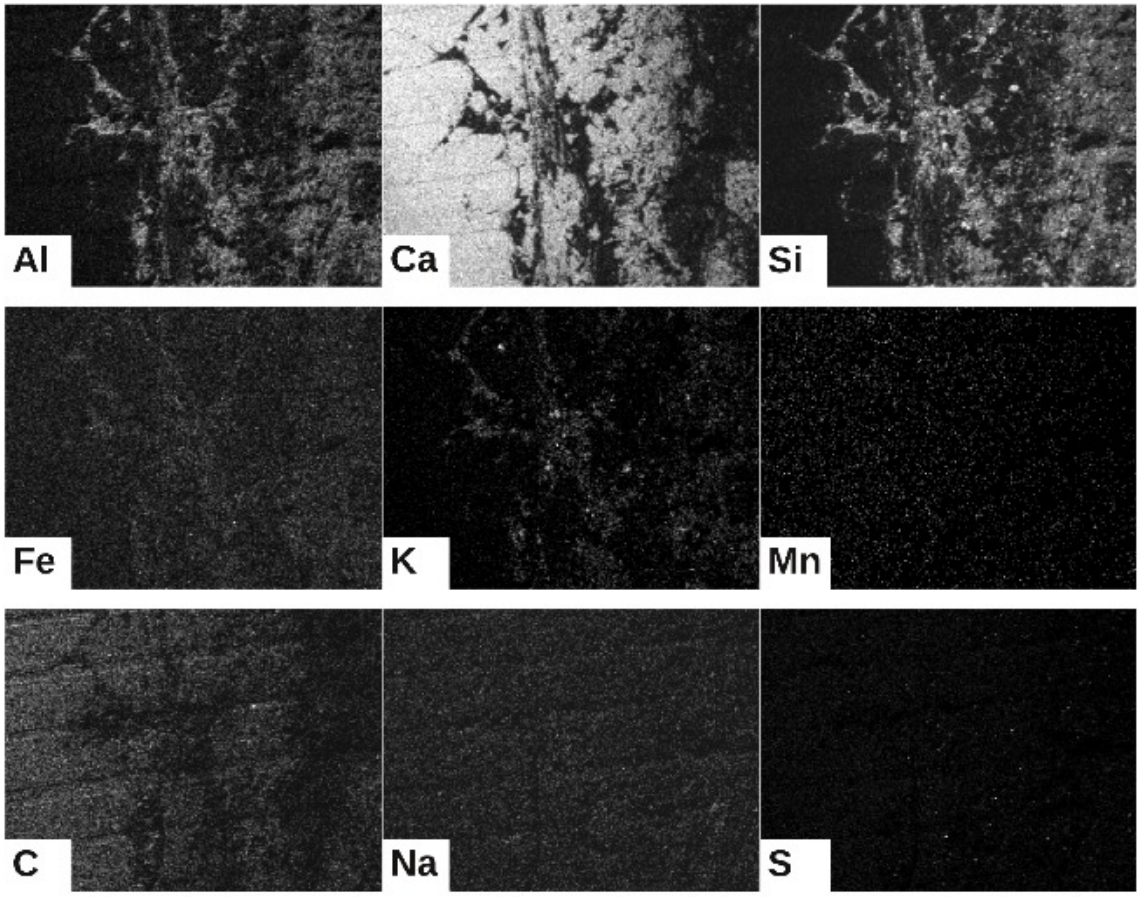

Fig. 71: BSE element maps.
Major element maps of a portion of sample KMR-GOB18B_A. Siliciclastic, marly host rock at the right, and calcite to the left, and a heterogeneous zone of calcite crystals and aggregates in a marly matrix in between, are distinguishable in the Al, Ca and Si maps. Except for the K map, the other maps are nearly featureless. Whether the calcite grew in the marl, the marl was pressed in between calcite grains, or whether this is a zone of mechanical mixing, is not obvious. This zone would be avoided in dating attempts. Image width 2.4 mm.

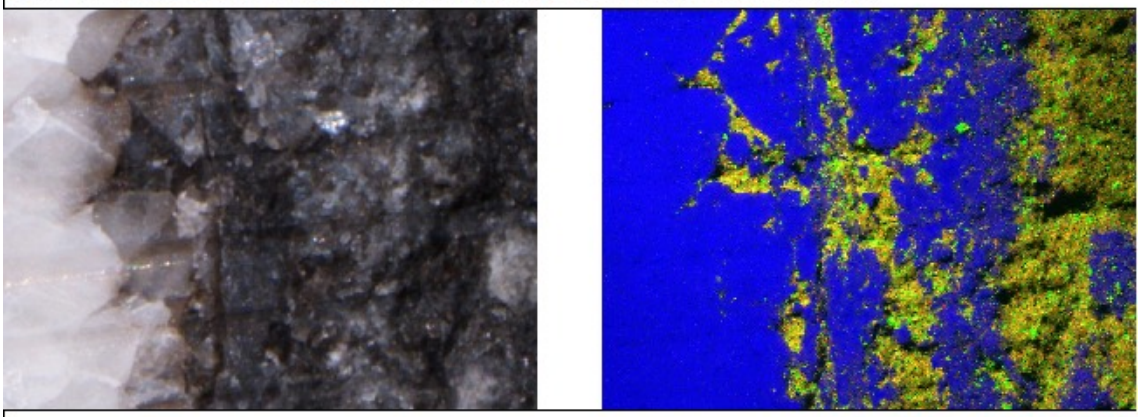

Fig. 72: False colour combined element map of BSE data.
Left: microphotograph of the area pictured in Fig. 71. Right: false colour image composed of the Al, Si and Ca element maps from Fig. 71 as red, green and blue components, respectively. Calcite appears blue, host rock in yellow and green colours. Image width 2.4 mm.

5.4 Sample screening & dating

5.4.1 General remarks and data tables

In the following sections (5.4.2 - 5.4.7), data obtained by different methods, LA-ICPMS screening data (1D and 2D) and ages obtained in situ by quadrupole LA-ICPMS and from solutions by MC-ICPMS, are presented together, arranged by sampling area.

One-dimensional laser ablation tracks were routinely analysed on all samples as a means of determining element concentrations and distribution. Approximately 80 tracks were analysed. The main criteria determining a sample as "suitable" for further analyses were an elevated U/Pb ratio, as high U concentrations as possible (the highest concentrations observed were almost 2 ppm, but most samples were well below 1 ppm), Pb concentrations low but above detection limit (few tens of ppb depending on background noise), and absence of mineral phases other than calcite.

In samples showing clearly defined homogeneous subdomains, this information was sufficient to establish suitability for further analysis and plan microsampling for chemical work. This screening also identified samples unsuitable for U-Pb dating (U/Pb < 1, clay minerals) with a minimum of preparation and time necessary.

Al, Ba, Ca, Eu, Fe, Mg, Mn, Pb, Rb, Si, Sr, Th, U and Yb were measured. An add-on package for the "R language for statistical computing" (R Development Core Team, 2010; Grunsky, 2002), was developed and used for data reduction of mass spectrometer data, see Rittner & Müller, 2012, in Appendix A. Although this software is aimed at calculation of two-dimensional element distribution maps from an array of single tracks, the initial steps of converting raw element signals to concentrations can be applied to single tracks, as applied here. Concentrations are in this case plotted against distance from track start.

High Al and Si values indicate minerals other than calcite, like clay and host rock minerals, thus data are not quantifiable in these zones and only qualitative information about the presence of clays and/or host hock can be obtained.

From arrays of individual tracks analysed on selected samples, two-dimensional element distribution maps were calculated. The before-mentioned add-on package for the "R language for statistical computing" was utilised for data reduction of the raw acquired signals, correlation of the data to the geometry of the ablated tracks, and 2D interpolation into maps. A detailed description of the software package can be found in Rittner & Müller, 2012, in Appendix A.

This data processing technique was developed throughout the course of this study, and although promising as a screening technique, it was not intended to be applied to all samples. 1D screening in combination with optical diagnosis of homogeneous domains was sufficient to plan further sample processing in most cases. In the following sections, element maps of all five mapped samples are presented.

The same 14 elements as for 1D tracks were measured for mapping (Al, Ba, Ca, Eu, Fe, Mg, Mn, Pb, Rb, Si, Sr, Th, U, Yb); Ce, Rb and Yb will not be shown (Ce and Yb maps usually show distributions very similar to Eu; Rb concentrations in the calcite are below detection limit in most samples). Fe measurements turned out to be inaccurate using NIST SRM 612 as an external standard, and concentrations shown are not reliable.

In the maps presented here, the interpolation algorithm utilised sometimes produces areas of sub-LOD values, additional to areas where the actual measurements were below LOD. The maps show holes where calculated values fall below LOD. Likewise, sometimes higher concentration values than actually measured are calculated, especially around thin clay “peaks” and sharp material boundaries (e.g. calcite – host rock). These areas were given the maximum measured value. The (colour) scale bars on the element maps do not show exact LOD and maximum values, but comprise a range of closest rounded values that contain all data values.

As sample preparation for MC-ICPMS is time-consuming and sensitive to contamination during the process, and subsequent analysis requires another mass spectrometer in addition to the quadrupole ICPMS used for sample screening, direct measurement of U-Pb isotopic composition on the LA-ICPMS system would be desirable. Feasibility of such analyses is mainly limited by the signal-to-background

ratio of the Pb isotopes. Typical signals during screening of the examined samples were close to and often below LOD for ^{206}Pb, ^{207}Pb and ^{208}Pb. ^{204}Pb is the least abundant Pb isotope, and suffers from interference of ^{204}Hg, abundant in commercially available gases (He, Ar) and gas handling hardware (tubing, valves, mass flow controllers). Hence, ^{204}Pb can not be measured reliably on the RHUL LA-ICPMS system (and most other quadrupole LA-ICPMS systems elsewhere).

To gain the atomic mass of measured Pb for calculation of ^{238}U/^{206}Pb, a typical radiogenic ^{206}Pb/^{204}Pb ratio can be assumed as a first order approximation, and the three measured isotopes can then be used to calculate abundance of all four Pb isotopes (see chapter 4.12.3 Data reduction). These data are presented here.

Data accuracy can be inferred from two isotopic measurements conducted on the USGS MACS3 standard, see chapter "4.5.5 Comparison with published values". ^{207}Pb/^{206}Pb, ^{208}Pb/^{206}Pb and U/Pb elemental ratios are within error of the preliminary values available at time of writing.

Tab. 11: Next pages: Isotopic ratios for selected samples, acquired in situ by LA-ICPMS.
Pb isotopic abundances calculated based on an assumed elevated (radiogenic) ^{206}Pb/^{204}Pb ratio of 200. Data points assumed to be outliers (e.g. foreign minerals ablated) are highlighted in grey.

Sample / point	$^{207}Pb/^{206}Pb$	2 se	$^{208}Pb/^{206}Pb$	2 se	$^{238}U/^{206}Pb$	2 se
KMR-GOB18A_A						
18AAiso1	0.180	0.027	0.358	0.077	140.848	3.970
18AAiso2	0.224	0.245	0.449	0.145	147.267	8.449
18AAiso3	0.099	0.015	0.174	0.027	178.345	5.947
18AAiso4	0.163	0.022	0.315	0.064	122.267	5.432
18AAiso5	0.199	0.034	0.369	0.065	112.561	4.152
18AAiso6	0.106	0.025	0.201	0.027	199.457	7.656
18AAiso7	0.127	0.038	0.197	0.036	200.185	12.635
KMR-GOB18B_B						
18BBiso1	0.750	0.014	1.846	0.027	17.504	1.565
18BBiso2	0.755	0.029	1.874	0.104	15.471	1.065
18BBiso3	0.729	0.018	1.824	0.076	20.726	1.957
18BBiso4	0.697	0.011	1.701	0.029	29.010	2.353
18BBiso5	0.719	0.015	1.766	0.042	22.664	1.651
18BBiso6	0.581	0.018	1.402	0.047	49.880	3.671
18BBiso7	0.703	0.014	1.731	0.039	26.059	1.831
18BBiso8	0.711	0.010	1.737	0.023	24.640	1.705
KMR-FOB28B_A						
28BAiso1	0.698	0.062	1.920	0.209	157.748	22.159
28BAiso2	0.844	0.041	2.057	0.087	21.394	2.323
28BAiso3	1.056	0.291	3.175	0.742	37.020	7.101
28BAiso4	0.668	0.158	1.374	0.076	257.167	17.150
28BAiso5	0.688	0.034	1.836	0.326	137.592	13.572
28BAiso6	0.883	0.522	1.671	0.935	40.047	18.975
28BAiso7	0.980	0.267	2.447	0.567	21.810	6.042
KMR-GOB23B_A						
23BAiso1	0.496	0.531	1.160	0.747	104.213	116.737
23BAiso2	0.182	0.152	0.278	0.247	418.479	91.318
23BAiso3	0.385	0.454	1.040	0.769	193.707	131.850
23BAiso4	0.539	0.108	1.282	0.393	12.785	2.571
23BAiso5	0.442	0.409	1.090	1.874	189.824	159.288
23BAiso6	0.678	0.162	1.584	0.391	29.950	15.830
KMR-SEF39A_A						
39AAiso1	0.213	0.027	0.454	0.075	79.895	4.771
39AAiso2	0.304	0.305	0.225	0.452	88.867	42.393
39AAiso3	0.406	0.437	0.785	0.734	105.292	36.130
39AAiso4	0.138	0.018	0.240	0.048	93.272	5.926
39AAiso5	0.046	0.009	0.031	0.018	78.870	6.200
39AAiso6	0.071	0.022	0.030	0.023	113.036	5.185
39AAiso7	0.335	0.607	0.922	1.224	101.888	35.150
39AAiso8	0.703	0.510	0.062	0.506	162.050	63.173
39AAiso9	0.094	0.036	0.163	0.125	131.504	8.849
KMR-GOB21B_A						
21BAiso1	0.803	0.023	1.955	0.052	11.379	0.761
21BAiso2	0.837	0.020	2.037	0.090	9.337	0.510
21BAiso3	0.762	0.014	1.855	0.052	23.997	1.718
21BAiso4	0.624	0.018	1.515	0.052	68.753	4.737

Sample / point	$^{207}Pb/^{206}Pb$	2 se	$^{208}Pb/^{206}Pb$	2 se	$^{238}U/^{206}Pb$	2 se
KMR-LIV34B_A						
pt1	0.799	0.112	2.067	0.371	44.405	11.760
pt2	0.595	0.171	1.260	1.211	2197.278	1724.115
pt3	0.215	0.071	0.548	0.118	4708.431	1257.464
pt4	0.479	2.942	1.158	2.295	1168.289	1987.121
pt5	0.484	0.102	1.243	0.287	1051.184	160.620
pt6	0.538	0.185	1.172	0.390	1027.954	281.124
pt7	0.722	0.655	0.948	1.116	1236.322	674.200
pt8	0.342	0.303	0.833	0.216	1816.570	771.520
pt9	0.300	0.109	0.661	0.153	3412.800	1172.401
pt10	0.819	0.679	2.301	2.382	1415.855	788.233
pt11	0.461	0.284	0.808	0.240	2317.382	742.090
KB2						
pt1	0.222	0.001	0.533	0.001	444.729	349.011
pt2	0.433	0.002	1.083	0.002	158.554	19.799
pt3	0.353	0.045	0.727	0.044	233.675	19.844
pt4	0.457	0.041	1.107	0.041	127.460	39.286
pt5	0.495	0.029	1.169	0.029	112.377	15.288
pt6	0.148	0.046	0.271	0.045	571.049	118.626
pt7	0.363	0.027	0.847	0.027	416.916	202.760
pt8	0.330	0.023	0.749	0.023	376.022	120.289
pt9	-0.135	0.038	1.155	0.037	-319.982	326.052
pt10	0.051	0.058	0.106	0.058	-5343.170	2517.058
pt11	0.057	0.437	0.136	0.434	-1595.456	1299.264
pt12	0.692	0.047	1.685	0.047	17.560	4.868
pt13	0.132	0.052	0.392	0.052	366.438	188.056
pt14	0.533	0.036	1.071	0.036	153.144	121.593
pt15	0.393	0.049	0.857	0.049	1111.771	290.522
pt16	0.213	0.798	0.291	0.792	272.793	140.578
D1WA						
pt1	0.748	0.027	1.852	0.026	51.581	1.465
pt2	0.791	0.032	1.933	0.032	8.834	0.418
pt3	0.805	0.055	1.885	0.054	13.160	1.259
pt4	0.780	0.036	1.930	0.035	23.979	0.768
pt5	0.808	0.042	1.998	0.041	6.577	0.239
pt6	0.779	0.032	1.901	0.032	32.936	0.881
pt7	0.783	0.025	1.907	0.025	30.524	0.941
pt8	0.795	0.023	1.941	0.023	25.320	0.840
pt9	0.782	0.023	1.919	0.023	32.835	0.849

Microsamples prepared from samples that seemed most promising based on the 1D and 2D screening methods, and of some that were of greatest interest in a regional geological context, were prepared and analysed according to the methods described in chapter 4 Methodology II: application.

Due to the very small amounts of lead extracted from each individual subsample and the delicate nature of the chemical preparation, any disturbance in the wet-chemical and analytical workflow can lead to contamination or (partial) sample loss, and thus erroneous results. During separation, possible handling errors were noted for several subsamples, see Tab. 12. In most cases, these data points proved to be outliers in the resulting concordia diagrams, and thus were omitted.

Despite high analytical precision of individual measurements on the MC-ICPMS, in most samples geological scatter resulted in imprecise age estimates, i.e. the data points do not lie on a straight line in the Tera-Wasserburg diagram (see 3.2.3 Concordia diagrams), resulting in a regression line with a large error margin. Prevalence of scatter over analytical error is indicated by very large MSWD values for the calculated regression lines. Scatter might be caused by later alterations of the samples not noticed during optical examination and LA-ICPMS screening, and thus the basic assumption of an undisturbed isotopic system might not be met.

Age calculation from $^{238}U/^{206}Pb$ – $^{207}Pb/^{206}Pb$ isotopic ratios in a Tera-Wasserburg diagram (Tera & Wasserburg, 1972; Woodhead et al., 2006) is incorporated into the software package developed during this project, although this functionality is not mentioned in Rittner & Müller, 2012 (Appendix A). The regression line is calculated based on York et al., 2004, and age and age errors are constructed geometrically by intersection with the concordia. This method is less sophisticated, especially in terms of error calculation, than the MS Excel add-on "IsoPlot" (Ludwig, 1999; Ludwig, 2003) which is utilised in many work groups. However, York et al., 2004 points out that several published algorithms for the calculation of regression lines simply represent special cases of the general equations derived in that paper, and recommends use of these as a uniform method throughout geosciences.

In the presented diagrams, correlated errors are represented by error ellipses indicating 95% confidence interval (2 sd). See Tab. 13 for numerical data. Confidence band on the regression line, and thus, age errors, is 95%, as is the resulting error on the intercept (initial $^{207}Pb/^{206}Pb$ ratio).

sample	smpl mass [mg]	conc U [ppb]	conc Th [ppb]	conc Pb [ppb]	mass Pb [pg]	$^{208}Pb/^{204}Pb$	$^{207}Pb/^{204}Pb$	$^{238}U/^{206}Pb$	$^{208}Pb/^{206}Pb$	$^{207}Pb/^{206}Pb$	$^{208}Pb/^{206}Pb$	$^{238}U/^{204}Pb$	$^{238}U/^{204}Pb$
MHH06													
MHH06 / s1	28 (138)	373.16 ± 0.06	3.201 ± 0.016	38.337 ± 0.016	1061.2 ± 0.5	1.9430 ± 0.0007	0.78386 ± 0.00005	36.4948 ± 0.0068	20.0396 ± 0.0081	15.7082 ± 0.0065	38.9365 ± 0.0213	731.34 ± 0.11	5.30413 ± 0.00000
MHH06 / s2	56 (279)	269.94 ± 0.04	1.401 ± 0.008	23.260 ± 0.011	1298.3 ± 0.6	1.8962 ± 0.0006	0.76530 ± 0.00006	42.7456 ± 0.0082	20.5677 ± 0.0089	15.7404 ± 0.0069	39.0013 ± 0.0207	879.18 ± 0.14	6.37634 ± 0.00000
MHH06 / s5	32 (159)	447.27 ± 0.09	1.264 ± 0.011	26.467 ± 0.020	839.8 ± 0.6	1.8879 ± 0.0007	0.76181 ± 0.00007	62.0384 ± 0.0164	20.7732 ± 0.0147	15.8252 ± 0.0113	39.2180 ± 0.0318	1288.73 ± 0.25	9.34669 ± 0.00000
MHH06 / s6	27 (137)	447.67 ± 0.08	3.985 ± 0.021	29.217 ± 0.016	797.9 ± 0.4	1.8907 ± 0.0012	0.76266 ± 0.00008	56.3103 ± 0.0123	20.6088 ± 0.0106	15.7176 ± 0.0082	38.9659 ± 0.0318	1160.49 ± 0.20	8.41659 ± 0.00000
MHH06 / s7	38 (190)	256.04 ± 0.05	2.955 ± 0.030	35.642 ± 0.013	1353.0 ± 0.5	1.9336 ± 0.0004	0.78050 ± 0.00006	26.8408 ± 0.0056	20.1160 ± 0.0070	15.7005 ± 0.0056	38.8956 ± 0.0161	539.93 ± 0.10	3.91590 ± 0.00000
MHH06 / s9	79 (396)	265.59 ± 0.16	2.182 ± 0.028	31.595 ± 0.006	2504.8 ± 0.5	1.9111 ± 0.0003	0.77222 ± 0.00003	31.1472 ± 0.0191	20.3672 ± 0.0037	15.7279 ± 0.0029	38.9233 ± 0.0087	634.38 ± 0.39	4.60091 ± 0.00000
DGN55e													
DGN55e_B / s3	63 (316)	1326.15 ± 1.07	2.754 ± 0.084	93.615 ± 0.008	5916.5 ± 0.5	1.8503 ± 0.0002	0.75234 ± 0.00003	51.3360 ± 0.0411	20.9717 ± 0.0019	15.7779 ± 0.0015	38.8046 ± 0.0053	1076.60 ± 0.86	7.80820 ± 0.00000
DGN55e_B / s4	11 (56)	4080.76 ± 2.61	0.625 ± 0.012	118.883 ± 0.034	1319.6 ± 0.4	1.6642 ± 0.0004	0.67938 ± 0.00004	115.3980 ± 0.0737	23.3789 ± 0.0063	15.8832 ± 0.0044	38.9082 ± 0.0137	2697.87 ± 1.71	19.56665 ± 0.00000
DGN55e_B / s5	12 (59)	5429.21 ± 6.11	0.476 ± 0.015	119.647 ± 0.038	1399.9 ± 0.4	1.5699 ± 0.0007	0.64341 ± 0.00004	146.5692 ± 0.1641	24.7743 ± 0.0075	15.9401 ± 0.0049	38.8926 ± 0.0202	3631.15 ± 4.06	26.71192 ± 0.00001
DGN55e_B / s6	16 (81)	6341.31 ± 7.77	0.019 ± 0.011	118.548 ± 0.041	1908.6 ± 0.7	1.5019 ± 0.0004	0.61807 ± 0.00004	167.7349 ± 0.2044	25.8844 ± 0.0085	15.9984 ± 0.0053	38.8769 ± 0.0159	4341.72 ± 5.28	31.29280 ± 0.00001
DGN55e_B / s7	36 (182)	6105.85 ± 5.09	0.846 ± 0.033	119.557 ± 0.019	4351.9 ± 0.7	1.5273 ± 0.0003	0.62830 ± 0.00003	161.9857 ± 0.1341	25.4309 ± 0.0041	15.9781 ± 0.0027	38.8418 ± 0.0090	4119.43 ± 3.41	29.16075 ± 0.00000
DGN55e_B / s8	8 (38)	3711.16 ± 3.62	1.159 ± 0.030	106.181 ± 0.055	796.4 ± 0.4	1.6585 ± 0.0012	0.67616 ± 0.00007	117.1826 ± 0.1144	23.4818 ± 0.0114	15.8774 ± 0.0079	38.9445 ± 0.0344	2751.66 ± 2.66	19.95673 ± 0.00001
MHH01_A													
MHH01_A / s1	33 (163)	317.64 ± 0.09	0.229 ± 0.002	6.069 ± 0.020	197.2 ± 0.7	1.5514 ± 0.0042	0.62811 ± 0.00012	167.2568 ± 0.1426	25.3384 ± 0.0766	15.9154 ± 0.0482	39.3103 ± 0.1612	4238.01 ± 1.18	30.73669 ± 0.00002
MHH01_A / s2	30 (149)	391.27 ± 0.08	17.142 ± 0.099	22.323 ± 0.015	663.0 ± 0.4	1.8115 ± 0.0011	0.73417 ± 0.00007	62.5062 ± 0.0158	21.4857 ± 0.0132	15.7740 ± 0.0098	38.9210 ± 0.0344	1342.99 ± 0.27	9.74017 ± 0.00000
MHH01_A / s3	32 (158)	395.97 ± 0.08	16.193 ± 0.102	10.180 ± 0.017	320.7 ± 0.5	1.6269 ± 0.0118	0.65955 ± 0.00010	128.5091 ± 0.0586	24.0497 ± 0.0379	15.8620 ± 0.0251	39.1270 ± 0.2942	3090.61 ± 0.61	24.23307 ± 0.00001
MHH01_A / s4	21 (103)	376.45 ± 0.07	11.875 ± 0.086	20.507 ± 0.031	420.4 ± 0.6	1.8024 ± 0.0017	0.72860 ± 0.00011	65.1932 ± 0.0268	21.6414 ± 0.0310	15.7679 ± 0.0227	39.0074 ± 0.0680	1410.87 ± 0.26	10.31027 ± 0.00000
MHH01_A / s6	26 (128)	305.76 ± 0.10	0.097 ± 0.001	3.667 ± 0.021	93.9 ± 0.5	1.3538 ± 0.0114	0.54309 ± 0.00025	242.6016 ± 0.3396	29.5248 ± 0.1447	16.0346 ± 0.0790	39.9712 ± 0.4014	7162.76 ± 2.31	51.94877 ± 0.00008
MHH01_A / s7	13 (64)	433.53 ± 0.07	12.615 ± 0.041	17.104 ± 0.049	217.2 ± 0.6	1.7902 ± 0.0113	0.71793 ± 0.00013	89.4211 ± 0.0630	21.9506 ± 0.0597	15.7589 ± 0.0429	39.2955 ± 0.2744	1962.84 ± 0.30	14.23575 ± 0.00001
MHH02													
MHH02 / s1	70 (350)	80.02 ± 0.02	3.348 ± 0.026	14.546 ± 0.010	1019.1 ± 0.7	1.7580 ± 0.0010	0.71561 ± 0.00005	19.2165 ± 0.0048	22.0905 ± 0.0137	15.8081 ± 0.0099	38.8340 ± 0.0329	424.50 ± 0.08	3.07874 ± 0.00000
MHH02 / s2	74 (371)	49.04 ± 0.02	0.194 ± 0.002	9.819 ± 0.009	727.9 ± 0.6	1.7620 ± 0.0014	0.71627 ± 0.00009	17.4699 ± 0.0090	22.0616 ± 0.0187	15.8020 ± 0.0135	38.8722 ± 0.0447	385.41 ± 0.18	2.79526 ± 0.00000
MHH02 / s3	55 (273)	31.64 ± 0.01	0.000 ± 0.001	8.466 ± 0.010	462.6 ± 0.6	1.7753 ± 0.0029	0.71921 ± 0.00011	13.1348 ± 0.0058	21.9568 ± 0.0248	15.7916 ± 0.0180	38.9799 ± 0.0783	288.40 ± 0.10	2.09163 ± 0.00000
MHH02 / s4	71 (357)	36.52 ± 0.01	0.007 ± 0.000	8.820 ± 0.010	629.1 ± 0.7	1.7732 ± 0.0081	0.72015 ± 0.00011	14.5452 ± 0.0056	21.9324 ± 0.0230	15.7946 ± 0.0168	38.8902 ± 0.1840	319.01 ± 0.09	2.31366 ± 0.00000
MHH02 / s5	63 (317)	48.83 ± 0.02	0.166 ± 0.006	11.892 ± 0.009	754.9 ± 0.6	1.7925 ± 0.0007	0.72964 ± 0.00006	14.5462 ± 0.0060	21.6248 ± 0.0157	15.7782 ± 0.0115	38.7630 ± 0.0318	314.56 ± 0.12	2.28137 ± 0.00000
MHH02 / s6	54 (268)	42.42 ± 0.01	1.225 ± 0.010	12.485 ± 0.010	668.4 ± 0.5	1.7862 ± 0.0013	0.72593 ± 0.00005	12.0003 ± 0.0033	21.7479 ± 0.0162	15.7875 ± 0.0118	38.8451 ± 0.0405	260.98 ± 0.05	1.89279 ± 0.00000
MHH02 / s7	50 (249)	35.68 ± 0.01	0.071 ± 0.001	10.074 ± 0.011	502.5 ± 0.6	1.7824 ± 0.0049	0.72247 ± 0.00007	12.4857 ± 0.0043	21.8552 ± 0.0229	15.7898 ± 0.0166	38.9541 ± 0.1144	272.88 ± 0.06	1.97908 ± 0.00000
MHH02 / s8	58 (289)	27.24 ± 0.01	0.048 ± 0.000	7.861 ± 0.008	453.8 ± 0.5	1.7875 ± 0.0012	0.72382 ± 0.00009	12.2372 ± 0.0046	21.7980 ± 0.0218	15.7778 ± 0.0159	38.9644 ± 0.0471	266.75 ± 0.07	1.93461 ± 0.00000
GOB21B-2													
GOB21B / s2	53 (265)	258.00 ± 0.05	0.013 ± 0.001	21.344 ± 0.007	1130.4 ± 0.4	1.7289 ± 0.0007	0.70584 ± 0.00004	41.7516 ± 0.0092	22.4364 ± 0.0070	15.8364 ± 0.0050	38.7902 ± 0.0206	936.75 ± 0.19	6.79392 ± 0.00000
GOB21B / s3b	65 (327)	268.38 ± 0.16	0.713 ± 0.040	21.293 ± 0.009	1394.3 ± 0.6	1.7196 ± 0.0003	0.70264 ± 0.00005	43.3767 ± 0.0258	22.5526 ± 0.0093	15.8464 ± 0.0066	38.7825 ± 0.0177	978.26 ± 0.57	7.09494 ± 0.00000
GOB21B / s4	54 (271)	33.18 ± 0.01	5.241 ± 0.050	6.866 ± 0.011	371.6 ± 0.6	1.8162 ± 0.0032	0.73196 ± 0.00011	17.2441 ± 0.0085	21.5552 ± 0.0319	15.7775 ± 0.0235	39.1487 ± 0.0916	371.70 ± 0.12	2.69580 ± 0.00000
GOB21B / s5b	77 (384)	17.55 ± 0.00	0.172 ± 0.001	0.393 ± 0.006	30.1 ± 0.4	0.9643 ± 0.0583	0.37401 ± 0.00031	104.7697 ± 0.3715	43.9446 ± 0.5335	16.4355 ± 0.2000	42.3762 ± 2.8891	4604.06 ± 1.43	33.39152 ± 0.00008
GOB21B / s7	20 (99)	25.98 ± 0.01	1.926 ± 0.015	6.118 ± 0.023	121.2 ± 0.4	1.8530 ± 0.0085	0.73370 ± 0.00021	15.3168 ± 0.0142	21.4154 ± 0.0745	15.7125 ± 0.0549	39.6837 ± 0.2334	328.02 ± 0.08	2.37898 ± 0.00000
DGN55c													
DGN55c / s1	80 (399)	195.81 ± 0.04	10.334 ± 0.066	15.049 ± 0.005	1200.7 ± 0.4	1.9210 ± 0.0007	0.77699 ± 0.00005	48.4068 ± 0.0102	20.2268 ± 0.0062	15.7161 ± 0.0049	38.8559 ± 0.0194	979.11 ± 0.19	7.10114 ± 0.00000
DGN55c / s2	58 (291)	177.09 ± 0.06	21.380 ± 0.134	27.434 ± 0.009	1595.3 ± 0.5	1.9454 ± 0.0004	0.78630 ± 0.00004	24.2341 ± 0.0079	19.9748 ± 0.0065	15.7061 ± 0.0052	38.8595 ± 0.0151	484.07 ± 0.15	3.51080 ± 0.00000
DGN55c / s3	57 (285)	137.62 ± 0.02	6.205 ± 0.032	7.445 ± 0.009	424.2 ± 0.5	1.8535 ± 0.0025	0.74652 ± 0.00010	66.9361 ± 0.0212	21.0608 ± 0.0231	15.7224 ± 0.0174	39.0366 ± 0.0684	1409.73 ± 0.21	10.22425 ± 0.00000
DGN55c / s5	47 (234)	125.48 ± 0.02	7.427 ± 0.048	0.108 ± 0.006	5.0 ± 0.3	2.0227 ± 0.3264	0.59201 ± 0.00086	4227.8115 ± 57.8644	24.8877 ± 1.0614	14.7337 ± 0.6287	50.3396 ± 10.9137	105220.67 ± 85.22	763.12530 ± 0.00530
DGN55c / s6	73 (363)	117.88 ± 0.03	1.820 ± 0.011	4.685 ± 0.007	340.1 ± 0.5	1.7689 ± 0.0015	0.71304 ± 0.00009	88.0981 ± 0.0365	22.0957 ± 0.0282	15.7550 ± 0.0202	39.0850 ± 0.0602	1946.59 ± 0.47	14.11788 ± 0.00000
DGN55c / s7	48 (242)	106.34 ± 0.13	5.615 ± 0.567	5.457 ± 0.006	263.9 ± 0.3	1.8451 ± 0.0029	0.73948 ± 0.00010	70.2544 ± 0.0892	21.2469 ± 0.0229	15.7117 ± 0.0171	39.2017 ± 0.0752	1492.69 ± 1.85	10.82591 ± 0.00001
DGN55c / s8	85 (426)	102.32 ± 0.05	1.151 ± 0.012	4.258 ± 0.007	362.4 ± 0.6	1.8118 ± 0.0226	0.73018 ± 0.00012	85.6059 ± 0.0536	21.5560 ± 0.0323	15.7397 ± 0.0237	39.0551 ± 0.4940	1845.32 ± 0.91	13.38339 ± 0.00001
KB2													
KB2 / s3	24 (118)	636.17 ± 0.13	0.843 ± 0.009	6.237 ± 0.007	146.9 ± 0.2	1.2769 ± 0.0038	0.52301 ± 0.00004	286.7795 ± 0.0973	30.8694 ± 0.0339	16.1451 ± 0.0178	39.4176 ± 0.1287	8852.70 ± 1.86	64.20527 ± 0.00001
KB2 / s7	37 (184)	311.66 ± 0.11	0.133 ± 0.002	1.720 ± 0.058	63.3 ± 2.1	0.2128 ± 0.0126	0.11750 ± 0.00020	240.1339 ± 1.9562	200.4493 ± 4.2124	23.5531 ± 0.4965	42.6483 ± 3.0226	48134.67 ± 28.70	349.10235 ± 0.00115
KB2 / s9	27 (135)	203.86 ± 0.04	11.725 ± 0.109	348.436 ± 0.051	9402.9 ± 1.4	1.8186 ± 0.0002	0.73968 ± 0.00004	2.0941 ± 0.0004	21.2486 ± 0.0031	15.7171 ± 0.0024	38.6428 ± 0.0070	44.50 ± 0.01	0.32271 ± 0.00000
KB2 / s13	23 (117)	218.29 ± 0.11	3.237 ± 0.069	22.687 ± 0.017	528.7 ± 0.4	1.7065 ± 0.0013	0.69327 ± 0.00006	32.8943 ± 0.0169	22.7459 ± 0.0169	15.7690 ± 0.0118	38.8162 ± 0.0411	748.21 ± 0.36	5.42650 ± 0.00000
KB2 / s15	34 (171)	738.25 ± 0.29	29.640 ± 0.456	588.090 ± 0.042	20110.3 ± 1.4	1.6581 ± 0.0001	0.67450 ± 0.00002	4.2067 ± 0.0016	23.3206 ± 0.0020	15.7298 ± 0.0014	38.6683 ± 0.0040	98.10 ± 0.04	0.71149 ± 0.00000
GOB21B_IIIb													
GOB21B IIIb / s1	108 (542)	49.73 ± 0.01	2.054 ± 0.010	1.232 ± 0.003	133.4 ± 0.4	1.1611 ± 0.0049	0.48282 ± 0.00010	107.1427 ± 0.0714	33.5361 ± 0.0854	16.1920 ± 0.0414	38.9381 ± 0.1976	3593.15 ± 0.47	26.05971 ± 0.00001
GOB21B IIIb / s2	122 (610)	72.90 ± 0.01	2.183 ± 0.011	1.571 ± 0.004	191.5 ± 0.5	0.9138 ± 0.0072	0.38689 ± 0.00011	107.0440 ± 0.0663	43.2339 ± 0.0822	16.7267 ± 0.0321	39.5065 ± 0.3252	4627.93 ± 0.84	33.56460 ± 0.00001
GOB21B IIIb / s4	105 (524)	50.97 ± 0.01	1.042 ± 0.006	1.205 ± 0.005	126.1 ± 0.5	1.0723 ± 0.0095	0.44226 ± 0.00014	106.7726 ± 0.1124	37.0318 ± 0.1400	16.3778 ± 0.0621	39.7074 ± 0.3945	3953.98 ± 0.91	28.67671 ± 0.00002
GOB21B IIIb / s5	153 (765)	37.31 ± 0.01	0.584 ± 0.004	1.143 ± 0.005	174.9 ± 0.8	1.1532 ± 0.0058	0.47893 ± 0.00013	86.2344 ± 0.0948	34.0253 ± 0.1201	16.2957 ± 0.0577	39.2387 ± 0.2471	2934.15 ± 1.06	21.28026 ± 0.00003
GOB21B IIIb / s7	91 (454)	65.74 ± 0.01	6.554 ± 0.036	2.380 ± 0.007	216.1 ± 0.6	1.3550 ± 0.0037	0.55830 ± 0.00011	80.8311 ± 0.0560	28.6282 ± 0.0742	15.9830 ± 0.0415	38.7906 ± 0.1491	2314.05 ± 0.39	16.78290 ± 0.00001

sample	smpl mass [mg]	conc U [ppb]	conc Th [ppb]	conc Pb [ppb]	mass Pb [pg]	$^{206}Pb/^{204}Pb$	$^{208}Pb/^{206}Pb$	$^{238}U/^{206}Pb$	$^{206}Pb/^{204}Pb$	$^{207}Pb/^{204}Pb$	$^{238}U/^{204}Pb$	$^{232}Th/^{204}Pb$
GOB21B Ia												
GOB21B Ia / s2	57 (286)	43.94 ± 0.01	1.171 ± 0.008	2.694 ± 0.019	154.2 ± 1.1	1.6336 ± 0.0237	0.66813 ± 0.00030	54.1405 ± 0.0925	23.6362 ± 0.1560	15.7921 ± 0.1045	38.6119 ± 0.6276	1279.68 ± 0.30	9.28100 ± 0.00001
GOB21B Ia / s3	31 (156)	35.50 ± 0.01	0.886 ± 0.010	0.784 ± 0.030	24.4 ± 0.9	1.1632 ± 0.1008	0.43313 ± 0.00083	117.9605 ± 1.0890	37.1973 ± 1.1543	16.1111 ± 0.5009	43.2684 ± 4.4576	4387.81 ± 2.80	31.82314 ± 0.00031
GOB21B Ia / s5	39 (196)	42.18 ± 0.03	0.645 ± 0.015	2.268 ± 0.022	89.1 ± 0.9	1.6055 ± 0.0270	0.63623 ± 0.00035	60.6029 ± 0.1491	24.8707 ± 0.2330	15.8234 ± 0.1485	39.9296 ± 0.7936	1507.24 ± 0.92	10.93141 ± 0.00006
GOB21B Ia / s6	49 (243)	30.66 ± 0.01	0.263 ± 0.003	0.604 ± 0.024	29.4 ± 1.2	1.0395 ± 0.0894	0.39809 ± 0.00102	124.0148 ± 1.2092	40.9908 ± 1.3795	16.3179 ± 0.5507	42.6082 ± 4.3541	5083.46 ± 3.49	36.86839 ± 0.00041
GOB21B Ia / s7	65 (324)	40.87 ± 0.01	0.441 ± 0.004	2.883 ± 0.021	187.1 ± 1.3	1.6812 ± 0.0263	0.68485 ± 0.00052	47.9847 ± 0.0837	23.0406 ± 0.1575	15.7793 ± 0.1085	38.7346 ± 0.6711	1105.59 ± 0.34	8.01845 ± 0.00002
LIV34B												
LIV34B / s5	38 (190)	309.05 ± 0.05	49.102 ± 0.332	7.467 ± 0.042	284.4 ± 1.6	1.3646 ± 0.0134	0.55251 ± 0.00038	121.2718 ± 0.1664	29.0530 ± 0.1534	16.0521 ± 0.0855	39.6466 ± 0.4475	3523.31 ± 0.63	25.55320 ± 0.00002
LIV34B / s6	26 (131)	478.70 ± 0.05	63.262 ± 0.153	10.413 ± 0.016	271.8 ± 0.4	1.3816 ± 0.0037	0.56104 ± 0.00008	135.8910 ± 0.0507	28.6597 ± 0.0397	16.0792 ± 0.0224	39.5948 ± 0.1199	3894.59 ± 0.40	28.24600 ± 0.00000
LIV34B / s7	36 (181)	227.67 ± 0.07	29.779 ± 0.228	4.008 ± 0.015	145.0 ± 0.5	1.1199 ± 0.0071	0.45059 ± 0.00019	146.4960 ± 0.1385	36.1675 ± 0.1232	16.2968 ± 0.0559	40.5034 ± 0.2993	5298.39 ± 1.57	38.42720 ± 0.00003
LIV34B / s8	54 (270)	280.55 ± 0.03	35.557 ± 0.080	3.639 ± 0.005	196.4 ± 0.3	0.8813 ± 0.0027	0.35999 ± 0.00007	173.2027 ± 0.0660	45.6145 ± 0.0628	16.4209 ± 0.0228	40.1988 ± 0.1383	7900.56 ± 0.92	57.29975 ± 0.00001
GOB21_I1-I												
GOB21 I1-I / s2	31 (155)	292.17 ± 0.15	1.339 ± 0.026	15.268 ± 0.012	473.1 ± 0.4	1.5716 ± 0.0010	0.64253 ± 0.00006	61.8272 ± 0.0330	24.7851 ± 0.0189	15.9251 ± 0.0122	38.9513 ± 0.0392	1532.39 ± 0.76	11.11384 ± 0.00000
GOB21 I1-I / s3	46 (229)	246.58 ± 0.03	0.475 ± 0.002	10.448 ± 0.011	479.4 ± 0.5	1.4813 ± 0.0033	0.60825 ± 0.00018	73.2762 ± 0.0203	26.3002 ± 0.0260	15.9970 ± 0.0165	38.9596 ± 0.0944	1927.18 ± 0.21	13.97709 ± 0.00000
GOB21 I1-I / s4	30 (152)	344.61 ± 0.06	0.438 ± 0.005	11.873 ± 0.014	362.0 ± 0.4	1.3969 ± 0.0024	0.57472 ± 0.00006	86.6604 ± 0.0291	27.9548 ± 0.0316	16.0661 ± 0.0182	39.0510 ± 0.0801	2422.58 ± 0.40	16.84354 ± 0.00000
GOB21 I1-I / s8	32 (161)	216.74 ± 0.02	0.401 ± 0.001	11.533 ± 0.112	371.7 ± 3.6	1.5801 ± 0.0113	0.64470 ± 0.00054	60.9213 ± 0.1427	24.6825 ± 0.2248	15.9127 ± 0.1455	39.0004 ± 0.4561	1503.69 ± 0.25	10.90569 ± 0.00001
FOB28B												
FOB28B / s1	62 (309)	14.42 ± 0.00	0.136 ± 0.001	1.825 ± 0.007	112.6 ± 0.5	1.9972 ± 0.0127	0.78946 ± 0.00019	30.0993 ± 0.0308	19.8206 ± 0.0752	15.6476 ± 0.0595	39.5860 ± 0.3004	596.59 ± 0.17	4.32681 ± 0.00000
FOB28B / s2	37 (186)	1084.47 ± 0.25	9.921 ± 0.065	17.338 ± 0.013	645.8 ± 0.5	1.2964 ± 0.0013	0.53801 ± 0.00008	178.0641 ± 0.0516	30.1292 ± 0.0194	16.2099 ± 0.0108	39.0582 ± 0.0470	5364.92 ± 1.23	38.90972 ± 0.00001
FOB28B / s3	31 (153)	258.81 ± 0.03	8.683 ± 0.023	24.952 ± 0.023	765.8 ± 0.7	1.8974 ± 0.0021	0.76824 ± 0.00015	38.2476 ± 0.0096	20.5057 ± 0.0176	15.7533 ± 0.0139	38.9077 ± 0.0544	784.29 ± 0.09	5.62008 ± 0.00000
FOB28B / s4	40 (202)	180.07 ± 0.05	18.839 ± 0.144	39.717 ± 0.010	1604.2 ± 0.4	1.9790 ± 0.0004	0.80063 ± 0.00005	17.2411 ± 0.0050	19.6459 ± 0.0049	15.7291 ± 0.0041	38.8798 ± 0.0126	338.72 ± 0.10	2.52740 ± 0.00000
GOB21B-1												
GOB21B / s1	45 (226)	293.83 ± 0.04	1.253 ± 0.004	34.683 ± 0.016	1564.9 ± 0.7	1.7786 ± 0.0019	0.72552 ± 0.00009	29.8570 ± 0.0050	21.8097 ± 0.0093	15.8234 ± 0.0070	38.7911 ± 0.0442	651.17 ± 0.08	4.86008 ± 0.00000
GOB21B / s3a	71 (354)	326.16 ± 0.06	0.030 ± 0.000	18.929 ± 0.008	1340.8 ± 0.5	1.6142 ± 0.0004	0.66253 ± 0.00005	56.7624 ± 0.0119	24.0109 ± 0.0092	15.9081 ± 0.0062	38.7574 ± 0.0180	1362.92 ± 0.25	9.56090 ± 0.00000
GOB21B / s5a	56 (279)	17.77 ± 0.00	0.119 ± 0.000	1.277 ± 0.011	71.2 ± 0.6	1.9749 ± 0.0345	0.76772 ± 0.00029	52.3857 ± 0.1127	20.3242 ± 0.2094	15.6033 ± 0.1609	40.1386 ± 0.8462	1064.70 ± 0.18	9.31326 ± 0.00001
GOB21B / s8	21 (105)	57.42 ± 0.01	1.537 ± 0.004	9.336 ± 0.011	195.8 ± 0.2	1.0652 ± 0.0606	0.45065 ± 0.00020	15.5289 ± 0.0046	36.5478 ± 0.0218	16.4702 ± 0.0123	38.9308 ± 2.2542	567.55 ± 0.06	4.11620 ± 0.00000

Tab. 12: All U-Pb isotopic data measured in solution mode by MC-ICPMS.
This page and previous: Pb isotopic ratios and Pb, U and Th concentrations measured on the GVI IsoProbe (MC-ICPMS). Concentrations were determined by isotope dilution. Analyses indicated in orange were recorded during chemical preparation to involve handling errors or other problems, proved to be outliers, and were not further considered.

sample	this study [Ma] $^{238}U/^{206}Pb$ – $^{207}Pb/^{206}Pb$		IsoPlot [Ma] ^{238}U – ^{206}Pb	^{235}U - ^{207}Pb
MHH01_A	9.05 ± 0.94	9.0 ± 1.4 (1)	8.94 ± 0.84 (3)	6.3 ± 2.4 (1)
(MHH06)	4.3 ± 5.7	4.3 ± 6.2 (1)	5.4 ± 4.5 (3)	15 ± 20 (3)
(MHH02)	12.5 ± 11.1	12 ± 12 (1)	12 ± 12 (3)	21 ± 20 (1)
DGN55e_B	9.59 ± 0.02	9.59 ± 0.17 (1)	9.58 ± 0.29 (3)	9.38 ± 0.99 (3)
DGN55c	8.4 ± 3.5	8.4 ± 3.9 (1)	9.1 ± 3.1 (3)	3.1 ± 2.4 (1)
GOB21B_Ia	29.5 ± 2.0	29.5 ± 1.7 (1)	28.5 ± 3.1 (1)	17 ± 29 (1)
(GOB21B_IIIb)	28.7 ± 9.6	29 ± 65 (1)	31 ± 86 (3)	28 ± 10 (1)
(GOB21B_I1-I)	23.0 ± 1.2	23.0 ± 1.6 (1)	22.9 ± 2.7 (3)	24.7 ± 7.3 (1)
(GOB21B_2)	10.0 ± 1.7	10.0 ± 2.1 (1)	10.5 ± 2.0 (3)	17.9 ± 9.9 (1)
(KB2)	5.9 ± 12.9	6 ± 13 (1)	6.3 ± 3.8 (3)	6.7 ± 1.3 (3)
(LIV34B)	27.7 ± 1.3	27.7 ± 7.0 (1)	25.6 ± 8.9 (3)	11.7 ± 2.1 (1)
(FOB28B)	13.44 ± 0.84	13.44 ± 0.97 (1)	13.6 ± 1.2 (3)	13.35 ± 0.62 (1)

(1) Model 1 (3) Model 3

Tab. 13: Ages calculated with Isoplot.
$^{238}U/^{206}Pb$ – $^{207}Pb/^{206}Pb$ ages calculated based on a regression following York2004 are in excellent agreement with results from the program *Isoplot* (Ludwig1999Ludwig2003) if “Model 1” is utilised, which is based on York1969. Age errors in this table only take into account errors from the regression, errors in decay constants and isotopic weights were not considered. Uncertainty resulting from reproducibility of standard measurements is not included in this table. ^{238}U – ^{206}Pb and ^{235}U – ^{207}Pb isochrons calculated in *Isoplot* yield concordant ages within error for most samples. For the isochrons, use of “Model 3” was accepted if Isoplot deemed the probability of fit too low for “Model 1”. Samples in brackets are not considered reliable due to small number of data points (subsamples) or lack of spread of data points.

5.4.2 Fohnsdorf Basin

Sample KMR-FOB28B_A

This is a sample of the "Mariabucher Marmor" from the Fohnsdorf basin, Austria, a probably hydrothermal travertine grown in marginal crevasses or fissures at the basin margin, tectonically linked to subsidence ongoing throughout basin evolution (Wagreich & Strauss, 2005, see 2.2.5 Fohnsdorf Basin). The immediate host rock is a polymict conglomerate that developed as an alluvial fan between ~15 and ~13 Ma ("Apfelberg Fm." of Wagreich & Strauss, 2005). Hydrothermal activity was likely influenced by tectonic pulses, which together with the wide range of lithologies in the close vicinity and host rock, and a possible interplay of hydrothermal and meteoric water, accounts for the strongly varying compositions observed.

The sample is clearly laminated in growth bands of white and yellowish-amber calcite, with some seams between layers possibly indicating growth interruption. Al concentrations show some distinctively elevated values, e.g. at y-coordinates ~8.5 mm and ~10.5 mm in the element maps (Fig. 74), possibly indicating episodical influx of clay minerals.

Not only vary the concentrations of all elements by about one to two orders of magnitude between growth strata, but notably, so do relative concentrations, as is best visualised in the false colour maps (Fig. 75 & Fig. 76). This can not be explained simply by varying dilution of one solution source of constant composition, but indicates mixing of different sources.

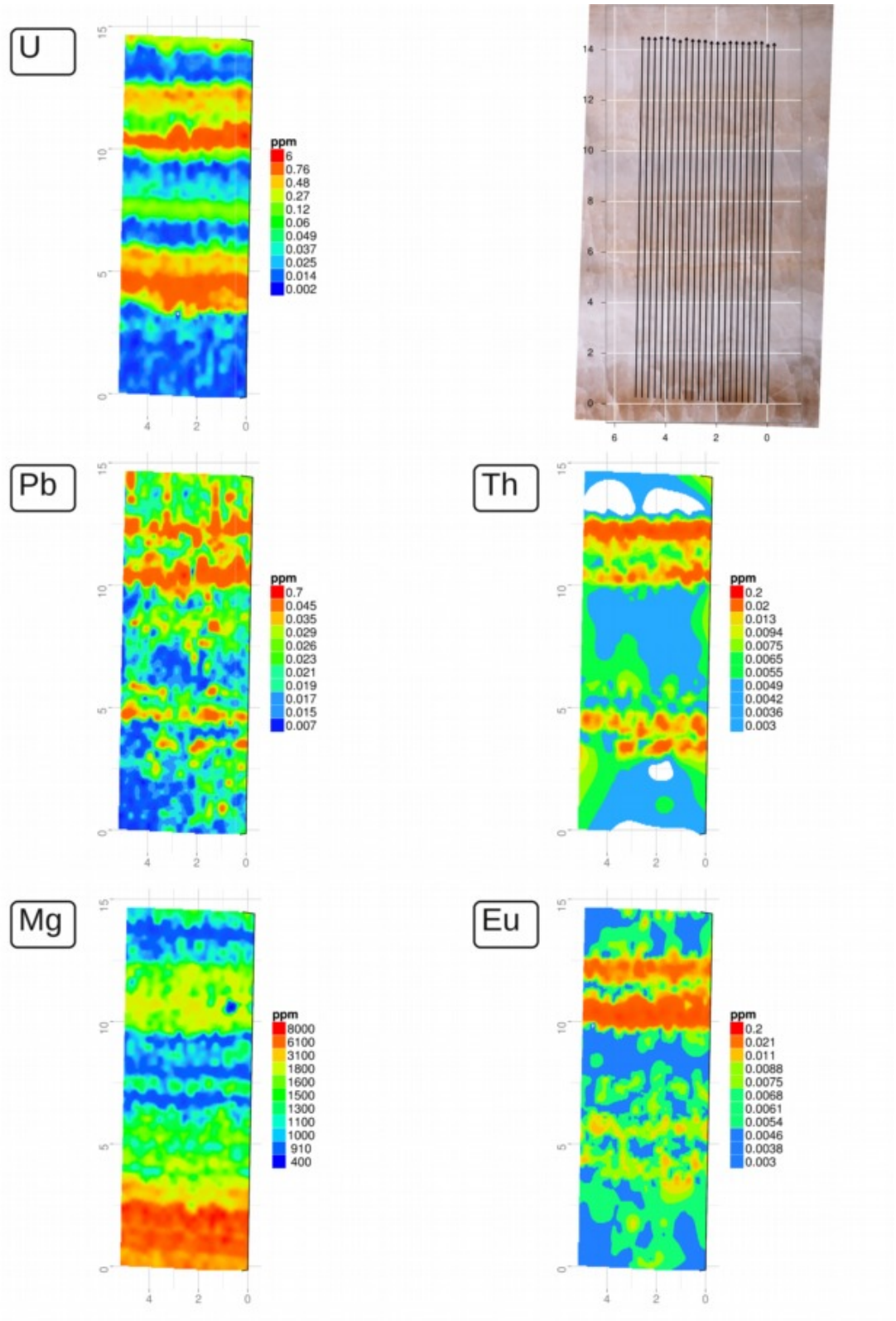

Fig. 73: Sample KMR-FOB28B_A, LA-ICPMS track overview and element maps.

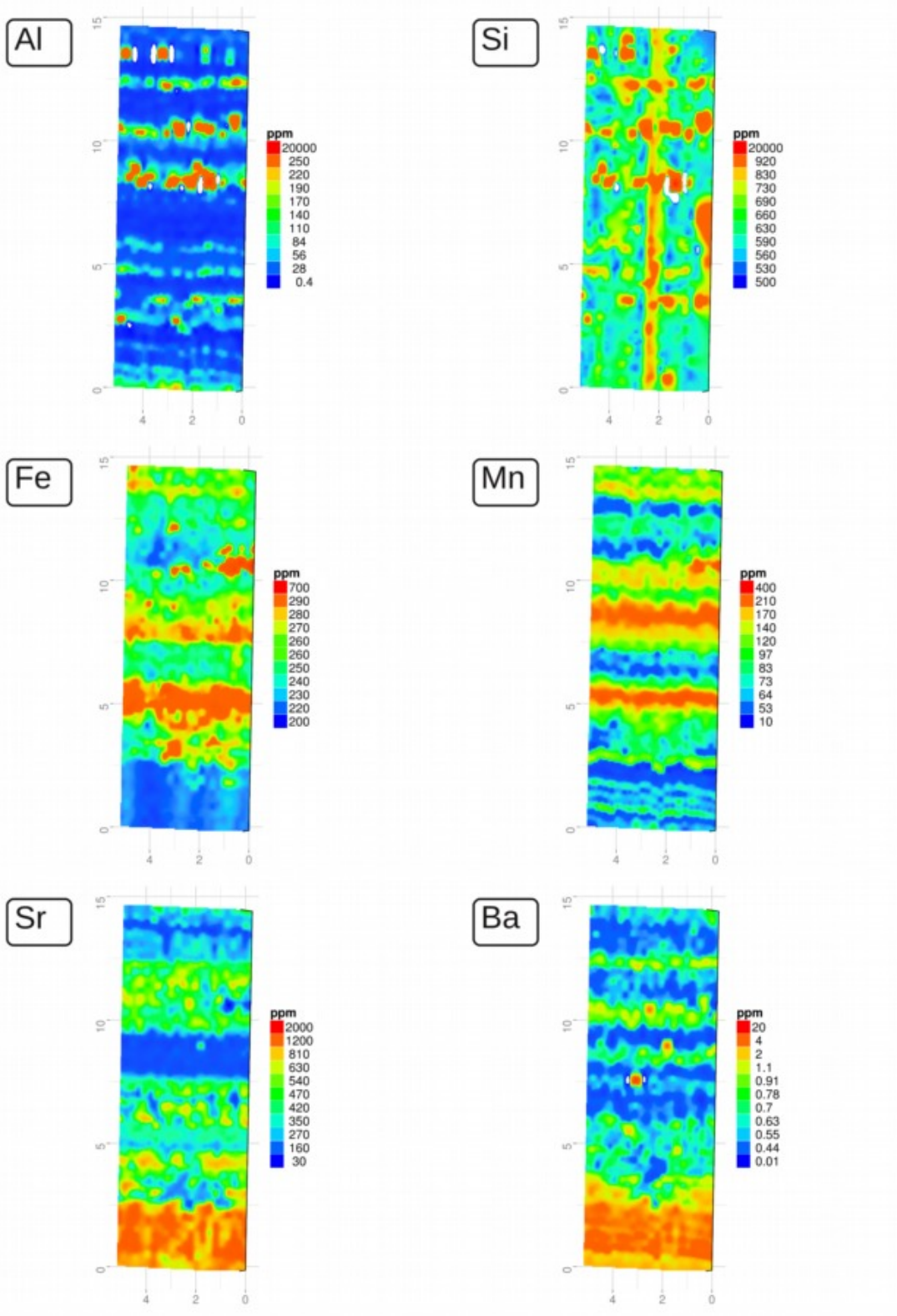

Fig. 74: Sample KMR-FOB28B_A, LA-ICPMS element maps.

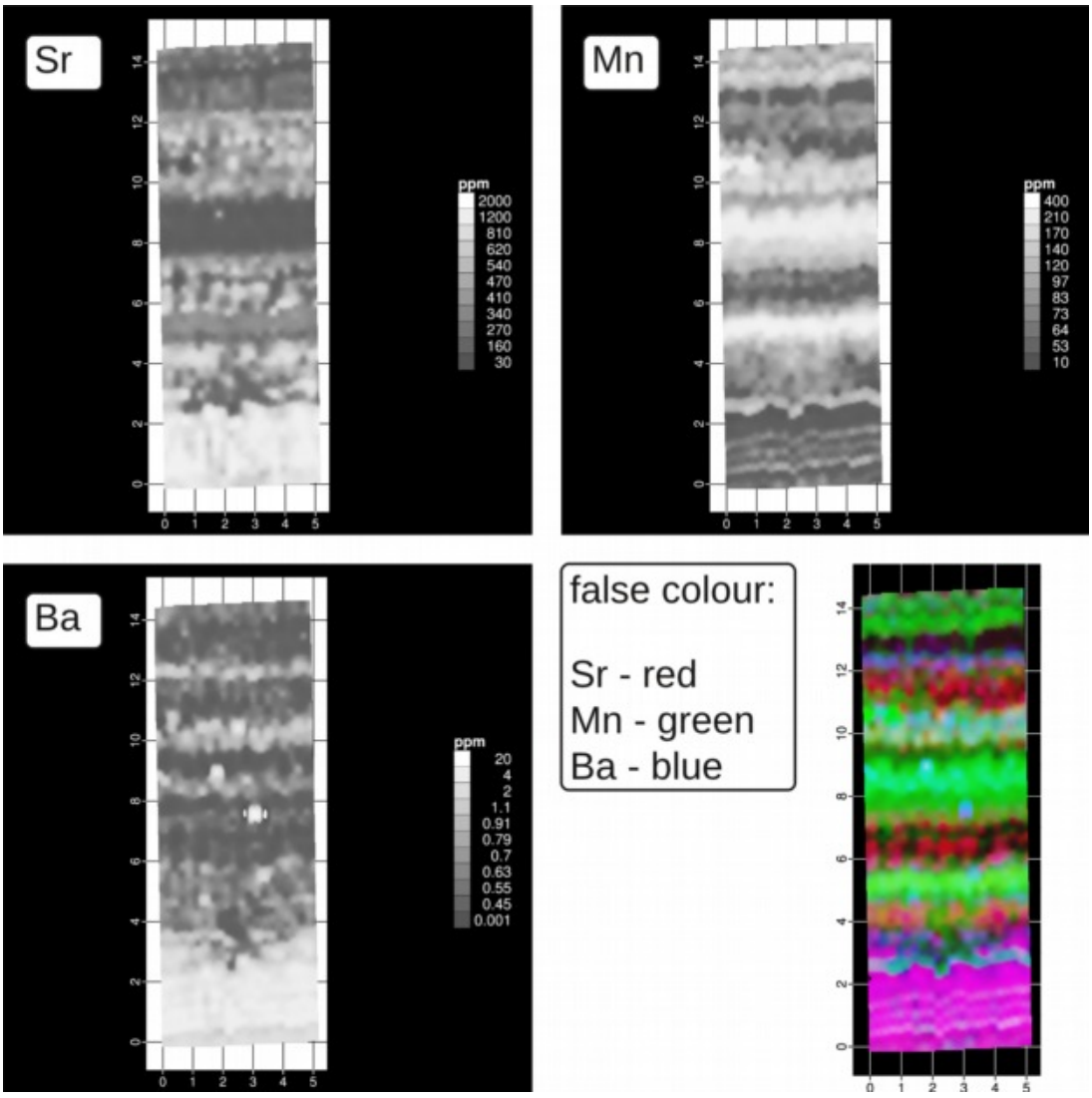

Fig. 75: False colour map composed of Sr, Mn and Ba concentration maps of sample KMR-FOB28B_A.
Differences in hue, not only in colour intensity, indicate changes in solution chemistry, not simple periodic growth from and dilution of one constant source.
Note reversed x-axis, compared to Fig. 73 & Fig. 74.

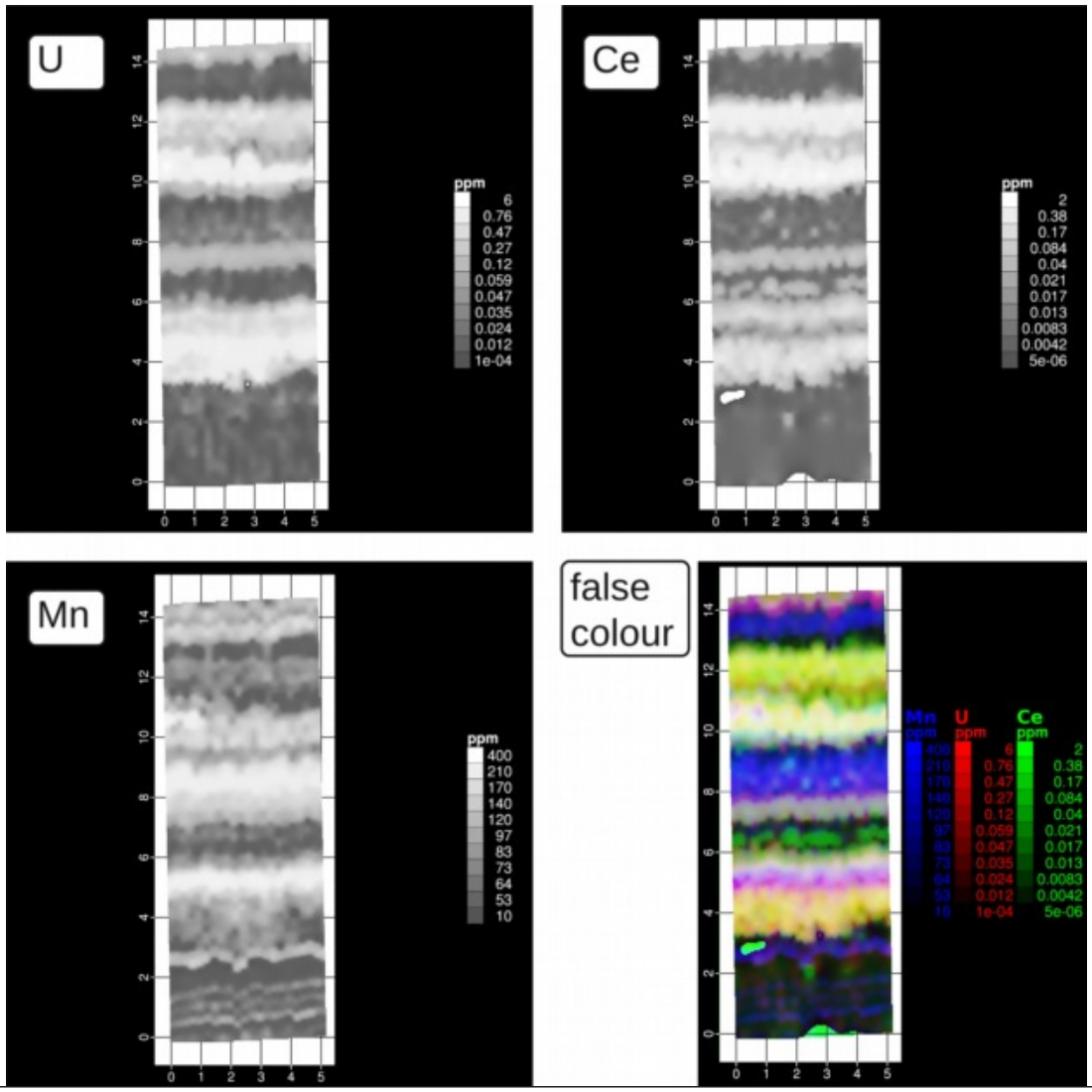

Fig. 76: False colour map composed of U, Ce and Mn concentration maps of sample KMR-FOB28B_A.
Differences in hue, not only in colour intensity, indicate changes in solution chemistry, not simple periodic growth from and dilution of one constant source.
Note reversed x-axis, compared to Fig. 73 & Fig. 74.

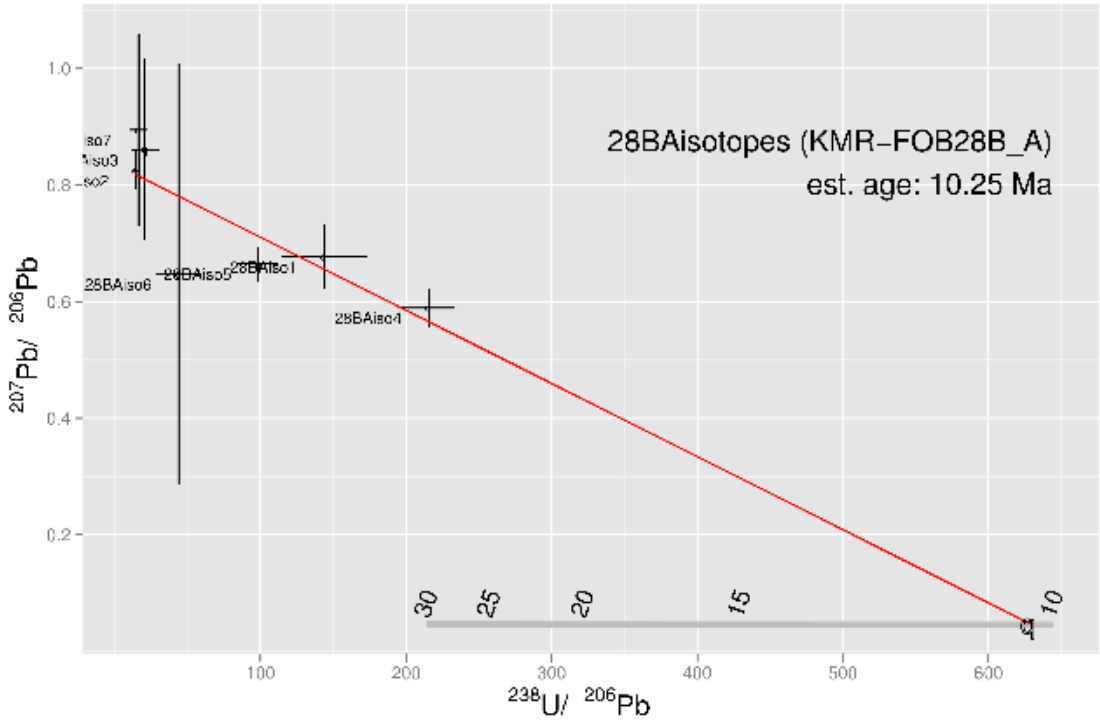

Fig. 77: In situ isotopic ratio measurements from sample KMR-FOB28B_A.
Disregarding point no. 6 with a very large error, the remaining data gives an average age of ~10 Ma, compared to 13.4 Ma determined by MC-ICPMS (see 6.4 Regional tectonic discussion and interpretation for interpretation).

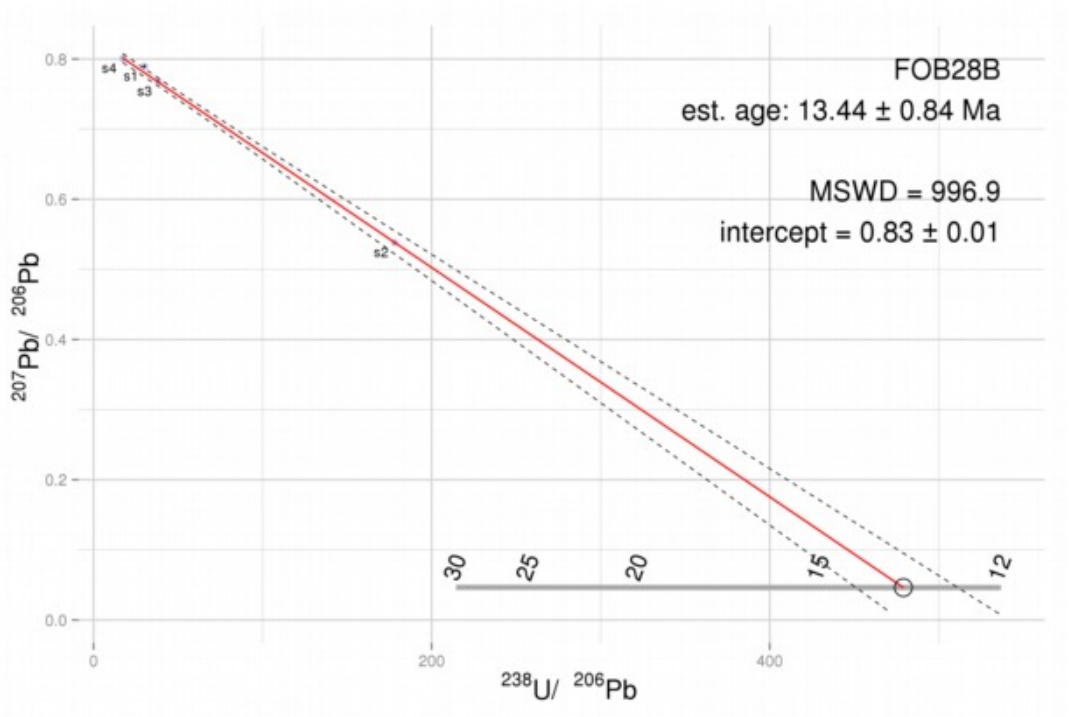

Fig. 78: MC-ICPMS isotopic ratio measurements from sample FOB28B.
Although a regression line calculated from only 4 points is inherently unreliable, the calculated age of 13.4 Ma is consistent with regional geological considerations (see chapter 6 Interpretation and Discussion.

5.4.3 Digne area

The area around Digne, Haute Provence, France, is characterised by structures associated with the Miocene-Pliocene (possibly ongoing) transport of the Digne Nappe onto the European foreland (see 2.2.2 Digne). Deformation on any scale from microscopic to km size can be observed in a wide range of sedimentary lithologies.

Samples were chosen to reflect this spectrum of possible settings of tectonic carbonates. However, of the 22 samples collected, only some specimens collected from one outcrop (KMR-DGN55 / D1W) proved suitable for dating, showing an elevated U/Pb ratio and variability.

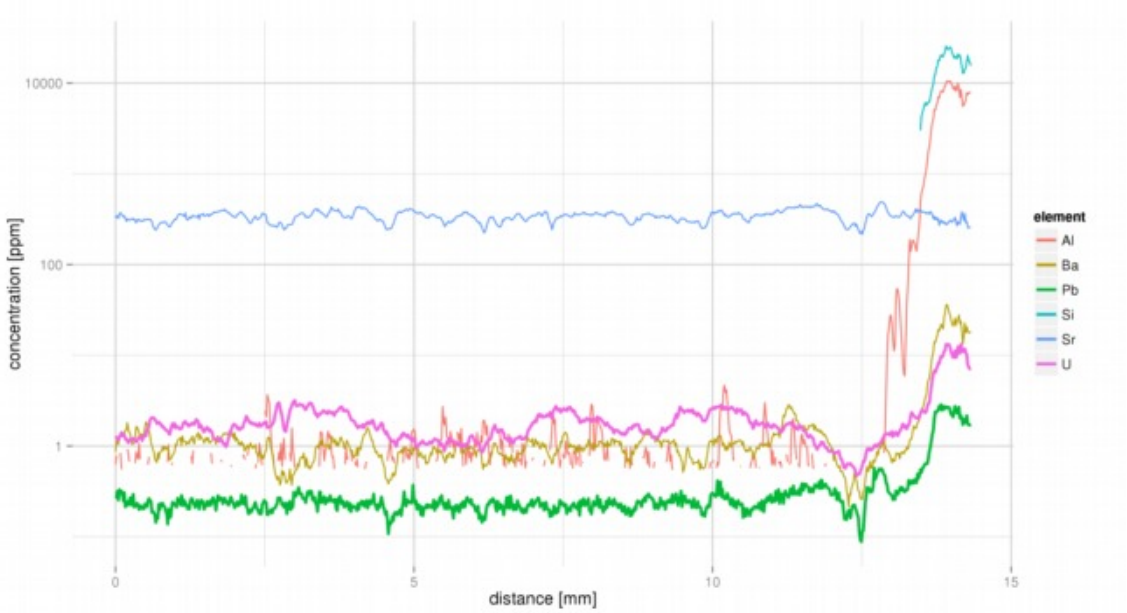

Fig. 79: Laser ablation track analysed on sample KMR-D1W_B.
The relatively pure calcite (x-position 0 - ~12 mm) is clearly distinguishable from the host rock (~13 mm to end of track). The latter shows much elevated Al values and is the only zone with Si concentrations greater than LoD, indicating different minerals than calcite (element concentrations in the host rock are not quantifiable, but qualitative information about host rock location can be gained). U concentrations in the calcite are ~10 × higher than Pb concentrations.

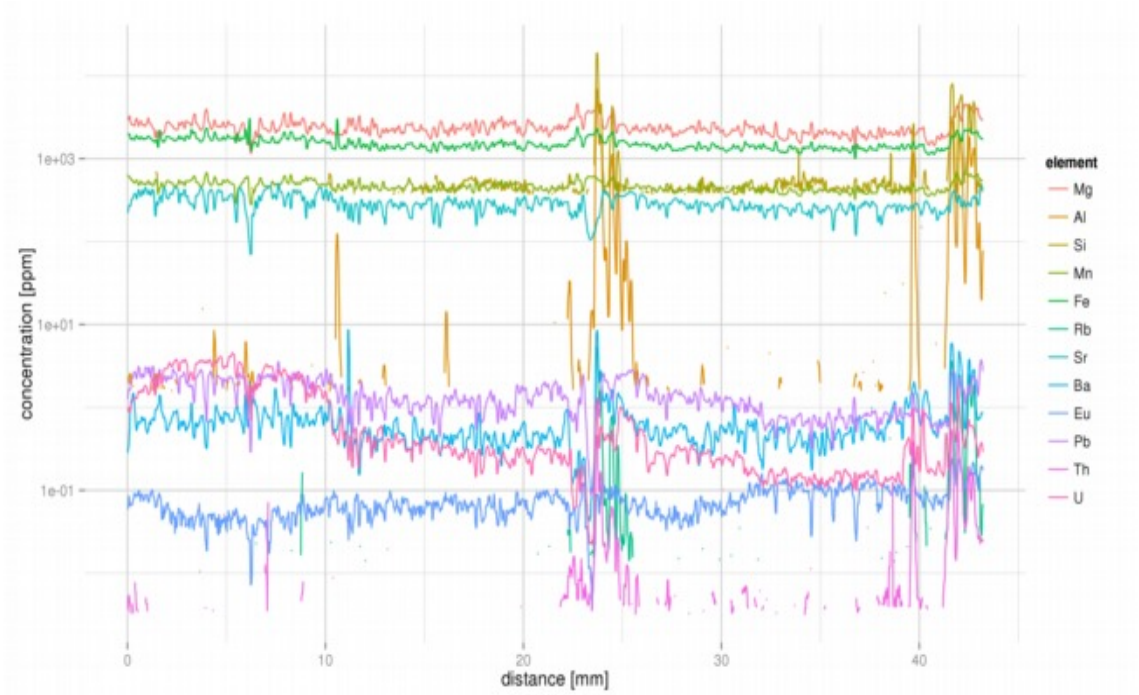

Fig. 80: Laser ablation track analysed on sample KMR-DGN55d_B.
Although not further analysed (Pb concentration > U for most of the sample), this illustrates organisation of a sample into zones of varying U/Pb ratios, which could be prepared as individual subsamples under more favourable conditions.

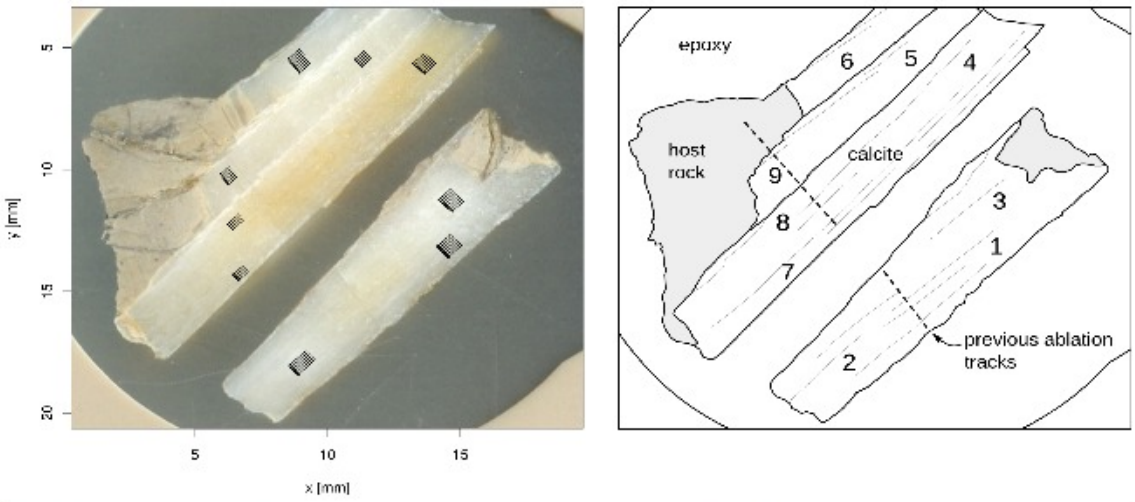

Fig. 81: Areas sampled for in situ isotopic analysis on sample D1W_A.
Left: Scan of sample surface before analysis, reprojected to sample stage coordinates by GeoStar, with individual tracks overlain. Right: Sketch of the sample (fragments embedded in epoxy resin), illustrating lithologies and sample "point" (averaged areas) numbers. See Fig. 82 for analysis results.

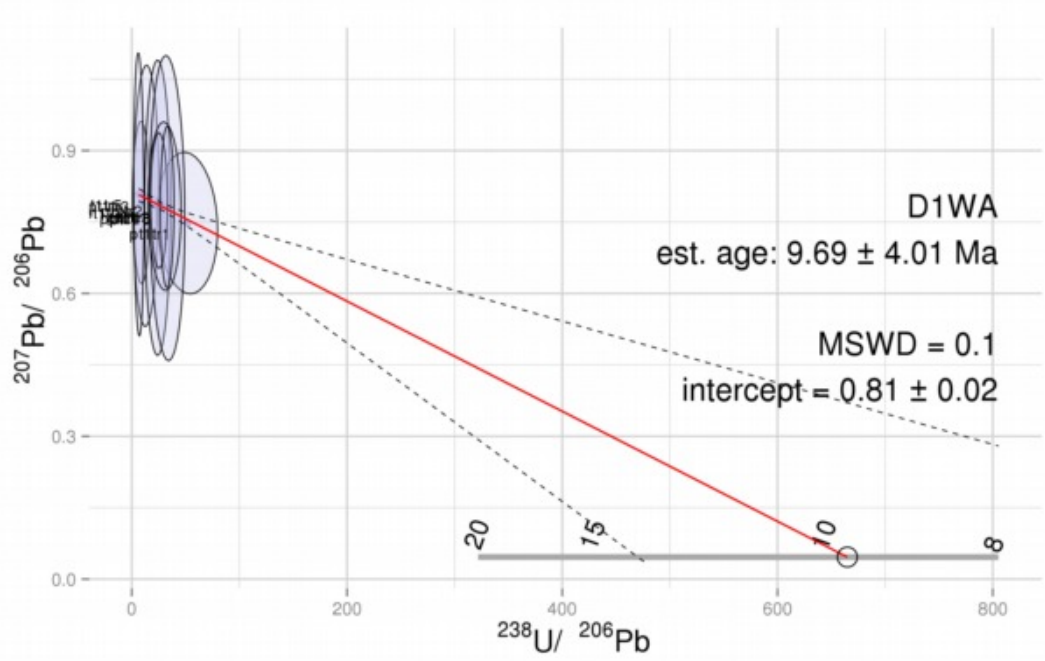

Fig. 82: Age estimate for in situ data of sample D1W_A.
Age estimate for the data from sampling points indicated in Fig. 81. The age of 9.7 ± 4.0 is imprecise due to large errors and small spread, but in good agreement with MC-ICPMS data obtained from samples from the same area and tectonic setting (samples DGN55c and DGN55e, see below).

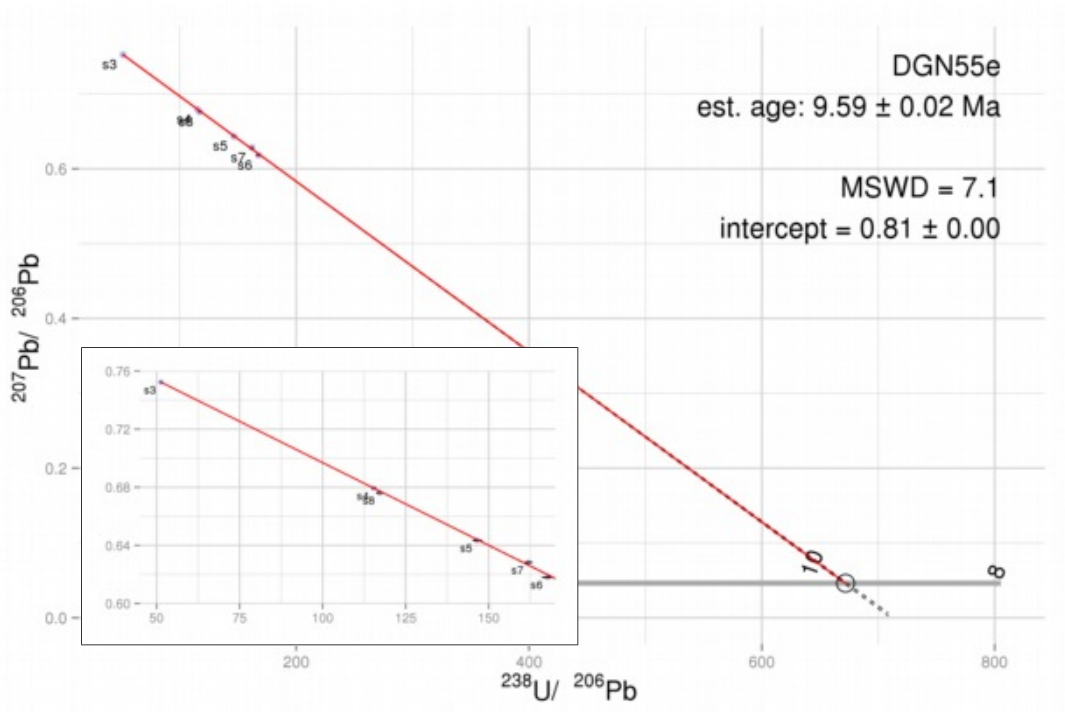

Fig. 83: MC-ICPMS isotopic ratio measurements from sample DGN55e.
One of the most precise ages in this study (see 5.4.6 Swiss Jura below for another example). Because error from reproducibility of SRM measurements was omitted in these plots, age uncertainty is likely underestimated.

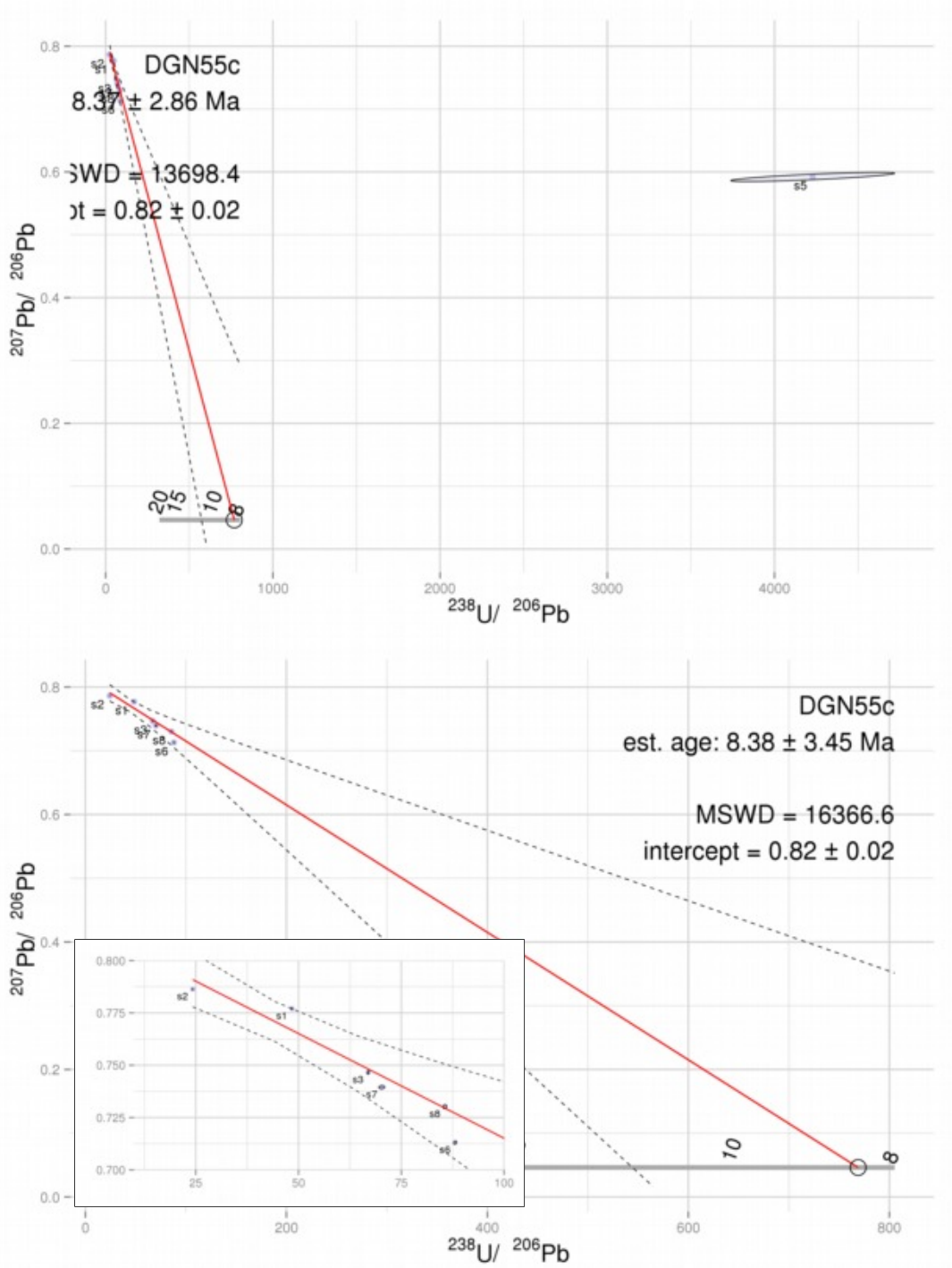

Fig. 84: MC-ICPMS isotopic ratio measurements from sample DGN55c.
Top: all data. Below: subsample s5 omitted, which was invalidated by a handling error during processing. Due to the large error in s5, the regression produces the same age estimate even in the first case.

5.4.4 Gosau basin

The Gosau Basin was the only sampling area yielding several convincing ages from outcrops within relative geographical proximity. The observed deformation ages represent different tectonic phases, clearly distinguishable in terms of age resolution and from structural considerations of the respective outcrops.

Some of the most interesting results were obtained from KMR-GOB21, different generations of slickenfibres yielded two different ages. A third age was found in tension gashes from KMR-GOB18. See 2.2.4 Gosau Basin, and 6.4 Regional tectonic discussion and interpretation for a compilation of how these ages fit into the established framework of deformation phases.

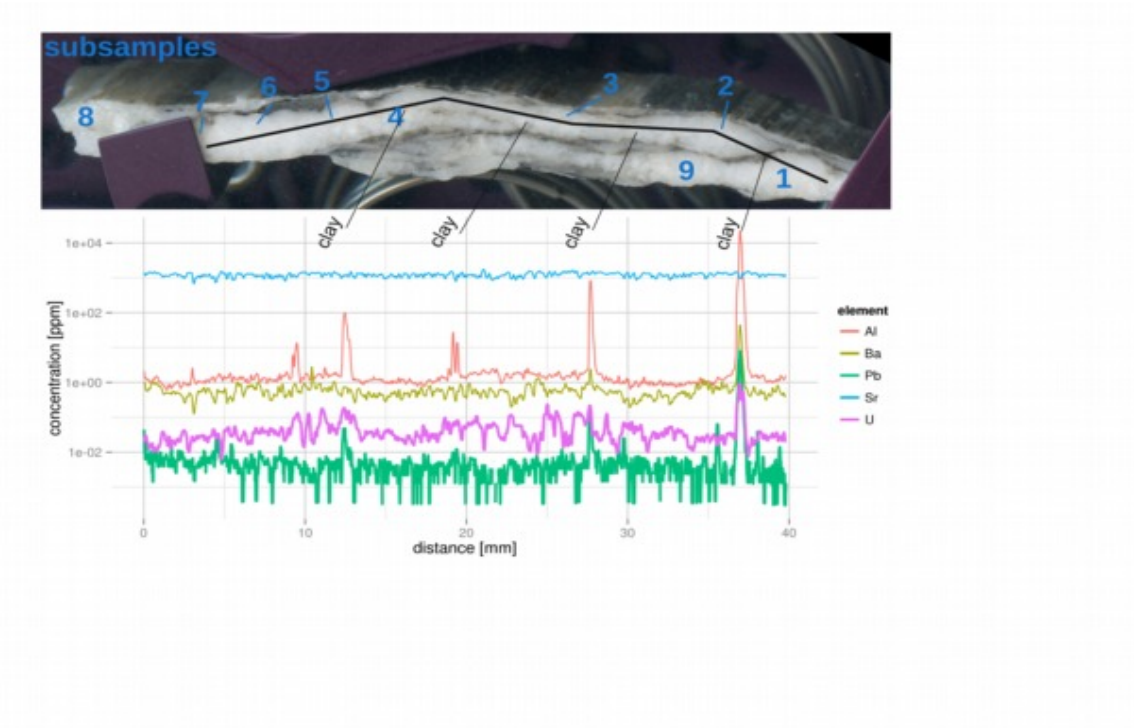

Fig. 85: Above: Sample KMR-GOB21B mounted for laser ablation, track overlain. Blue numbers indicate microsamples later prepared for chemical processing and MC-ICPMS analysis. Below: concentrations of selected elements along ablated track. High Al concentrations indicate presence of clay minerals; these zones were avoided in subsample preparation. Pb concentrations are at and below LoD (for laser ablation).

Sample KMR-GOB18B_A

Sample KMR-GOB18B_A is a thin tension gash from the Hochmoos formation of the Gosau Basin. Although only 3-5 mm thick, initial 1D scans revealed preferable U/Pb concentrations, but also impurities of host rock / clay minerals. To better understand element distributions and to assess the possibility to obtain microsamples from this sample, element maps were created (Fig. 86 & Fig. 87).

Variable U concentrations of up to ~2 ppm and low Pb concentrations of ≤ 0.8 ppm for the calcite portions indicate good suitability for further MC-ICPMS work, but the maps confirm indications from optical examination of clay or host rock seams between individual calcite packages. Individual homogeneous calcite domains would be less than 2 mm in thickness, which makes preparation with a hand-held cutting wheel challenging, and further mechanical abrasion of surfaces and subsequent acid etching for surface cleaning would leave unfavourably thin and platy samples.

In the maps, the host rock of the tension gash clearly shows as regions of qualitatively high concentrations in all maps (quantification not possible due to unknown Ca concentration). The dark seam in the centre of the mapped region also shows elevated Al and Si values, indicating clay / host rock. Thus, the elevated values in this region for U, Pb, Th and Ba are likely artefacts.

Of interest are well resolvable concentration differences between the domain above, and the domain below the clay seam, as seen in the Sr and Eu maps and less pronounced in the U map. Strontium concentration is about 400 ppm above, ~300 ppm below the seam. Europium concentration is ~200 to ~10 ppb, respectively, U concentrations are less homogeneous in the two domains, but vary from ~1.8 to ~0.9 ppm. Mn shows variations in the same regions, but of opposite trend (~300 – 340 ppm). It is conceivable, but could not be tested, that the different calcite packages represent separate tectonic phases, and the clay seam in between marks the actual event of reactivation.

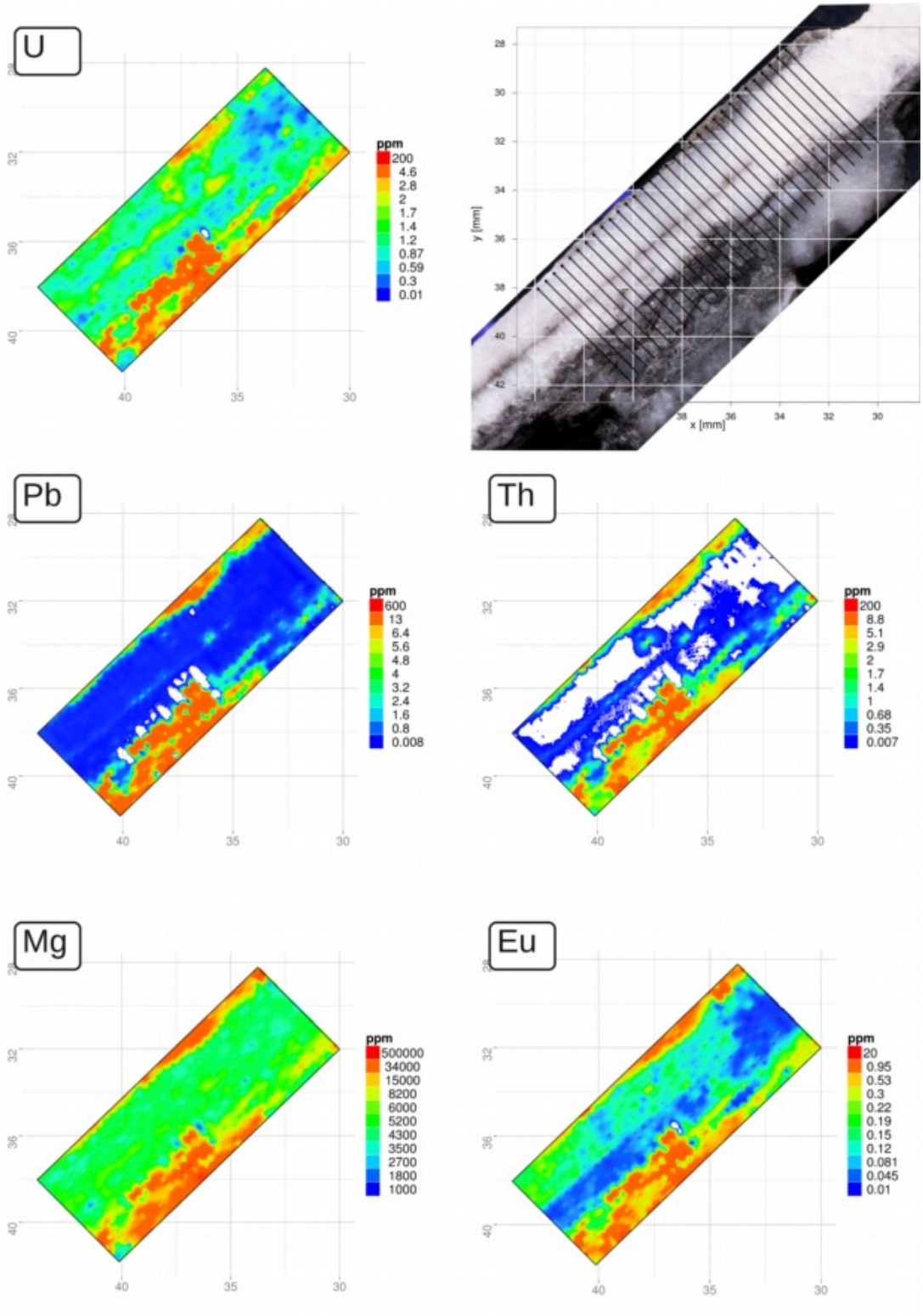

Fig. 86: Sample KMR-GOB18B_A, LA-ICPMS track overview and element maps.

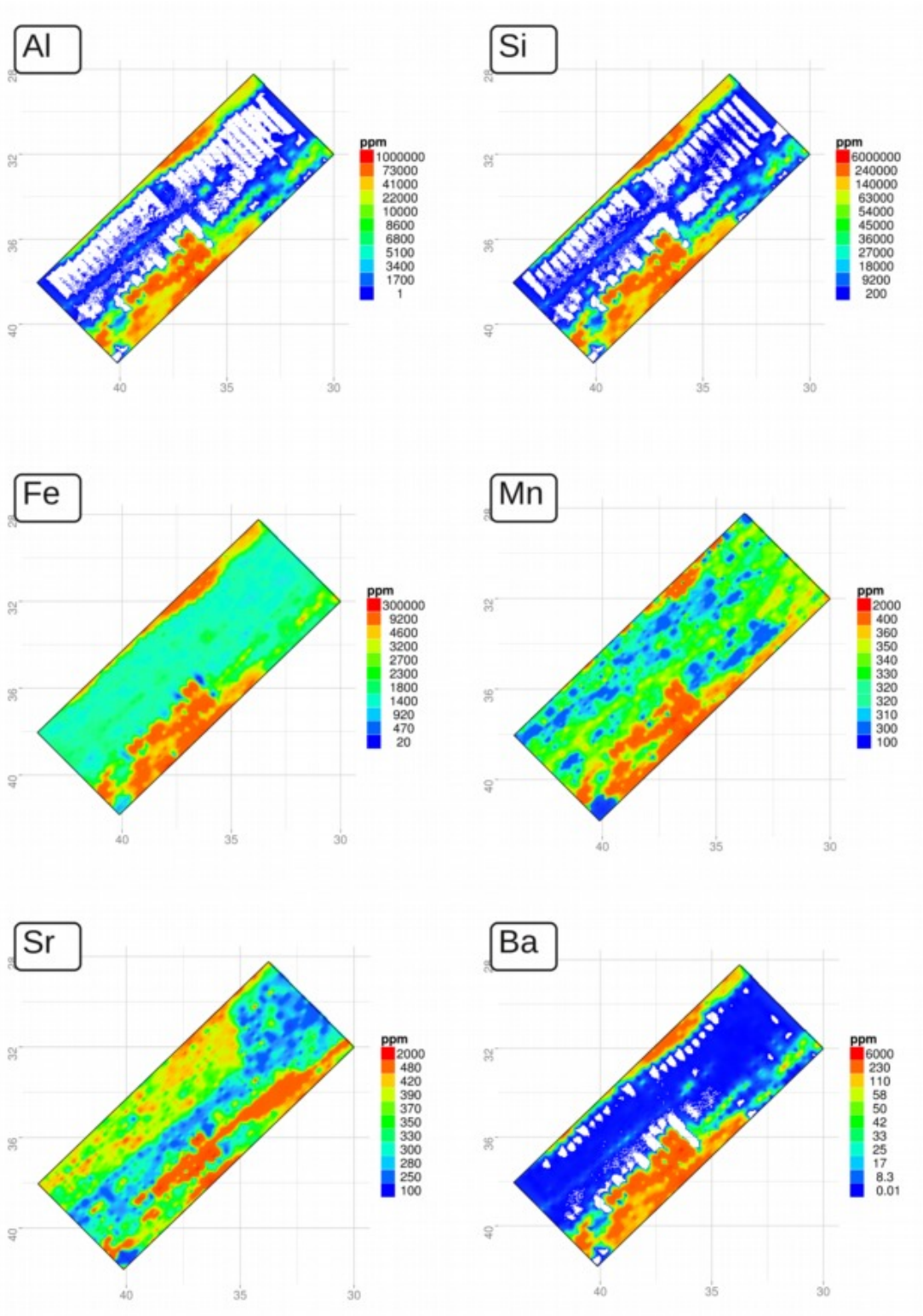

Fig. 87: Sample KMR-GOB18B_A, LA-ICPMS element maps.

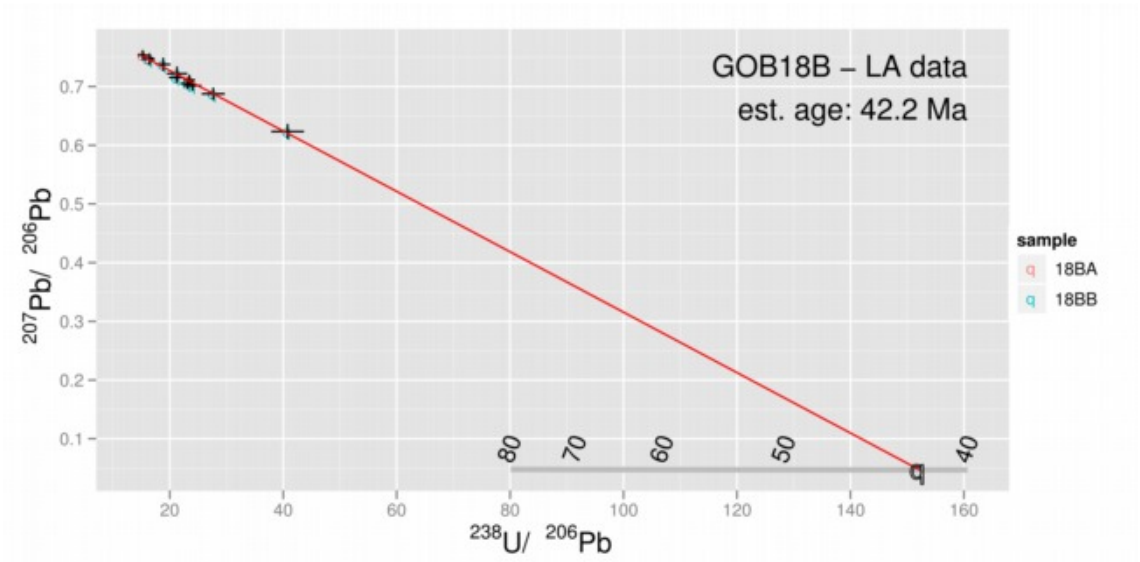

Fig. 88: Isotopic ages measured in situ by laser ablation on samples KMR-GOB18B_A and B. The pooled data gives an age estimate of ~42 Ma (M-Eocene), an age clearly distinct from ages for KMR-GOB21 (see below) from the same area (Gosau basin). See 6.4 Regional tectonic discussion and interpretation for interpretation.

Sample KMR-GOB21B_A

Sample KMR-GOB21B_A comes from an outcrop of the Upper Santonian Hochmoos formation in the central Gosau Basin, which exhibits clear indications of multiphase deformation. Slickenfibres of different orientation overprint each other on the same fault planes (see 2.2.4 Gosau Basin for outcrop photos and structural data).

In the sample maps (Fig. 89 & Fig. 90), several packages of calcite are distinguishable, with intercalated seams of clay minerals, probably ground-up host rock or fault gauge. Whereas optically, two packages with a crack/clay seam in between are visible, the trace element maps, especially U, reveal a more complex picture: both calcite packages are further structured by narrow high-U zones, likely tracing a further subdivision of the slickenfibres.

The calcite to the left and to the right of the prominent seam show very different element concentrations: the left is lower in U, Sr, Fe, and higher in Mn. The right package shows higher concentrations in said elements (~0.3 ppm vs. few 10s of ppb U; ~1200 vs. ~400 ppm Sr; ~560 vs. ~200 ppm Fe; but ~160 vs. ~230 ppm Mn), and a thin and discrete, not visually obvious, high-U zone following the main trend of seams.

High Al, Si and Fe values in the prominent clay seam indicate clay minerals, as was expected from optical examination, apparently high values for other elements can thus not be quantified.

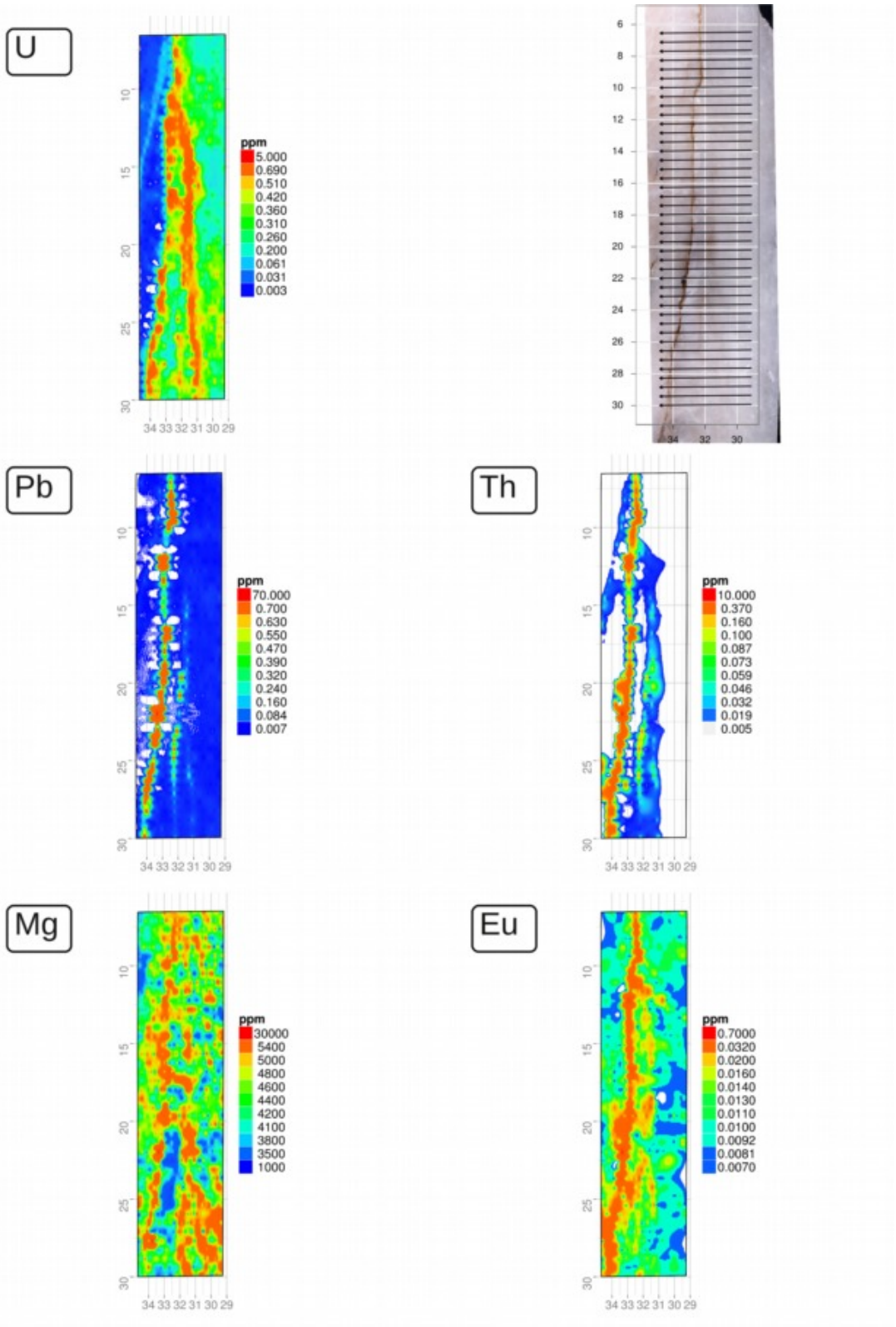

Fig. 89: Sample KMR-GOB21B_A, LA-ICPMS track overview and element maps.

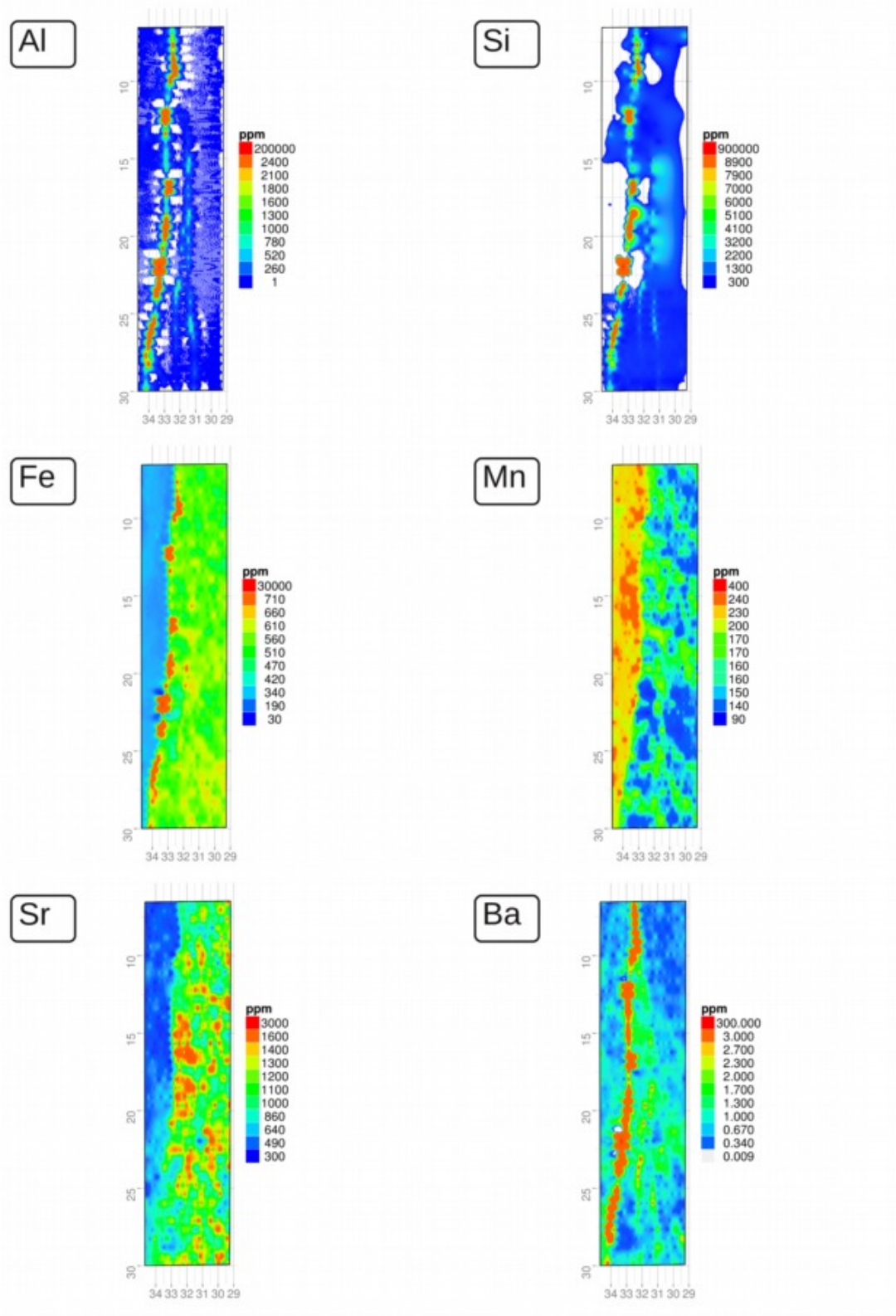

Fig. 90: Sample KMR-GOB21B_A, LA-ICPMS element maps.

Outcrop GOB21 yielded calcite slickenfibres of considerable size and at least two distinct deformation directions. The largest sampled slickenfibre (Fig. 92) was microsampled at the opposite ends for MC-ICPMS analysis, in an attempt to resolve minimum deformation duration. Due to scatter of the data points, no significantly different ages were obtained.

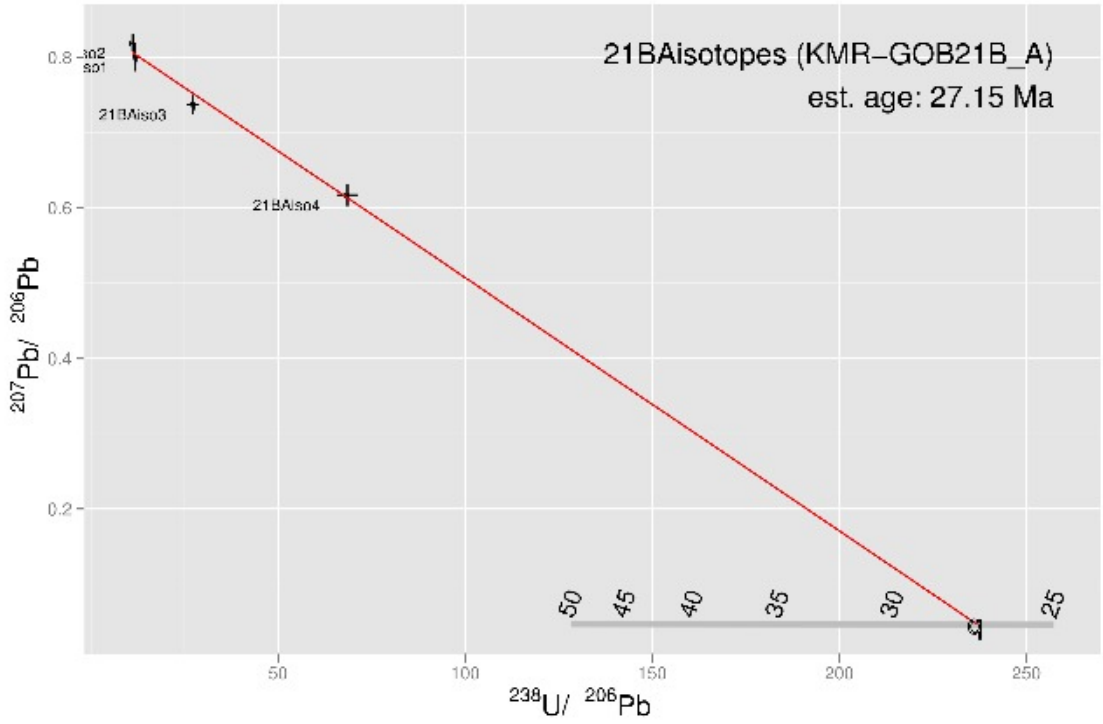

Fig. 91: Isotopic ages measured in situ by laser ablation on sample KMR-GOB21B_A. Although only four data points were obtained, the estimated age of ~27 Ma lies within the age range obtained by MC-ICPMS (see Fig. 92ff)

Fig. 92: Sample KMR-GOB21.
Red and yellow are locations of micro-sampling for MC-ICPMS analysis of the opposite ends of the slickenfibre (see Fig. 93).
Blue indicates location of laser ablation (in situ) analysis (Fig. 91). Geological scatter amongst subsamples was too large to clearly define the (minimal) deformation interval. However, the pooled average age of ~22 Ma (Aquitanian) fits local deformation history for this locality (see following figures and 6.4 Regional tectonic discussion and interpretation).

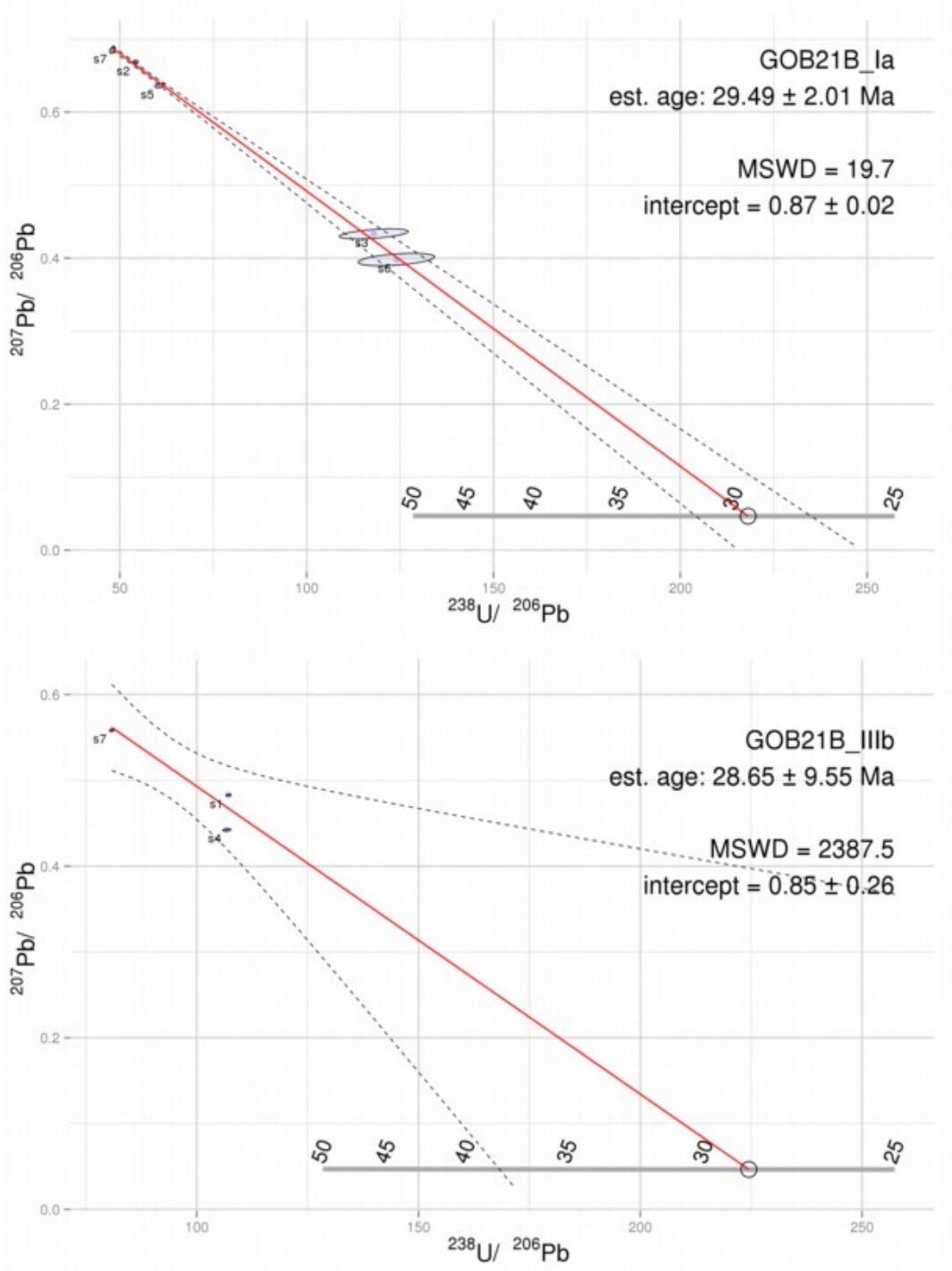

Fig. 93: MC-ICPMS isotopic ratio measurements from sample GOB21B.
Two opposite ends (Ia, IIIb) of a long slickenfibre were analysed. For GOB21B_IIIb, two sub-samples marked as handling errors during processing were omitted, the resulting regression is based on only three data points and thus unreliable.

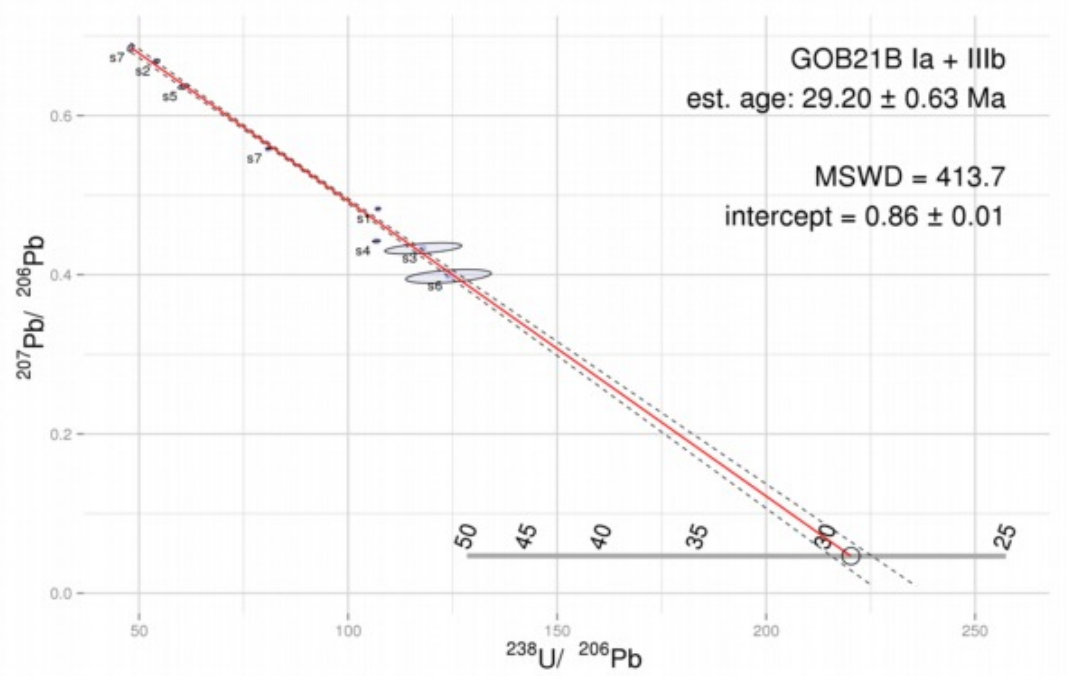

Fig. 94: MC-ICPMS isotopic ratio measurements from sample GOB21B.
Combined data plot of GOB21B_Ia and GOB21B_IIIb. Due to larger number of data points, age error decreases despite the inclusion of points with large error.

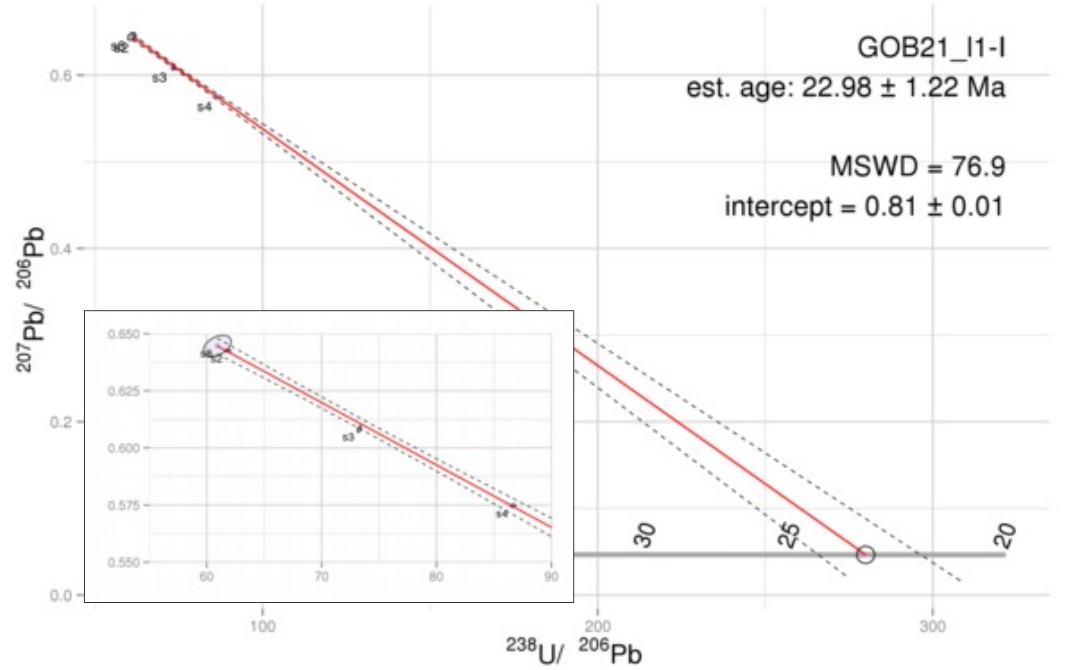

Fig. 95: MC-ICPMS isotopic ratio measurements from sample GOB21B_l1.
Isotopic data from a kinematically different slickenfibre than the main deformation observed in this outcrop. Bottom-left: Enlarged view of data.

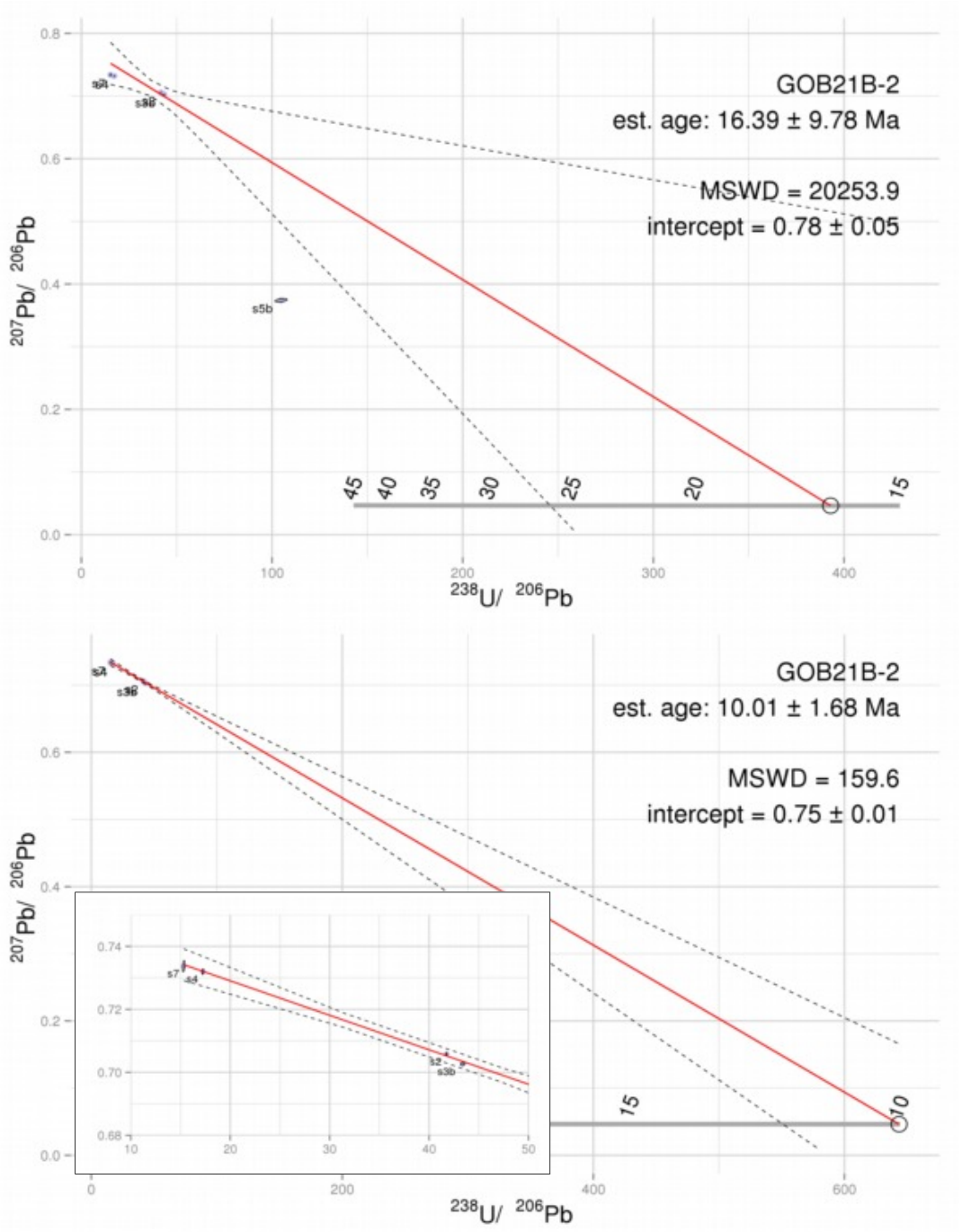

Fig. 96: MC-ICPMS isotopic ratio measurements from sample GOB21B.
Rerun of an analysis failed earlier (see Error: Reference source not found). This analysis might have subsampled a different fibre package and thus represent another deformation phase (this was not recognised during sample preparation), yet small spread amongst just 4 data points puts a large uncertainty on this interpretation. This analysis was not treated as indication for a separate deformation phase. Top: all acquired data. Below: excluding subsample s5b, which was marked with a handling error; bottom-left: enlarged view of data.

Sample KMR-GOB23B_B

KMR-GOB23B_B is a sample of a Miocene (pers. comm. M. Wagreich, 2011) tension gash in Rhaethian biogenic limestone from the margin of the Gosau basin. Optically, the tension gash seems homogeneous, except for some discolouration (clay minerals) between calcite crystals in the central zone. However, the element distribution maps show some zonation, towards the fracture walls occurs a zone of Mn, Fe, Mg and Eu concentrations 2-3 × higher than in the centre. This zone seems not to differ in concentration for other elements.

The U map, and less pronounced the Ba and Sr maps, trace a younger fracture cutting both host rock and tension gash diagonally from ~38.5 mm on the x-axis at the top to ~36 mm at the bottom, which is not immediately obvious in the photograph. This demonstrates the strength of 2D element mapping for sample characterisation.

The apparent Si concentration difference between the left and the right of the tension gash is probably an artefact of data acquisition.

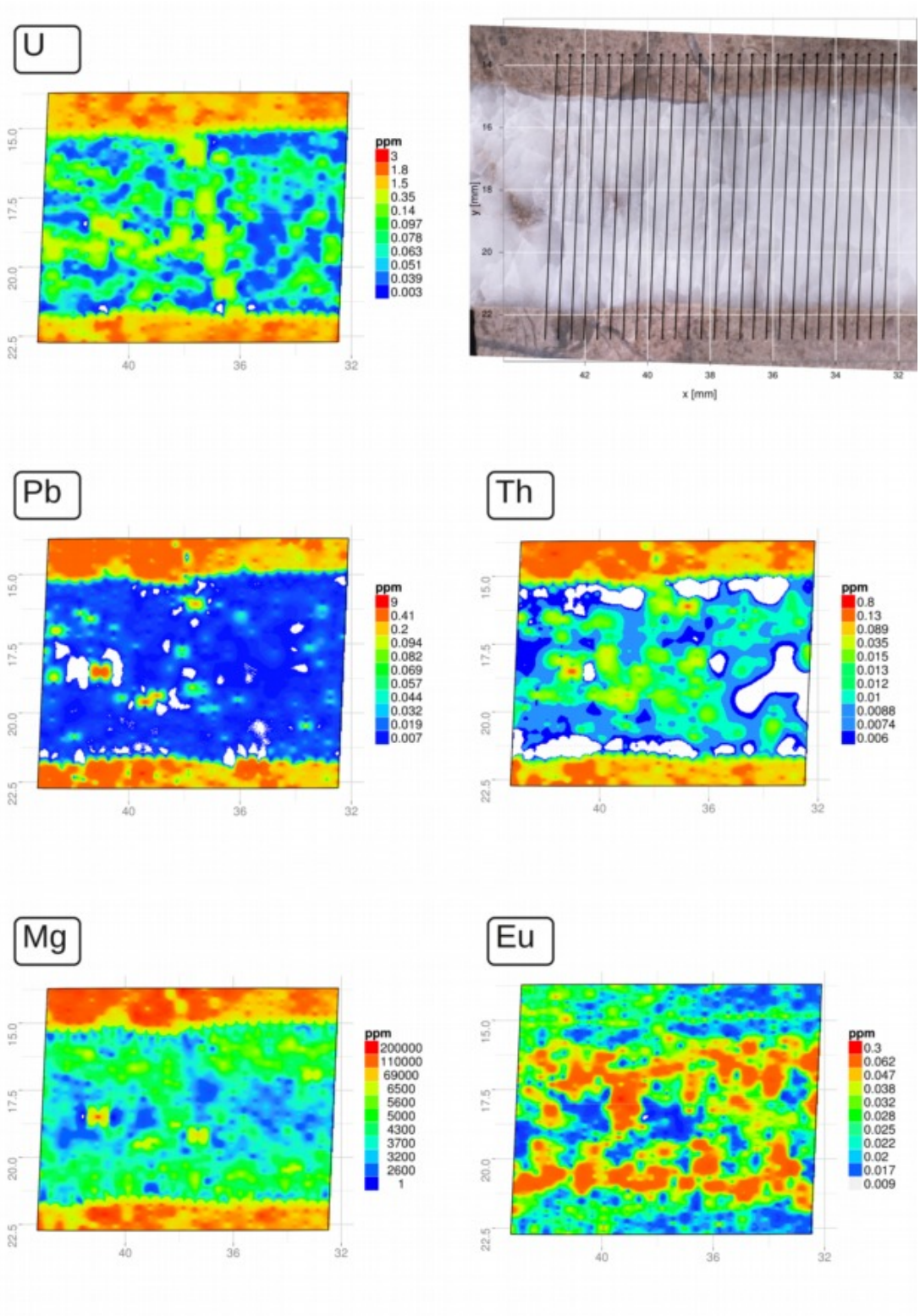

Fig. 97: Sample KMR-GOB23B_B, LA-ICPMS track overview and element maps.

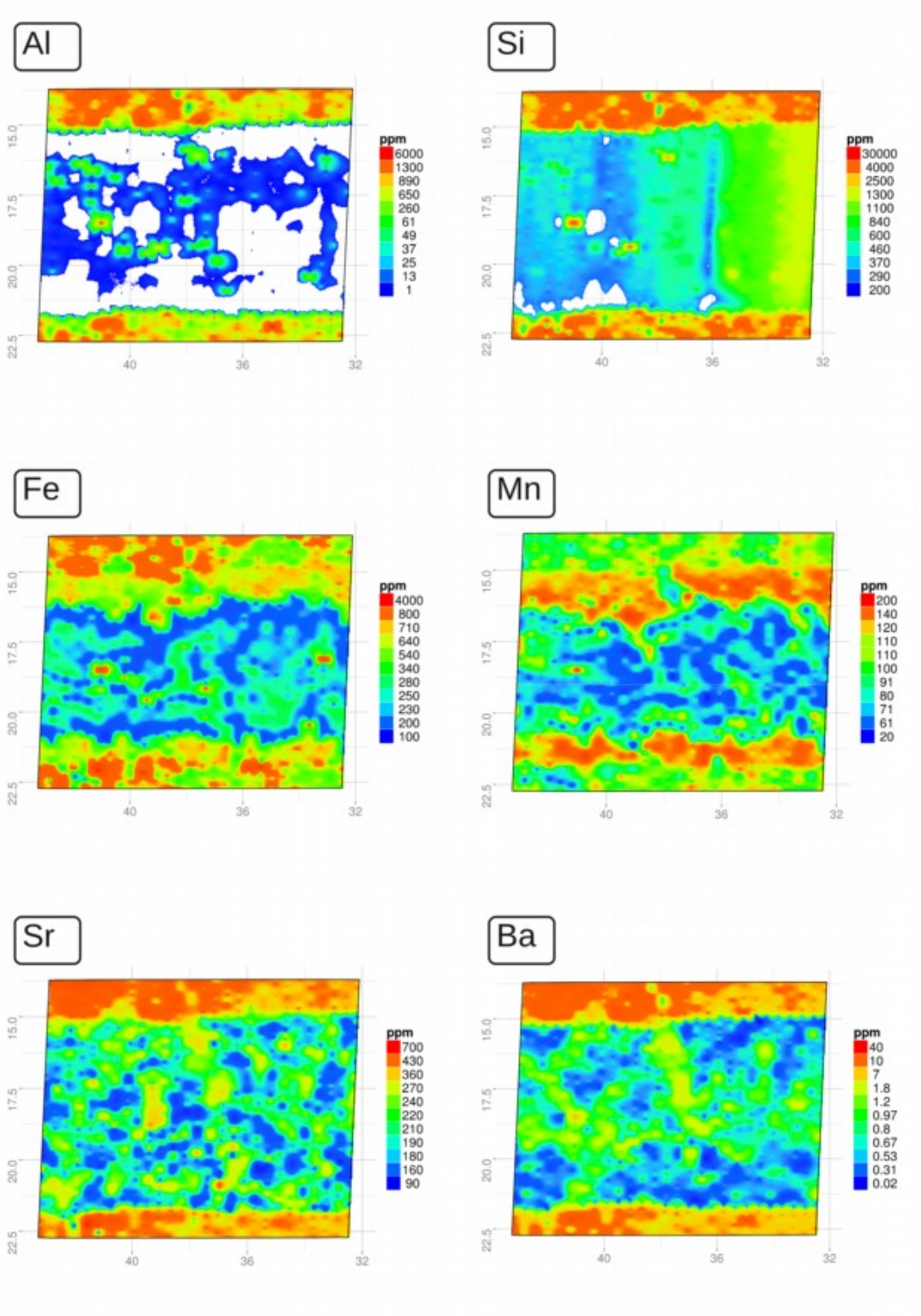

Fig. 98: Sample KMR-GOB23B_B, LA-ICPMS element maps.

5.4.5 Lower Inn valley

Most samples from this area are from marly to sandy sediments with varying limestone content, of the Intramontane Molasse of the Inn Valley, Austria (Ortner, 2003b). The succession is Late Eocene to Oligocene in age, see 2.2.6 Lower Inn Valley. Initial formation of the depositional space was due to horst-and-graben-like tectonics, and the area has since been deformed in conjunction with movements on the Inntal Fault Zone. Sample KB2 (below) is not strictly of the Molasse sediments, but a local scarp breccia.

Sample KB2

This sample of a fault scarp breccia from the Lower Inn Valley was contributed by Dr. Hugo Ortner, University of Innsbruck, Austria. The sample is referenced as "Kalkbruch 2" in Ortner, 2003b. It exhibits several different generations of calcite cements filling the voids between components of the breccia. Based on petrographic microscopy, trace element concentrations and O and C isotopic composition, Ortner, 2003b, have distinguished cement generations derived from distinctly different fluid sources, the earlier cements likely being marine in origin, the later showing meteoric signature. These cement generations are clearly seen optically and in the 2D element concentration maps, but the larger range of elements analysed (as compared to Ortner, 2003b), allow for a further subdivision of growth phases based on trace element concentrations (see Fig. 99 and Fig. 100):

At the top left of the mapped area, a host rock component is distinguishable in most maps. The host rock itself is inhomogeneous, in the mapped area a carbonate component (dark grey on the photo) is contained in a beige, marly carbonate matrix. The marly matrix shows high values in Al, Si, Fe, Pb and Th, as expected for clay minerals, but lower Sr, Mg and Mn values compared to the carbonate fragment. Since internal standardisation on Ca is only valid for calcite, the concentration data for the marl must be considered with caution, and only qualitative observations can be made for the host rock.

The space between components is filled with several generations of calcite cement. Optically, an early, yellowish-beige cement is divided by a sharp grey band from the white, coarse-grained calcite of the youngest generation ("cement 1 and 2" of Ortner, 2003b). The element maps reveal several layers within the early yellowish cement, from the top right (oldest) towards the lower left (towards the grey layer):

The first layer shows low Ba and elevated Mn values (~3 and ~90 ppm, respectively). Sr and Mg are high (~600 and ~5000 ppm, respectively), U and Eu low at or below LOD. Maintaining the values for Sr, Mg, U and Eu, the next layer, optically distinguishable by a slightly darker colour, shows half the Mn and up to 7 × higher Ba values of ~50 and up to ~20 ppm, respectively. In the successive, slightly lighter coloured layer, U and Eu rise to ~250 and ~25 ppb, respectively, Mg, Ba and Sr drop, and Mn shows the highest concentrations of ~250 ppm. This very distinct high-Mn layer is clearly traceable along the right and the top of the element map, in straight lines meeting at a sharp angle. There is indication of a narrow zone of low U, low Eu (LOD), with reduced Mn and slightly elevated Ba and Sr values, adjacent to the distinct grey band following next.

The grey layer, clearly visible optically, shows high Al, Si and Fe values, indicating influx of clay minerals. Thus, the seemingly high U, Pb, Th and Eu values can not be considered quantitatively.

The central, white, blocky cement ("cement 2" of Ortner, 2003b) consists mainly of very pure calcite (low Mg, Mn, Sr, Ba) with ~0.2 – 0.4 ppm U and ~10 times less Pb. Mn and Sr values are initially elevated, and the Ba map, and less pronounced, the Sr map, might indicate a younger curved fracture running from top to bottom at ~30 – 31 mm on the x-axis (possibly "cement 3" of Ortner, 2003b).

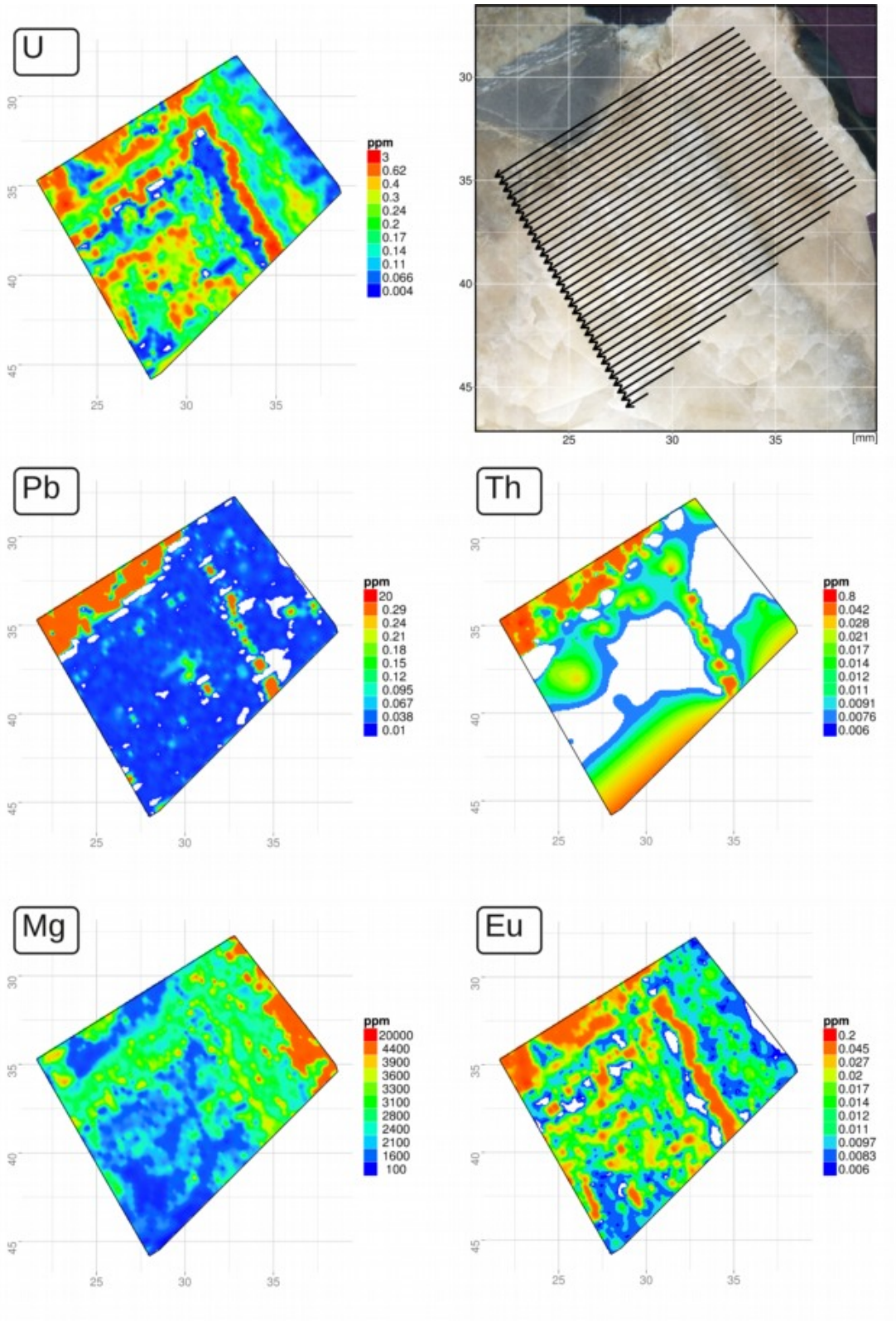

Fig. 99: Sample KB2, LA-ICPMS track overview and element maps.

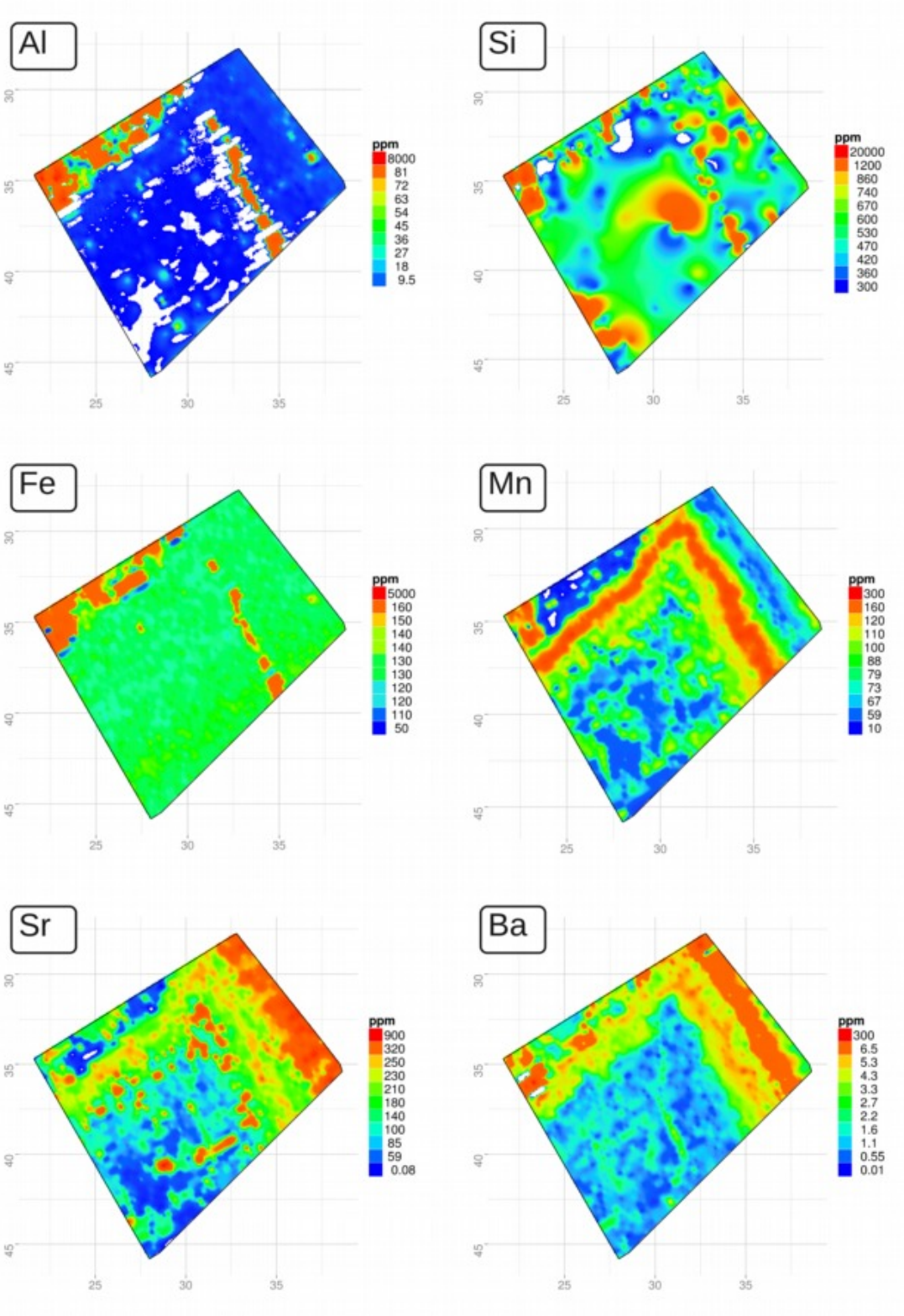

Fig. 100: Sample KB2, LA-ICPMS element maps.

Sample KB2 did not yield a good age fit, due to very low concentrations of Pb and U causing large errors. These data are presented here only as an example of less suitable data.

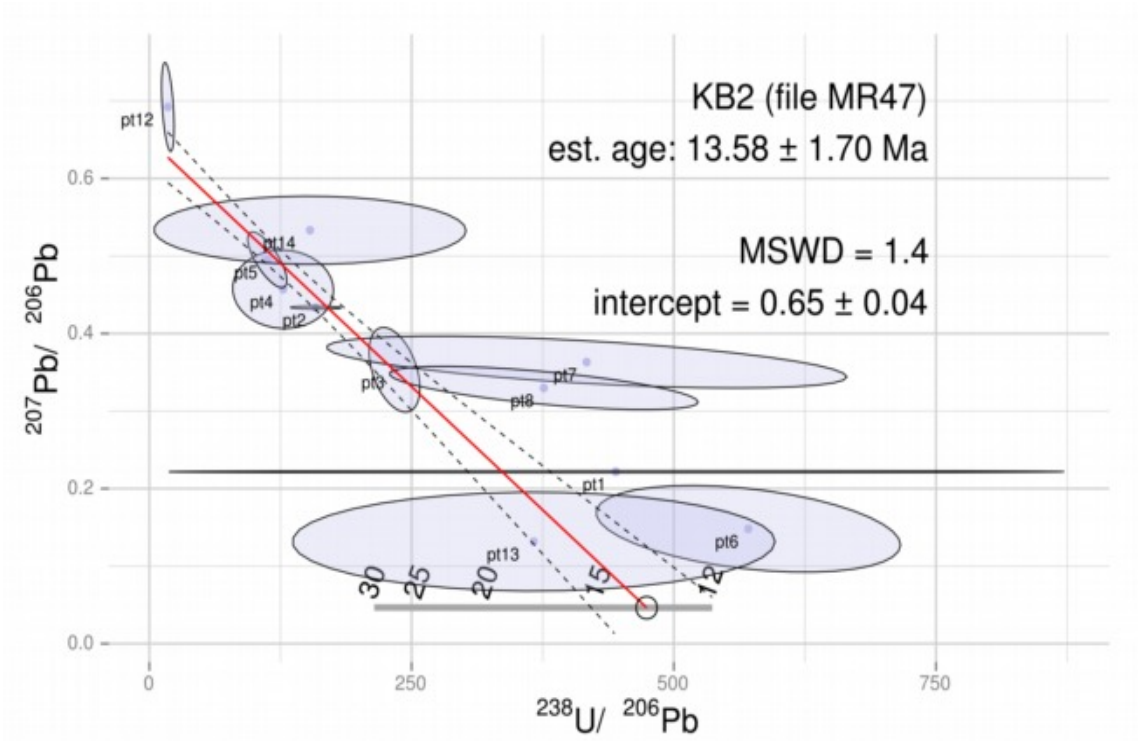

Fig. 101: Isotopic ratio data obtained in situ by laser ablation on sample KB2.
Low concentrations result in very large errors. Pt 9, 10 and 11 yielded negative x-values, and pt 15 and 16 are outliers with error ellipses stretching beyond the extends of the presented plot. These points were omitted in plotting and calculation of the regression line.

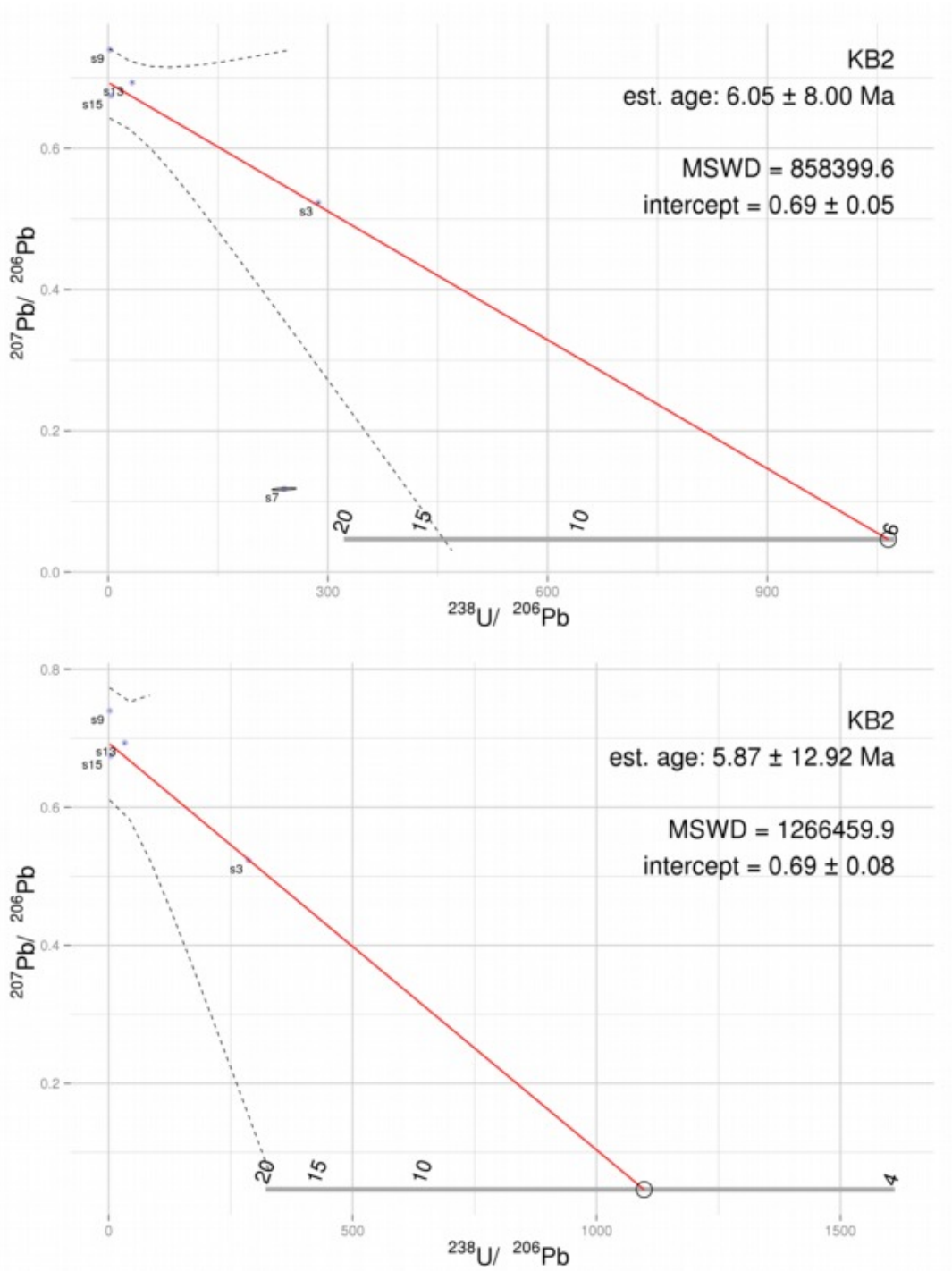

Fig. 102: MC-ICPMS isotopic ratio measurements from sample KB2 (Lower Inn Valley). Top: including all subsamples. Below: excluding subsample s7, which was marked as handling error during processing. Due to relatively much larger error on s7, the age calculated from the regression line does not shift significantly, but error increases.

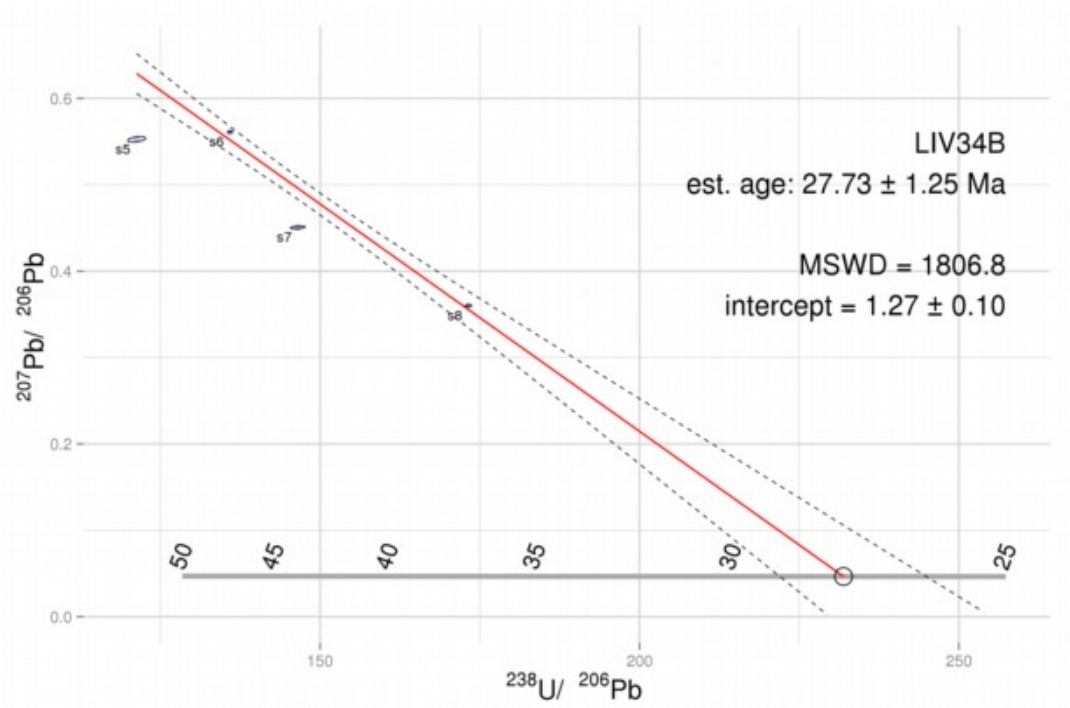

Fig. 103: MC-ICPMS isotopic ratio measurements from sample LIV34B.
Another sample from the Lower Inntal Valley. The beige calcite contained impurities (bituminous fluid inclusions, pers. comm. H. Ortner, 2011), which impaired chemical sample preparation, resulting in larger errors on the individual MC-ICPMS analyses. However, these errors are far outweighed by the scatter amongst data points. The calculated age fits deformation shortly after, or syndepositional to the Oligocene host rock (see 6.4 Regional tectonic discussion and interpretation).

5.4.6 Swiss Jura

Samples from fault planes on the edge of the Swiss Jura mountains were provided by Dr. H. Madritsch (NAGRA, Switzerland). One sample (MHH01) yielded a good data set resulting in a calculated age of 9.05 ± 0.94 Ma (see Fig. 104). Dating by MC-ICPMS was attempted on two additional samples (MHH02 and MHH06), yet the resulting data did not spread enough to allow calculation of a reliable regression line (Fig. 105).

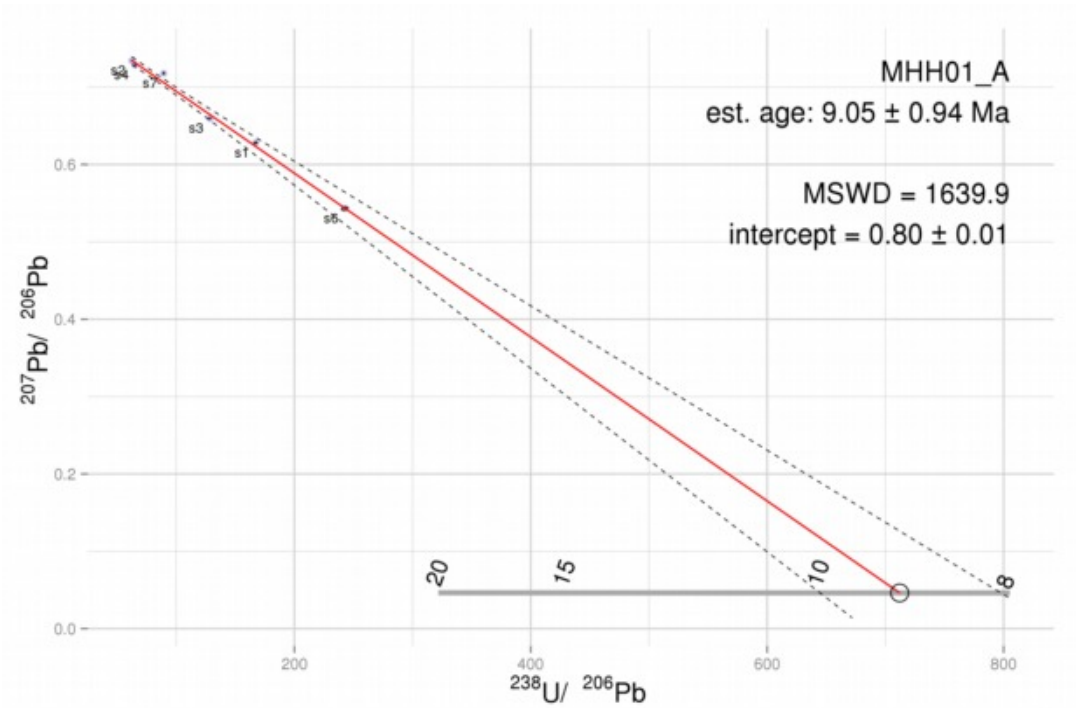

Fig. 104: MC-ICPMS isotopic ratio measurements from sample MHH01_A.
One of the most precise ages in this study. Unfortunately, the age could not be reproduced with confidence on other samples from the same area (Fig. 105).

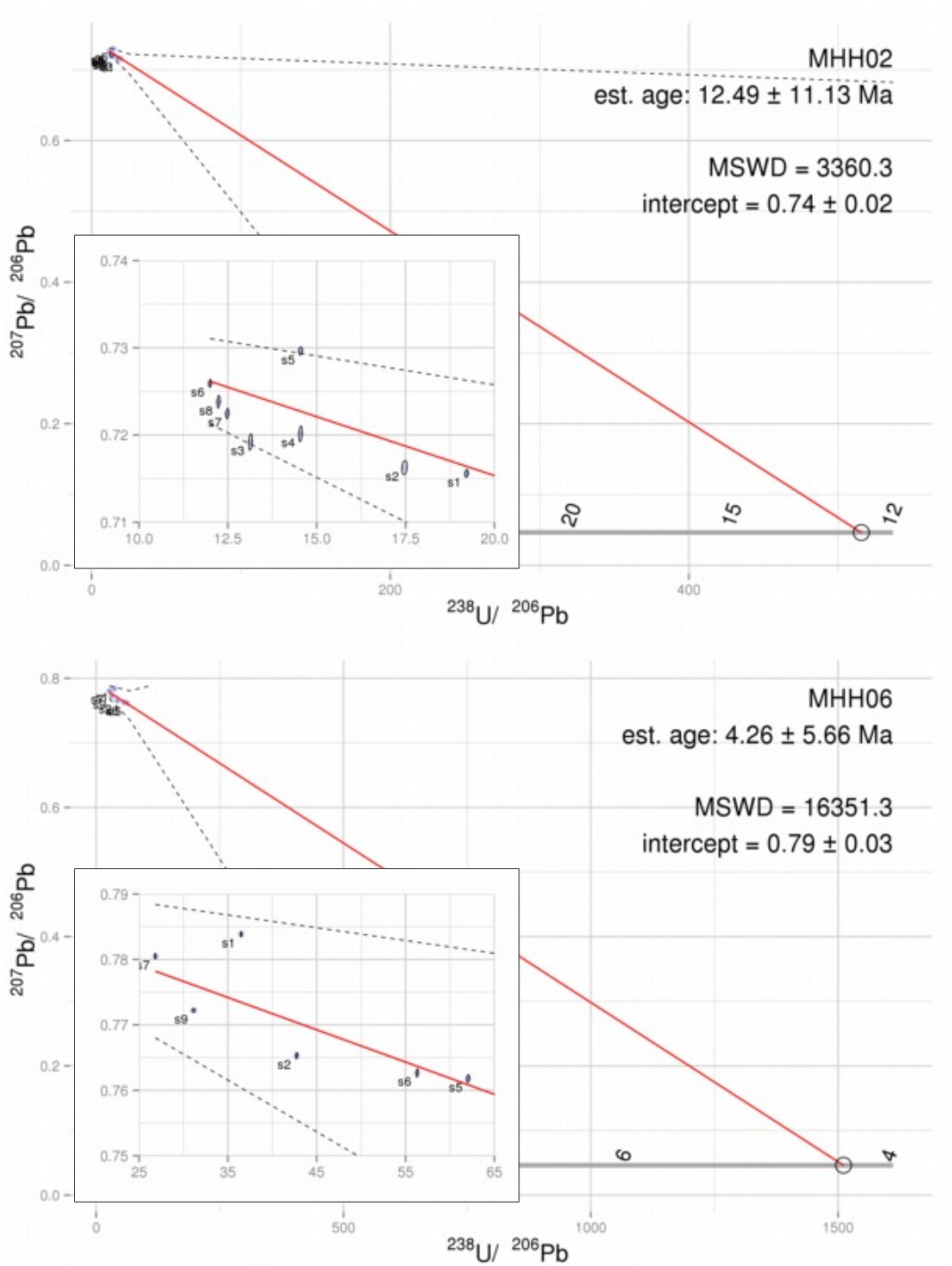

Fig. 105: MC-ICPMS isotopic ratio measurements from samples MHH02 and MHH06. Insufficient spread in isotopic ratio values between subsamples results in tight clustering of the data points, thus a very weakly constrained regression line.

5.4.7 Other samples

No samples from other sampling areas, including those contributed by collaborators, proved suitable for dating. Typical reasons to exclude samples from further processing where a U/Pb ratio < 1, contamination of the calcite with clay minerals or host rock, U- and/or Pb-concentrations below LoD, and, rarely, the lack of variability in U/Pb ratio despite otherwise favourable indications. In the following, a few examples for data from samples deemed unsuitable for further processing after screening are given.

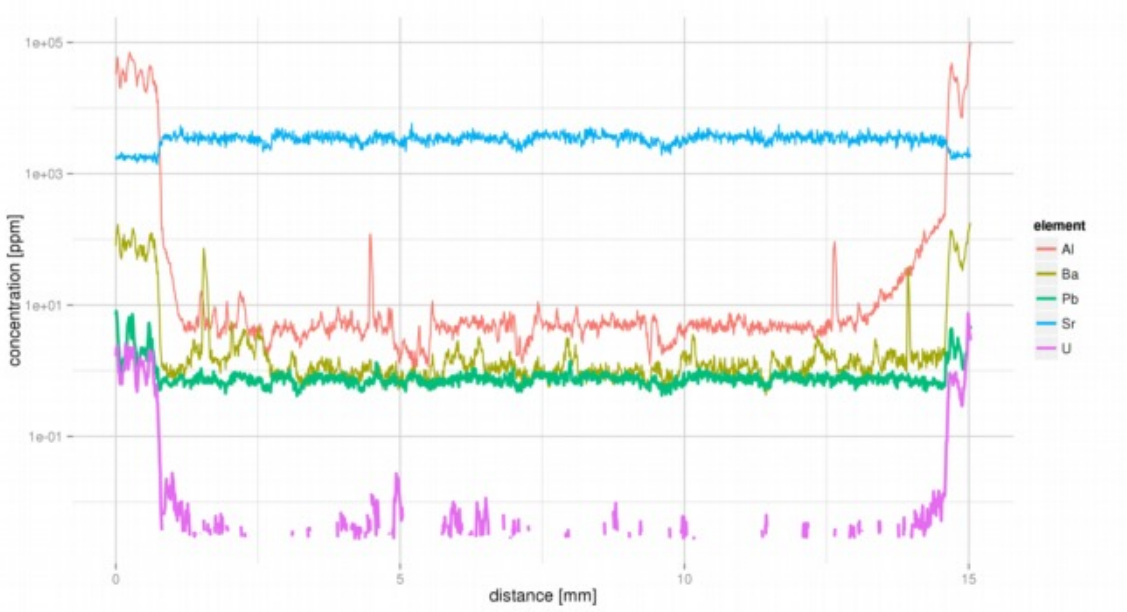

Fig. 106: LA-ICPMS track on Sample KMR-DGN03_A.
Calcite tension gash (host rock indicated by elevated Al values on both sides). Pb concentrations are constantly high at ~1 ppm, U concentration is constantly more than 2 orders of magnitude less, at or below LoD. This sample was not further processed.

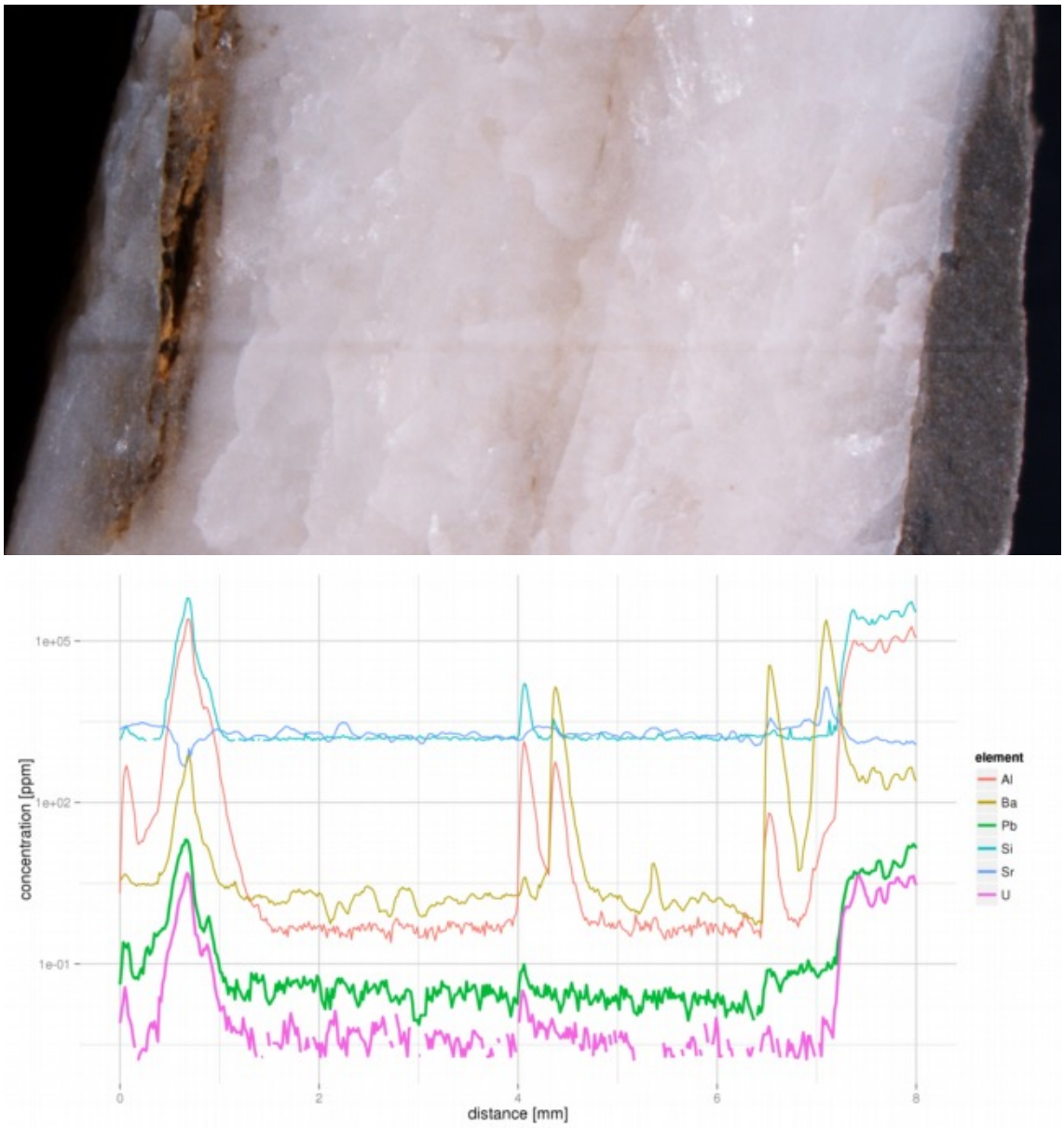

Fig. 107: Microphotograph and laser ablation track of sample s30_A.
Above: Microphotograph of sample after analysis – the ablated track is visible. Below: Data for ablated track. Host rock, on the sides, and a clay-enriched seam in the middle of the tension gash are clearly detectable by their elevated Al and Si values (and are therefore not quantifiable). U concentrations at and below the LoD combined with Pb concentration 5x – 10x higher than U indicate a dominant common Pb source, rendering this sample unsuitable for further dating attempts. A central clay-rich seam is a common feature in tension gashes, yet without other evidence does not have any implications on the calcite growth mechanism. It may be residual host rock from initial fracture opening (implying antitaxial growth), or material filled in in each new opening increment, concentrated in the centre by crystallisation pressure of the calcite growing to close the gap (syntaxial growth). Image width 10 mm.
Sample from Northern Canada, contributed by Simon Craggs, RHUL at that time.

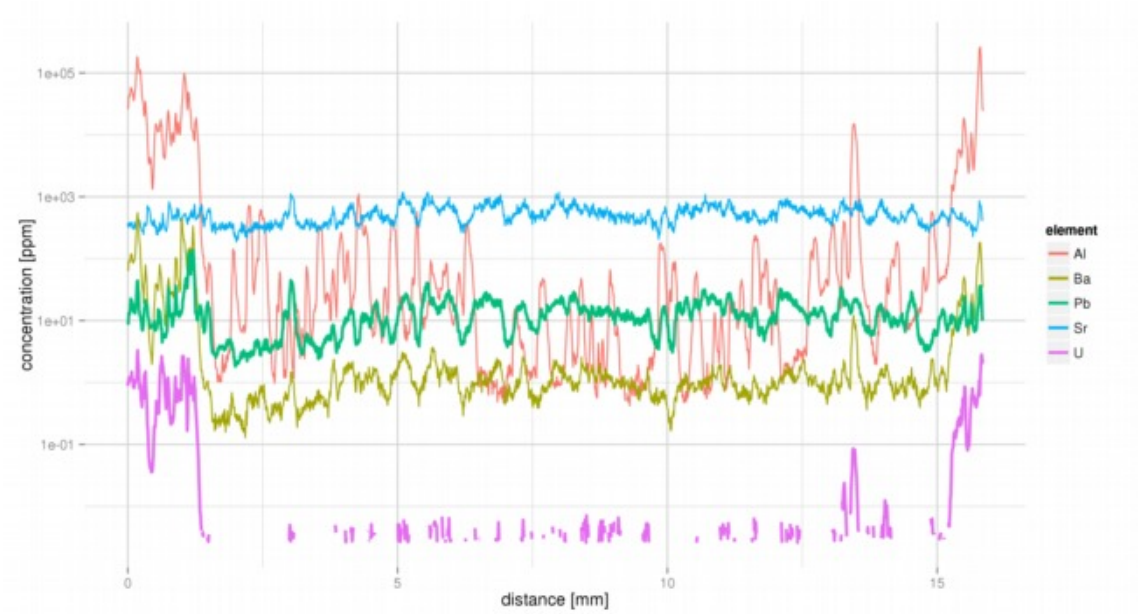

Fig. 108: LA-ICPMS track on Sample KMR-DGN09_A.
Calcite tension gash (host rock indicated by elevated Al values on both sides). The data seems to indicate extremely low U/Pb ratios, with Pb concentrations at ~10 ppm, and U over 4 orders of magnitude lower, at and below LoD. The noisy, elevated Al signal throughout the calcite might indicate impurities like clay minerals in the calcite, thus, real Pb concentrations might be much lower. This sample was not further processed.

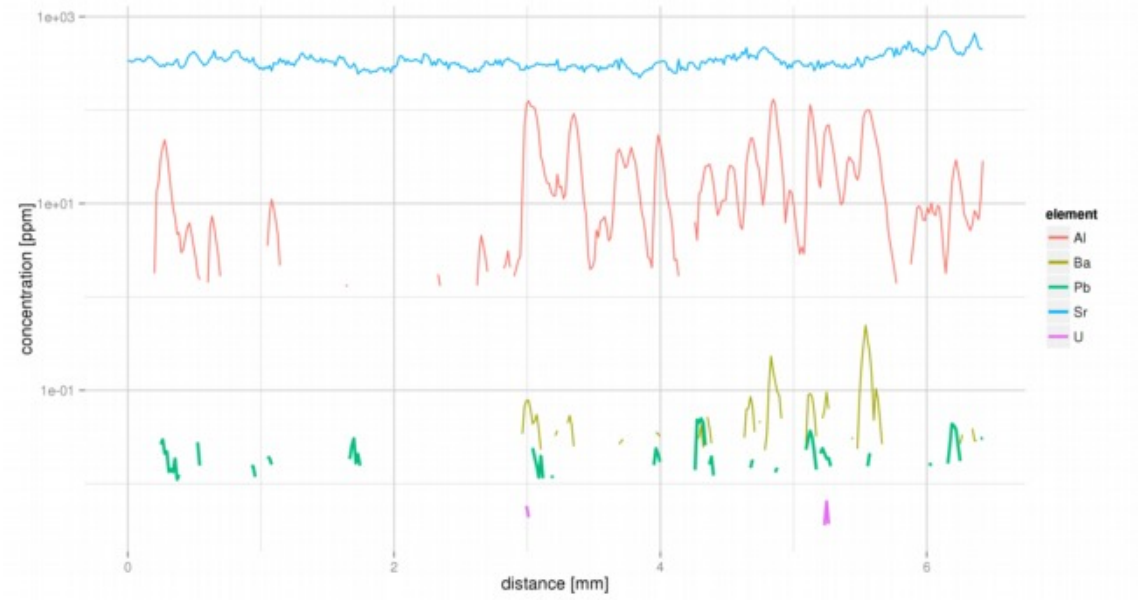

Fig. 109: LA-ICPMS track on Sample KMR-DGN10_A.
Calcite slickenfibre from the Valensole conglomerate. This sample consists of extremely pure calcite, U, Pb and Ba are below LoD. This sample was not further processed.

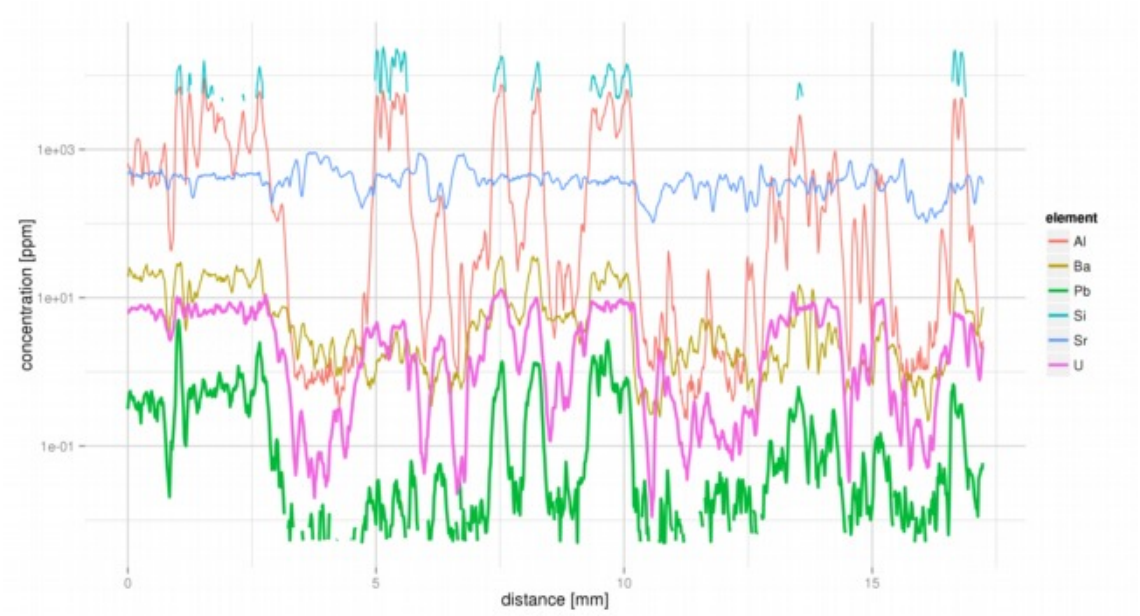

Fig. 110: LA-ICPMS track on Sample KMR-LIV31_B.
Calcite slickenfibre from a marlstone. Al- and Si-spikes indicate heavy contamination with clay minerals. This sample was not further processed.

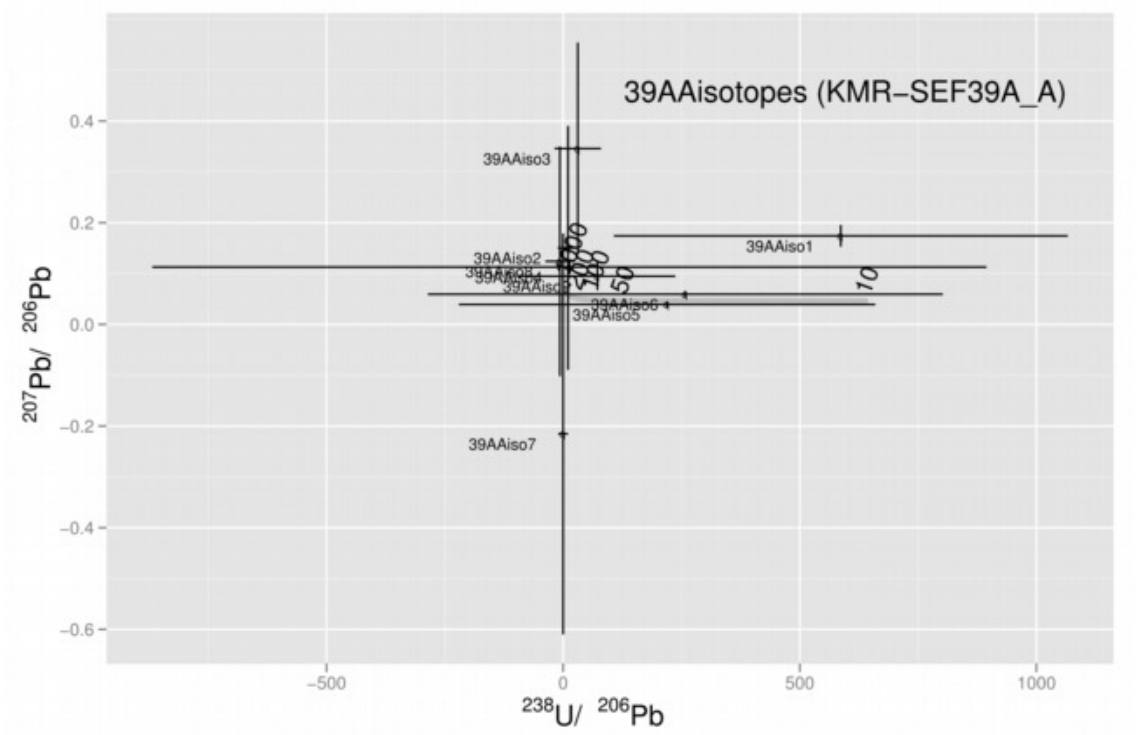

Fig. 111: LA-ICPMS in situ isotope data of KMR-SEF39A_A.
Despite initial track scans showing elevated U/Pb ratios, ratio variations, and areas of relatively pure calcite, isotope data obtained in situ on samples from the Seefeld area did not yield any meaningful results. The most likely reason is alteration of the calcite in later tectonic deformation.

6. Interpretation and Discussion

6.1 Dating calcite

Although calcite exhibits lower concentrations in radioactive elements, when compared to minerals more commonly utilised in geochronology like zircon, micas, feldspars or hornblendes (and many others), its ubiquity throughout most geological settings makes it a valuable archive and time marker, in cases where the samples allow isotopic dating. As shown in chapters 1.3 Previous work and 3.1 Geochemistry of Uranium and Lead in calcite, calcite records the U-Pb isotopic system and retains it in a stable manner over geological times (see e.g. Rasbury & Cole, 2009; Kelly et al., 2006; Rasbury et al., 1997; Smith et al., 1991; Wang et al., 1998).

For the application described in this study, dating of slickenfibres and tension gashes, no other mineral would be as well suitable. Although quartz abundantly forms the same structures in many geological settings, this mineral does not readily incorporate radioactive elements that would allow isotopic dating. Weis & Wasserburg, 1987, could date cherts with the Rb-Sr method, but this material is not applicable for tectonic studies. Rossman et al., 1987, found Nd and Sm concentrations in quartz of 0.127 to 2.81 ppb and 0.0159 to 0.48 ppb, respectively and Rb and Sr concentrations of 1.17 to 177 ppb and 3.26 to 1027 ppb, respectively. Other minerals which would allow isotopic dating form slickenfibres only in rare occasions (e.g. Eyal et al., 1992).

To determine the formation age of the calcites studied herein, other geochronological methods would not be applicable, as detailed below:

- K-Ar dating (Wasserburg & Hayden, 1955; Wasserburg et al., 1956) was applied to a range of lithologies, but usually relies on micas or feldspars, generally minerals with K concentrations between tens of ppm and over 10 % w/w.

In this study, K concentration was not measured during sample screening. However, geochemically similar Rb was typically encountered in concentrations below LOD or just above, in ~10 to few tens of ppb. Assuming a Rb concentration of 20 ppb, and 5 ppm K (based on an average upper crustal K/Rb ratio of 250, Taylor & McLennan, 1985), with an isotopic abundance for ^{40}K of 0.0117%, samples would contain ~5.85 × 10^{-10} g/g ^{40}K. Assuming an initial 5 ppm K (of natural isotopic composition) 20 Ma ago, radioactive decay of ^{40}K would have produced about 9.95 × 10^{10} atoms of ^{40}Ar per gram of calcite, or 6.5 × 10^{-12} g/g. This does not take into account Ar diffusion.

- Similarly, the Rb/Sr method would not be applicable for the analysed samples, due to the very low Rb concentrations (see above) and due to the comparatively very high Sr concentrations typically found in calcites (very variable, typically several 100 ppm in this study).
- ^{147}Sm decays to ^{143}Nd with a half-life of 1.06 × 10^{11} years. Although not screened for in this study, the concentrations for these elements can be assumed to be similar to the other rare earth elements, in most samples below or just above LOD (see also below).
- Lu and Hf concentrations were not determined during sample screening, but Lu can be assumed to be similar to analysed Yb. Concentrations typically range from few ppb to tens of ppb, in many samples not raising above LOD. Ce exceptionally reached ppm-level concentrations in localised domains. Hf is not well soluble in neutral aqueous solution and likely to be easily expelled from the calcite lattice. Lu-Hf dating requires highest precision element separation (extraction column chemistry) and measurements, and with a half-life of ~37 Ga for ^{176}Lu decaying to ^{176}Hf (Scherer et al., 2001; Söderlund et al., 2004), measurements on the young samples in question would likely not be possible.
- The siderophile elements Re and Os would not be compatible under assumed formation conditions of calcite slickenfibres. These elements have been shown to occur under reducing conditions and have been utilised to date black shales

and similar sediments (e.g. Cohen et al., 1999; Kendall et al., 2004; Zhu et al., 2012).

Sr and O stable isotopic ratio methods (isotope stratigraphy) are indirect dating methods based on the calcite being formed from, and in equilibrium with, a large body of water (usually, the global oceans), the isotopic composition of which for said elements is known a priori and varies over time. An age is then assigned from comparison of measured values to the known curve of isotopic composition variation. The Sr and O isotopic composition in solutions circulating in faults, fractures and throughout the rock body is usually not known, but will differ greatly from average sea water composition.

One of the most common calcite materials dated by the U-Pb method are speleothems (e.g. Woodhead et al., 2006; Richards et al., 1998; Cliff et al., 2010). Speleothems often show clear growth structures and even from only several age determinations on a large sample, growth rates can often be interpolated (e.g. Scholz & Hoffmann, 2011). Growth conditions in caves tend to be stable over long periods of time and evaporation in the cave, as well as seeping of the water through the rock and soil above and leaching processes on the way, often result in elevated U concentrations. In contrast, growth rates of slickenfibres are not known, and can be assumed to be non-continuous (phases of tectonic activity).

U-Pb dating of speleothems (and combined methods with e.g. U-series) have been utilised in palaeoclimate studies, tectonic studies, palaeontology and archaeology (e.g. Pickering et al., 2011; Meyer et al., 2009; Meyer et al., 2011; Pickering et al., 2010; Walker et al., 2006; Fairchild et al., 2006).

The direct U-Pb dating of calcite fossils (sometimes primary aragonite), palaeosols and whole rock allows to calibrate the bio- and lithostratigraphy of a region to absolute ages (e.g. Getty et al., 2001; Cole et al., 2005; Becker et al., 2004; Israelson et al., 1996). Aragonite can potentially build in more U than calcite (Lazar et al., 2004; Smith

et al., 1994), and although U seems to be retained sufficiently well during recrystallisation to validate U-Pb dating of calcite samples that formed from primary aragonite (Kelly et al., 2006; Kelly et al., 2003), Pb loss may occur during recrystallisation (Smith et al., 1994).

The main challenges in U-Pb dating of calcite are uncertainty on initial ^{234}U disequilibrium and the precise measurement of the radiogenic Pb isotopes. Thus, suitability of a sample is mainly limited by the initial U concentration. Consequently, even very young samples can be dated under favourable conditions (Richards et al., 1998; Cliff et al., 2010), but as more Pb accumulates over time, studies on older samples are more numerous (Cole et al., 2005; Becker et al., 2004; Israelson et al., 1996; Jahn et al., 1990; Jahn & Cuvellier, 1994; Polyak et al., 2008; Rasbury & Cole, 2009; Rasbury et al., 1998; Rasbury et al., 1997; Wang et al., 1998). For the age range of samples worked on in this study, age uncertainties resulting from ^{234}U disequilibrium were assumed to be insignificant compared to other error sources (mainly, compared to geological scatter of data).

U-Pb dating of calcite cements in sediments can give valuable information about secondary geological processes and diagenesis (Smith et al., 1991; Sanders et al., 2010; Jones et al., 1995). This study expands the range of applications for the method to structural geology and tectonics.

Many studies utilise U-series isotopes for dating calcite speleothems, cements, palaeosols, fossils and other samples (e.g. Andersen et al., 2004; Eggins et al., 2005; Richards & Dorale, 2003; Plan et al., 2010; Edwards et al., 2003; Eggins et al., 2003; Pons-Branchu et al., 2005; Potter et al., 2005; Scholz et al., 2004 and see Bourdon et al., 2003; Goldstein & Stirling, 2003; Richards & Dorale, 2003 with references therein). Due to the short half-life(s) involved, U-series dating only reaches to a maximum age of ~500 ka (exceptionally 800 ka) and is thus not suitable for the geological time frame of most tectonic studies, including this study. However, Plan et al., 2010 could apply U-series dating in tectonics by dating damaged speleothems growing over a fault.

Conceptionally, U-series dating faces similar uncertainties over element retention or expulsion during recrystallisation from aragonite to calcite and diagenesis, as mention above (see e.g. Pons-Branchu et al., 2005).

6.2 Dating brittle deformation

Brittle deformation of rocks is the expression of sudden rupturing processes releasing tension that has built up in the rock body. Much of the observed movements in the Earth's upper crust on a plate-tectonic to outcrop scale is in detail accommodated by movements along fault zones, faults and fractures (the rest in mineral deformation and recrystallisation). Continuous flow and deformation of the crust on a large scale and over geological times includes a multitude of slip and fracture events, when studied in closer detail. For general treatment of the topic see e.g. Twiss & Moores, 1992; Ramsay & Huber, 1987; Pollard & Fletcher, 2005; Gudmundsson, 2011.

These rupturing processes introduce new discontinuities into the rock body, and, if large enough, cause seismic tremors and earthquakes. Therefore, understanding the timing of brittle deformation is not just of scientific interest, but has great relevance for civil engineering and public safety. From the timing of fault activity, seismicity and earthquake recurrence for an area can be determined. From the texture and development of the existing fault and fracture pattern, predictions on the location, orientation and nature of future rock failure can be made.

Because of the inhomogeneities introduced into a rock body by fracturing and faulting, brittle deformation and its timing are also of great interest in the exploration and exploitation of natural resources. For example, fracturing and faulting can generate porosity in a rock body, necessary to store water, natural gas and oil. The fracture network provides pathways along which these fluids can migrate and be extracted. Faulting can both open new pathways and seal existing ones, both of which may be advantageous or disadvantageous for the development of a reservoir at a given time. The opening and closing of fluid pathways also plays a crucial role in the development of many mineral deposits of economic importance.

Because of this broad interest, a multitude of methods has been applied to date brittle deformation, and thus better understand fracturing and faulting processes from the micro- to the mapscale.

One of the methods applied most commonly is the dating of fault gauges by the K-Ar method (treated synonymously here with "the Ar-Ar method"; for examples, see e.g. Lyons & Snellenburg, 1971; Vrolijk & van der Pluijm, 1999van der Pluijm et al., 2001; Kralik et al., 1987; Zwingmann et al., 2004; Zwingmann & Mancktelow, 2004; Wang et al., 2009; Och et al., 2009; Zwingmann et al., 2010). The main difficulty in this method is identifying syndeformationally grown minerals with a sufficient K content in the fault gauge, most commonly illite and muscovite, and distinguishing these from ground-up host rock and other older mineral generations. By definition, grain sizes of the minerals under consideration in a fault gauge will be very small (~0.1 – 10 µm). Such grains in the often "open" system of a brittle fault are easily susceptible to alteration and resetting, Ar loss and gain. A large difficulty, more pronounced the smaller the grains in question are, is ^{39}Ar loss by recoil: the proton emission from the nucleus during radioactive decay can push ^{39}Ar atoms close to a grain boundary out of the crystal lattice.

Main disadvantages compared to the method presented herein are the applicability only to faults with a distinctive offset and in certain lithologies (fault gauge forms dynamically during fault movement, not in tension fractures), and that successive deformation phases and directions can not usually be distinguished as easily in fault gauges, as by slickenfibres.

The complex problem of time and temperature-dependent Ar loss and gain has no equivalent in U-Pb dating of tectonic carbonates, as all elements involved are non-volatile (except for short-lived Rn) and calcite slickenfibres are formed under relatively low temperatures. U (and Pb) can be mobilised during recrystallisation, but the large uranyl ion does not readily diffuse out of the calcite lattice. Because no irradiation activation is necessary for U-Pb measurements, problems similar to ^{39}Ar recoil loss (Hess & Lippolt, 1986) are also avoided.

Where host rock lithologies allow it, and fault slip was large and fast enough to generate enough heat, pseudotachylytes can be used for dating fault movement, e.g by the Ar-Ar or the Rb-Sr method (e.g. Kelley et al., 1994; Thompson et al., 1998; Müller

et al., 2001; Müller et al., 2002; Müller et al., 2000a). Whereas the occurrence of pseudotachylytes is based on the assumption of fast fault movement, the more abundantly observed slickenfibres indicate at least periods of slower movement ("fault creep") to allow growth of mineral fibres. The exact mechanism of slickenfibre growth is still poorly understood (e.g. Renard et al., 2005; Cox, 1987; Means & Li, 2001 and chapter "2.1 Tectonic carbonates"), and probably several different mechanisms occur, depending on conditions (e.g. Hilgers & Urai, 2002; Urai et al., 1991), but calcite fibres closely following fault movement, including direction changes, indicate that growth occurs during fault movement.

Similar to the principles applied in dating pseudotachylytes, the dating of syndeformational intrusions is based on the assumption that the injected melt cools rapidly, thus recording the time of fault activity (e.g Ring & Collins, 2005; Kanjanapayont et al., 2012; Watkinson et al., 2008; Glodny & Hetzel, 2007). Similar to fault gauges (and in part, pseudotachylytes), the possibility of older crystallites being contained in the intruded magma or of recycling host rock minerals exists. When considering higher temperature settings and the transition from brittle to (semi-)ductile deformation, the thematic complex of dating deformation structures in shear zones becomes relevant (e.g. Shaw et al., 2001; Rolland et al., 2009; Lips et al., 1998; Müller et al., 2000b, and many others), which is not further considered in this study.

In contrast to the above, the presented method applies to low-temperature deformational events, likely in the very shallow crust (below 150-250° C, depending on pressure). Deformation direction is as well recorded by slickenfibres as e.g. in ductile shear zones, and the potential to record several deformation phases of different directions in slickenfibres is high, whereas older indicators in ductile shear zones are easily overprinted. However, the higher temperatures in shear zones cause many more minerals to grow, potentially offering a wider range of dating methods.

Other minerals than calcite and quartz can form slickenfibres, some of which may contain higher concentrations of radioactive elements (e.g. Eyal et al., 1992), but the conditions for such minerals to form slickenfibres are much less common.

Electron spin resonance (ESR) dating is based on the principle that various minerals will accumulate magnetic moments due to exposure to sources of radiation (e.g. natural radioactive background in a rock body), which can be measured to determine the duration of exposure (Grün, 1989). Since the magnetic moments are caused by lattice defects, heating events, but also strong mechanical shock, reset the system. This allows to date a range of fault rocks, including cataclasites (e.g. Tanaka et al., 1995).

Movement on brittle faults can lead to magnetic resetting in the components and matrix of fault breccia and/or in associated mylonites, given favourable mineralogy, which has been utilised to date the faulting by palaeomagnetic methods (Torsvik et al., 1992; Eide et al., 1997).

Dating fault movement by cosmogenic nuclides requires the fault plane to be (progressively) exposed to cosmic rays at the Earth's surface, and weathering rate negligible or exactly known.

Similar restrictions apply to optically stimulated luminescence (OSL) dating, which is further limited by choice of minerals, most commonly quartz or feldspar. OSL is restricted to an age range of ~100 ka.

In the present study, one of the basic premisses was to directly date calcite slickenfibres and tension gashes. This excludes methods that are based on other materials (fault gauges, pseudotachylytes and syntectonic intrusions). Magnetism would be carried by microscopic inclusions rather than calcite itself, whereas U-Pb dating requires high-purity calcite for analysis, rendering this method and palaeomagnetic dating mutually exclusive. The samples in question were taken from as freshly exposed material as possible and should in principle not be restricted to surface outcrops (samples from underground outcrops or e.g. drill cores would be equally suitable), which excludes cosmogenic nuclides and OSL as equal alternatives.

"Passive dating" of fault movements, e.g. inferring fault movement from exhumation ages of the fault blocks or from the sedimentary record on the fault blocks, is common, and allows a wide range of methods to be used to determine relative movements of blocks, but the goal of this study was to determine deformation ages directly on the fault planes or fractures. Relative block exhumation ages also do not allow dating of predominantly strike-slip faults.

6.3 Discussion of approach and possible alternatives

Having established the reasons for choosing U-Pb dating of calcite slickenfibres for the present study in the previous sections of this chapter, alternative approaches to the actual analysis might be considered.

The present study utilised a Resonetics RESOlution M-50 with a 193 nm Coherent COMPexPro110 ArF excimer laser coupled to an Agilent 7500ce quadrupole ICPMS for LA-ICPMS sample screening.

Hathorne et al., 2008, demonstrated that a laser wavelength of 193 nm is favourable over widely used 213 nm or longer, in terms of particle sizes produced and fractionation processes during ablation and particle transport.

Femtosecond lasers, as opposed to laser pulses lasting nanoseconds on the utilised system, are not readily available and expensive. Possible advantages due to lower mass fractionation during ablation would only be advantageous for in situ dating, which was not the main focus of this study. For trace element screening, no improvements would be expected from the use of a fs laser.

Utilising a MC-ICPMS for direct in situ dating (e.g.Eggins et al., 2005; Potter et al., 2005) would be desirable for its higher precision (mainly for the Pb isotopes), but the observed concentrations (Pb) would likely not yield large enough signals to utilise the Faraday detectors, or would require more sample over a larger area being ablated, which in return elevates the risk of contamination by ablating impurities and would yield a smaller spread of data points on the isochron diagrams due to averaging, effectively counteracting the desired improvements.

For dynamic measurements on a MC-ICPMS, the magnetic field needs to be altered, and a stable ion beam must be achieved before each consecutive measurement. Switching masses this way on a MC-ICPMS (like the IsoProbe at RHUL) is relatively slow compared to switching masses (effectively, the singe mass) on a quadrupole ICPMS, thus, for the same amount of data, much larger sample sizes would be required,

with the above mentioned adverse effects. Thus, in situ LA-MC-ICPMS could only use static mode measurements.

An instrument with an electrostatic mass filter could switch masses much faster, and in combination with the magnetic mass filter, would allow to filter more unwanted interferences.

Instead of the MC-ICPMS, (chemically separated) samples could also have been measured on the TIMS at RHUL. Sample preparation would have introduced an additional potential source of contamination, and TIMS usually does not allow for mass fractionation correction based on an internal, constant isotope ratio (like ^{203}Tl and ^{205}Tl added for MC-ICPMS in this study). Todt et al., 1996, have utilised a mixed ^{202}Pb-^{205}Pb double spike in TIMS Pb isotopic measurements, on an instrument with nine Faraday detectors as opposed to five on the TIMS in house.

Woodhead & Hergt, 1997, and Woodhead et al., 1995, describe a ^{204}Pb-^{207}Pb double-spike technique for determining the Pb-isotopic composition, which would yield a higher precision than the employed technique. However, this procedure requires three TIMS runs per sample, and uncertainties from other error sources and scatter of data points by far outweighs uncertainties from individual measurements in the observed data in this study, thus no improvement in age age precision could be expected.

Many studies utilise an anion resin workflow for separation of U, Th and Pb. The procedure described e.g. in Cole et al., 2005 (based on Wang et al., 1998) requires precipitation of Pb with Fe-hydroxydes and consecutive redissolution in HBr, introducing additional reagents, and thus, possible contamination sources, compared to the presented workflow. Cole et al., 2005, estimated procedural Pb blanks of ~200 ± 100 pg, compared to ~5.3 pg in this study (see "4.5.2 Blanks").

Eichrom Technologies Inc., the manufacturer of the extraction resins utilised in this study, offers a resin specifically for Pb separation. This resin is optimised to allow for an easier elusion of Pb from the resin, which results from a slightly lower retention

potential for Pb than the resin used herein, which is marketed primarily for Sr separation. However, in the column calibrations in the early stages of this study, Pb elusion from the resin was shown to be thorough (see "4.4.1 Extraction chromatography") and no problems with this work step were encountered.

In terms of minimal sample size and procedural Pb blank, the wet chemical sample preparation presented herein (chapter 4.12.2 Detailed clean lab/column chemistry workflow) appears to be optimised under the conditions of current technical possibilities.

In chapter 4.11.3 SEM, the use of SEM element mapping is demonstrated. This technique is widely applied and very fast, but detection levels are several tens to hundreds of ppm, which is not given for many elements in the samples presented here.

No clear indicators for suitability of samples applicable in the field could be determined. Although important for the solubility of U in aqueous solution (see chapter 3.1 Geochemistry of Uranium and Lead in calcite), the content of organic Carbon (C_{org}) in the host rock seems not to be a factor influencing the U content of tectonic carbonates in these rocks. The same is true for other intuitively probable sources of U in tectonic carbonates, like crystalline/metamorphic rocks or an outcrop known to yield suitable samples in the vicinity. Marly-sandy sediments might be beneficial, but are not guaranteed to yield elevated U concentrations.

The redox potential in the water at time of sedimentation determines the oxidation state of U, and thus solubility (chapter 3.1 Geochemistry of Uranium and Lead in calcite). Yet, determination of palaeoredox potential is problematic, as it can only be inferred indirectly. Wright et al., 1987, describe a negative Ce REE anomaly as an indicator for oxidising conditions, but biogenic phosphate is required for reliable preservation of the REE spectrum. German & Elderfield, 1990, and Algeo & Lyons, 2006, show that proxies used for palaeoredox determination are in fact influenced by many further factors, mainly palaeooceanographic conditions. Tribovillard et al., 2006,

describes the use of trace element concentrations, uranium amongst them, as a proxy for palaeoredox, but this does not allow for any reverse conclusions usable in the presented study. All the mentioned methods for palaeoredox determination require sophisticated preparation of suitable samples, which would not give any advantage over the direct determination of U and Pb concentrations by LA-ICPMS described herein.

As tectonic deformation in most cases takes place long after sedimantation, the determination of palaeoredox of the host rock is of minor value. Determination of palaeoredox of fissure waters would be further complicated by the lack of mineral suitable for recording the described proxies, and the unknown and highly variable chemistry of these fluids.

Stable isotope analyses, which could give further insight into formation conditions of the host rock, would add an additional wet chemical preparation and high-precision analysis, the value of which for the present study would be minimal, for the same reasons mentioned.

Hand-held XRF spectrometers and gamma spectrometers are available, but element detection limits for the former do not allow determination of trace element concentrations in the range observed in the samples, and the latter only allows bulk determination of radioactivity. Both methods do not offer the spatial resolution necessary to distinguish measurements on a slickenfibre from those on the surrounding host rock in most cases. Only in rare cases, advantages from the information gained from these instruments would justify the effort to carry these instruments on fieldwork.

An alternative imaging method to reveal U (and Th, if present) concentration differences in rock samples in order to aid sample selection, is “phosphor imaging”, applied in several studies about U-Pb dating of carbonates (e.g. Pickering et al., 2010; Cole et al., 2003; Cole et al., 2005). The technique utilises a radiographic imaging medium that is put in direct contact with the flat (cut) sample surface and develops an image of the radioactivity ("activity") in the rock. The technique is simple, cheap (the medium is reusable), non-destructive and suited for large samples (a major advantage

over LA-ICPMS element mapping presented in this study), but depending on activity, requires days to months of irradiation to yield an image. Different sources of radioactivity (U, Th, K, ...) can not be distinguished.

6.4 Regional tectonic discussion and interpretation

Gosau

The Gosau basin underwent deformation in all major phases of the evolution of the Northern Calcareous Alps, since the basin opened in the Upper Cretaceous (Wagreich & Decker, 2001; Wagreich & Faupl, 1994; Willingshofer et al., 1999; Wagreich & Faupl, 1994). As such, faults generated during early basin opening, Eoalpine nappe stacking, and any of the Tertiary Alpine deformation phases might be expected (e.g. Peresson & Decker, 1997; Linzer et al., 2002; Schmid et al., 2004).

According to Peresson & Decker, 1997, six Tertiary deformation phases can be distinguished in brittle deformation data from the Northern Calcareous Alps. Not all deformations would be expected to be recorded at any one location. Generally, a fault plane, once created, might be only slightly reactivated in a later phase, effectively transferring tectonic stress to another location where fresh deformation will occur, or it may lie in an orientation unfavourable for reactivation, or it may be intensely reactivated, obliterating all traces of older deformation phases.

MC-ICPMS data obtained at outcrop 240 (KMR-GOB21) indicate deformation at ~29 ± 2 and ~23 ± 1 Ma, in the N-S-compressional phase "T2" of Peresson & Decker, 1997 (see Fig. 112), and LA-ICPMS in situ data from a tension gash at location 236 (KMR-GOB18) seems to belong to an earlier deformation phase at ~42 Ma. The correlation to these deformation phases is corroborated by the geometry of the sampled tectonic features, being compatible with the respective tectonic stress directions in Fig. 112.

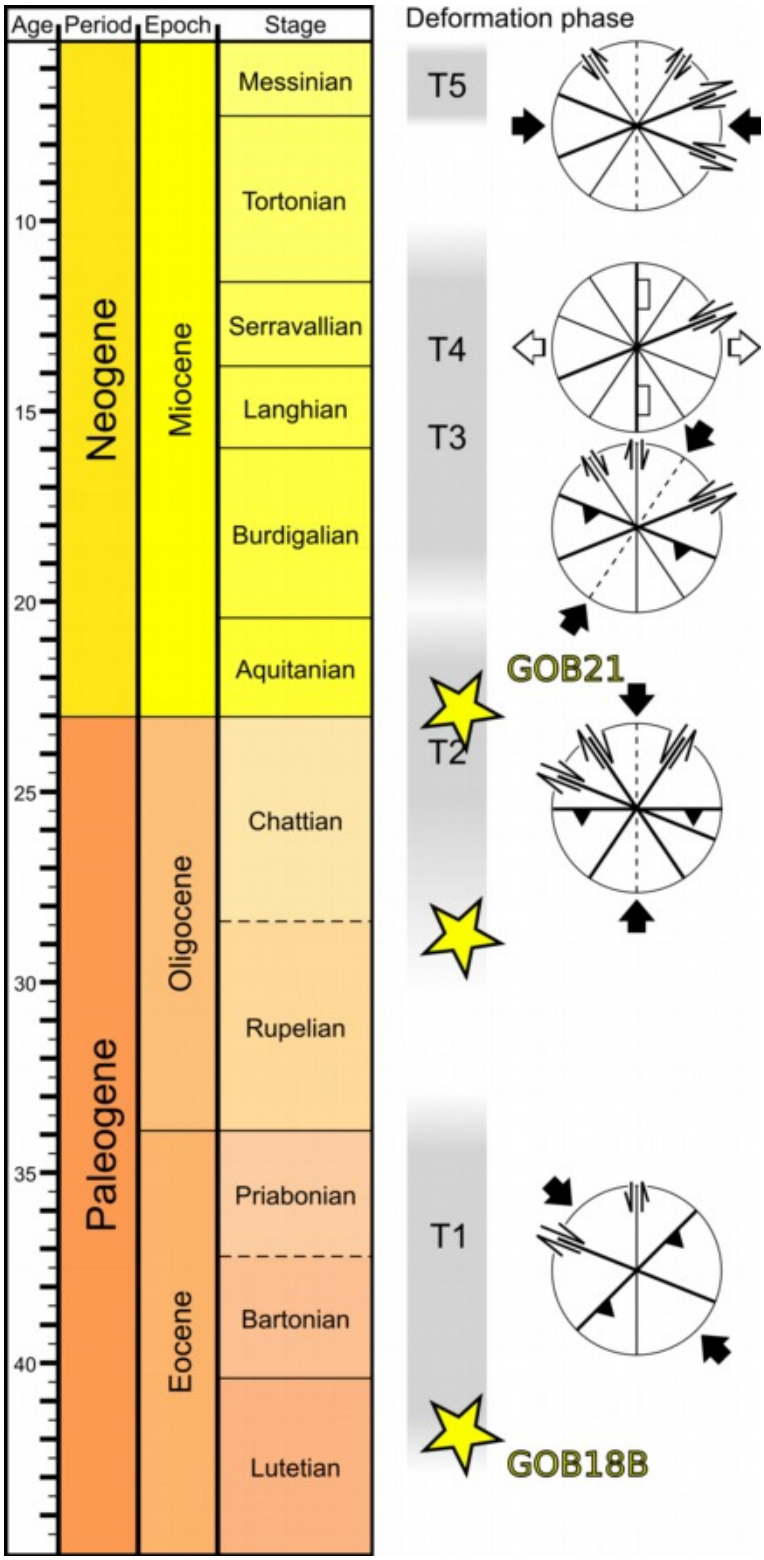

Fig. 112: Deformation phases of the NCA.
Based on Peresson1997#203 (see also 2.2.4 Gosau Basin).

The structural data presented in 2.2.4 Gosau Basin and Fig. 113 for these outcrops is compatible with the regional stress fields proposed in the literature (Fig. 112) at the respective times: Conjugate NNW-SSE and WSW-ENE oriented tension gashes observed at outcrop 236 (KMR-GOB18) could have been formed in a NW-SE compressional regime at ~42 Ma (deformation phase T1 in Fig. 112). This outcrop lies close to the basin margin.

At outcrop 240 (KMR-GOB21), in the depocentre of the basin, NE-SW striking sinistral faults are the main structures, on which WSW dipping, dextral secondary faults developed. This implies a N-S to NNE-SSW compression direction, similar to deformation phase T2 in Fig. 112. Although the main calcite fibre package in the outcrop (l1) was dated at ~29 ± 2 Ma, and a younger (l2, established by cross-cutting relationship) slickenfibre in a different direction was dated at ~23 ± 1 Ma, both fit the overall proposed stress regime of this phase.

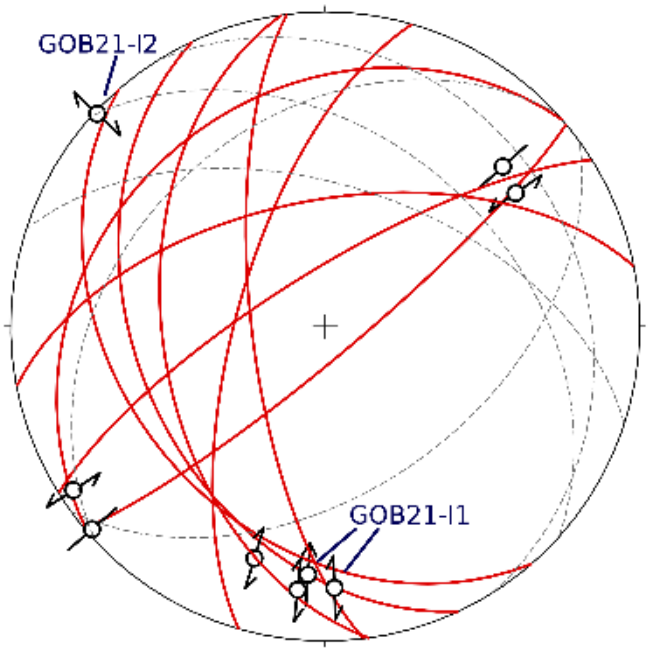

Fig. 113: Structural elements observed at outcrop 240. Slickenfibres l1 and l2, although cross-cutting each other and dated to different ages, formed at structurally equvalent, dextral, NNW-SSE stricking secondary faults. Dashed grey lines: folded bedding planes.

Most other samples from the Gosau Basin appeared not suitable for dating in initial screening, either because of too low U concentrations, or too low U/Pb ratios. In sampling, tectonic carbonates out of various lithologies, from massy biogenic marine limestone to sandy terrigeneous marl and from different stratigraphic levels of the basin fill, were collected.

The two outcrops yielding the dated samples are both of the Upper Santonian Hochmoos fm., a shallow marine marly unit dominated by input of terrigeneous, sandy material. In this case, stratigraphic control seems likely, the terrigeneous input could have contained U in solution aided by humic acids, or the terrigeneous sand might provide additional U. No obvious other criterion for (non-)suitability could be observed, some other samples were collected from different stratigraphic units in close proximity to KMR-GOB18, but proved not date-able. However, in no other sampling area could such a clear correlation of sample quality with stratigraphic unit be established.

Digne

The Digne nappe is the most external tectonic unit of the Alps in this part of the orogen. The front of the Digne nappe overthrusts the Pliocene (~12 – ~5 Ma) Valensole conglomerate, as indicated by intensive deformation in these young sediments. This indicates that nappe movement occurred until at least that time (Lickorish & Ford, 1998; Fournier et al., 2008; Hippolyte, 2001; Hippolyte et al., 2011), but GPS measurements indicate ongoing movement (e.g. Jouanne et al., 2001).

A wide spectrum of lithologies and stratigraphic units was sampled in this area, yet only one sample could be dated (KMR-DGN55). The sample location (outcrop 300) is a small cliff formed by a thrust fault within the frontal Digne Nappe (see 2.2.2 Digne). From this position, if faulting occurred in a normal outwards-progressing imbricated stack of thrust sheets, a young age, slightly older than the latest nappe movements, would be expected.

The fault plane is a thrust of deformed Tithonian limestone onto an overturned sequence of Palaeogene to Miocene sediment ("Red" and "Green Molasse"). The structure appears to be a fault propagation fold, the sampling location being situated in the overturned frontal limb of the fold. This structure would indicate an out-of-sequence thrust within the nappe.

Both models fit well with the measured ages of 9.59 ± 0.02 and ~8.4 ± 3.5 Ma measured by MC-ICPMS on slickenfibres from the fault. An age of ~9.7 ± 4.0 Ma measured by LA-ICPMS in situ, on a sample from another part of the outcrop, falls in the same age range.

It is not clear why this outcrop yielded date-able samples, whereas all other outcrops in the area did not. The same stratigraphic units present in outcrop 300 have been sampled elsewhere, therefore a stratigraphic control on U/Pb is unlikely. The fault rock at this outcrop is finely tectonised, possibly the higher surface area allowed for more intense leaching of the host rock, or solutions were circulating from a deeper source.

Swiss Jura

Samples from the Swiss Jura were contributed by Dr. Herfried Madritsch, NAGRA, Switzerland (see 2.2.8 Swiss Jura). The slickenfibres are sampled from fault planes that were folded in later deformation events (Madritsch, pers. comm.). Thus, faulting ages obtained in this study give maximum folding ages for the fault planes.

The Swiss Jura mountains are a thin-skinned foreland fold-and-thrust belt made up of sediments of the sedimentary cover of the European plate, mobilised in a late stage of the Alpine orogeny (Late Miocene to Pliocene, e.g. Schmid et al., 2004; Madritsch et al., 2010b). Studies of Neogene drainage patterns and fluvial sediments indicate Late Quaternary to ongoing deformation in the region (Ziegler & Fraefel, 2009; Madritsch et al., 2010b). It has been suggested that the recent, slower deformation represents a different phase of deformation, commencing at ~9-4 Ma, and characterised by thick-skinned thrusting of the European basement (e.g. Becker, 2000; Ustaszewski & Schmid, 2007).

The age of 9.05 ± 0.94 Ma obtained by MC-ICPMS fits into the model that the slickenfibres were formed before the youngest deformation. In the scope of this study, and looking at only one sample, no further conclusions about the regional tectonic history can be drawn. Other samples from the same area did not show enough spread between data points to construct a reliable regression line for an age estimate (see 5 Results).

Lower Inn valley

Various deformation structures in relation to Tertiary and younger deformation at the Inntal Fault were sampled. Deformation is believed to have been substantial during Miocene Alpine evolution (Ortner, 2001b; Linzer et al., 2002; Ratschbacher et al., 1989), and is ongoing to the present day, as indicated by smaller earthquakes occurring along the Inn Valley (e.g. Reiter et al., 2003; Ortner et al., 2006). Most samples are marly to sandy sediments of the Lower Inn Valley Intramontane Molasse, Late Eocene to Oligocene in age. Sample KB2 is a tectonic breccia from a basal fault, the sample was provided by Dr. H. Ortner. Few samples proved to be datable.

An age of 27.7 ± 1.3 Ma for a fault plane in Tertiary lime marls (KMR-LIV34B) deposited in the Lower Inn Valley intramontane Molasse basin (Ortner & Stingl, 2001) is in line with the expected syndepositional to early deformation age. Sample KB2 yielded indication of a young age of ~10-15 Ma, expected for the Inntal Fault, but due to low concentrations in the sample, scatter and errors on the data points was too large to confirm that age.

Some samples from the basal bituminous marls ("Bitumenmergel") comprised beige slickenfibres, rich in fluid inclusions of hydrocarbons. Above mentioned KMR-LIV34B was amongst these, and wet chemical preparation of this material proved problematic, as there is no designated step for dissolving organic compounds in the developed workflow until after extraction chromatography. Measurements of this sample were of low precision and sample wash-out in the mass spectrometer took a very long time, the utilised PTFE labware was not easily cleaned after analysis. Samples with a significant content of organic compounds should be prepared differently, or be avoided.

Fohnsdorf

In the Fohnsdorf basin, mainly the basin margins were sampled, the sediments in the centre are not well exposed and do not show deformation structures (in surface outcrops). Slickenfibres from marginal faults within metasedimentary units of the surrounding or from faults separating exterior host rock from basin sediments were sampled, but turned out to be not suitable for dating, due to low U concentrations and U/Pb ratios.

It the polymikt conglomerates of the Apfelberg fm., a marginal facies of the sedimentary basin fill, hydrothermal travertine filling fissures of up to several 10 cm width and several 10 m in extent, the so-called "Mariabucher Marmor" was sampled and yielded an age of 13.4 ± 0.8 Ma (see 5 Results). This age coincides with the forming age of the Apfelberg fm (~15-13 Ma), consistent with the depositional model, in which the coarse, polymikt conglomerates are thought to have been derived from the surrounding host rocks as a very proximal facies of debris flows and fans, deposited syntectonically on the steep slopes of the rapidly subsiding basin (Strauss et al., 2001; Wagreich & Strauss, 2005).

These samples are different in nature from the other tectonic carbonates collected throughout this study. The growth strata of the travertine, filling up the opening fissures, are not strictly coeval in formation. The different layers might represent individual tectonic pulses of fissure widening, or periodic influx of more and less saturated solutions. Episodic growth and mixing of different solution sources is demonstrated by the changing relative concentrations of trace elements, as seen in 5 Results.

In the conducted analyses, no age differences between layers could be resolved. As far as can be determined with the number of data points measured, growth seems to have been sufficiently fast to yield a good age estimate within analytical error even from data measured on different growth layers of the same sample.

Older and younger deformation phases affecting the basin (see e.g. Sachsenhofer et al., 2000, Wagreich & Strauss, 2005) could not be verified in the collected samples.

The other sampling areas (Seefeld, Leytron, Tauern Window North, Kilve) did not yield samples that appeared suitable for dating after initial LA-ICPMS screening, or the attempted dating of samples did not result in data allowing a linear regression through data points, thus, these data do not justify age interpretation. See 5 Results for some examples.

7. Conclusions and Summary

7.1 Strengths and limitations of the method

A new workflow for dating calcite samples has been presented.

The technique provides new data on tectonic events, and in a wider view, allows under favourable conditions (U/Pb ratio >> 1, Pb concentrations above LoD, elevated U concentrations) direct dating of deformation in lithologies where no other geochronometers are present.

Tectonic events from several sampling areas have been dated in this study:

- In the Gosau basin, N-S compressional tectonic movement was dated to have occurred at 29 ± 2 and 23 ± 1 Ma and NW-SE compression at ~42 Ma on the basin margin. These ages fit within established deformation phases for the region.
- ENE-WSW movement on a fault in the external Digne nappe was dated to ~9.59 ± 0.02 Ma, supported by very imprecise ages of ~8.4 ± 3.5 and ~9.7 ± 4.0 in accordance to regional tectonic studies.
- A sample of the "Mariabucher Marmor" from the margin of the Fohnsdorf basin was dated to 13.4 ± 0.8 Ma, fitting within the previously assumed formation age of the host rock.
- Fault movement on a fault in the Swiss Jura was dated to 9.05 ± 0.94 Ma, setting a maximum age for the later folding that deformed the fault plane.
- Samples from the Lower Inn Valley yielded plausible, but very imprecise ages of 27.3 ± 1.3 and ~10-15 Ma for samples that structurally fit these ages.

1D LA-ICPMS screening has proven to be a valuable, quick tool to select samples for further analysis, and subsamples for chemical processing.

The power of 2D LA-ICPMS for imaging spatial distribution of trace elements in geological samples has been demonstated. These data can reveal information about samples that is not available from other methods, at high spatial resolution and with minimal preparation.

A software package for creation of element maps was created, and the produced maps were utilised to aid in subsample selection for chemical preparation.

However, the presented method is only applicable under favourable conditions of high U/Pb ratio, little or no common lead contamination, and sufficiently high U concentrations. These conditions are often not met.

So far, no clear field criteria for selection of samples meeting above requirements could be established. Tectonic carbonate samples should be as fresh as possible, and the calcite should optically appear free of inclusions and white. Host rock lithology, stratigraphic age and tectonic setting seem not to systematically influence sample quality.

The highest precision ages are obtained by MC-ICPMS analysis involving time-consuming wet-chemical sample preparation prone to contamination and handling errors.

Detailed workflow and preparation instructions are presented that allow reproduction of the data quality presented, depending on the samples processed.

In the future, with higher-precision quadrupole-, or with higher-sensitivity MC-ICPMS, a workflow completely in situ (involving only LA-ICPMS analysis), would be

desirable. High sample throughput with minimal preparation could outweigh the disadvantages of lower-precision in individual measurements.

The technique of 2D LA-ICPMS element mapping can be further optimised if the data files produced by the laser ablation software (GeoStar) are optimised and simplified, and the presented data processing software can be greatly improved both in speed and ease of use, e.g. by adding a graphical user interface.

7.2 Possible future applications

The presented technique, in its unique application to tectonic carbonates, could provide valuable new insights in geodynamic processes, faulting processes and individual fault evolution, and the study of tectonic carbonates themselves.

In structural geology, timing of faulting processes, and thus a detailed record of fault development could be obtained.

In the energy and natural resources sector, fault activity can both generate or destroy reservoirs of gas, oil or water. Dating these events allows for more detailed basin modelling studies and risk assessment. Timing of fluid flow is also a crucial information to evaluate and explore natural metal and mineral resources.

In the public sector, detailed information of past fault activity can help assess natural hazards due to earthquakes and secondary processes like landslides and tsunamis, and may help predict location and magnitude of future events.

8. Bibliography

ALGEO, T.J. & LYONS, T.W. (2006) *Mo–total organic carbon covariation in modern anoxic marine environments: Implications for analysis of paleoredox and paleohydrographic conditions*. Paleoceanography 21. p.PA1016.

ANDERSEN, M.B., STIRLING, C.H., POTTER, E.K. & HALLIDAY, A.N. (2004) *Toward epsilon levels of measurement precision on U-234/U-238 by using MC-ICPMS*. International Journal of Mass Spectrometry 237. p.118.

ANGELIER, J. (1979) *Determination of the mean principal directions of stresses for a given fault population*. Tectonophysics 56. p.T17-T26.

ARBUZOV, S., VOLOSTNOV, A., RIKHVANOV, L., MEZHIBOR, A. & ILENOK, S. (2011) *Geochemistry of radioactive elements (U, Th) in coal and peat of northern Asia (Siberia, Russian Far East, Kazakhstan, and Mongolia)*. International Journal of Coal Geology 86. pp. 318-328.

ARROWSMITH, P. (1987) *Laser ablation of solids for elemental analysis by inductively coupled plasma mass spectrometry*. Analytical Chemistry 59. pp. 1437-1444.

ARROWSMITH, P. & HUGHES, S.K. (1988) *Entrainment and Transport of Laser Ablated Plumes for Subsequent Elemental Analysis*. Applied Spectroscopy 42. pp. 1231-1239.

BANERJEE, D., SINGHVI, A.K., PANDE, K., GOGTE, V.D. & CHANDRA, B. (1999) *Towards a direct dating of fault gouges using luminescence dating techniques - Methodological aspects*. Current Science 77. pp. 256-268.

BANNER, J.L. (2004) *Radiogenic isotopes: systematics and applications to earth surface processes and chemical stratigraphy*. Earth-Science Reviews 65. pp. 141-194.

BAR, M., KOLODNY, Y. & BENTOR, Y. (1974) *Dating faults by fission track dating of epidotes -- an attempt*. Earth and Planetary Science Letters 22. pp. 157-162.

BARGER, M. & KORETSKY, C.M. (2011) *The influence of citric acid, EDTA, and fulvic acid on U(VI) sorption onto kaolinite*. Applied Geochemistry 26. p.S158-S161.

BAROUX, E., BETHOUX, N. & BELLIER, O. (2001) *Analyses of the stress field in southeastern France from earthquake focal mechanisms*. Geophysical Journal International 145. pp. 336-348.

BECHTEL, A., GAWLICK, H., GRATZER, R., TOMASELLI, M. & PÜTTMANN, W. (2007) *Molecular indicators of palaeosalinity and depositional environment of small scale basins within carbonate platforms: The Late Triassic Hauptdolomite Wiestalstausee section near Hallein (Northern Calcareous Alps, Austria)*. Organic Geochemistry 38. pp. 92-111.

BECKER, A. (2000) *The Jura Mountains — an active foreland fold-and-thrust belt?*. Tectonophysics 321. pp. 381-406.

BECKER, M.L., RASBURY, E.T., MEYERS, W.J. & HANSON, G.N. (2004) *"U-Pb calcite age of the Late Permian Castile Formation, Delaware Basin: a constraint on the age of the Permian-Triassic boundary(?)": Reply to a comment by Ian Metcalfe*. Earth and Planetary Science Letters 217. pp. 469-471.

Belayneh, M. & Cosgrove, J.W. (2010) *Hybrid veins from the southern margin of the Bristol Channel Basin, UK*. Journal of Structural Geology 32. pp. 192-201.

Berger, A. & Bousquet, R. (2008) *Subduction-related metamorphism in the Alps; review of isotopic ages based on petrology and their geodynamic consequences*. In Siegesmund, S., Fuegenschuh, B. & Froitzheim, N. (Eds.) (2008): Tectonic aspects of the Alpine-Dinaride-Carpathian system. Geological Society of London, London. pp. 117-144.

Berra, F., Jadoul, F. & Anelli, A. (2010) *Environmental control on the end of the Dolomia Principale/Hauptdolomit depositional system in the central Alps: Coupling sea-level and climate changes*. Palaeogeography, Palaeoclimatology, Palaeoecology 290. pp. 138-150.

Blanckenburg, F., Villa, I.M., Baur, H., Morteani, G. & Steiger, R.H. (1989) *Time calibration of a PT-path from the Western Tauern Window, Eastern Alps: the problem of closure temperatures*. Contributions to Mineralogy and Petrology 101. pp. 1-11.

Bonhomme, M.G., Baubron, J. & Jebrak, M. (1987) *Minéralogie, géochimie, terres bares et âge K-Ar des argiles associées aux minéralisations filoniennes*. Chemical Geology: Isotope Geoscience section 65. pp. 321-339.

Bons, P.D. & Jessell, M.W. (1997) *Experimental simulation of the formation of fibrous veins by localised dissolution-precipitation creep*. Mineralogical Magazine 61. pp. 53-63.

Bourdon, B., Turner, S., Henderson, G.M. & Lundstrom, C.C. (2003) *Introduction to U-series Geochemistry*. Reviews in Mineralogy and Geochemistry 52. pp. 1-21.

Bousquet, R., Goffe, B., Vidal, O., Oberhänsli, R. & Patriat, M. (2002) *The tectono-metamorphic history of the Valaisan domain from the Western to the Central Alps: New constraints on the evolution of the Alps*. Geological Society of America Bulletin 114. pp. 207-225.

Bousquet, R., Oberhänsli, R., Goffé, B., Wiederkehr, M., Koller, F., Schmid, S.M., Schuster, R., Engi, M., Berger, A. & Martinotti, G. (2008) *Metamorphism of metasediments at the scale of an orogen; a key to the Tertiary geodynamic evolution of the Alps*. In Siegesmund, S., Fügenschuh, B. & Froitzheim, N. (Eds.) (2008): Tectonic aspects of the Alpine-Dinaride-Carpathian system. Geological Society of London. pp. 393-411.

Bruno, J. (1990) *The influence of dissolved carbon dioxide on trace metal speciation in seawater*. Marine Chemistry 30. pp. 231-240.

Buhay, W., Schwarcz, H. & Grün, R. (1988) *ESR dating of fault gouge: The effect of grain size*. Quaternary Science Reviews 7. pp. 515-522.

Catanzaro, E.J., Murphy, T.J., Shields, W.R. & Garner, E.L. (1968) *Absolute isotopic abundance ratios of common, equal-atom, and radiogenic lead isotopic standards*. J. Res. Nat. Bur. Stand. 72A. pp. 261-267.

Champagnac, J., Schlunegger, F., Norton, K., von Blanckenburg, F., Abbühl, L. & Schwab, M. (2009) *Erosion-driven uplift of the modern Central Alps*. Tectonophysics 474. pp. 236-249.

Champagnac, J., Sue, C., Delacou, B. & Burkhard, M. (2004) *Brittle deformation in the inner NW Alps: from early orogen-parallel extrusion to late orogen-perpendicular collapse*. Terra Nova 16. pp. 232-242.

Channell, J.E.T. & Kozur, H. (1997) *How many oceans? Meliata, Vardar, and Pindos oceans in Mesozoic Alpine paleogeography*. Geology 25. pp. 183-186.

Channell, J.E.T., Brandner, R., Spieler, A. & Stoner, J.S. (1992) *Paleomagnetism and Paleogeography of the Northern Calcareous Alps (Austria)*. Tectonics Vol 11. pp. 792-810.

Chappaz, A., Gobeil, C. & Tessier, A. (2010) *Controls on uranium distribution in lake sediments*. Geochimica et Cosmochimica Acta 74. pp. 203-214.

Chen, J., Lawrence Edwards, R. & Wasserburg, G. (1986) *238U,234U and232Th in seawater*. Earth and Planetary Science Letters 80. pp. 241-251.

Chester, R. (1990) *Marine Geochemistry*, Unwin Hyman, London. p.698.

Choo, C.O. & Chang, T.W. (2000) *Characteristics of clay minerals in gouges of the Dongrae fault, Southeastern Korea, and implications for fault activity*. Clays and Clay Minerals 48. pp. 204-212.

Christie-Blick, N. (2012) *Geological Time Conventions and Symbols*. GSA Today : a Publication of the Geological Society of America 22. pp. 28-29.

Cliff, R.A. (1985) *Isotopic dating in metamorphic belts*. Journal of the Geological Society 142. pp. 97-110.

Cliff, R.A., Spötl, C. & Mangini, A. (2010) *U-Pb dating of speleothems from Spannagel Cave, Austrian Alps: A high resolution comparison with U-series ages*. Quaternary Geochronology 5. pp. 452-458.

Cohen, A.S., Coe, A.L., Bartlett, J.M. & Hawkesworth, C.J. (1999) *Precise Re–Os ages of organic-rich mudrocks and the Os isotope composition of Jurassic seawater*. Earth and Planetary Science Letters 167. pp. 159-173.

Cole, J.M., Nienstedt, J., Spataro, G., Rasbury, E.T., Lanzirotti, A., Celestian, A.J., Nilsson, M. & Hanson, G.N. (2003) *Phosphor imaging as a tool for in situ mapping of ppm levels of uranium and thorium in rocks and minerals*. Chemical Geology 193. pp. 127-136.

Cole, J.M., Rasbury, E.T., Hanson, G.N., Montanez, I.P. & Pedone, V.A. (2005) *Using U-Pb ages of Miocene tufa for correlation in a terrestrial succession, Barstow Formation, California*. Geological Society of America Bulletin 117. pp. 276-287.

Compston, W. (1996) *SHRIMP: Origins, impact and continuing evolution*. Journal of the Royal Society of Western Australia 79. pp. 109-117.

Compston, W. (1999) *Geological age by instrumental analysis; the 29th Hallimond Lecture*. Mineralogical Magazine 63. pp. 297-311.

Compston, W. & Clement, S. (2006) *The geological microprobe: The first 25 years of dating zircons*. Applied Surface Science 252. pp. 7089-7095.

Compston, W. & Pidgeon, R.T. (1986) *Jack Hills, evidence of more very old detrital zircons in Western Australia*. Nature 321. pp. 766-769.

Compston, W., Williams, I.S. & Meyer, C. (1984) *U-Pb geochronology of zircons form lunar Breccia 73217 using a sensitive high mass-resolution ion microprobe*, In: Boynton, W.V. & Schubert G (Eds.) Lunar and Planetary Science Conference Proceedings, Lunar and Planetary Science Conference Proceedings 14. pp. 525-534.

Costa, S. & Maluski, H. (1988) *Use of the 40Ar-39Ar stepwise heating method for dating mylonite zones: An example from the St. Barthélémy massif (Northern Pyrenees, France)*. Chemical Geology: Isotope Geoscience section 72. pp. 127-144.

Cox, S.F. (1987) *Antitaxial crack-seal vein microstructures and their relationship to displacement paths*. Journal of Structural Geology 9. pp. 779-787.

Csontos, L. & Voros, A. (2004) *Mesozoic plate tectonic reconstruction of the Carpathian region*. Palaeogeography Palaeoclimatology Palaeoecology 210. pp. 1-56.

Dal Piaz, G., Bistacchi, A. & Massironi, M. (2003) *Geological outline of the Alps*. Episodes 26. pp. 175-180.

Dart, C.J., McClay, K. & Hollings, P.N. (1995) *3D analysis of inverted extensional fault systems, southern Bristol Channel basin, UK*. Geological Society, London, Special Publications 88. pp. 393-413.

Davison, I. (1995) *Fault slip evolution determined from crack-seal veins in pull-aparts and their implications for general slip models*. Journal of Structural Geology 17. pp. 1025-1034.

Decker, K., Meschede, M. & Ring, U. (1993) *Fault slip analysis along the northern margin of the Eastern Alps (Molasse, Helvetic nappes, North and South Penninic flysch, and the Northern Calcareous Alps)*. Tectonophysics 223. pp. 291-312.

Delacou, B., Sue, C., Champagnac, J. & Burkhard, M. (2004) *Present-day geodynamics in the bend of the western and central Alps as constrained by earthquake analysis*. Geophysical Journal International 158. pp. 753-774.

Delacou, B., Sue, C., Champagnac, J. & Burkhard, M. (2005) *Origin of the current stress field in the western/central Alps: Role of gravitational re-equilibration constrained by numerical modelling*. - In : . Vol. 243. , 2005.

Donofrio, D.A., Brandner, R. & Poleschinski, W. (2003) *Conodonten der Seefeld-Formation: Ein Beitrag zur Bio- und Lithostratigraphie der Hauptdolomit-Plattform (Obertrias, Westliche Nördliche Kalkalpen, Tirol)*. Geologisch-Paläontologische Mitteilungen Innsbruck 26. pp. 91-107.

Doucelance, R. & Manhès, G. (2001) *Reevaluation of precise lead isotope measurements by thermal ionization mass spectrometry: comparison with determinations by plasma source mass spectrometry*. Chemical Geology 176. pp. 361-377.

Dunk, R.M., Mills, R.A. & Jenkins, W.J. (2002) *A reevaluation of the oceanic uranium budget for the Holocene*. Chemical Geology 190. pp. 45-67.

Dunlap, W.J., Teyssier, C., McDougall, I. & Baldwin, S. (1991) *Ages of deformation from K/Ar and 40Ar/39Ar dating of white micas*. Geology 19. pp. 1213-1216.

Dunstan, L.P., Gramlich, J.W., Barnes, I.L. & Purdy, W.C. (1980) *Absolute isotopic abundance and the atomic weight of a reference sample of thallium*. J. Res. Nat. Bur. Stand. 85. pp. 1-10.

Durney, D.W. & Ramsay, J.G. (1973) *Incremental strains measured by syntectonic crystal growths*. In De Jong, K.A. & Scholten, R. (Eds.) (1973): Gravity and Tectonics. John Wiley. p.67–96.

Durrant, S.F. (1999) *Laser ablation inductively coupled plasma mass spectrometry: achievements, problems, prospects*. Journal of Analytical Atomic Spectrometry 14. pp. 1385-1403.

Duval, M., Aubert, M., Hellstrom, J. & Grün, R. (2011) *High resolution LA-ICP-MS mapping of U and Th isotopes in an early Pleistocene equid tooth from Fuente Nueva-3 (Orce, Andalusia, Spain)*. Quaternary Geochronology In Press, Corrected Proof. p.-.

Edwards, R., Gallup, C. & Cheng, H. (2003) *Uranium-series Dating of Marine and Lacustrine Carbonates*. Reviews in Mineralogy and Geochemistry 52. pp. 363-405.

Eggins, S.M. & Shelley, J.M.G. (2002) *Compositional Heterogeneity in NIST SRM 610-617 Glasses*. Geostandards and Geoanalytical Research 26. pp. 269-286.

Eggins, S.M., Grün, R., McCulloch, M.T., Pike, A.W.G., Chappell, J., Kinsley, L., Mortimer, G., Shelley, J.M.G., Murray-Wallace, C.V., Spötl, C. & Taylor, L. (2005) *In situ U-series dating by laser-ablation multi-collector ICPMS: new prospects for Quaternary geochronology*. Quaternary Science Reviews 24. p.2538.

Eggins, S.M., Grün, R., Pike, A.W.G., Shelley, M. & Taylor, L. (2003) *238U, 232Th profiling and U-series isotope analysis of fossil teeth by laser ablation-ICPMS*. Quaternary Science Reviews 22. pp. 1373-1382.

Eggins, S.M., Kinsley, L.P.J. & Shelley, J.M.G. (1998) *Deposition and element fractionation processes during atmospheric pressure laser sampling for analysis by ICP-MS*. Applied Surface Science 127-129. pp. 278-286.

Eide, E.A., Torsvik, T.H. & Andersen, T.B. (1997) *Absolute dating of brittle fault movements: Late Permian and late Jurassic extensional fault breccias in western Norway*. Terra Nova 9. pp. 135-139.

Elburg, M.A., Bons, P.D., Foden, J. & Passchier, C.W. (2002) *The origin of fibrous veins: constraints from geochemistry*, In: de Meer, S., Drury, M.R., de Besser, J.H.P. & Pennock, G.M. (Eds.) Deformation, Mechanisms, Rheology and Tectonics: Current Status and Future Perspectives, Geological Society of London Special Publications 200. pp. 103-118.

Elzinga, E.J., Tait, C.D., Reeder, R.J., Rector, K.D., Donohoe, R.J. & Morris, D.E. (2004) *Spectroscopic investigation of U(VI) sorption at the calcite-water interface*. Geochimica et Cosmochimica Acta 68. pp. 2437-2448.

Essene, E.J. (1989) *The current status of thermobarometry in metamorphic rocks*. In Daly, J.S., Cliff, R.A. & Yardley, B.W.D. (Eds.) (1989): Evolution of metamorphic belts; proceedings of the 1987 joint meeting of the Metamorphic Studies Group and IGCP project 235. Geological Society of London. pp. 1-44.

Eva, E., Solarino, S., Eva, C. & Neri, G. (1997) *Stress tensor orientation derived from fault plane solutions in the southwestern Alps*. Journal of Geophysical Research 102. pp. 8171-8185.

Eyal, Y., Kaufman, A. & Bar-Matthews, M. (1992) *Use of 230Th/U ages of striated carnotites for dating fault displacements*. Geology 20. pp. 829-832.

Fairchild, I.J., Smith, C.L., Baker, A., Fuller, L., Spötl, C., Mattey, D. & McDermott, F. (2006) *Modification and preservation of environmental signals in speleothems*. Earth-Science Reviews 75. p.153.

Fasset, J.E., Heaman, L.M. & Simonetti, A. (2011) *Direct U-Pb dating of Cretaceous and Paleocene dinosaur bones, San Juan Basin, New Mexico* . Geology 39. pp. 159-162.

Faure, G. & Mensing, T.M. (2005) *Isotopes: principles and applications*, John Wiley & Sons, Inc.. p.897.

Fillipone, J.A., Yin, A., Harrison, T.M., Gehrels, G., Smith, M. & Sample, J.C. (1995) *Age and Magnitude of Dip-Slip Faulting Deduced from Differential Cooling Histories: An Example from the Hope Fault, Northwest Montana*. The Journal of Geology 103. pp. 199-211.

Ford, M., Duchêne, S., Gasquet, D. & Vanderhaeghe, O. (2006) *Two-phase orogenic convergence in the external and internal SW Alps*. Journal of the Geological Society 163. pp. 815-826.

Fossen, H. & Dallmeyer, R.D. (1998) *40Ar/39Ar muscovite dates from the nappe region of southwestern Norway: dating extensional deformation in the Scandinavian Caledonides*. Tectonophysics 285. pp. 119-133.

Fournier, M., Agard, P. & Petit, C. (2008) *Micro-tectonic constraints on the evolution of the Barles half-window (Digne nappe, southern Alps). Implications for the timing of folding in the Valensole foreland basin*. Bull. Soc. géol. Fr. 179. pp. 551-568.

Freeman, S.R., Butler, R.W.H., Cliff, R.A. & Rex, D.C. (1998) *Direct dating of mylonite evolution: a multi-disciplinary geochronological study from the Moine Thrust Zone, NW Scotland*. Journal of the Geological Society 155. pp. 745-758.

Frisch, W., Dunkl, I. & Kuhlemann, J. (2000) *Post-collisional orogen-parallel large-scale extension in the Eastern Alps*. Tectonophysics 327. pp. 239-265.

Froude, D.O., Ireland, T.R., Kinny, P.D., Williams, I.S., Compston, W., Williams, I.R. & Myers, J.S. (1983) *Ion Microprobe identification of 4,100-4,200 Myr-old terrestrial Zircons*. Nature 304. pp. 616-618.

Fruth, I. & Scherreiks, R. (1982) *Hauptdolomit (Norian) -- stratigraphy, paleogeography and diagenesis*. Sedimentary Geology 32. pp. 195-205.

Fruth, I. & Scherreiks, R. (1984) *Hauptdolomit - Sedimentary and Paleogeographic Models (Norian, Northern Calcareous Alps)*. Geologische Rundschau 73. pp. 305-319.

Fry, N. (1992) *A robust approach to the calculation of paleostress fields from fault plane data: discussion*. Journal of Structural Geology 14. pp. 635-637.

FRYER, B.J., JACKSON, S.E. & LONGERICH, H.P. (1993) *The application of laser ablation microprobe-inductively coupled plasma-mass spectrometry (LAM-ICP-MS) to in situ (U)---Pb geochronology*. Chemical Geology 109. pp. 1-8.

FRYER, B.J., JACKSON, S.E. & LONGERICH, H.P. (1995) *The design, operation and role of the laser-ablation microprobe coupled with an inductively coupled plasma; mass spectrometer (LAM-ICP-MS) in the earth sciences*. Canadian Mineralogist 33. pp. 303-312.

GASCOYNE, M. (1992) *Geochemistry of the actinides and their daughters*. In Ivanovich, M. & Harmon, R.S. (Eds.) (1992): Uranium-series disequilibrium: Applications to Earth, marine and environmental sciences (2nd ed.). Clarendon Press, Oxford. pp. 34-61.

GERMAN, C.R. & ELDERFIELD, H. (1990) *Application of the Ce Anomaly as a Paleoredox Indicator: The Ground Rules*. Paleoceanography 5. pp. 823-833.

GETTY, S.R., ASMEROM, Y., QUINN, T.M. & BUDD, A.F. (2001) *Accelerated Pleistocene coral extinctions in the Caribbean Basin shown by uranium-lead (U-Pb) dating*. Geology 29. pp. 639-642.

GILL, R. (1997) *Modern Analytical Geochemistry*, Addison Wesley Longman Limited. p.329.

GLEN, R., HANCOCK, P. & WHITTAKER, A. (2005) *Basin inversion by distributed deformation: the southern margin of the Bristol Channel Basin, England*. Journal of Structural Geology 27. pp. 2113-2134.

GLODNY, J. & HETZEL, R. (2007) *Precise U-Pb ages of syn-extensional Miocene intrusions in the central Menderes Massif, western Turkey*. Geological Magazine 144. pp. 235-246.

GOLDSTEIN, S.J. & STIRLING, C.H. (2003) *Techniques for Measuring Uranium-series Nuclides: 1992-2002*. Reviews in Mineralogy and Geochemistry 52. pp. 23-57.

GRAY, A.L. (1985) *Solid sample introduction by laser ablation for inductively coupled plasma source mass spectrometry*. The Analyst 110. pp. 551-556.

GRÜN, R. (1989) *Electron spin resonance (ESR) dating*. Quaternary International 1. pp. 65-109.

GRUNSKY, E.C. (2002) *R: a data analysis and statistical programming environment-an emerging tool for the geosciences*. Computers & Geosciences 28. pp. 1219-1222.

GUDMUNDSSON, A. (2011) *Rock Fractures in Geological Processes*, Cambridge University Press. p.578.

GÜNTHER, D. & HATTENDORF, B. (2005) *Solid sample analysis using laser ablation inductively coupled plasma mass spectrometry*. Trends in Analytical Chemistry 24. pp. 255-265.

GÜNTHER, D., AUDÉTAT, A., FRISCHKNECHT, R. & HEINRICH, C.A. (1998) *Quantitative analysis of major, minor and trace elements in fluid inclusions using laser ablation–inductively coupled plasma mass spectrometry*. Journal of Analytical Atomic Spectrometry 13. pp. 263-270.

Günther, D., Frischknecht, R., Heinrich, C.A. & Kahlert, H. (1997) *Capabilities of an Argon Fluoride 193 nm Excimer Laser for Laser Ablation Inductively Coupled Plasma Mass Spectometry Microanalysis of Geological Materials*. Journal of Analytical Atomic Spectrometry 12. pp. 939-944.

Halter, W.E., Pettke, T. & Heinrich, C.A. (2004) *Laser-ablation ICP-MS analysis of silicate and sulfide melt inclusions in an andesitic complex I: analytical approach and data evaluation* . Contributions to Mineralogy and Petrology. Beitrage zur Mineralogie und Petrologie 147. pp. 385-396.

Hathorne, E.C., James, R.H. & Lampitt, R.S. (2009) *Environmental versus biomineralization controls on the intratest variation in the trace element composition of the planktonic foraminifera G. inflata and G. scitula* . Paleoceanography 24. p.PA4204.

Hathorne, E.C., James, R.H., Savage, P. & Alard, O. (2008) *Physical and chemical characteristics of particles produced by laser ablation of biogenic calcium carbonate*. Journal of Analytical Atomic Spectrometry 23. pp. 240-243.

Hellstrom, J., Paton, C., Woodhead, J. & Hergt, J. (2008) *Iolite: software for spatially resolved LA-(Quad and MC)-ICP-MS analysis*, In: Sylvester, P. (Ed.) Laser Ablation-ICP-MS in the Earth Sciences: Current Practices and Outstanding Issues, Mineralogical Association of Canada Short Course Series 40. pp. 343-348.

Hess, J. & Lippolt, H. (1986) *Kinetics of Ar isotopes during neutron irradiation: 39Ar loss from minerals as a source of error in 40Ar/39Ar dating*. Chemical Geology: Isotope Geoscience section 59. pp. 223-236.

Hilgers, C. & Urai, J.L. (2002) *Microstructural observations on natural syntectonic fibrous veins: implications for the growth process*. Tectonophysics 352. pp. 257-274.

Hilgers, C., Koehn, D., Bons, P. & Urai, J. (2001) *Development of crystal morphology during unitaxial growth in a progressively widening vein: II. Numerical simulations of the evolution of antitaxial fibrous veins*. Journal of Structural Geology 23. pp. 873-885.

Hippolyte, J. (2001) *Palaeostress and neotectonic analysis of sheared conglomerates: Southwest Alps and Southern Apennines*. Journal of Structural Geology 23. pp. 421-429.

Hippolyte, J., Clauzon, G. & Suc, J. (2011) *Messinian-Zanclean canyons in the Digne nappe (southern Alps): tectonic implications*. Bulletin de la Société Géologique de France 182. pp. 109-131.

Hoffmann, D., Paterson, B. & Joncкheere, R. (2008) *Measurements of the uranium concentration and distribution in a fossil equid tooth using fission tracks, TIMS and laser ablation ICPMS: Implications for ESR dating*. Radiation Measurements 43. pp. 5-13.

Holden, N.E., Bonardi, M.L., De Bièvre, P., Renne, P.R. & Villa, I.M. (2011) *IUPAC-IUGS common definition and convention on the use of the year as a derived unit of time (IUPAC Recommendations 2011)*. Pure and Applied Chemistry. Chimie Pure et Appliquee 83. pp. 1159-1162.

Hopf, H., Thiel, V. & Reitner, J. (2001) *An example for black shale development on a carbonate platform (Late Triassic, Seefeld, Austria)*. Facies 45. pp. 203-210.

Horwitz, E.P., Chiarizia, R. & Dietz, M.L. (1992) *A novel Strontium-selective extraction chromatographic resin*. Solvent Extration & Ion Exchange 10. pp. 313-336.

Hubbard, M. & Mancktelow, N.S. (1992) *Lateral displacement during Neogene convergence in the Western and Central Alps*. Geology 20. pp. 943-946.

Ikeya, M., Miki, T. & Tanaka, K. (1982) *Dating of a Fault by Electron Spin Resonance on Intrafault Materials*. Science 215. p.pp. 1392-1393.

Israelson, C., Halliday, A.N. & Buchardt, B. (1996) *U-Pb dating of calcite concretions from Cambrian black shales and the Phanerozoic time scale*. Earth and Planetary Science Letters 141. pp. 153-159.

Jackson, S.E., Longerich, H.P., Dunning, G.R. & Fryer, B.J. (1992) *The application of laser-ablation microprobe - inductively coupled plasma - mass spectrometry (LAM-ICP-MS) to in situ trace-element determination in minerals*. Canadian Mineralogist 30. pp. 1049-1064.

Jahn, B. & Cuvellier, H. (1994) *Pb-Pb and U-Pb geochronology of carbonate rocks: an assessment*. Chemical Geology 115. pp. 125-151.

Jahn, B., Bertrand-Sarfati, J., Morin, N. & Macé, J. (1990) *Direct dating of stromatolitic carbonates from the Schmidtsdrif Formation (Transvaal Dolomite), South Africa, with implications on the age of the Ventersdorp Supergroup*. Geology 18. pp. 1211-1214.

Jarvis, I. & Jarvis, K.E. (1992) *Plasma spectrometry in the earth sciences: techniques, applications and future trends*. Chemical Geology 95. pp. 1-33.

Jeffries, T.E., Jackson, S.E. & Longerich, H.P. (1998) *Application of a frequency quintupled Nd:YAG source (λ=213 nm) for laser ablation inductively coupled plasma mass spectrometric analysis of minerals*. J. Anal. At. Spectrom. 13. pp. 935-940.

Jochum, K.P., Dingwell, D.B., Rocholl, A., Stoll, B., Hofmann, A.W., Becker, S., Besmehn, A., Bessette, D., Dietze, H., Dulski, P., Erzinger, J., Hellebrand, E., Hoppe, P., Horn, I., Janssens, K., Jenner, G., Klein, M., McDonough, W., Maetz, M., Mezger, K., MÃ¼ker, C., Nikogosian, I., Pickhardt, C., Raczek, I., Rhede, D., Seufert, H., Simakin, S., Sobolev, A., Spettel, B., Straub, S., Vincze, L., Wallianos, A., Weckwerth, G., Weyer, S., Wolf, D. & Zimmer, M. (2000) *The Preparation and Preliminary Characterisation of Eight Geological MPI-DING Reference Glasses for In-Situ Microanalysis*. Geostandards Newsletter 24. pp. 87-133.

Jochum, K.P., Stoll, B., Herwig, K., Willbold, M., Hofmann, A.W., Amini, M., Aarburg, S., Abouchami, W., Hellebrand, E., Mocek, B., Raczek, I., Stracke, A., Alard, O., Bouman, C., Becker, S., Dücking, M., Brätz, H., Klemd, R., de Bruin, D., Canil, D., Cornell, D., de Hoog, C., Dalpé, C., Danyushevsky, L., Eisenhauer, A., Gao, Y., Snow, J.E., Groschopf, N., Günther, D., Latkoczy, C., Guillong, M., Hauri, E.H., Höfer, H.E., Lahaye, Y., Horz, K., Jacob, D.E., Kasemann, S.A., Kent, A.J.R., Ludwig, T., Zack, T., Mason, P.R.D., Meixner, A., Rosner, M., Misawa, K., Nash, B.P., Pfänder, J., Premo, W.R., Sun, W.D., Tiepolo, M., Vannucci, R., Vennemann, T., Wayne, D. & Woodhead, J.D. (2006) *MPI-DING reference glasses for in situ microanalysis: New reference values for element concentrations and isotope ratios*. Geochem. Geophys. Geosyst 7. p.Q02008.

Jochum, K.P., Weis, U., Stoll, B., Kuzmin, D., Yang, Q., Raczek, I., Jacob, D.E., Stracke, A., Birbaum, K., Frick, D.A., Günther, D. & Enzweiler, J. (2011) *Determination of Reference Values for NIST SRM 610–617 Glasses Following ISO Guidelines*. Geostandards and Geoanalytical Research . p.33.

Jones, C.E., Halliday, A.N. & Lohmann, K.C. (1995) *The impact of diagenesis on high-precision U-Pb dating of ancient carbonates: An example from the Late Permian of New Mexico*. Earth and Planetary Science Letters 134. pp. 409-423.

Jouanne, F., Hippolyte, J.C., Gamond, J.F. & Martinod, J. (2001) *Current deformation of the Digne Nappe (southwestern Alps) from a comparison between triangulation and GPS data* . Geophys. J Int. 144. pp. 432-440.

Kanjanapayont, P., Klötzli, U., Thöni, M., Grasemann, B. & Edwards, M.A. (2012) *Rb–Sr, Sm–Nd, and U–Pb geochronology of the rocks within the Khlong Marui shear zone, southern Thailand*. Journal of Asian Earth Sciences 56. pp. 263-275.

Kaven, J., Maerten, F. & Pollard, D. (2011) *Mechanical analysis of fault slip data: Implications for paleostress analysis*. Journal of Structural Geology 33. pp. 78-91.

Kelley, S.P., Reddy, S.M. & Maddock, R. (1994) *Laser-probe 40Ar/39Ar investigation of a pseudotachylyte and its host rock from the Outer Isles thrust, Scotland*. Geology 22. pp. 443-446.

Kelly, S.D., Newville, M.G., Cheng, L., Kemner, K.M., Sutton, S.R., Fenter, P., Sturchio, N.C. & Spötl, C. (2003) *Uranyl Incorporation in Natural Calcite*. Environmental Science & Technology 37. pp. 1284-1287.

Kelly, S.D., Rasbury, E.T., Chattopadhyay, S., Kropf, A.J. & Kemner, K.M. (2006) *Evidence of a Stable Uranyl Site in Ancient Organic-Rich Calcite*. Environmental Science & Technology 40. pp. 2262-2268.

Kendall, B.S., Creaser, R.A., Ross, G.M. & Selby, D. (2004) *Constraints on the timing of Marinoan "Snowball Earth" glaciation by 187Re–187Os dating of a Neoproterozoic, post-glacial black shale in Western Canada*. Earth and Planetary Science Letters 222. pp. 729-740.

Koehn, D. & Passchier, C.W. (2000) *Shear sense indicators in striped bedding-veins*. Journal of Structural Geology 22. pp. 1141-1151.

Kohút, M. & Sherlock, S.C. (2003) *Laser microprobe Ar-40-Ar-39 analysis of pseudotachylyte and host-rocks from the Tatra Mountains, Slovakia: evidence for late Palaeogene seismic/tectonic activity*. TERRA NOVA 15. pp. 417-424.

Komárek, M., Ettler, V., Chrastný, V. & Mihaljevic, M. (2008) *Lead isotopes in environmental sciences: A review*. Environment International 34. pp. 562-577.

Kosaka, K. & Chikashige, S. (2002) *Kinematics and age of faulting in the allochthonous fault zone between the Yorii Formation and the Yorii Welded Tuff in the northeastern Kanto Mountains*. Journal of the Geological Society of Japan 108. pp. 385-393.

Košler, J. (2007) *Laser ablation ICP-MS - a new dating tool in Earth science*. Proceedings of the Geologists' Association 118. pp. 19-24.

Kralik, M., Clauer, N., Holnsteiner, R., Huemer, H. & Kappel, F. (1992) *Recurrent fault activity in the Grimsel Test Site (GTS, Switzerland): revealed by Rb-Sr, K-Ar and tritium isotope techniques*. Journal of the Geological Society, London 149. pp. 293-301.

Kralik, M., Klima, K. & Riedmüller, G. (1987) *Dating fault gouges*. Nature 327. pp. 315-317.

Kravchenko, A. & Bullock, D.G. (1999) *A Comparative Study of Interpolation Methods for Mapping Soil Properties*. Agronomy Journal 91. pp. 393-400.

Krohe, A. (1987) *Kinematics of Cretaceous nappe tectonics in the Austroalpine basement of the Koralpe region (eastern Austria)*. Tectonophysics 136. pp. 171-196.

Kuhlemann, J. (2007) *Paleogeographic and paleotopographic evolution of the Swiss and Eastern Alps since the Oligocene*. Global and Planetary Change 58. pp. 224-236.

Kuhlemann, J. & Kempf, O. (2002) *Post-Eocene evolution of the North Alpine Foreland Basin and its response to Alpine tectonics*. Sedimentary Geology 152. pp. 45-78.

Lammerer, B. & Weger, M. (1998) *Footwall uplift in an orogenic wedge: The Tauern Window in the Eastern Alps of Europe*. Tectonophysics 285. pp. 213-230.

Langmuir, D. & Herman, J.S. (1980) *The mobility of thorium in natural waters at low temperatures*. Geochimica et Cosmochimica Acta 44. pp. 1753-1766.

Lazar, B., Enmar, R., Schossberger, M., Bar-Matthews, M., Halicz, L. & Stein, M. (2004) *Diagenetic effects on the distribution of uranium in live and Holocene corals from the Gulf of Aqaba*. Geochimica et Cosmochimica Acta 68. p.4593.

Leloup, P.H., Harrison, T.M., Ryerson, F.J., Wenji, C., Qi, L., Tapponnier, P. & Lacassin, R. (1993) *Structural, Petrological and Thermal Evolution of a Tertiary Ductile Strike-Slip Shear Zone, Diancang Shan, Yunnan*. J. Geophys. Res 98. pp. 6715-6743.

Lickorish, H.W. & Ford, M. (1998) *Sequential restoration of the external Alpine Digne thrust system, SE France, constrained by kinematic data and synorogenic sediments*. Geological Society of London, Special Publications 134. pp. 189-211.

Linzer, H., Decker, K., Peresson, H., Dell'Mour, R. & Frisch, W. (2002) *Balancing lateral orogenic float of the Eastern Alps*. Tectonophysics 354. pp. 211-237.

Lips, A.L.W., White, S.H. & Wijbrans, J.R. (1998) *40Ar/39Ar laserprobe direct dating of discrete deformational events: a continuous record of early Alpine tectonics in the Pelagonian Zone, NW Aegean area, Greece*. Tectonophysics 298. pp. 133-153.

Ludwig, K.R. (1998) *On the Treatment of Concordant Uranium-Lead Ages*. Geochimica et Cosmochimica Acta 62. pp. 665-676.

Ludwig, K.R. (1999) *Using Isoplot/Ex, Version 2.01: a geochronological toolkit for Microsoft Excel*, In: Berkeley Geochronology Center Special Publication, No. 1a, . p.47.

Ludwig, K.R. (2001) *Eliminating mass-fractionation effects on U-Pb isochron ages without double spiking*. Geochimica et Cosmochimica Acta 65. pp. 3139-3145.

Ludwig, K.R. (2003) *Mathematical-Statistical Treatment of Data and Errors for 230Th/U Geochronology*. Reviews in Mineralogy and Geochemistry 52. pp. 631-656.

Luo, X., Rehkämper, M., Lee, D. & Halliday, A.N. (1997) *High Precision 230Th/232Th and 234U/238U measurements using energy-filtered ICP magnetic sector multiple collector mass spectrometry*. International Journal of Mass Spectrometry and Ion Processes 171. pp. 105-117.

Lüschen, E., Borrini, D., Gebrande, H., Lammerer, B., Millahn, K., Neubauer, F. & Nicolich, R. (2006) *TRANSALP--deep crustal Vibroseis and explosive seismic profiling in the Eastern Alps*. Tectonophysics 414. pp. 9-38.

Lüschen, E., Lammerer, B., Gebrande, H., Millahn, K., Nicolich, R. & Grp, T.W. (2004) *Orogenic structure of the Eastern Alps, Europe, from TRANSALP deep seismic reflection profiling*. Tectonophysics 388. pp. 85-102.

Lyons, J.B. & Snellenburg, J. (1971) *Dating Faults*. Geological Society of America Bulletin 82. pp. 1749-1752.

Madritsch, H., Fabbri, O., Hagedorn, E., Preusser, F., Schmid, S. & Ziegler, P. (2010a) *Feedback between erosion and active deformation: Geomorphic constraints from the frontal Jura fold-and-thrust belt (eastern France)*. International Journal of Earth Sciences 99. pp. 103-122.

Madritsch, H., Preusser, F., Fabbri, O., Bichet, V., Schlunegger, F. & Schmid, S. (2010b) *Late Quaternary folding in the Jura Mountains: Evidence from syn-erosional deformation of fluvial meanders*. Terra Nova 22. pp. 147-154.

Mancktelow, N.S., Stöckli, D.F., Grollimund, B., Müller, W., Fügenschuh, B., Viola, G., Seward, D. & Villa, I.M. (2001) *The DAV and Periadriatic fault systems in the Eastern Alps south of the Tauern window*. International Journal of Earth Sciences 90. pp. 593-622.

Mandl, G.W. (2000) *The Alpine sector of the Tethyan shelf - Examples of Triassic to Jurassic sedimentation and deformation from the Northern Calcareous Alps*. Mitt Österr Geol Ges 92 (1999). pp. 61-77.

Marton, E. & Fodor, L. (2003) *Tertiary paleomagnetic results and structural analysis from the Transdanubian Range (Hungary): rotational disintegration of the Alcapa unit*. Tectonophysics 363. pp. 201-224.

Masuda, A., Sugino, K. & Toyoda, K. (1995) *Lead isotopic compositions in fault gouges and their parent rocks: implications for ancient fault activities*. Applied Geochemistry 10. pp. 437-446.

McGrath, A.G. & Davison, I. (1995) *Damage zone geometry around fault tips*. Journal of Structural Geology 17. pp. 1011-1024.

Means, W.D. (1987) *A newly recognized type of slickenside striation*. Journal of Structural Geology 9. pp. 585-590.

Means, W.D. & Li, T. (2001) *A laboratory simulation of fibrous veins: some first observations*. Journal of Structural Geology 23. pp. 857-863.

Meinhard, J.E. (1976) *The concentric glass nebulizer*. ICP Info. Newsl. 2. p.163.

Meyer, M., Cliff, R., Spötl, C., Knipping, M. & Mangini, A. (2009) *Speleothems from the earliest Quaternary: Snapshots of paleoclimate and landscape evolution at the northern rim of the Alps*. Quaternary Science Reviews 28. pp. 1374-1391.

Meyer, M.C., Cliff, R.A. & Spötl, C. (2011) *Speleothems and mountain uplift*. Geology 39. pp. 447-450.

Mezger, K., Rawnsley, C., Bohlen, S. & Hanson, G. (1991) *U-Pb garnet, sphene, monazite, and rutile ages: implications for the duration of high-grade metamorphism and cooling histories, Adirondack Mts., New York*. Journal of Geology 99. pp. 415-428.

Moorbath, S., Taylor, P.N., Orpen, J.L., Treloar, P. & Wilson, J.F. (1987) *First direct radiometric dating of Archaean stromatolitic limestone*. Nature 326. pp. 865-867.

Morton-Bermea, O., Rodríguez-Salazar, M.T., Hernández-Alvarez, E., García-Arreola, M.E. & Lozano-Santacruz, R. () *Lead isotopes as tracers of anthropogenic pollution in urban topsoils of Mexico City*. Chemie der Erde - Geochemistry In Press, Corrected Proof. p.-.

Mostafa, M.E. (2005) *Iterative direct inversion: An exact complementary solution for inverting fault-slip data to obtain palaeostresses*. Computers & Geosciences 31. pp. 1059-1070.

Mueller, T.G., Pusuluri, N.B., Mathias, K.K., Cornelius, P.L., Barnhisel, R.I. & Shearer, S.A. (2004) *Map Quality for Ordinary Kriging and Inverse Distance Weighted Interpolation*. Soil Science Society of America Journal. Soil Science Society of America 68. pp. 2042-2047.

Müller, W. (1998) *Isotopic dating of deformation using microsampling techniques: The evolution of the Periadriatic fault system (Alps)* (Thesis). . 1998.

Müller, W. (2003) *Strengthening the link between geochronology, textures and petrology*. Earth and Planetary Science Letters 206. pp. 237-251.

Müller, W., Aerden, D. & Halliday, A.N. (2000b) *Isotopic Dating of Strain Fringe Increments: Duration and Rates of Deformation in Shear Zones*. Science 288. pp. 2195-2198.

Müller, W., Kelley, S.P. & Villa, I.M. (2002) *Dating fault-generated pseudotachylites: comparison of 40Ar/39Ar stepwise-heating, laser-ablation and Rb-Sr microsampling analyses*. Contributions to Mineralogy and Petrology. Beitrage zur Mineralogie und Petrologie 144. pp. 57-77.

Müller, W., Mancktelow, N.S. & Meier, M. (2000a) *Rb-Sr microchrons of synkinematic mica in mylonites: an example from the DAV fault of the Eastern Alps*. Earth and Planetary Science Letters 180. pp. 385-397.

Müller, W., Prosser, G., Mancktelow, N., Villa, I., Kelley, S., Viola, G. & Oberli, F. (2001) *Geochronological constraints on the evolution of the Periadriatic Fault System (Alps)*. International Journal of Earth Sciences 90. pp. 623-653.

Müller, W., Shelley, M., Miller, P. & Broude, S. (2009a) *Initial performance metrics of a new custom-designed ArF excimer LA-ICPMS system coupled to a two-volume laser-ablation cell*. J. Anal. At. Spectrom 24. pp. 209-214.

Müller, W., Shelley, M., Miller, P. & Broude, S. (2009b) *Initial performance metrics of a new custom-designed ArF excimer LA-ICPMS system coupled to a two-volume laser-ablation cell*. Journal of Analytical Atomic Spectrometry 24. pp. 209-214.

Murakami, M. & Tagami, T. (2004) *Dating pseudotachylyte of the Nojima fault using the zircon fission-track method*. Geophysical Research Letters 31. .

Neubauer, F., Ebner, F. & Wallbrecher, E. (1995) *Geological evolution of the internal Alps, Carpathians and of the Pannonian basin: an introduction*. Tectonophysics 242. pp. 1-4.

Neubauer, F., Genser, J. & Handler, J. (2000) *The Eastern Alps: Result of a two-stage collision process*. Mitt Österr Geol Ges Bd. 92. pp. 117-134.

Neugebauer, J., Greiner, B. & Appel, E. (2001) *Kinematics of the Alpine-West Carpathian orogen and palaeogeographic implications*. Journal of the Geological Society 158. pp. 97-110.

Nier, A.O. (1940) *A Mass Spectrometer for Routine Isotope Abundance Measurements*. Review of Scientific Instruments 11. pp. 212 -216.

Och, D.J., Offler, R., Zwingmann, H., Braybrooke, J. & Graham, I.T. (2009) *Timing of brittle faulting and thermal events, Sydney region: association with the early stages of extension of East Gondwana*. Australian Journal of Earth Sciences: An International Geoscience Journal of the Geological Society of Australia 56. pp. 873 - 887.

Ortner, H. (2001a) *Growing folds and sedimentation of the Gosau Group, Muttekopf, Northern Calcareous Alps, Austria*. INTERNATIONAL JOURNAL OF EARTH SCIENCES 90. pp. 727-739.

Ortner, H. (2001b) *Cretaceous thrusting in the western part of the Northern Calcareous Alps (Austria) - evidences from synorogenic sedimentation and structural data*. Mitt. Österr. Geol. ges. 94. pp. 63-77.

Ortner, H. (2003a) *Cretaceous thrusting in the western part of the Northern Calcareous Alps (Austria) - evidences from synorogenic sedimentation and structural data*. Mitt. Österr. Geol. Ges. 94. pp. 63-77.

Ortner, H. (2003b) *Cementation and tectonics in the Inneralpine Molasse of the Lower Inn Valey*. Geologisch-Paläontologische Mitteilungen Innsbruck 26. pp. 71-89.

ORTNER, H. (2003c) *Local and far field stress- analysis of brittle deformation in the western part of the Northern Calcareous Alps*. Geologisch-Paläontologische Mitteilungen Innsbruck 26. pp. 109-136.

ORTNER, H. & STINGL, V. (2001) *Facies and basin development of the Oligocene in the Lower Inn Valley, Tyrol/Bavaria*. In Piller, W. & Rasser, M.W. (Eds.) (2001): Paleogene of the Eastern Alps. Österr. Akad. Wiss.. pp. 153-196.

ORTNER, H., REITER, F. & ACS, P. (2002) *Easy handling of tectonic data: the programs TectonicVB for Mac and TectonicsFP for Windows(TM)*. Computers & Geosciences Vol.28/10. pp. 1193-1200.

ORTNER, H., REITER, F. & BRANDNER, R. (2006) *Kinematics of the Inntal shear zone-sub-Tauern ramp fault system and the interpretation of the TRANSALP seismic section, Eastern Alps, Austria*. Tectonophysics 414. pp. 241-258.

ORTNER, H., RITTNER, M., PATON, D., BORER, J. & TRUDGILL, B. (2008) *Stratal patterns of clastic wedges in transpressive systems: Gosau Group of Muttekopf revisited*. PanGeo 2008

PALMER, M.R. & EDMOND, J.M. (1993) *Uranium in river water*. Geochimica et Cosmochimica Acta 57. pp. 4947-4955.

PARRY, W.T., BUNDS, M.P., BRUHN, R.L., HALL, C.M. & MURPHY, J.M. (2001) *Mineralogy, 40Ar/39Ar dating and apatite fission track dating of rocks along the Castle Mountain fault, Alaska*. Tectonophysics 337. pp. 149-172.

PATON, C., WOODHEAD, J.D., HELLSTROM, J.C., HERGT, J.M., GREIG, A. & MAAS, R. (2010) *Improved laser ablation U-Pb zircon geochronology through robust downhole fractionation correction*. Geochem. Geophys. Geosyst 11. p.Q0AA06.

PEACOCK, D. & SANDERSON, D. (1999) *Deformation history and basin-controlling faults in the Mesozoic sedimentary rocks of the Somerset coast*. Proceedings of the Geologists' Association 110. pp. 41-52.

PERESSON, H. & DECKER, K. (1997) *The Tertiary dynamics of the northern Eastern Alps (Austria): changing palaeostresses in a collisional plate boundary*. Tectonophysics 272/2-4. pp. 125-157.

PETIT, J.P. (1987) *Criteria for the sense of movement on fault surfaces in brittle rocks*. Journal of Structural Geology 9. pp. 597-608.

PHAN-TRONG, T. (1993) *An inverse problem for the determination of the stress tensor from polyphased fault sets and earthquake focal mechanisms*. Tectonophysics 224. pp. 393-411.

PHILLIPS, W.J. (1974) *The development of vein and rock textures by tensile strain crystalisation*. Journal of the Geological Society 130. pp. 441-448.

PICKERING, R., KRAMERS, J.D., HANCOX, P.J., DE RUITER, D.J. & WOODHEAD, J.D. (2011) *Contemporary flowstone development links early hominin bearing cave deposits in South Africa*. Earth and Planetary Science Letters 306. pp. 23-32.

PICKERING, R., KRAMERS, J.D., PARTRIDGE, T., KODOLANYI, J. & PETTKE, T. (2010) *U-Pb dating of calcite-aragonite layers in speleothems from hominin sites in South Africa by MC-ICP-MS*. Quaternary Geochronology 5. pp. 544-558.

Pickhardt, C., Dietze, H. & Becker, J.S. (2005) *Laser ablation inductively coupled plasma mass spectrometry for direct isotope ratio measurements on solid samples*. International Journal of Mass Spectrometry 242. pp. 273-280.

Plan, L., Grasemann, B., Spötl, C., Decker, K., Boch, R. & Kramers, J. (2010) *Neotectonic extrusion of the Eastern Alps: Constraints from U/Th dating of tectonically damaged speleothems* . Geology 38. pp. 483-486.

Pollard, D.D. & Fletcher, R.C. (2005) *Fundamentals Of Structural Geology*, Cambridge University Press. p.500.

Polyak, V., Hill, C. & Asmerom, Y. (2008) *Age and Evolution of the Grand Canyon Revealed by U-Pb Dating of Water Table-Type Speleothems*. Science 319. pp. 1377-1380.

Pomella, H., Klötzli, U., Scholger, R., Stipp, M. & Fügenschuh, B. (2010) *The Northern Giudicarie and the Meran-Mauls fault (Alps, Northern Italy) in the light of new paleomagnetic and geochronological data from boudinaged Eo-/Oligocene tonalites*. International Journal of Earth Sciences . pp. 1-24.

Pons-Branchu, E., Hillaire-Marcel, C., Deschamps, P., Ghaleb, B. & Sinclair, D.J. (2005) *Early diagenesis impact on precise U-series dating of deep-sea corals: Example of a 100-200-year old Lophelia pertusa sample from the Northeast Atlantic*. Geochimica et Cosmochimica Acta 69. p.4879.

Porcelli, D. & Swarzenski, P.W. (2003) *The Behavior of U- and Th-series Nuclides in Groundwater*. Reviews in Mineralogy and Geochemistry 52. pp. 317-361.

Potter, E., Stirling, C.H., Wiechert, U.H., Halliday, A.N. & Spötl, C. (2005) *Uranium-series dating of corals in situ using laser-ablation MC-ICPMS*. International Journal of Mass Spectrometry 240. p.35.

R Development Core Team (2010) *R: A Language and Environment for Statistical Computing*. R Foundation for Statistical Computing. http://www.R-project.org

Ramsay, J.G. (1980) *The crack-seal mechanism of rock deformation*. Nature 284. pp. 135-139.

Ramsay, J.G. & Huber, M.I. (1987) *The Techniques of Modern Structural Geology: Folds and Fractures*, Academic Press. p.391.

Rasbury, E.T. & Cole, J.M. (2009) *Directly dating geologic events: U-Pb dating of carbonates*. Reviews of Geophysics 47. p.RG3001.

Rasbury, E.T., Hanson, G.N., Meyers, W.J. & Saller, A.H. (1997) *Dating of the time of sedimentation using U-Pb ages for paleosol calcite*. Geochimica et Cosmochimica Acta 61. pp. 1525-1529.

Rasbury, E.T., Hanson, G.N., Meyers, W.J., Holt, W.E., Goldstein, R.H. & Saller, A.H. (1998) *U-Pb dates of Paleosols; constraints on late Paleozoic cycle durations and boundary ages*. Geology 26. pp. 403-406.

Rasbury, E.T., Meyers, W.J., Hanson, G.N., Goldstein, R.H. & Saller, A.H. (2000) *Relationship of Uranium to Petrography of Caliche Paleosols with Application to Precisely Dating the Time of Sedimentation*. JOURNAL OF SEDIMENTARY RESEARCH 70. pp. 604-618.

Ratschbacher, L., Frisch, W. & Linzer, H.G. (1991b) *Lateral extrusion in the eastern Alps, part II: structural analysis*. Tectonics 10. pp. 257-271.

Ratschbacher, L., Frisch, W., Neubauer, F., Schmid, S. & Neugebauer, J. (1989) *Extension in compressional orogenic belts: The eastern Alps*. Geology 17. pp. 404-407.

Ratschbacher, L., Merle, O., Davy, P. & Cobbold, P. (1991a) *Lateral extrusion in the eastern Alps, part I: boundary conditions and experiments scaled for gravity*. Tectonics 10. pp. 245-256.

Reed, T.B. (1961) *Induction-Coupled Plasma Torch*. Journal of Applied Physics 32. pp. 821 -824.

Reed, W.P. (1992) *Certificate of Analysis, Standard Reference Materials 612, 613*. National Institute of Standards & Technology. p.3.

Regenspurg, S., Margot-Roquier, C., Harfouche, M., Froidevaux, P., Steinmann, P., Junier, P. & Bernier-Latmani, R. (2010) *Speciation of naturally-accumulated uranium in an organic-rich soil of an alpine region (Switzerland)*. Geochimica et Cosmochimica Acta 74. pp. 2082-2098.

Reiter, F., Ortner, H. & Brandner, R. (2003) *Transalp deep seismic section as a key for understanding neotectonic activity along the Inntal fault zone*. EGS - AGU - EUG Joint Assembly 2003

Renard, F., Andréani, M., Boullier, A. & Labaume, P. (2005) *Crack-seal patterns: records of uncorrelated stress release variations in crustal rocks*. - In Gapais, D., Brun, J.P. & Cobbold, P.R. (Eds.): Geological Society of London Special Publications. Vol. 243. Geological Society of London, 2005.

Resano, M., Marzo, P., Pérez-Arantegui, J., Aramendía, M., Cloquet, C. & Vanhaecke, F. (2008) *Laser ablation-inductively coupled plasma-dynamic reaction cell-mass spectrometry for the determination of lead isotope ratios in ancient glazed ceramics for discriminating purposes*. Journal of Analytical Atomic Spectrometry 23. pp. 1182-1191.

Richards, D.A. & Dorale, J.A. (2003) *Uranium-series Chronology and Environmental Applications of Speleothems*. Reviews in Mineralogy and Geochemistry 52. pp. 407-460.

Richards, D.A., Bottrell, S.H., Cliff, R.A., Ströhle, K. & Rowe, P.J. (1998) *U-Pb dating of a speleothem of Quaternary age*. Geochimica et Cosmochimica Acta 62. pp. 3683-3688.

Ring, U. & Collins, A.S. (2005) *U–Pb SIMS dating of synkinematic granites: timing of core-complex formation in the northern Anatolide belt of western Turkey*. Journal of the Geological Society 162. pp. 289-298.

Rittner, M. & Müller, W. (2012) *2D mapping of LA-ICPMS trace element distributions using R*. Computers & Geosciences 42. pp. 152-161.

Ritz, J.F., Brown, E.T., Bourles, D.L., Philip, H., Schlupp, A., Raisbeck, G.M., Yiou, F. & Enkhtuvshin, B. (1995) *Slip rates along active faults estimated with cosmic-ray-exposure dates: Application to the Bogd fault, Gobi-Altai, Mongolia*. Geology 23. pp. 1019-1022.

ROLLAND, Y., COX, S.F. & CORSINI, M. (2009) *Constraining deformation stages in brittle-ductile shear zones from combined field mapping and 40Ar/39Ar dating: The structural evolution of the Grimsel Pass area (Aar Massif, Swiss Alps)*. Journal of Structural Geology 31. pp. 1377-1394.

ROSENBERG, C. & BERGER, A. (2009) *On the causes and modes of exhumation and lateral growth of the Alps*. Tectonics 28. .

ROSSMAN, G.R., WEIS, D. & WASSERBURG, G. (1987) *Rb, Sr, Nd and Sm concentrations in quartz*. Geochimica et Cosmochimica Acta 51. pp. 2325-2329.

SACHSENHOFER, R.F., KOGLER, A., POLESNY, H., STRAUSS, P.E. & WAGREICH, M. (2000) *The Neogene Fohnsdorf Basin: basin formation and basin inversion during lateral extrusion in the Eastern Alps (Austria)*. International Journal of Earth Sciences 89. pp. 415-430.

SANCHEZ, G., ROLLAND, Y., SCHREIBER, D., GIANNERINI, G., CORSINI, M. & LARDEAUX, J. (2010) *The active fault system of SW Alps*. Journal of Geodynamics 49. pp. 296-302.

SANDERS, D., OSTERMANN, M., BRANDNER, R. & PRAGER, C. (2010) *Meteoric lithification of catastrophic rockslide deposits: Diagenesis and significance*. Sedimentary Geology 223. pp. 150-161.

SCHERER, E., MÜNKER, C. & MEZGER, K. (2001) *Calibration of the Lutetium-Hafnium Clock*. Science 293. pp. 683-687 .

SCHLAGER, W. (2005) *Carbonate sedimentology and sequence stratigraphy*, SEPM (Society for Sedimentary Geology). p.200.

SCHMID, S.M. & KISSLING, E. (2000) *The arc of the western Alps in the light of geophysical data on deep crustal structure*. Tectonics 19. pp. 62-85.

SCHMID, S.M., FÜGENSCHUH, B., KISSLING, E. & SCHUSTER, R. (2004) *Tectonic map and overall architecture of the Alpine orogen*. Eclogae Geologicae Helvetiae 97. pp. 93-117.

SCHMID, S.M., PFIFFNER, O.A., FROITZHEIM, N., SCHÖNBORN, G. & KISSLING, E. (1996) *Geophysical-geological transect and tectonic evolution of the Swiss-Italian Alps*. Tectonics 15. pp. 1036-1064.

SCHOLZ, D. & HOFFMANN, D.L. (2011) *StalAge – An algorithm designed for construction of speleothem age models*. Quaternary Geochronology 6. pp. 369-382.

SCHOLZ, D., MANGINI, A. & FELIS, T. (2004) *U-series dating of diagenetically altered fossil reef corals*. Earth and Planetary Science Letters 218. p.178.

SELVERSTONE, J. (2004) *Are the Alps collapsing?*. Annu. Rev. Earth Planet. Sci. 33. pp. 113-132.

SEWARD, D. & MANCKTELOW, N.S. (1994) *Neogene kinematics of the Central and Western Alps; evidence from fission-track dating*. Geology 22. pp. 803-806.

SHAW, C.A., KARLSTROM, K.E., WILLIAMS, M.L., JERCINOVIC, M.J. & MCCOY, A.M. (2001) *Electron-microprobe monazite dating of ca. 1.71-1.63 Ga and ca. 1.45-1.38 Ga deformation in the Homestake shear zone, Colorado: Origin and early evolution of a persistent intracontinental tectonic zone*. Geology 29. pp. 739-742.

Sherlock, S.C., Watts, L.M., Holdsworth, R.E. & Roberts, D. (2004) *Dating fault reactivation by Ar/Ar laserprobe: an alternative view of apparently cogenetic mylonite-pseudotachylite assemblages*. Journal of the Geological Society 161. pp. 335-338.

Shibata, K. & Takagi, H. (1988) *Isotopic ages of rocks and intrafault materials along the Median Tectonic Line - An example in the Bungui-toge area, Nagano Prefecture*. Jour. Geol. Soc. Japan 94. pp. 35-50.

Shpirt, M., Punanova, S. & Strizhakova, Y. (2007) *Trace elements in black and oil shales*. Solid Fuel Chemistry 41. pp. 119-127.

Siebel, W., Hann, H.P., Danisik, M., Shang, C.K., Berthold, C., Rohrmüller, J., Wemmer, K. & Evans, N.J. (2010) *Age constraints on faulting and fault reactivation: a multi-chronological approach*. International Journal of Earth Sciences 99. pp. 1187-1197.

Sinclair, D.J., Kinsley, L.P.J. & McCulloch, M.T. (1998) *High resolution analysis of trace elements in corals by laser-ablation ICP-MS*. Geochimica et Cosmochimica Acta 62. pp. 1889-1901.

Smith, P.E. & Farquhar, R.M. (1989) *Direct dating of Phanerozoic sediments by the 238U-206Pb method*. Nature 341. pp. 518-521.

Smith, P.E., Brand, U. & Farquhar, R.M. (1994) *U-Pb systematics and alteration trends of Pennsylvanian-aged aragonite and calcite*. Geochimica et Cosmochimica Acta 58:1. pp. 313-322.

Smith, P.E., Farquhar, R.M. & Hancock, R.G. (1991) *Direct radiometric age determination of carbonate diagenesis using U-Pb in secondary calcite*. Earth and Planetary Science Letters 105. pp. 474-491.

Söderlund, U., Patchett, P., Vervoort, J.D. & Isachsen, C.E. (2004) *The 176Lu decay constant determined by Lu–Hf and U–Pb isotope systematics of Precambrian mafic intrusions*. Earth and Planetary Science Letters 219. pp. 311-324.

Sperner, B. & Zweigel, P. (2010) *A plea for more caution in fault-slip analysis*. Tectonophysics 482. pp. 29-41.

Stampfli, G.M. (2000) *Tethyan oceans* . Geological Society, London, Special Publications 173. pp. 1-23.

Stampfli, G.M., Borel, G., Cavazza, W., Mosar, J. & Ziegler, P.A. (2001a) *The paleotectonic atlas of the Peritethyan domain. CD ROM*, European Geophysical Society. .

Stampfli, G.M., Borel, G.D., Cavazza, W., Mosar, J. & Ziegler, P.A. (2001b) *Palaeotectonic and palaeogeographic evolution of the western Tethys and PeriTethyan domain (IGCP Project 369)* . Episodes 24. pp. 222-228.

Stern, K.H. (2000) *High Temperature Properties and Thermal Decomposition of Inorganic Salts with Oxyanions*, Taylor & Francis. p.288.

Stirling, C.H., Lee, D.-., Christensen, J.N. & Halliday, A.N. (2000) *High-precision in situ 238U-234U-230Th isotopic analysis using laser ablation multiple-collector ICPMS*. Geochimica et Cosmochimica Acta 64. pp. 3737-3750.

Strauss, P., Wagreich, M. & Decker, K. (2001) *Tectonics and sedimentation in the Fohnsdorf-Seckau Basin (Miocene, Austria): from a pull-apart basin to a half-graben*. Inernational Journal of Earth Sciences 90. pp. 549-559.

Sue, C. (2003) *Neogene to ongoing normal faulting in the inner western Alps: A major evolution of the late alpine tectonics*. Tectonics 22. p.1050.

Sue, C. & Tricart, P. (2002) *Widespread post-nappe normal faulting in the Internal Western Alps: a new constraint on arc dynamics* . Journal of the Geological Society, London 159. pp. 61-70.

Takagi, H., Shibata, K. & Uchiumi, S. (1991) *K-Ar ages of fault gouges and felsite dykes from the Median Tectonic Line in Chubu Region, central Japan*. Journal of the Geological Society of Japan 97. pp. 377-384.

Tanaka, H., Saka, Y., Abe, T., Kohama, S. & Tetsumaru, I. (1992) *Fault gouges and their K-Ar ages from the Akaishi Tectonic Line, central Japan*. Journal of the Geological Society of Japan 98. pp. 39-48.

Tanaka, H., Uehara, N. & Itaya, T. (1995) *Timing of the cataclastic deformation along the Akaishi Tectonic Line, central Japan*. Contributions to Mineralogy and Petrology 120. pp. 150-158.

Taylor, S.R. & McLennan, S.M. (1985) *The continental crust: Its composition and evolution*, Blackwell Scientific Publications. p.328.

Tera, F. & Wasserburg, G.J. (1972) *U-Th-Pb systematics in three Apollo 14 basalts and the problem of initial Pb in lunar rocks*. Earth and Planetary Science Letters 14. pp. 281-304.

Thirlwall, M.F. (1991) *Long-term reproducibility of multicollector Sr and Nd isotope ratio analysis*. Chemical Geology: Isotope Geoscience section 94. pp. 85-104.

Thirlwall, M.F. (2002) *Multicollector ICP-MS analysis of Pb isotopes using a 207pb-204pb double spike demonstrates up to 400 ppm/amu systematic errors in Tl-normalization*. Chemical Geology 184. pp. 255-279.

Thompson, L.M., Spray, J.G. & Kelley, S.P. (1998) *Laser probe argon-40/argon-39 dating of pseudotachylyte from the Sudbury Structure: Evidence for postimpact thermal overprinting in the North Range*. Meteoritics & Planetary Science 33. pp. 1259-1269.

Thöny, W., Ortner, H. & Scholger, R. (2006) *Paleomagnetic evidence for large en-bloc rotations in the Eastern Alps during Neogene orogeny*. Tectonophysics 414. pp. 169-189.

Todt, W., Cliff, R.A., Hanser, A. & Hofmann, A.W. (1996) *Evaluation of a 202Pb - 205Pb double spike for high-precision lead isotope analysis*. In Basu, A. & Hart, S.R. (Eds.) (1996): Earth Processes: Reading the Isotopic Code. American Geophysical Union. pp. 429-437.

Torsvik, T.H., Sturt, B.A., Swensson, E., Andersen, T.B. & Dewey, J.F. (1992) *Palaeomagnetic dating of fault rocks: evidence for Permian and Mesozoic movements and brittle deformation along the extensional Dalsfjord Fault, western Norway*. Geophysical Journal International 109. pp. 565-580.

Tribovillard, N., Algeo, T.J., Lyons, T. & Riboulleau, A. (2006) *Trace metals as paleoredox and paleoproductivity proxies: An update*. Chemical Geology 232. pp. 12-32.

Twiss, R.J. & Moores, E.M. (1992) *Structural Geology*, W.H. Freeman. p.532.

Ulrich, T., Kamber, B.S., Jugo, P.J. & Tinkham, D.K. (2009) *Imaging element-distribution patterns in minerals by Laser Ablation - Inductively Coupled Plasma - Mass Spectrometry (LA-ICP-MS)*. Canadian Mineralogist 47. pp. 1001-1012.

Urai, J., Williams, P. & van Roermund, H. (1991) *Kinematics of crystal growth in syntectonic fibrous veins*. Journal of Structural Geology 13. pp. 823-836.

Ustaszewski, K. & Schmid, S. (2006) *Control of preexisting faults on geometry and kinematics in the northernmost part of the Jura fold-and-thrust belt*. Tectonics 25. .

Ustaszewski, K. & Schmid, S. (2007) *Latest Pliocene to recent thick-skinned tectonics at the Upper Rhine Graben - Jura Mountains junction*. Swiss Journal of Geosciences 100. pp. 293-312.

van der Pluijm, B.A., Hall, C.M., Vrolijk, P.J., Pevear, D.R. & Covey, M.C. (2001) *The dating of shallow faults in the Earth's crust*. Nature 412. pp. 172-175.

van der Pluijm, B.A., Vrolijk, P.J., Pevear, D.R., Hall, C.M. & Solum, J. (2006) *Fault dating in the Canadian Rocky Mountains: Evidence for late Cretaceous and early Eocene orogenic pulses*. Geology 34. pp. 837-840.

Venables, W.N. & Ripley, B.D. (2002) *Modern Applied Statistics with S*, Springer. .

Vrolijk, P. & van der Pluijm, B.A. (1999) *Clay gouge*. Journal of Structural Geology 21. pp. 1039-1048.

Wagreich, M. (1988) *Sedimentologie und Beckenentwicklung des tieferen Abschnittes (Santon-Untercampan) der Gosauschichtgruppe von Gosau und Rußbach (Oberösterreich - Salzburg)*. Jb. Geol. B.-A. 131. pp. 663-685.

Wagreich, M. (1995) *Subduction Tectonic Erosion and Late Cretaceous Subsidence Along the Northern Austroalpine Margin (Eastern Alps, Austria)*. Tectonophysics 242. pp. 63-78.

Wagreich, M. & Decker, K. (2001) *Sedimentary tectonics and subsidence modelling of the type Upper Cretaceous Gosau basin (Northern Calcareous Alps, Austria)*. International Journal of Earth Sciences 90. pp. 714-726.

Wagreich, M. & Faupl, P. (1994) *Palaeogeography and geodynamic evolution of the Gosau Group of the Northern Calcareous Alps (Late Cretaceous, Eastern Alps, Austria)*. Palaeogeography, Palaeoclimatology, Palaeoecology 110. pp. 235-254.

Wagreich, M. & Strauss, P.E. (2005) *Source area and tectonic control on alluvial-fan development in the Miocene Fohnsdorf intramontane basin, Austria*. Geological Society, London, Special Publications 251. pp. 207-216.

Wagreich, M., Summesberger, H. & Kroh, A. (2010) *Late Santonian bioevents in the Schattau section, Gosau Group of Austria - implications for the Santonian-Campanian boundary stratigraphy*. Cretaceous Research 31. pp. 181-191.

Walker, J., Cliff, R.A. & Latham, A.G. (2006) *U-Pb Isotopic Age of the StW 573 Hominid from Sterkfontein, South Africa*. Science 314. pp. 1592-1594.

WANG, Y.S., ZHU, G., HU, Z.Q., ZHANG, B.L., XIANG, B.W. & XIE, C.L. (2009) *K-Ar dating of extensional fault gouge from the Yi-Shu segment of the Tan-Lu fault zone*. Science in China Series D - Earth Sciences 52. pp. 489-503.

WANG, Z.H. & LU, H.F. (2000) *Ductile deformation and 40Ar/39Ar dating of the Changle-Nanao ductile shear zone, southeastern China*. Journal of Structural Geology 22. pp. 561-570.

WANG, Z.S., RASBURY, E.T., HANSON, G.N. & MEYERS, W.J. (1998) *Using the U-Pb system of calcretes to date the time of sedimentation of clastic sedimentary rocks*. Geochimica et Cosmochimica Acta 62. pp. 2823-2835.

WASSERBURG, G.J. & HAYDEN, R.J. (1955) *A40-K40 dating*. Geochimica et Cosmochimica Acta 7. pp. 51-60.

WASSERBURG, G.J., HAYDEN, R.J. & JENSEN, K.J. (1956) *A40-K40 dating of igneous rocks and sediments*. Geochimica et Cosmochimica Acta 10. pp. 153-165.

WASSERBURG, G.J., JACOUSEN, S.B., DEPAOLO, D.J., MCCULLOCH, M.T. & WEN, T. (1981) *Precise determination of ratios, Sm and Nd isotopic abundances in standard solutions*. Geochimica et Cosmochimica Acta 45. pp. 2311-2323.

WATKINSON, I., ELDERS, C. & HALL, R. (2008) *The kinematic history of the Khlong Marui and Ranong Faults, southern Thailand*. Journal of Structural Geology 30. pp. 1554-1571.

WEIS, D. & WASSERBURG, G. (1987) *Rb-Sr and Sm-Nd isotope geochemistry and chronology of cherts from the Onverwacht Group (3.5 AE), South Africa*. Geochimica et Cosmochimica Acta 51. pp. 973-984.

WELTJE, L., HEIDENREICH, H., ZHU, W., WOLTERBEEK, H.T., KORHAMMER, S., DE GOEIJ, J.J.M. & MARKERT, B. (2002) *Lanthanide concentrations in freshwater plants and molluscs, related to those in surface water, pore water and sediment. A case study in The Netherlands*. The Science of the Total Environment 286. pp. 191-214.

WENDT, I. (1984) *A three-dimensional U-Pb discordia plane to evaluate samples with common lead of unknown isotopic composition*. Chemical Geology 46. pp. 1-12.

WENDT, I. (1989) *Geometric considerations of the three-dimensional U/Pb data presentation*. Earth and Planetary Science Letters 94. pp. 231-235.

WENDT, I. & CARL, C. (1985) *U/Pb dating of discordant 0.1 Ma old secondary U minerals*. Earth and Planetary Science Letters 73. pp. 278-284.

WETHERILL, G.W. (1956) *Discordant uranium-lead ages.*. Trans. Am. Geophys. Union 37. pp. 320-326.

WETHERILL, G.W. (1963) *Discordant uranium-lead ages - Pt. 2; discordant ages resulting from diffusion of lead and uranium*. Journal of Geophysical Research 68. pp. 2957-2965.

WICKHAM, J.S. (1973) *An estimate of strain increments in a naturally deformed carbonate rock*. American Journal of Science 273. pp. 23-47.

WILL, T.M. & POWELL, R. (1991) *A robust approach to the calculation of paleostress fields from fault plane data*. Journal of Structural Geology 13. pp. 813-821.

Will, T.M. & Powell, R. (1992) *A robust approach to the calculation of paleostress fields from fault plane data: reply*. Journal of Structural Geology 14. pp. 639-640.

Williams, P. (1985) *Secondary Ion Mass Spectrometry*. Annu. Rev. Mater. Sci 15. pp. 517-548.

Willingshofer, E., Neubauer, F. & Cloetingh, S. (1999) *The significance of Gosau-type basins for the late cretaceous tectonic history of the Alpine-Carpathian belt*. Physics and Chemistry of the Earth, Part A: Solid Earth and Geodesy 24. pp. 687-695.

Wiltschko, D.V. & Morse, J.W. (2001) *Crystallization pressure versus "crack seal" as the mechanism for banded veins*. Geology 29. p.79-a-82.

Wölfler, A., Kurz, W., Fritz, H. & Stüwe, K. (2011) *Lateral extrusion in the Eastern Alps revisited: Refining the model by thermochronological, sedimentary, and seismic data*. Tectonics 30. .

Woodhead, J.D. & Hergt, J.M. (1997) *Application of the `double spike' technique to Pb-isotope geochronology*. Chemical Geology 138. pp. 311-321.

Woodhead, J.D., Hellstrom, J., Hergt, J.M., Greig, A. & Maas, R. (2007) *Isotopic and Elemental Imaging of Geological Materials by Laser Ablation Inductively Coupled Plasma-Mass Spectrometry*. Geostandards and Geoanalytical Research 31. pp. 331-343.

Woodhead, J.D., Hellstrom, J., Maas, R., Drysdale, R., Zanchetta, G., Devine, P. & Taylor, E. (2006) *U-Pb geochronology of speleothems by MC-ICPMS*. Quaternary Geochronology 1. p.221.

Woodhead, J.D., Hergt, J., Meffre, S., Large, R.R., Danyushevsky, L. & Gilbert, S. (2009) *In situ Pb-isotope analysis of pyrite by laser ablation (multi-collector and quadrupole) ICPMS*. Chemical Geology 262. pp. 344-354.

Woodhead, J.D., Volker, F. & McCulloch, M.T. (1995) *Routine lead isotope determinations using a lead-207-lead-204 double spike: a long-term assessment of analytical precision and accuracy*. The Analyst 120. pp. 35-39.

Wortmann, U., Weissert, H., Funk, H. & Hauck, J. (2001) *Alpine plate kinematics revisited: The Adria problem*. Tectonics 20. pp. 134-147.

Wright, J., Schrader, H. & Holser, W.T. (1987) *Paleoredox variations in ancient oceans recorded by rare earth elements in fossil apatite*. Geochimica et Cosmochimica Acta 51. pp. 631-644.

York, D. (1969) *Least squares fitting of a straight line with correlated errors*. Earth and Planetary Science Letters 5. pp. 320-324.

York, D., Evensen, N.M., López Martínez, M. & De Basabe Delgado, J. (2004) *Unified equations for the slope, intercept, and standard errors of the best straight line*. Am. J. Phys. 72. pp. 367-375.

Zheng, Y. (1989) *On the use of a three-dimensional method in solving the U-Pb two-stage model*. Geochem. J. 23. pp. 37-43.

Zheng, Y. (1990) *A further three-dimensional U-Pb method for solving the two-stage episodic model*. Geochemical Journal 24. pp. 29-37.

ZHENG, Y. (1992) *The three-dimensional U−Pb method: generalized models and implications for U−Pb two-stage systematics*. Chemical Geology 100. pp. 3-18.

ZHU, B., BECKER, H., JIANG, S., PI, D., FISCHER-GÖDDE, M. & YANG, J. (2012) *Re–Os geochronology of black shales from the Neoproterozoic Doushantuo Formation, Yangtze platform, South China*. Precambrian Research . p.-.

ZIEGLER, P. & FRAEFEL, M. (2009) *Response of drainage systems to Neogene evolution of the Jura fold-thrust belt and Upper Rhine Graben*. Swiss Journal of Geosciences 102. pp. 57-75.

ZIELINSKI, R.A. & MEIER, A.L. (1988) *The association of uranium with organic matter in Holocene peat: An experimental leaching study*. Applied Geochemistry 3. pp. 631-643.

ZOU, H. (2007) *Quantitative Geochemistry*, Imperial College Press. p.287.

ZWINGMANN, H. & MANCKTELOW, N. (2004) *Timing of Alpine fault gouges*. Earth and Planetary Science Letters 223. pp. 415-425.

ZWINGMANN, H., OFFLER, R., WILSON, T. & COX, S. (2004) *K-Ar dating of fault gouge in the northern Sydney Basin, NSW, Australia--implications for the breakup of Gondwana*. Journal of Structural Geology 26. pp. 2285-2295.

ZWINGMANN, H., YAMADA, K. & TAGAMI, T. (2010) *Timing of brittle deformation within the Nojima fault zone, Japan*. Chemical Geology 275. pp. 176-185.

9. Appendices

9.1 Appendix A: Rittner, M. & Müller, W. (2011) 2D mapping of LA-ICPMS trace element distributions using R

Due to copyrights held by Elsevier publishing, the article can not be included as an appendix in this online available version of the present work. Please find the article at the "Computers and Geosciences" homepage:

www.elsevier.com/locate/cageo

or with this reference:

doi:10.1016/j.cageo.2011.07.016

9.2 Appendix B: Clean lab workflow monitoring sheets

Sr-Spec (Pb) workflow

Date:	

250 mg cc in 2 M HNO3, 100 µL resin bed w/ 100 µL prefilter

	8 M HCl hp	8M HCl TD	2 M HNO3	H2O	sample, column no., vial no.	remarks
cleaning empty column		1 RV				
resin loading						
cleaning resin		1 RV				
		1 RV				
	1 RV					
conditioning			0.1 ml			
			0.2 ml			
			0.2 ml			
sample loading			(~2.6 ml)			
rinsing			0.4 ml			
			0.4 ml			
					collect in vial no.	collect → TRU, 7ml vials
Sr elution				0.1 ml		
				0.3 ml		
				0.6 ml		
					collect in vial no.	normally not collected
Pb elution	0.1 ml					
	0.3 ml					
	0.8 ml					
					collect in vial no.	3ml vials
2nd pass:						
dry down Pb fraction, add 100µl 15M HNO_3, dry down again, redissolve in 0.5ml 2M HNO3 (briefly on hotplate)						
cleaning resin	1 RV					keep same resin
conditioning			0.1 ml			
			0.2 ml			
			0.2 ml			
sample loading			0.5 ml			
rinsing			0.5 ml			
			0.5 ml			
Sr elution				0.1 ml		
				0.3 ml		
				0.6 ml		
					collect in vial no. (if collected w/Pb before)	normally not collected
Pb elution	0.1 ml					
	0.3 ml					
	0.8 ml					
					collect in vial no.	same vials (rinsed)
dry down, add 100µl 15M HNO_3, dry down again.						

TRU (U) workflow

Date:	

250 mg cc in 2 M HNO3, 100 µL resin bed w/ 100 µL prefilter

	0.2 M HCl	0.1M – 0.3M HCl - HF	2 M HNO3	3 M HCl	sample, column no.												remarks
cleaning empty column																	
resin loading																	
cleaning resin	6 ml	6 ml															
conditioning			0.1 ml 0.2 ml 0.2 ml														
sample loading			(~2.6 ml)														
rinsing			0.4 ml 0.4 ml														
major elements			0.5 ml 0.5 ml														
REE elution				0.1 ml 0.3 ml 0.5 ml 0.5 ml													
Th elution	0.1 ml 0.3 ml 0.7 ml 0.7 ml																
U elution		0.1 ml 0.3 ml 0.7 ml 0.7 ml															
					collect in vial no.												can use same vials, refluxed

dry down, add 200µl 2M HNO_3, dry down again.

9.3 Appendix C: Sample localities

outcrop	GPS point	longitude	latitude	elevation [m]
DGN02	158	6.305134	44.28578	1191.4
DGN03	157	6.304815	44.286351	1199.1
DGN04	159	6.306845	44.285543	1173.4
DGN05	160	6.273171	44.208515	801.4
DGN06	151	6.276016	44.216408	825.2
DGN07	161	6.246005	44.230237	1115.5
DGN08	162	6.246365	44.230214	1098.4
DGN09	163	6.247368	44.23003	1078.7
DGN10	164	6.167012	44.17415	943.7
DGN11	165	6.149257	44.161691	795.1
DGN30	260	6.088289	44.244647	1215.9
DGN55	300	6.23525	44.21793	1501.9
FOB27	247	14.572988	47.232295	855.2
FOB28	248	14.703477	47.152132	783.8
FOB29	249	14.844677	47.163522	923.9
GOB17	235	13.531949	47.553504	982.1
GOB18	236	13.550964	47.563012	1190.7
GOB19	237	13.535475	47.545191	1426.7
GOB20	238	13.536483	47.544404	1428.4
GOB21	240	13.514704	47.549978	787.0
GOB22	241	13.413808	47.625768	1285.6
GOB23	242	13.413568	47.625612	1285.4
GOB24	244	13.386225	47.612206	1160.4
GOB25	245	13.367385	47.603554	953.0
GOB26	246	13.461657	47.588414	801.9
GOB49, 50, 51	292	13.459896	47.567306	944.9
GOB52	293	13.513265	47.583139	1024.6
GOB53	294	13.497794	47.585596	1038.3
GOB54	295	13.490618	47.585508	1064.3
KIL40	280	-3.225128	51.192967	2.3
KIL41	281	-3.221172	51.193316	7.3
KIL42	283	-3.217348	51.194038	8.3
KIL43	284	-3.335941	51.183248	8.1
LEY12	224	7.868697	46.308876	681.5
LEY13	228	7.679341	46.313816	954.9
LEY14	229	7.679554	46.313854	956.6
LEY15	231	7.24834	46.209125	631.7
LEY16	233	7.209679	46.193124	617.3
LIV31	266	12.183326	47.586007	579.6
LIV32	267	12.177916	47.532008	638.7
LIV33	268	12.173977	47.531202	688.7
LIV34	269	12.125127	47.497929	822.8
LIV35	270	12.124192	47.496819	846.6
LIV36	271	12.12456	47.498757	829.0
LIV37	272	12.124366	47.498944	825.9
SEF38	273	11.217184	47.323683	1549.3
SEF39	274	11.218203	47.32376	1569.5
TNF44	288	12.974696	47.285424	1028.2
TNF45	289	12.973919	47.284408	900.4
TNF46, 47	290	13.193155	47.31061	858.6
TNF48	291	13.193561	47.30793	706.0

9.4 Appendix D: Detailed LA analyses data

1D LA-ICPMS tracks

Following, the 1D LA-ICPMS tracks analysed for sample screening are listed. The 2D mappings comprised of a large number of individual tracks, one representative track per mapping is presented here.

Host rock and clay impurities, indicated by elevated Al and Si values, can not be quantified (Ca concentration of calcite is assumed as internal standard), the information about the presence of other minerals is of qualitative nature only.

Not all analysed elements are plotted, to make the main features of samples, mainly U and Pb concentrations, and Al/Si peaks easier visible.

Digne

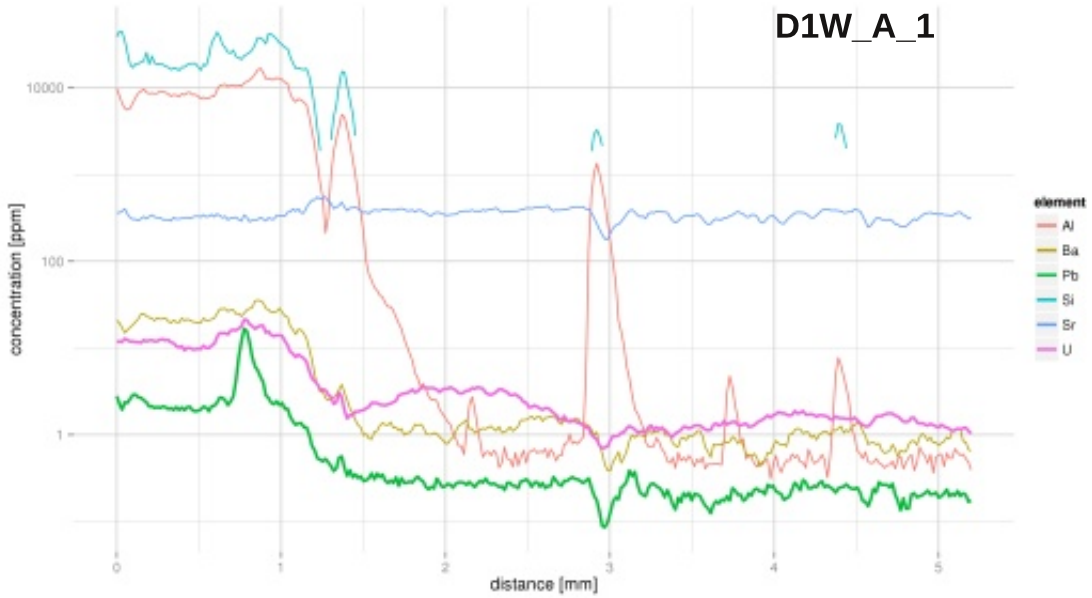
D1W_A_1
10000
100
1
concentration [ppm]
0
1
2
3
4
5
distance [mm]
element
Al
Ba
Pb
Si
Sr
U

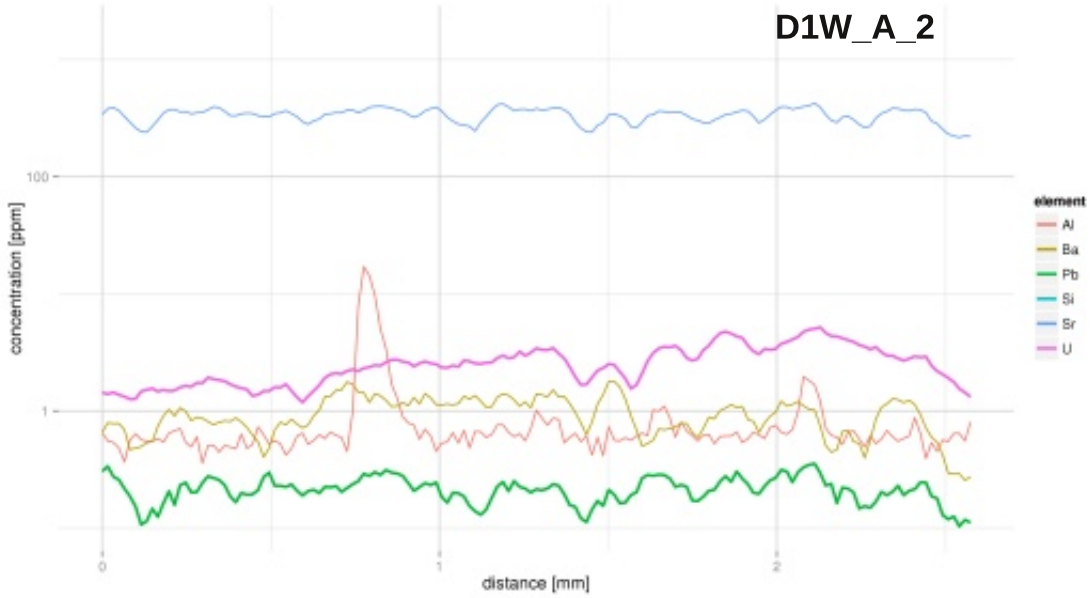
D1W_A_2
100
1
concentration [ppm]
0
1
2
distance [mm]
element
Al
Ba
Pb
Si
Sr
U

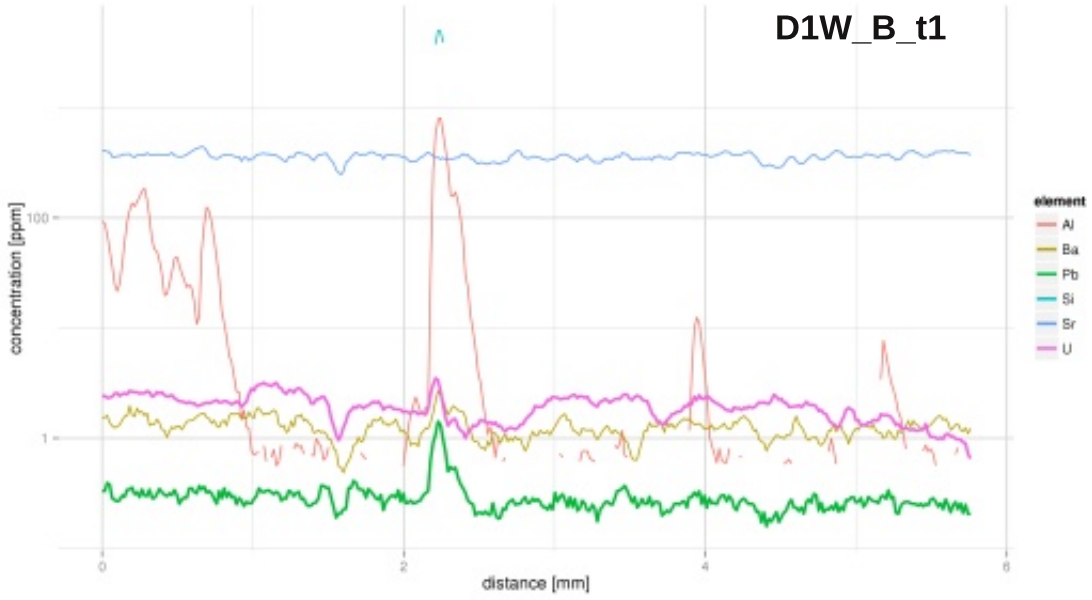
D1W_B_t1
concentration [ppm]
100
1
0
2
4
6
distance [mm]
element
Al
Ba
Pb
Si
Sr
U

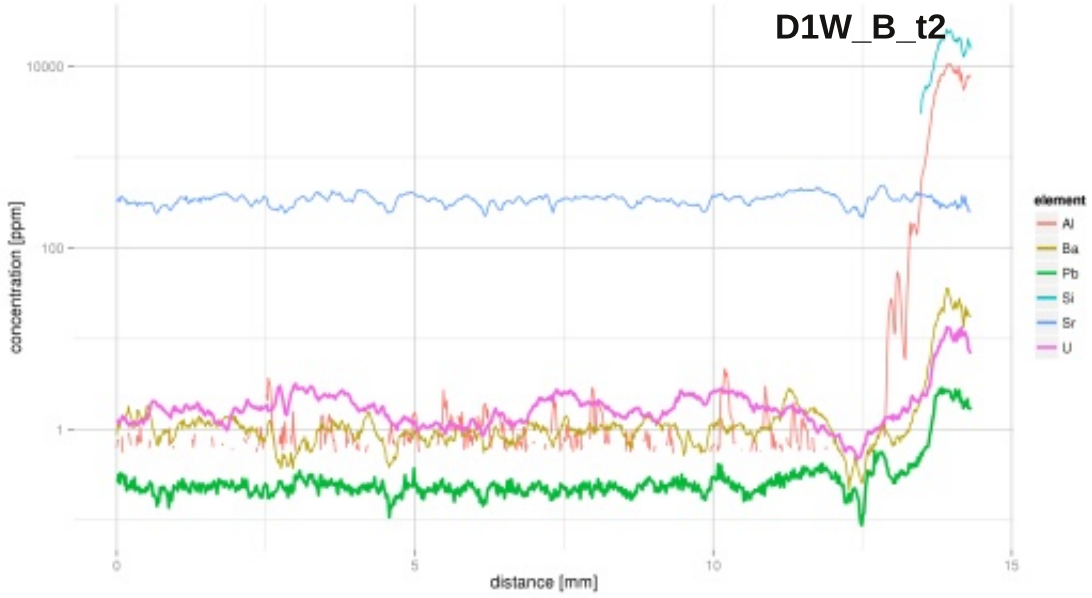
D1W_B_t2
concentration [ppm]
10000
100
1
0
5
10
15
distance [mm]
element
Al
Ba
Pb
Si
Sr
U

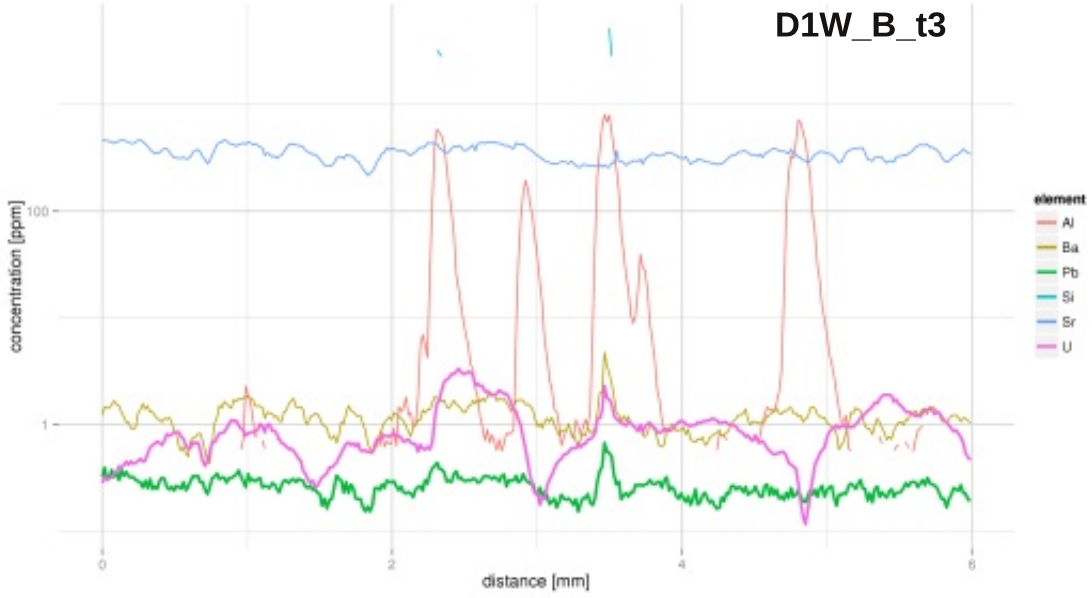
D1W_B_t3
concentration [ppm]
100
1
0
2
4
6
distance [mm]
element
Al
Ba
Pb
Si
Sr
U

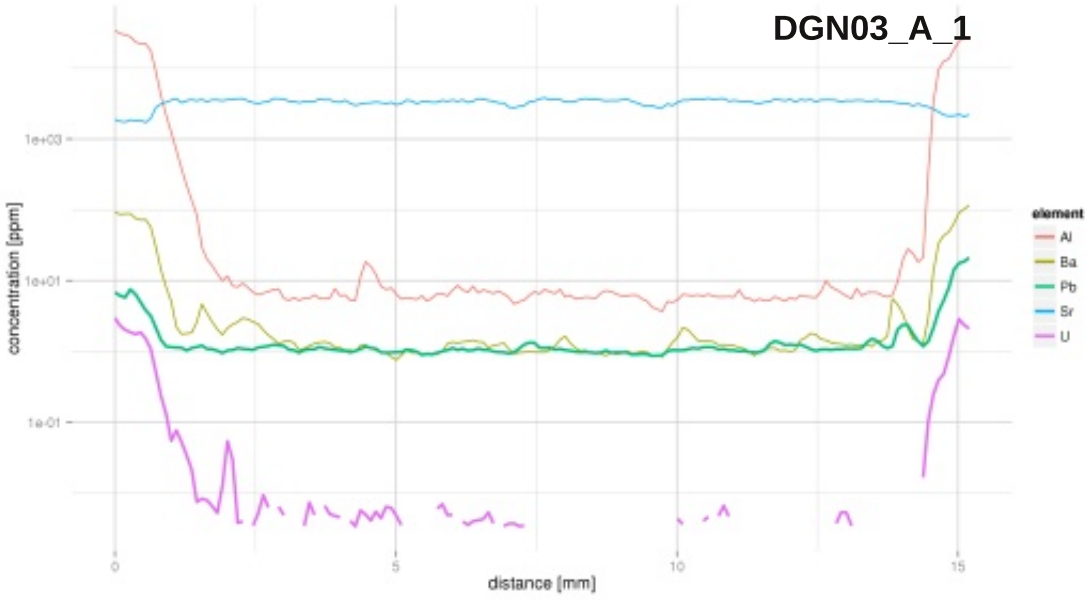
DGN03_A_1
concentration [ppm]
1e+03
1e+01
1e-01
0
5
10
15
distance [mm]
element
Al
Ba
Pb
Sr
U


DGN03_A_2
concentration [ppm]
1e+05
1e+03
1e+01
1e-01
0
5
10
15
distance [mm]
element
Al
Ba
Pb
Sr
U

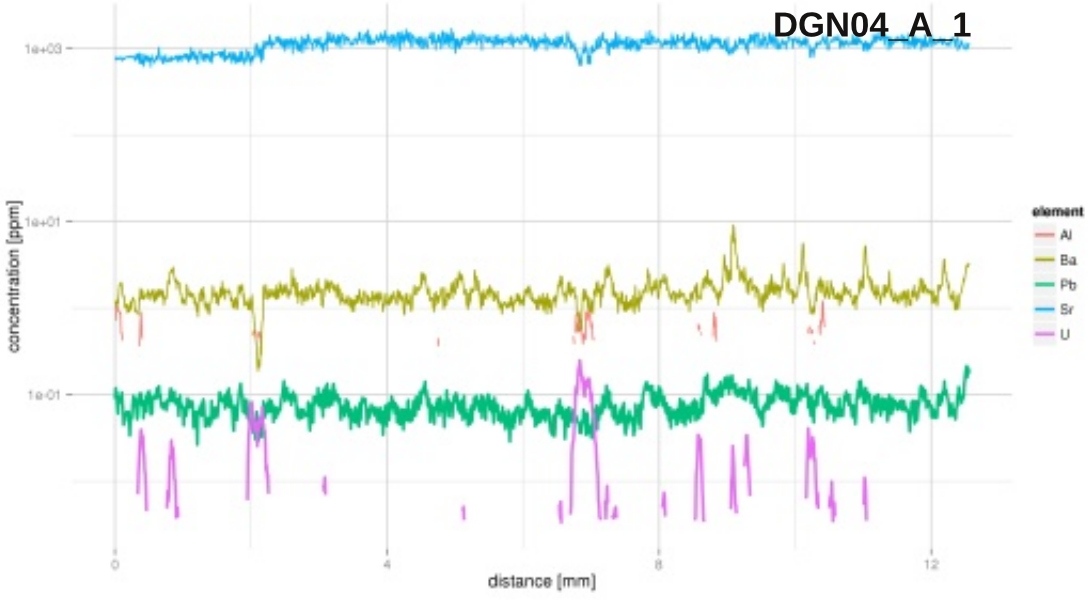
DGN04_A_1
concentration [ppm]
1e+03
1e+01
1e-01
0
4
8
12
distance [mm]
element
Al
Ba
Pb
Sr
U

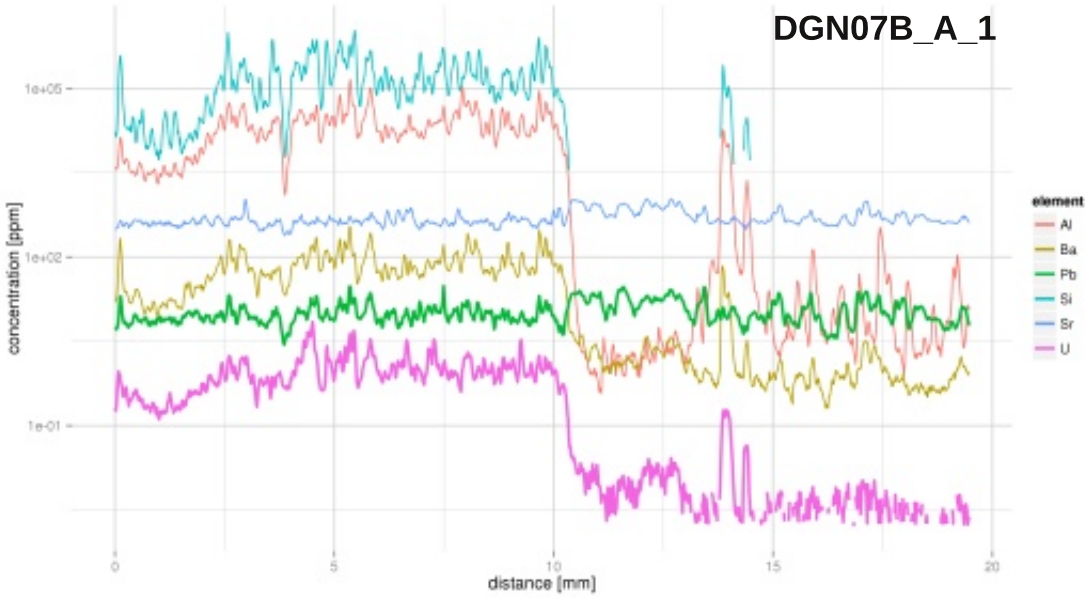
DGN07B_A_1
concentration [ppm]
1e+05
1e+02
1e-01
0
5
10
15
20
distance [mm]
element
Al
Ba
Pb
Si
Sr
U


DGN09_A_1
concentration [ppm]
1e+05
1e+03
1e+01
1e-01
0
5
10
15
distance [mm]
element
Al
Ba
Pb
Sr
U

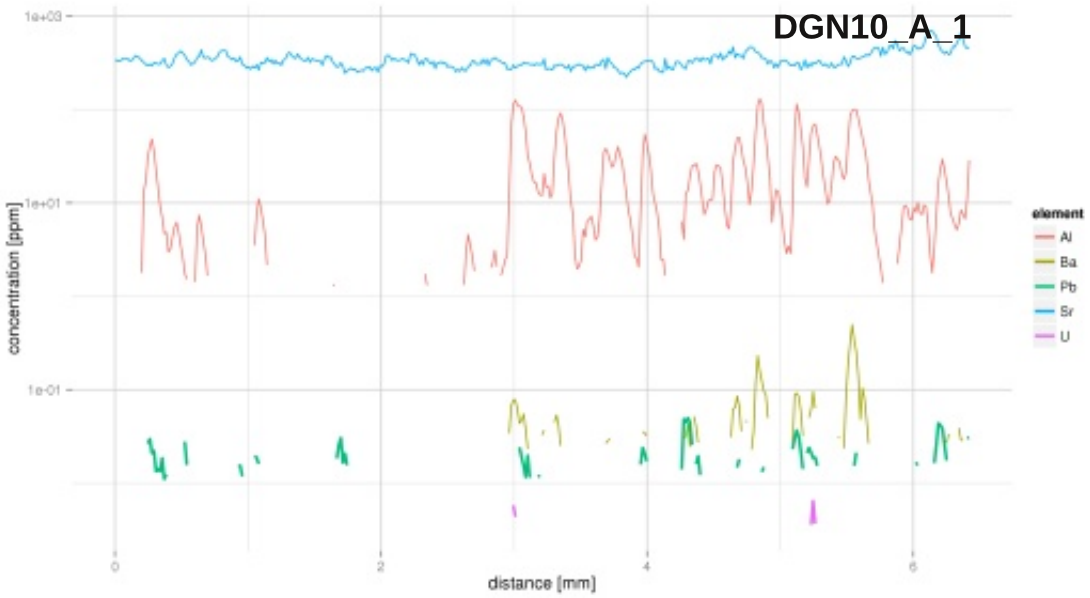
DGN10_A_1
concentration [ppm]
1e+03
1e+01
1e-01
0
2
4
6
distance [mm]
element
Al
Ba
Pb
Sr
U

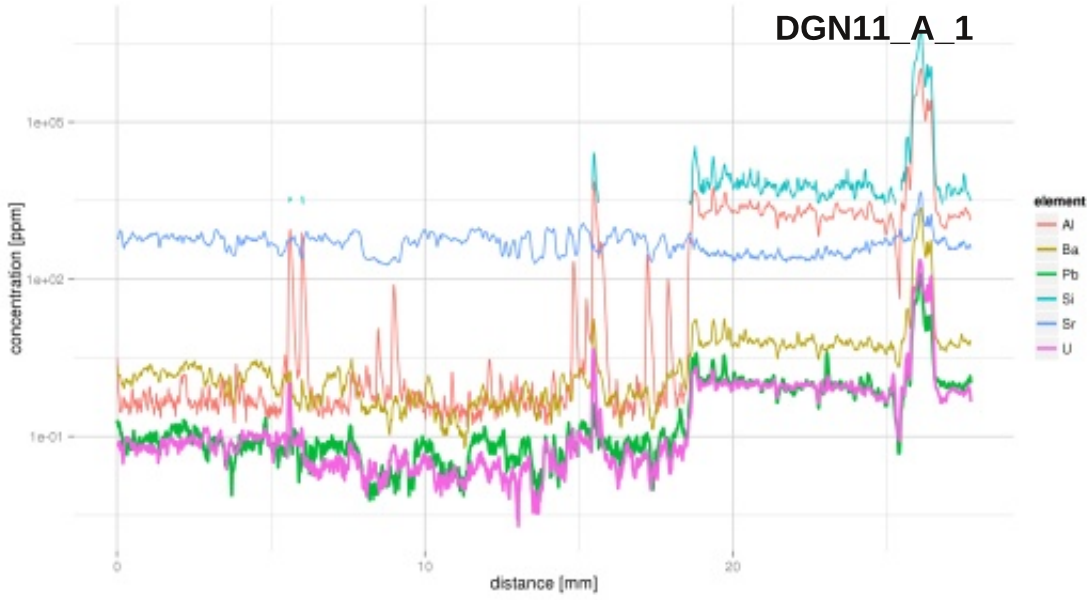
DGN11_A_1
concentration [ppm]
1e+05
1e+02
1e-01
0
10
20
distance [mm]
element
Al
Ba
Pb
Si
Sr
U

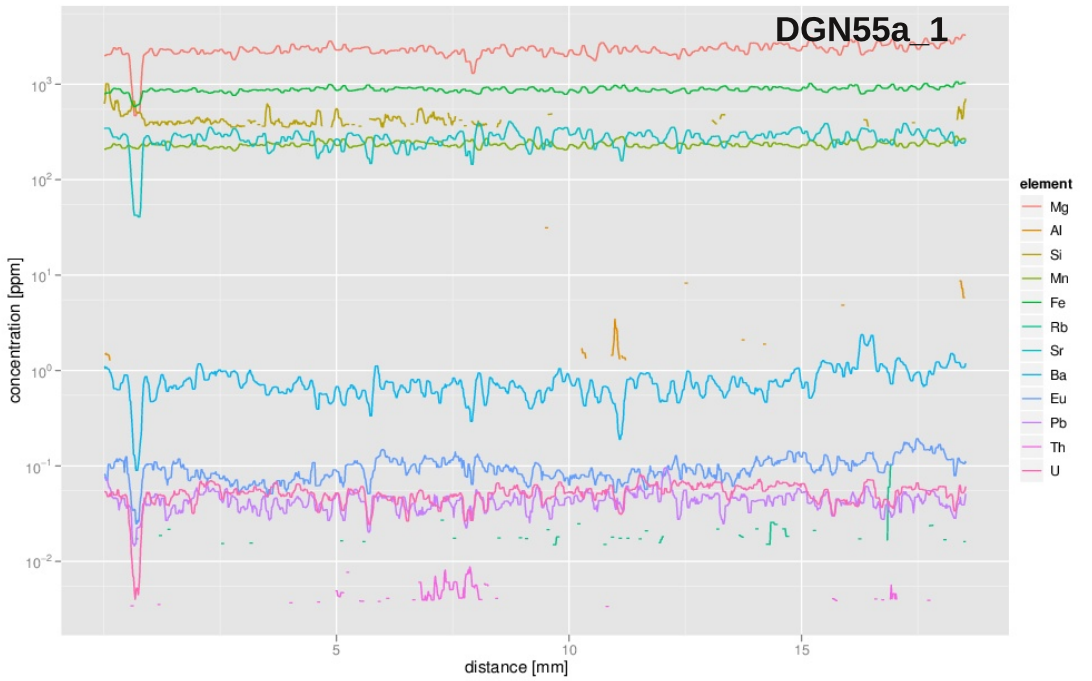
DGN55a_1
concentration [ppm]
10^3
10^2
10^1
10^0
10^{-1}
10^{-2}
5
10
15
distance [mm]
element
Mg
Al
Si
Mn
Fe
Rb
Sr
Ba
Eu
Pb
Th
U

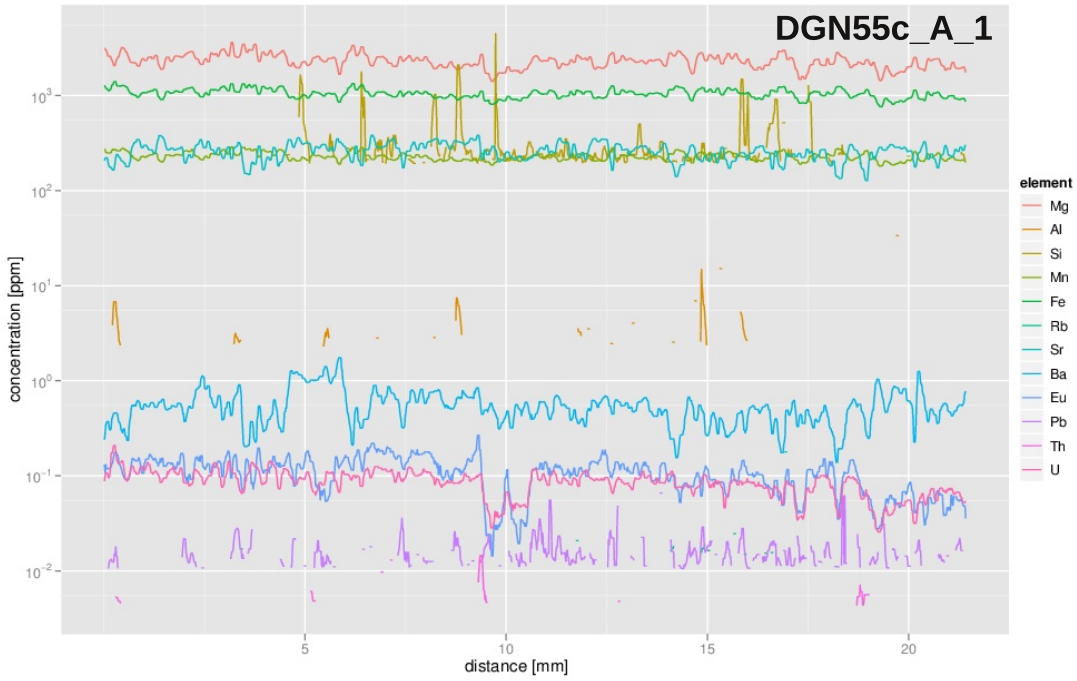
DGN55c_A_1
concentration [ppm]
distance [mm]
element
Mg
Al
Si
Mn
Fe
Rb
Sr
Ba
Eu
Pb
Th
U

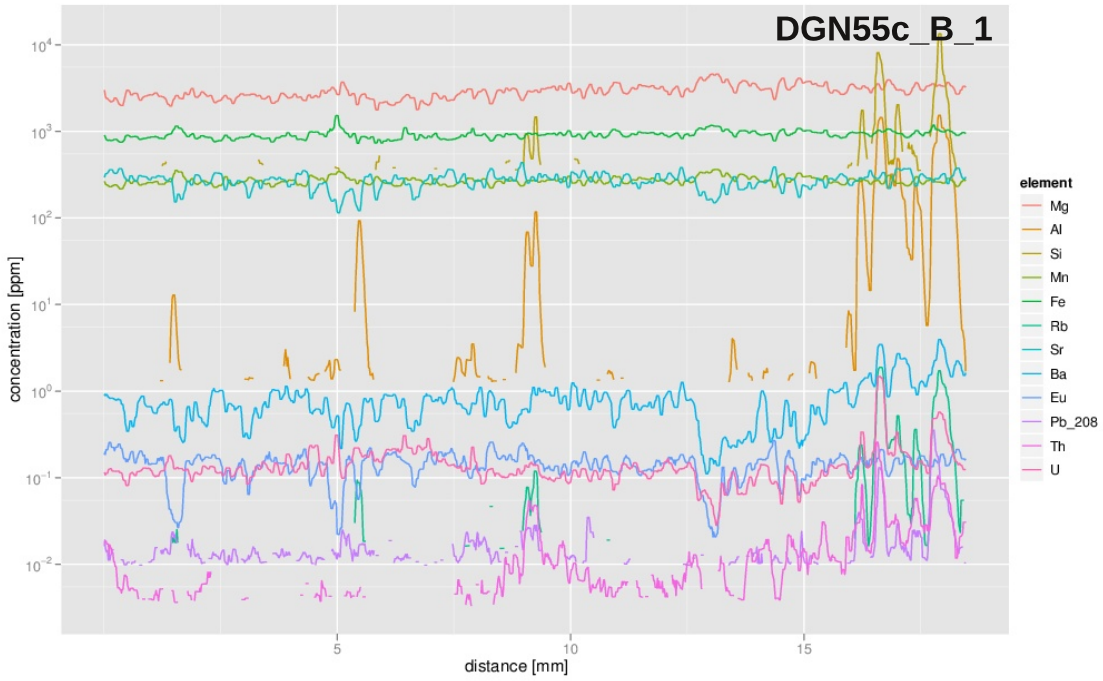
DGN55c_B_1
concentration [ppm]
distance [mm]
element
Mg
Al
Si
Mn
Fe
Rb
Sr
Ba
Eu
Pb_208
Th
U

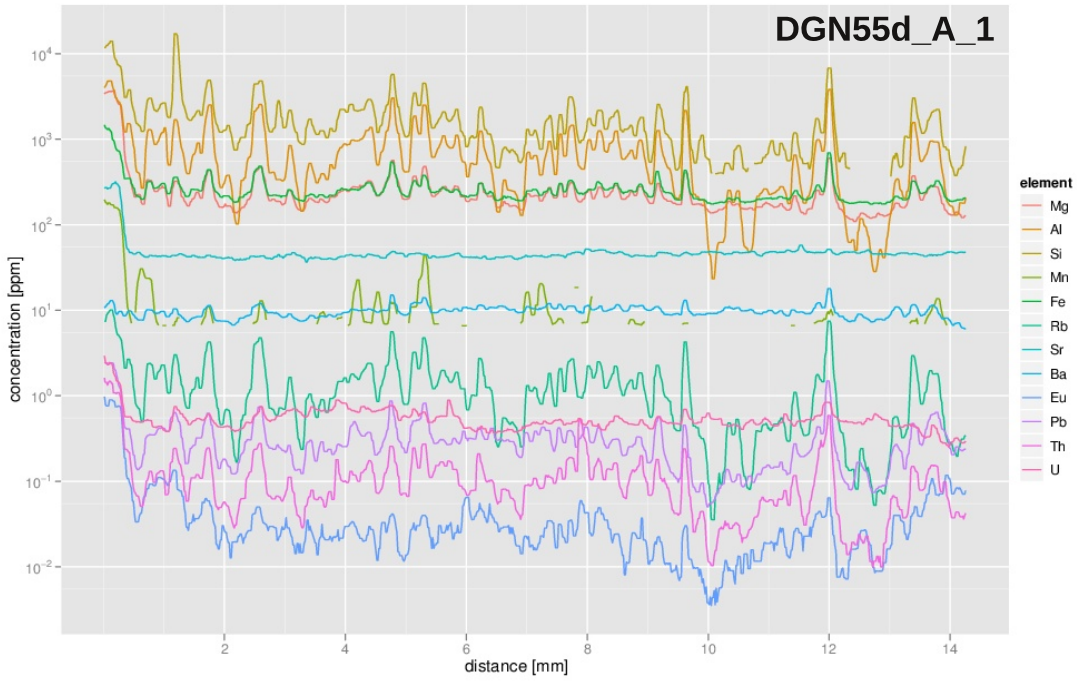
DGN55d_A_1
concentration [ppm]
distance [mm]
element
Mg
Al
Si
Mn
Fe
Rb
Sr
Ba
Eu
Pb
Th
U

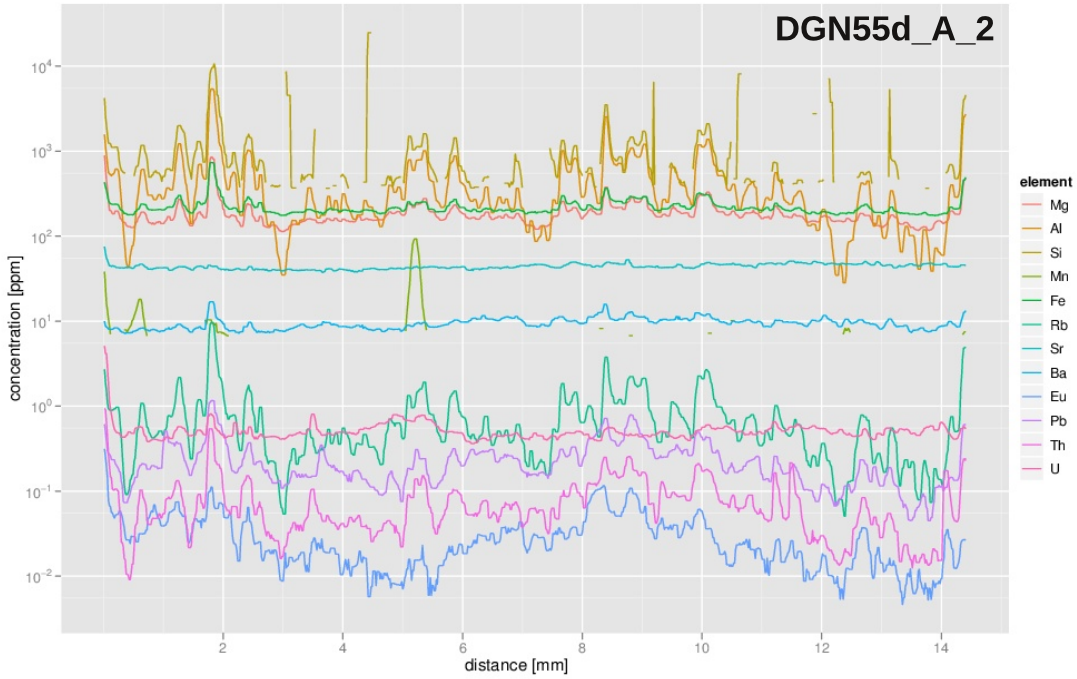
DGN55d_A_2
concentration [ppm]
distance [mm]
element
Mg
Al
Si
Mn
Fe
Rb
Sr
Ba
Eu
Pb
Th
U

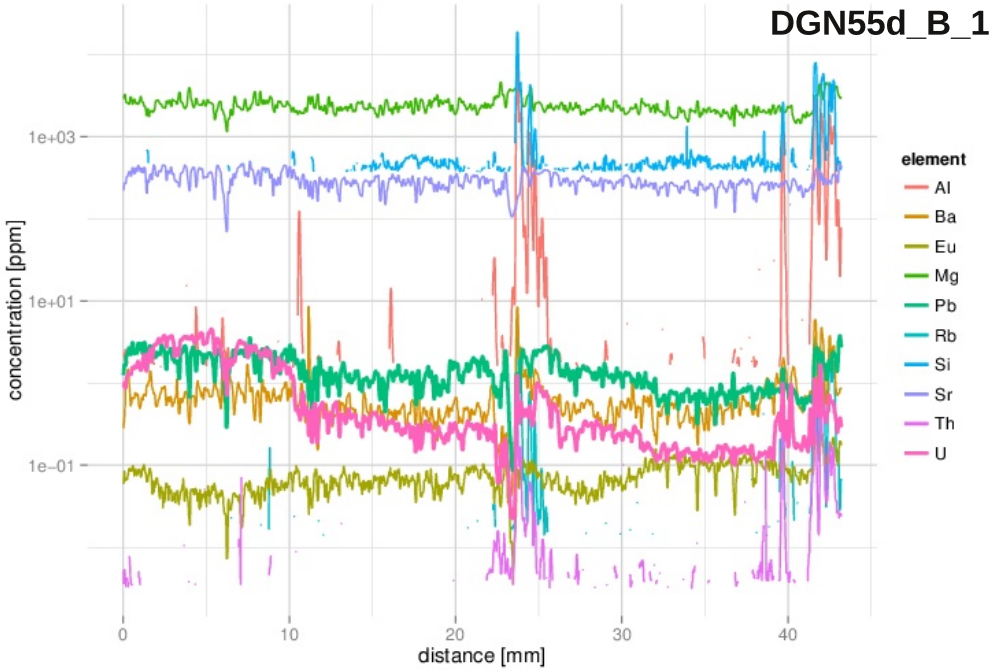
DGN55d_B_1
concentration [ppm]
1e+03
1e+01
1e−01
0
10
20
30
40
distance [mm]
element
Al
Ba
Eu
Mg
Pb
Rb
Si
Sr
Th
U

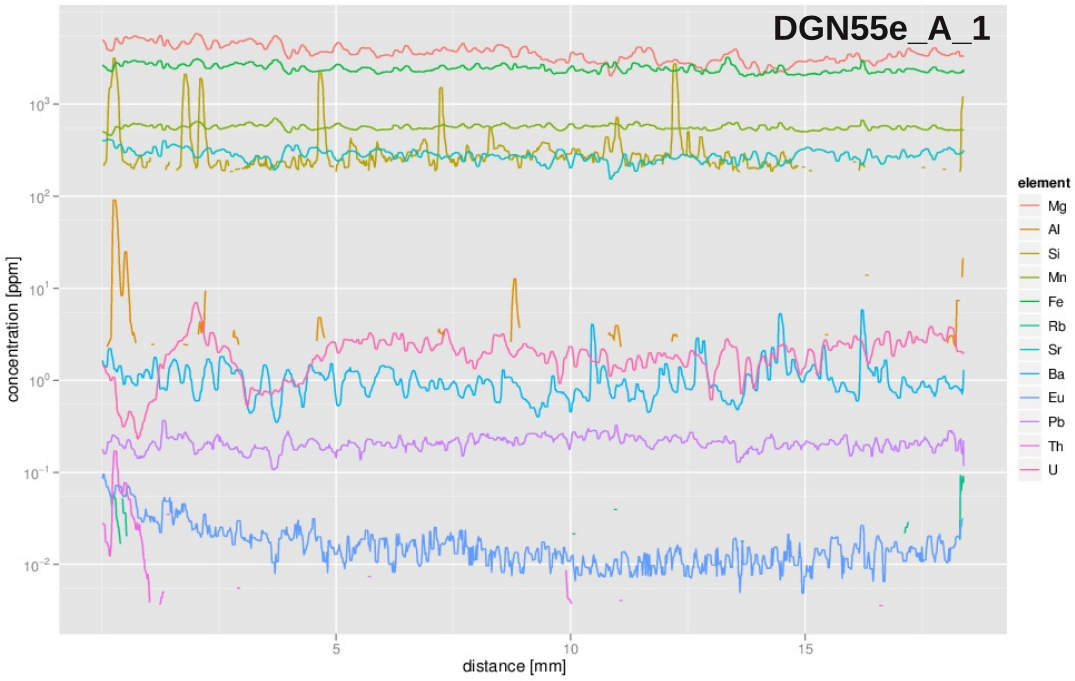
DGN55e_A_1
concentration [ppm]
10^{3}
10^{2}
10^{1}
10^{0}
10^{-1}
10^{-2}
5
10
15
distance [mm]
element
Mg
Al
Si
Mn
Fe
Rb
Sr
Ba
Eu
Pb
Th
U

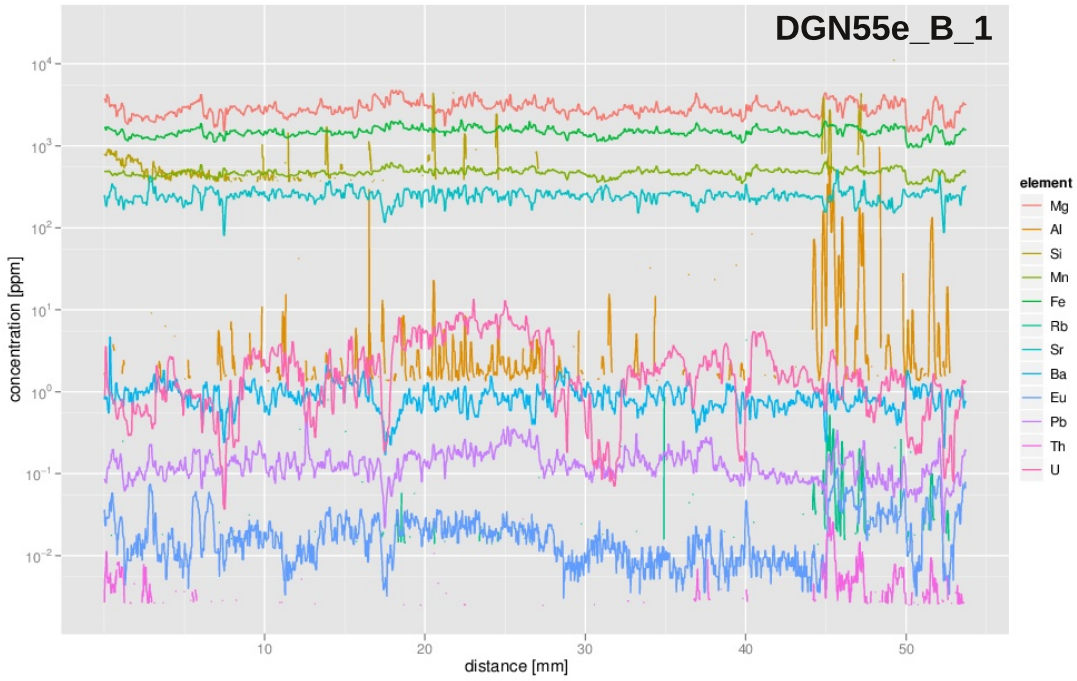
DGN55e_B_1
concentration [ppm]
distance [mm]
element
Mg
Al
Si
Mn
Fe
Rb
Sr
Ba
Eu
Pb
Th
U

Fohnsdorf Basin

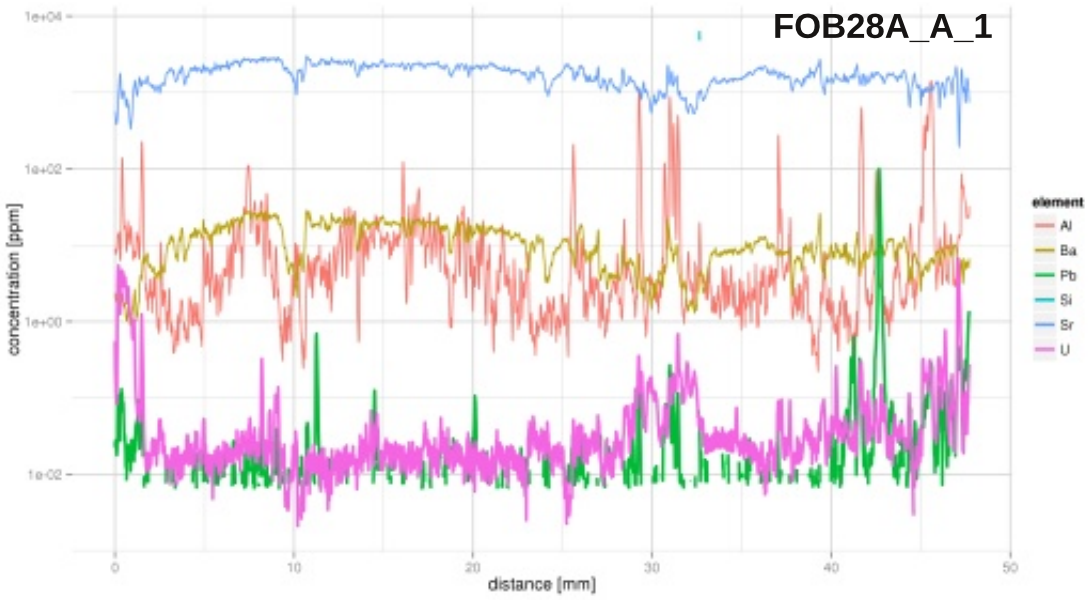

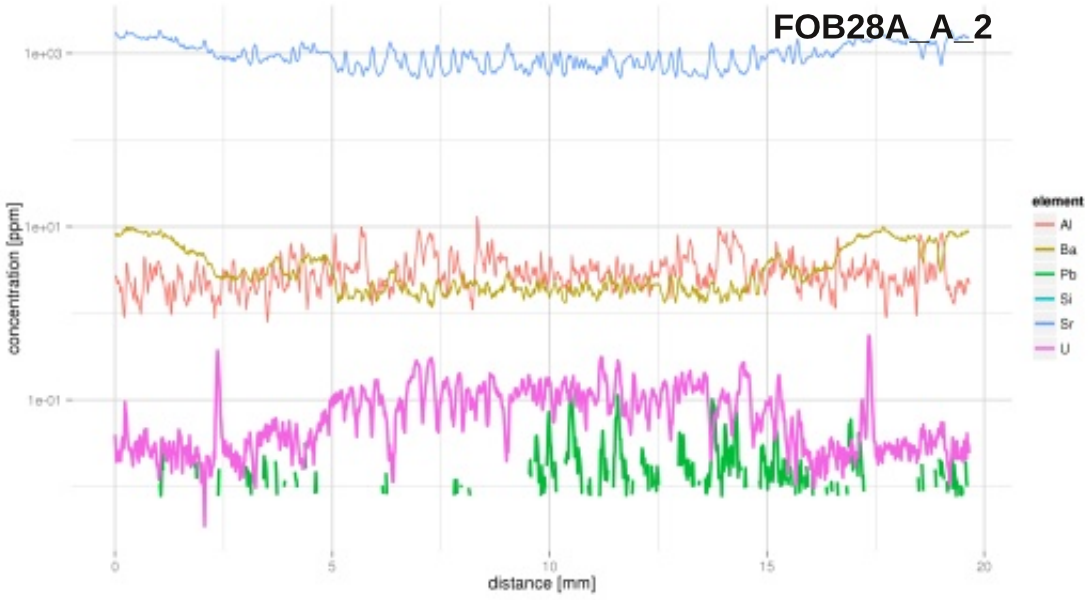

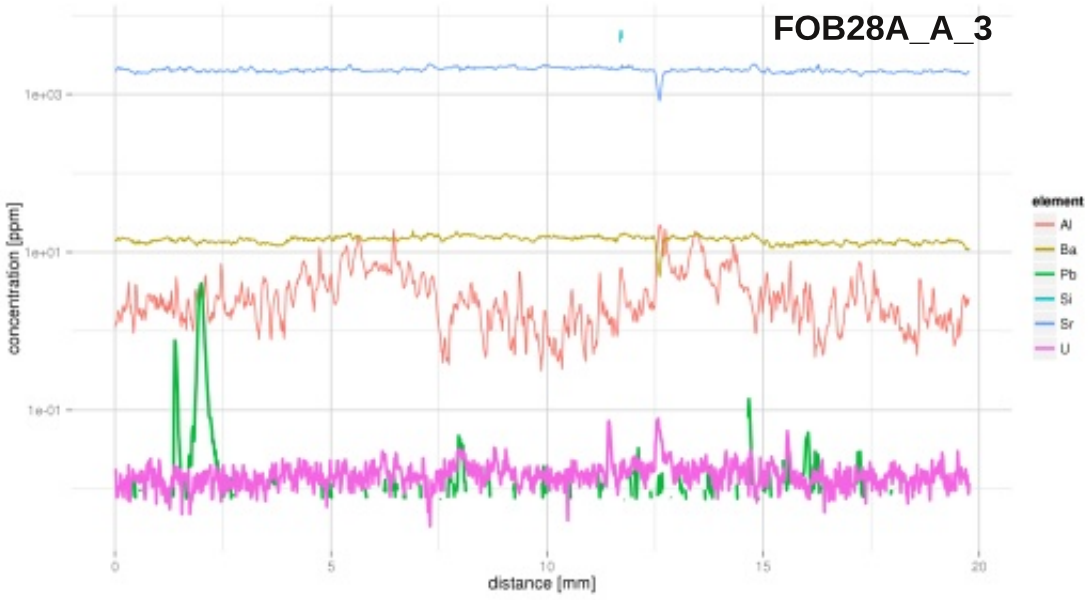
FOB28A_A_3
concentration [ppm]
1e+03
1e+01
1e-01
0
5
10
15
20
distance [mm]
element
Al
Ba
Pb
Si
Sr
U

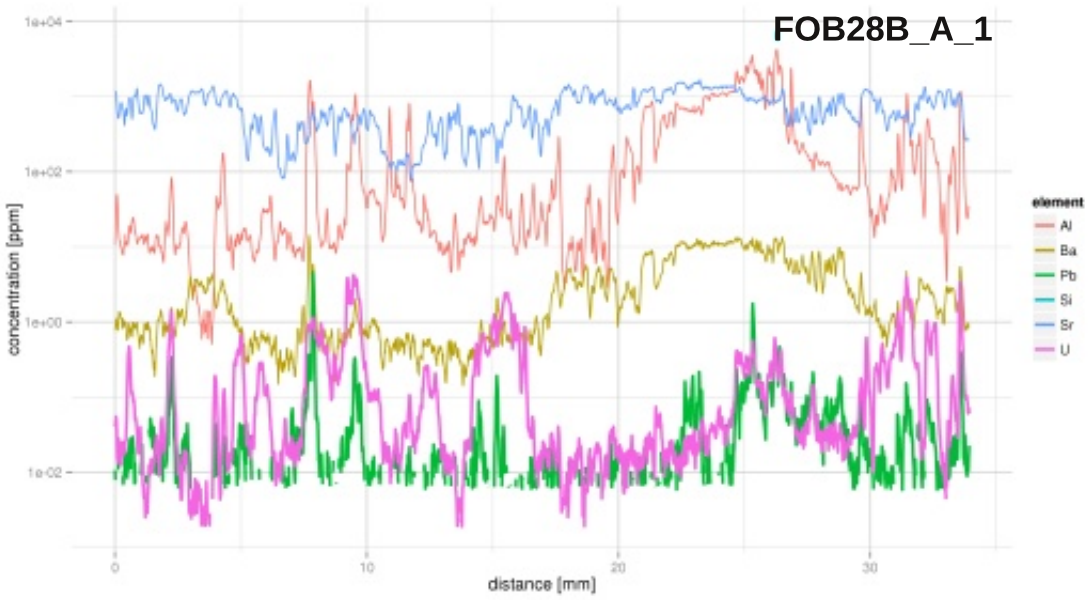
FOB28B_A_1
concentration [ppm]
1e+04
1e+02
1e+00
1e-02
0
10
20
30
distance [mm]
element
Al
Ba
Pb
Si
Sr
U

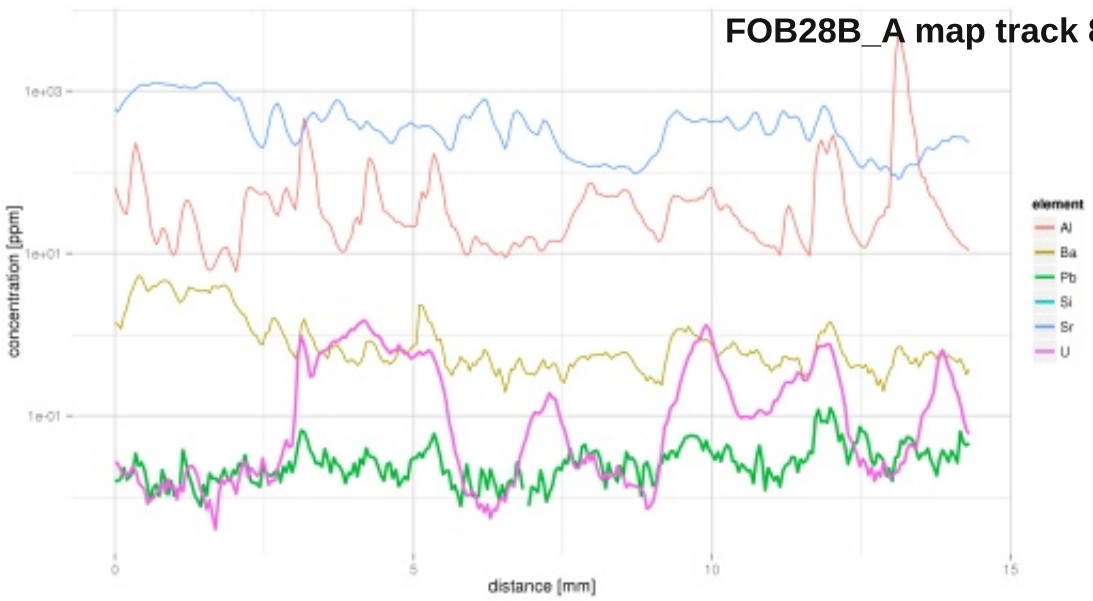
FOB28B_A map track 8
concentration [ppm]
1e+03
1e+01
1e-01
0
5
10
15
distance [mm]
element
Al
Ba
Pb
Si
Sr
U

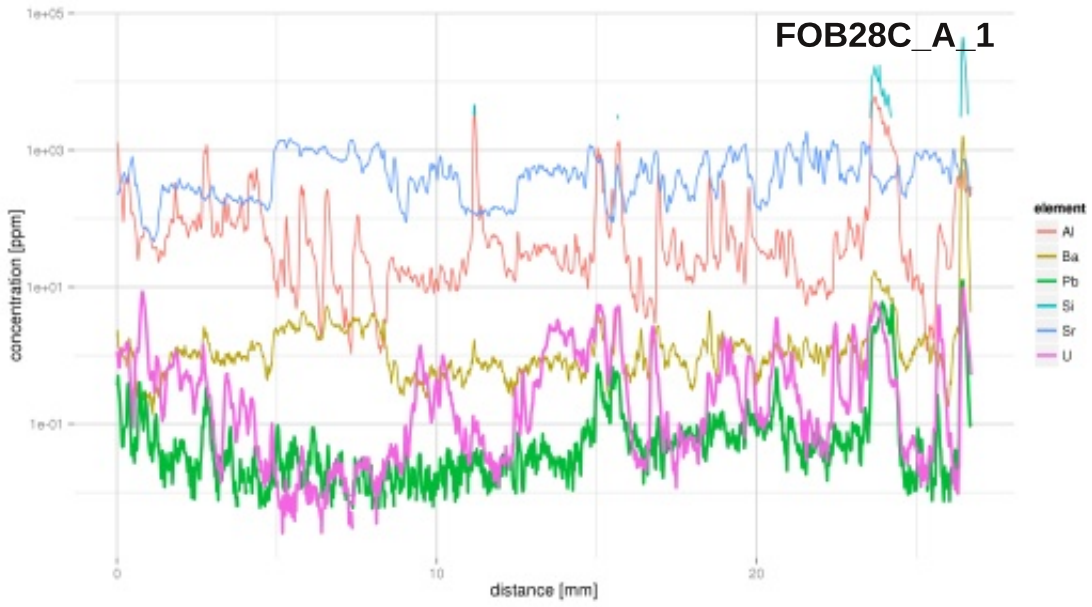
FOB28C_A_1
concentration [ppm]
1e+05
1e+03
1e+01
1e-01
0
10
20
distance [mm]
element
Al
Ba
Pb
Si
Sr
U

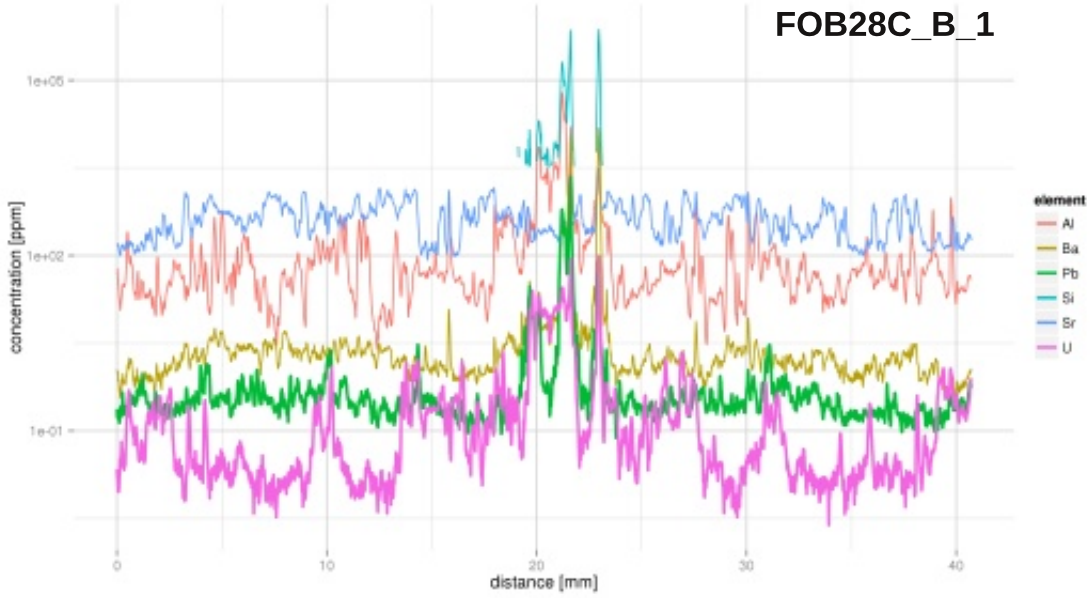
FOB28C_B_1
concentration [ppm]
1e+05
1e+02
1e-01
0
10
20
30
40
distance [mm]
element
Al
Ba
Pb
Si
Sr
U

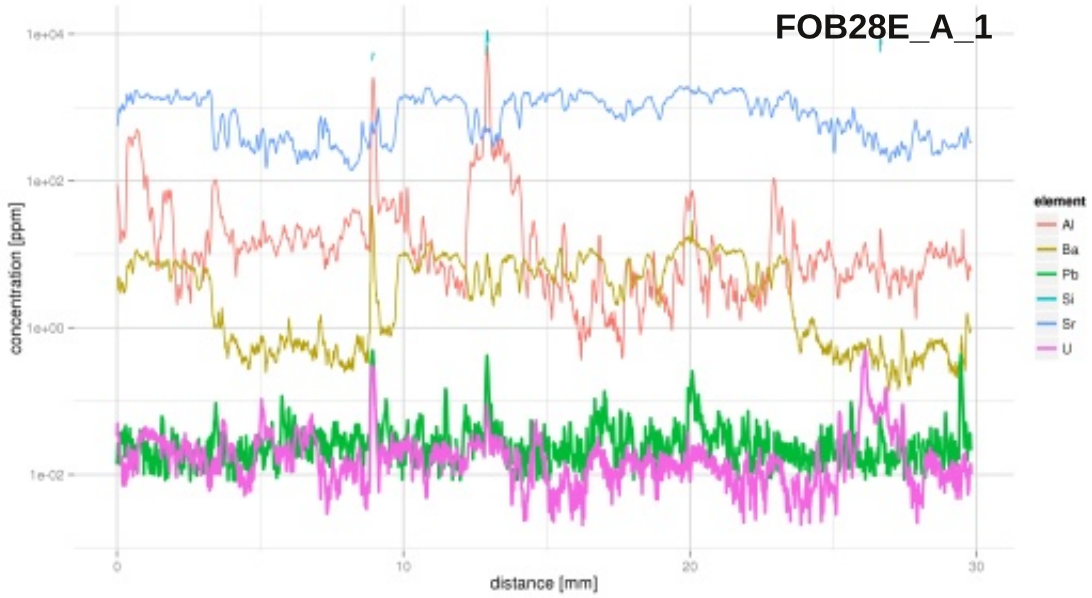
FOB28E_A_1
concentration [ppm]
1e+04
1e+02
1e+00
1e-02
0
10
20
30
distance [mm]
element
Al
Ba
Pb
Si
Sr
U


FOB28E_B_1
concentration [ppm]
1e+02
1e+00
1e-02
0
10
20
30
distance [mm]
element
Al
Ba
Pb
Si
Sr
U

Gosau Basin

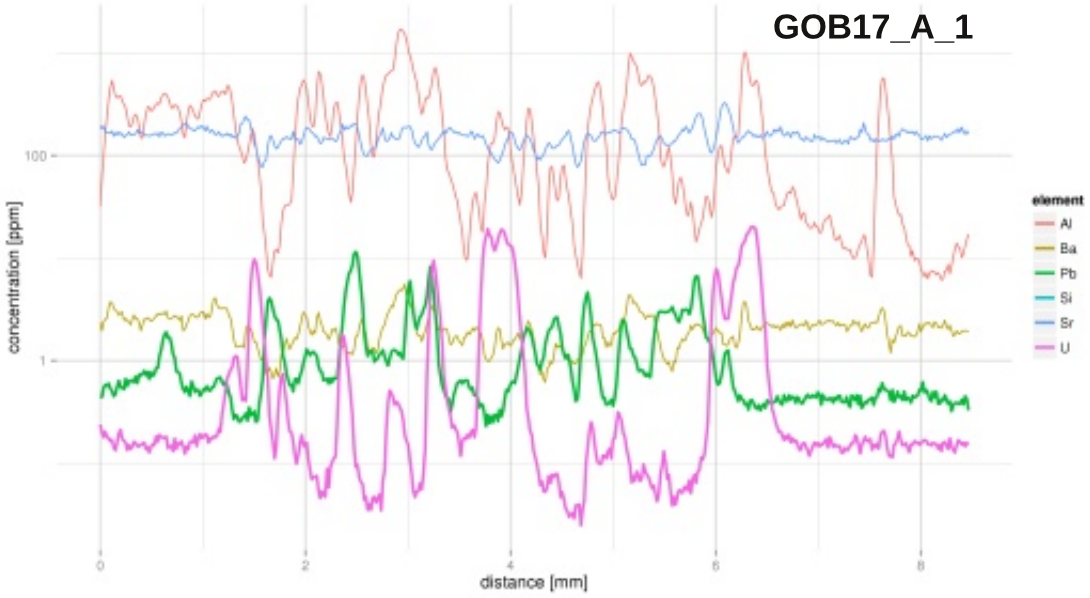
GOB17_A_1
concentration [ppm]
100
1
0
2
4
6
8
distance [mm]
element
Al
Ba
Pb
Si
Sr
U

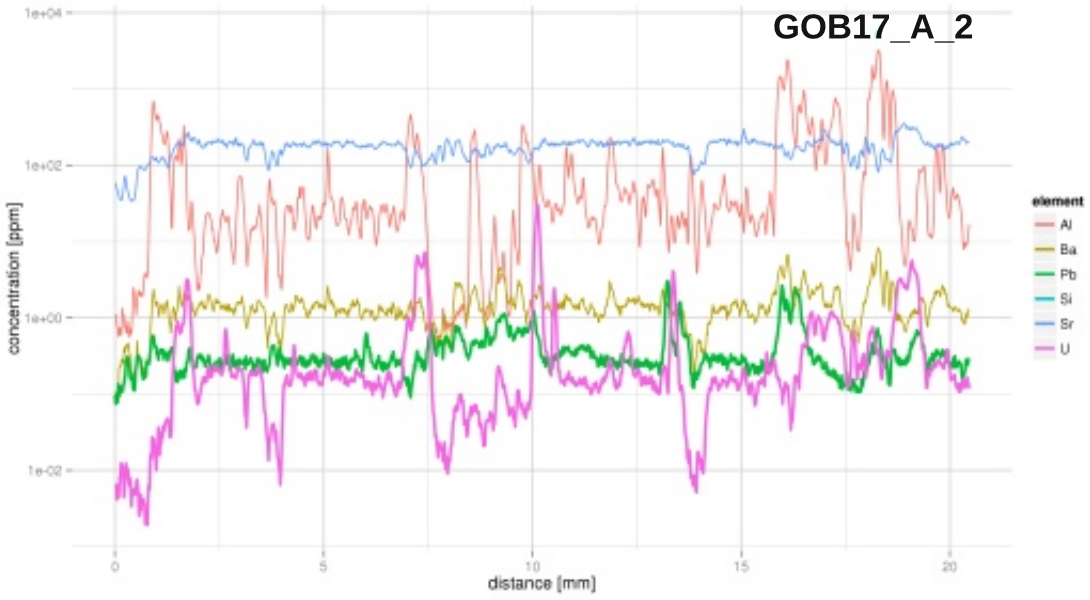
GOB17_A_2
concentration [ppm]
1e+04
1e+02
1e+00
1e-02
0
5
10
15
20
distance [mm]
element
Al
Ba
Pb
Si
Sr
U

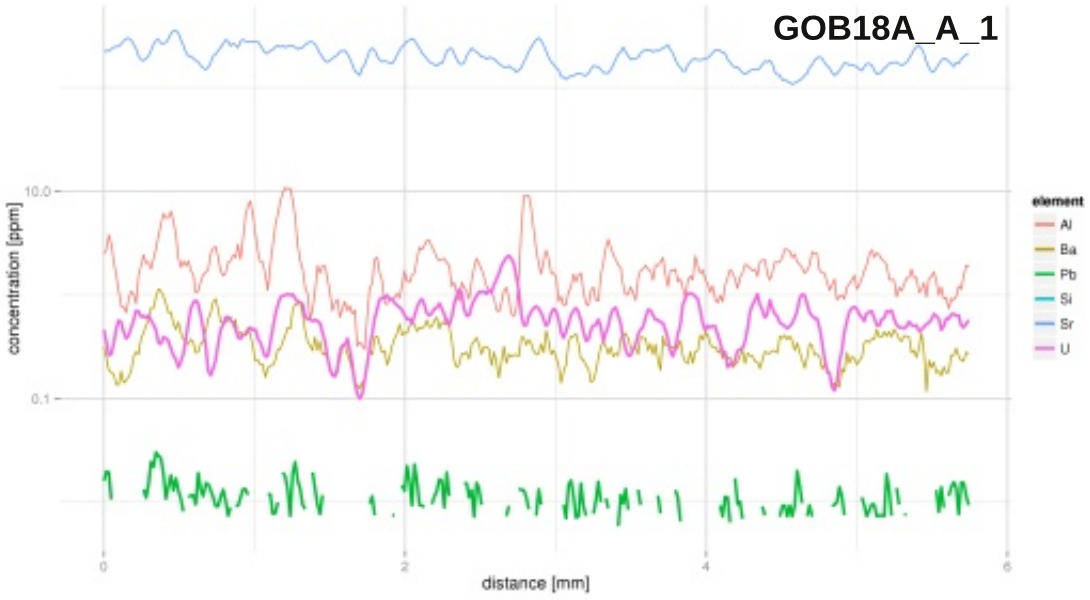
GOB18A_A_1
concentration [ppm]
10.0
0.1
0
2
4
6
distance [mm]
element
Al
Ba
Pb
Si
Sr
U

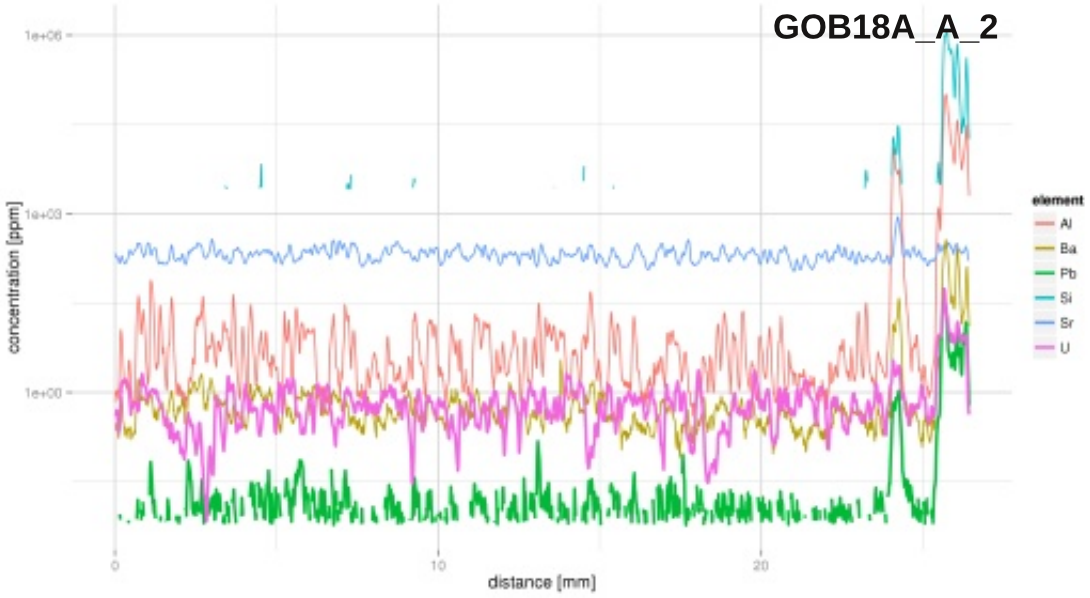
GOB18A_A_2
concentration [ppm]
1e+06
1e+03
1e+00
0
10
20
distance [mm]
element
Al
Ba
Pb
Si
Sr
U

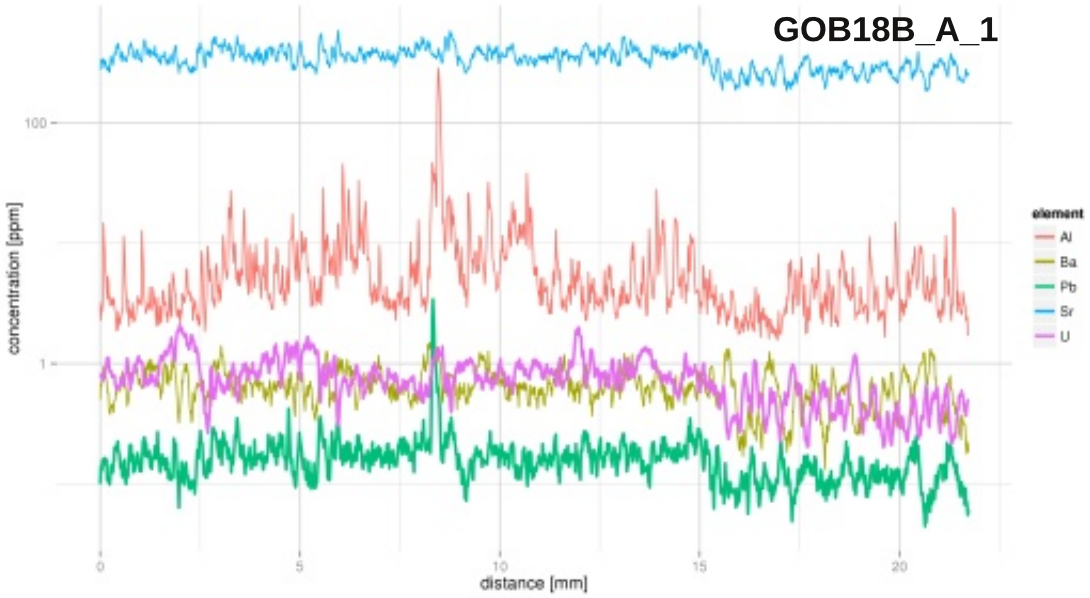
GOB18B_A_1
concentration [ppm]
100
1
0
5
10
15
20
distance [mm]
element
Al
Ba
Pb
Sr
U

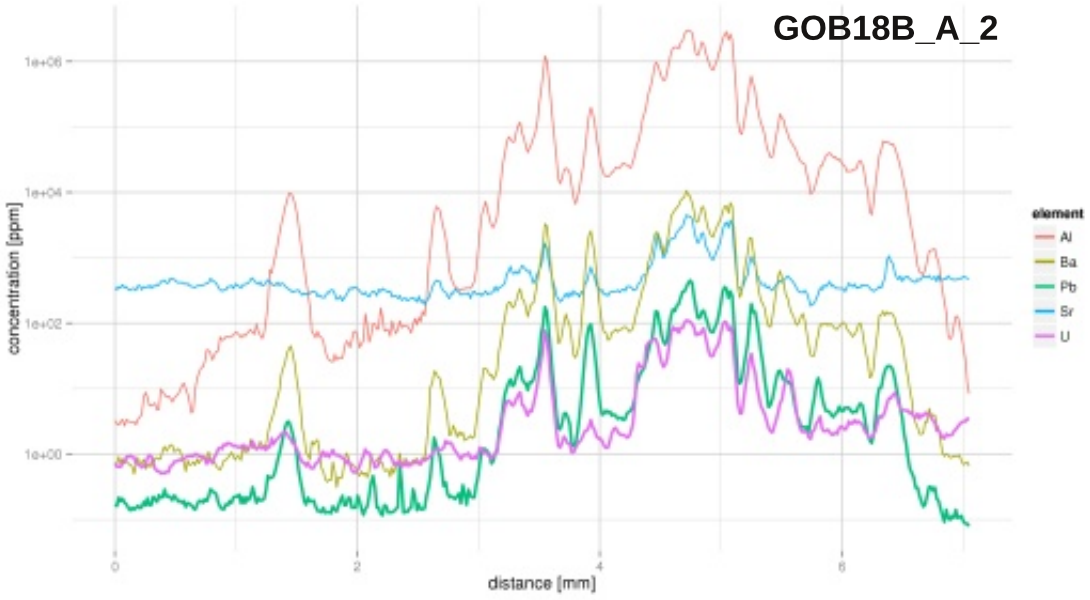
GOB18B_A_2
concentration [ppm]
1e+06
1e+04
1e+02
1e+00
0
2
4
6
distance [mm]
element
Al
Ba
Pb
Sr
U

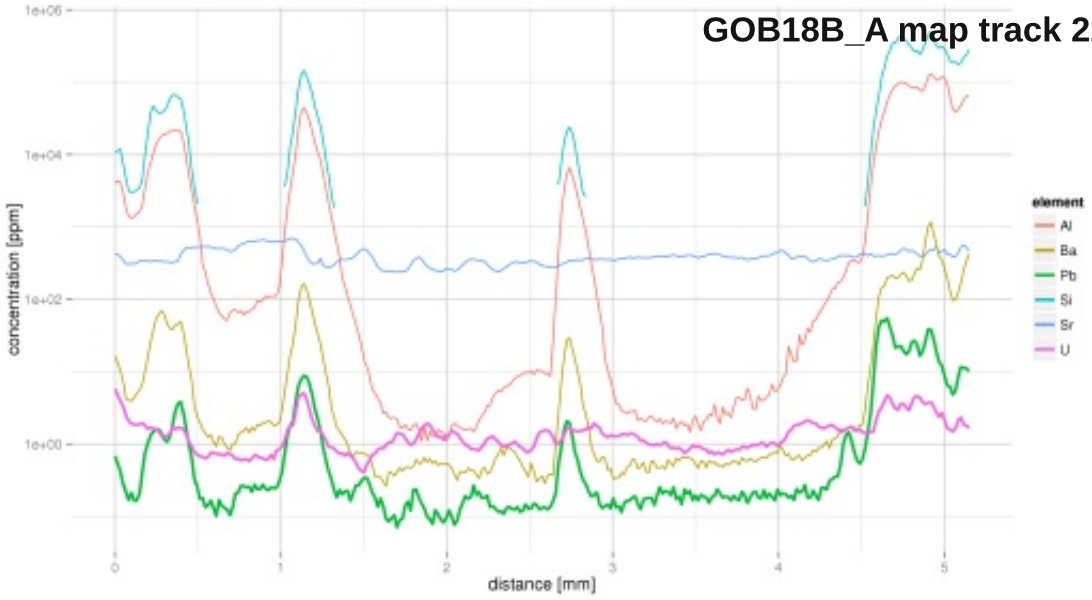
GOB18B_A map track 22
concentration [ppm]
1e+06
1e+04
1e+02
1e+00
0
1
2
3
4
5
distance [mm]
element
Al
Ba
Pb
Si
Sr
U

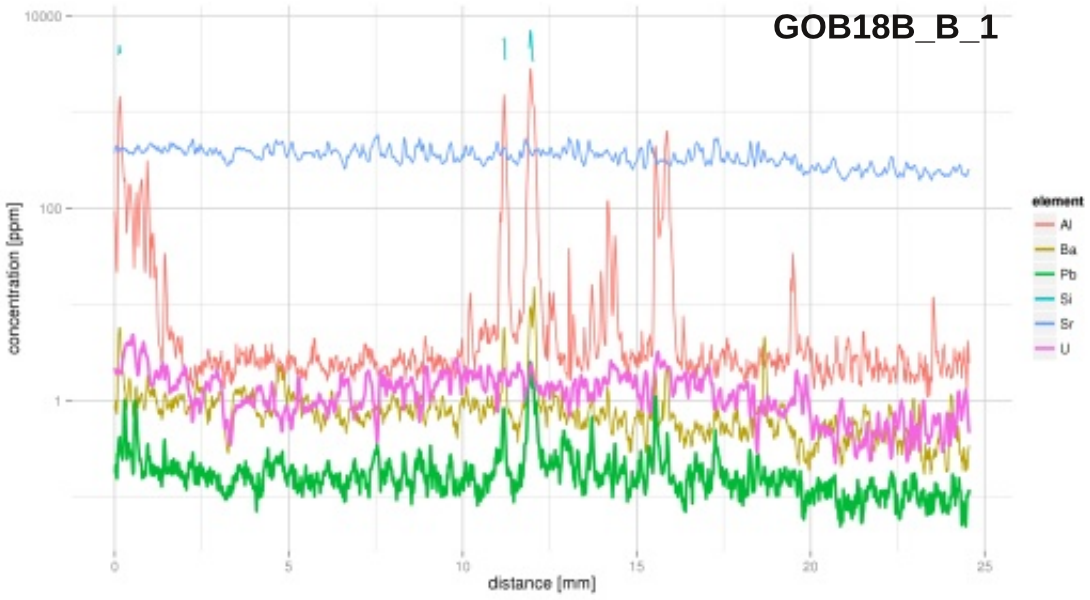
GOB18B_B_1
concentration [ppm]
10000
100
1
0
5
10
15
20
25
distance [mm]
element
Al
Ba
Pb
Si
Sr
U

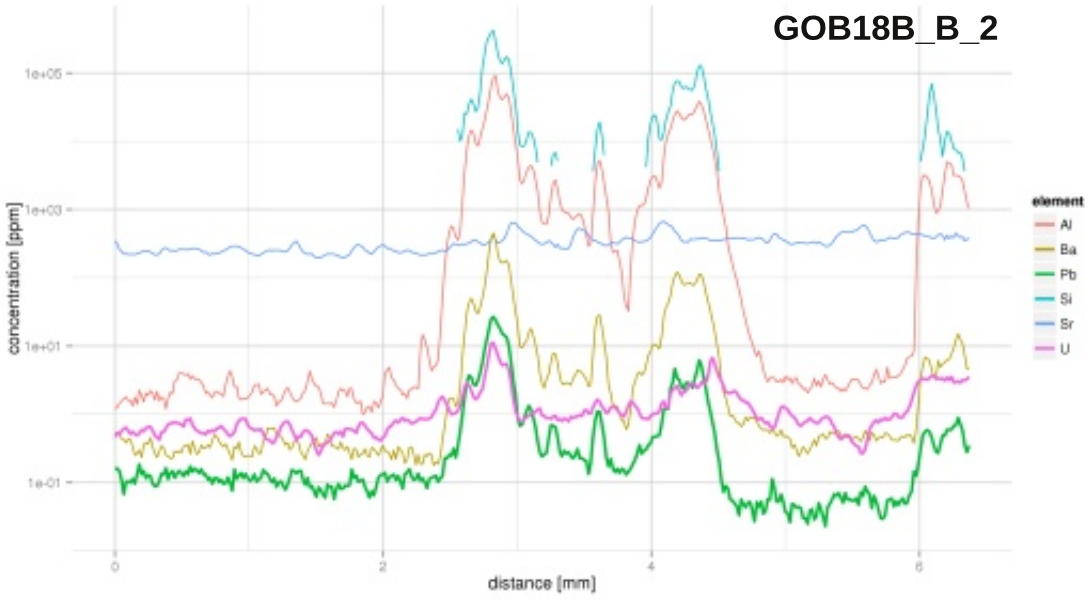
GOB18B_B_2
concentration [ppm]
1e+05
1e+03
1e+01
1e-01
0
2
4
6
distance [mm]
element
Al
Ba
Pb
Si
Sr
U

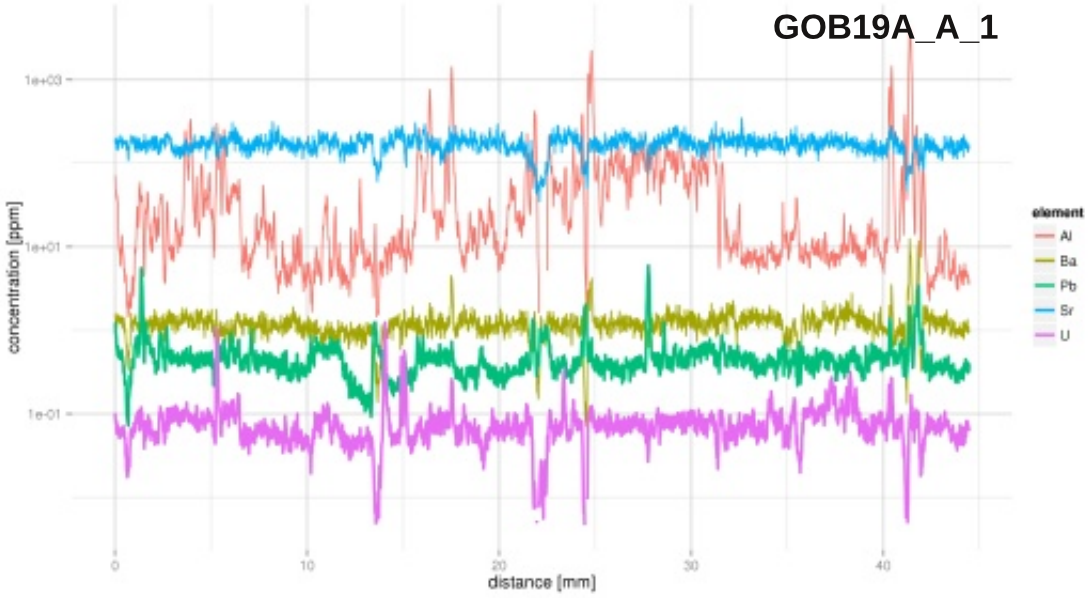
GOB19A_A_1
concentration [ppm]
1e+03
1e+01
1e-01
0
10
20
30
40
distance [mm]
element
Al
Ba
Pb
Sr
U

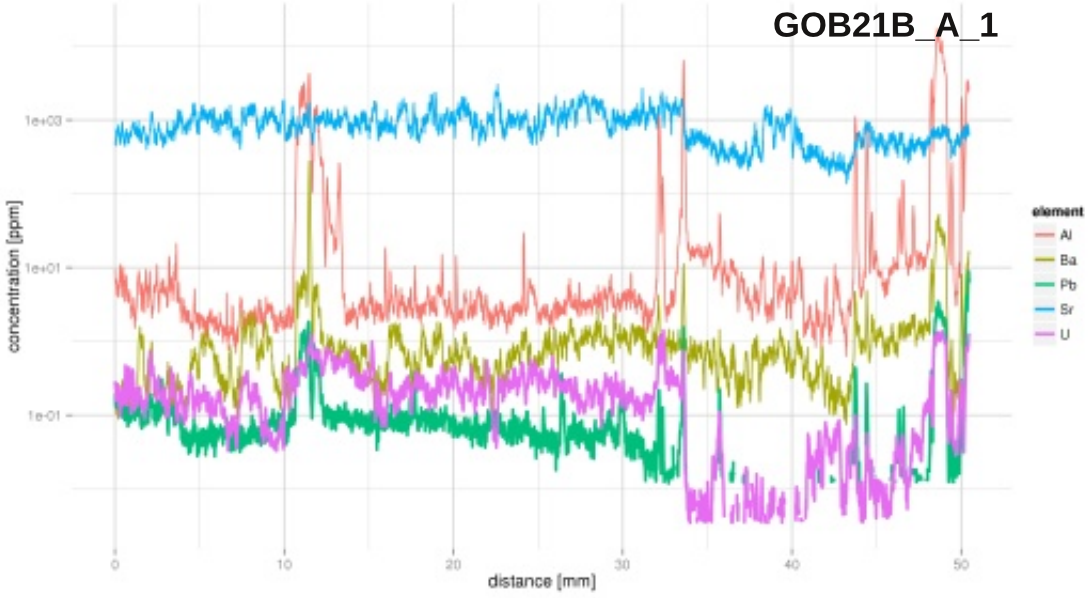
GOB21B_A_1
concentration [ppm]
1e+03
1e+01
1e-01
0
10
20
30
40
50
distance [mm]
element
Al
Ba
Pb
Sr
U

GOB21B_A_2

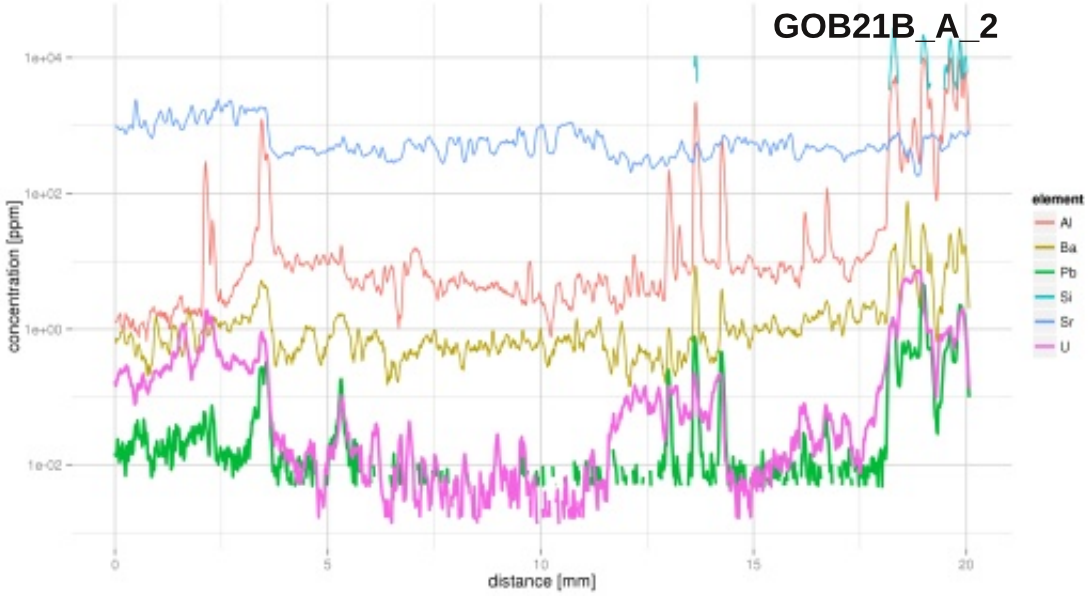

GOB21B_A map track 42

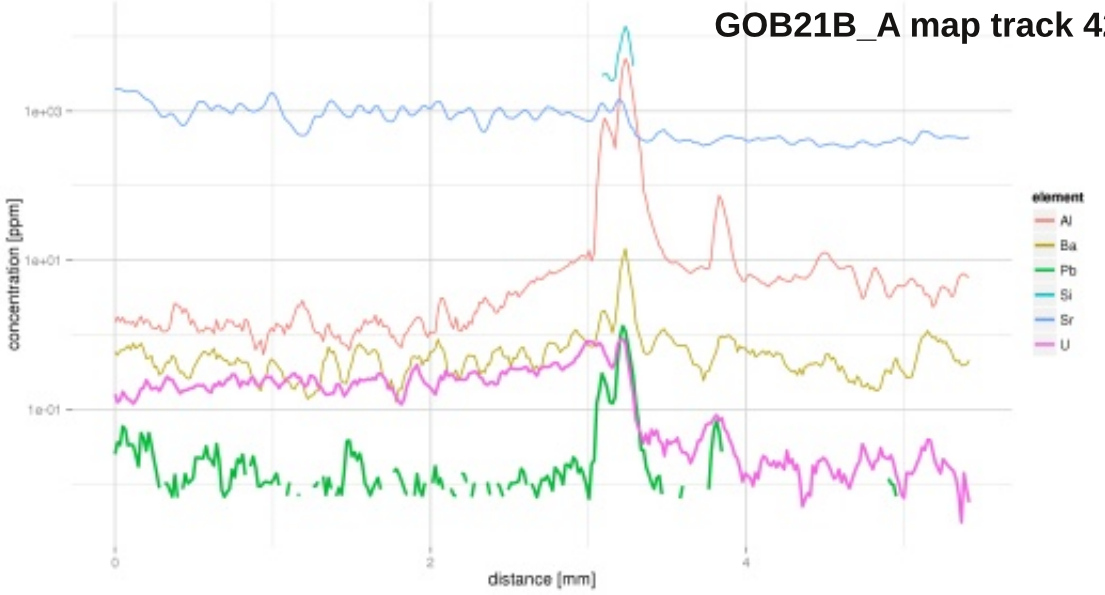

GOB23B_A_1

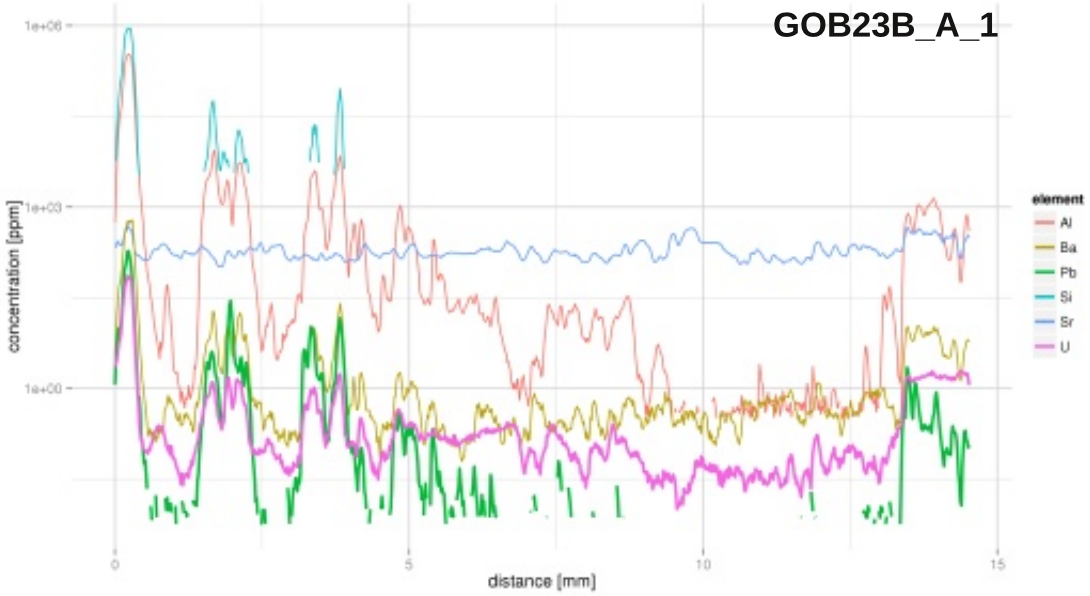

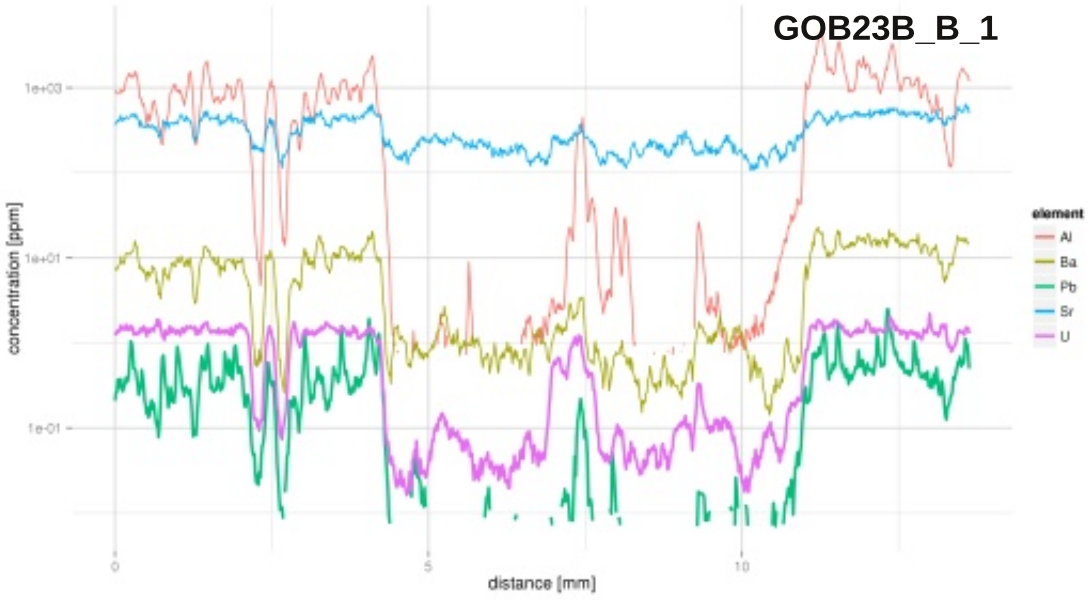
GOB23B_B_1
concentration [ppm]
1e+03
1e+01
1e-01
0
5
10
distance [mm]
element
Al
Ba
Pb
Sr
U

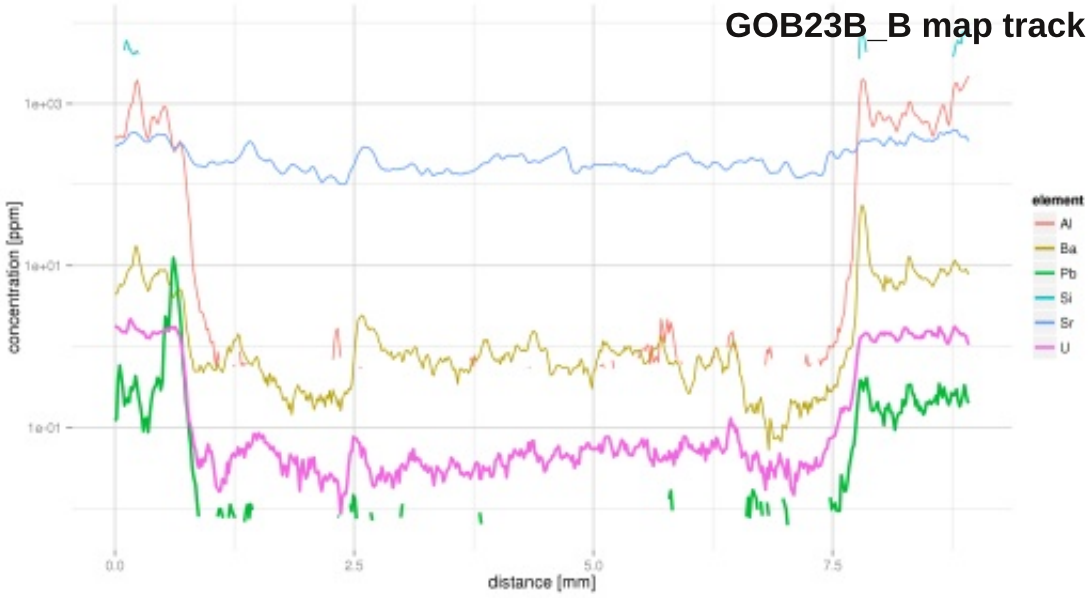
GOB23B_B map track 8
concentration [ppm]
1e+03
1e+01
1e-01
0.0
2.5
5.0
7.5
distance [mm]
element
Al
Ba
Pb
Si
Sr
U

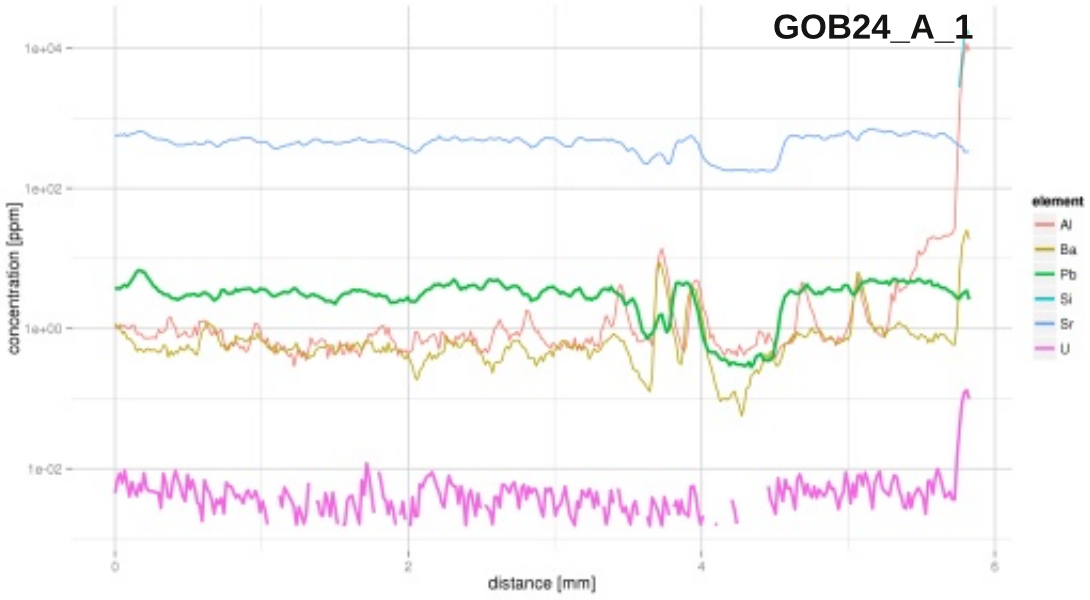
GOB24_A_1
concentration [ppm]
1e+04
1e+02
1e+00
1e-02
0
2
4
6
distance [mm]
element
Al
Ba
Pb
Si
Sr
U

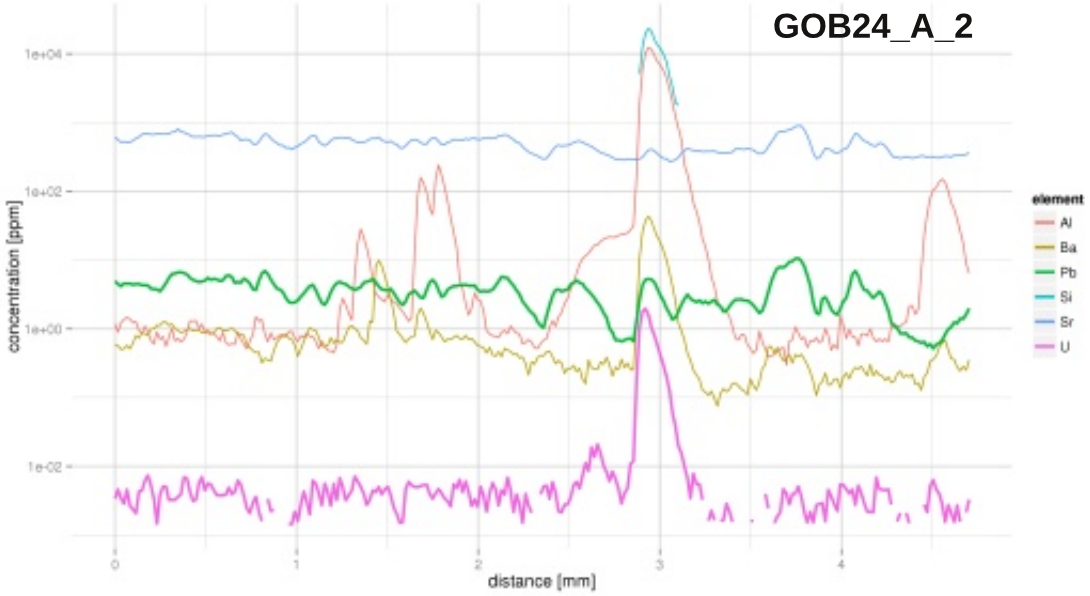
GOB24_A_2
concentration [ppm]
1e+04
1e+02
1e+00
1e-02
0
1
2
3
4
distance [mm]
element
Al
Ba
Pb
Si
Sr
U

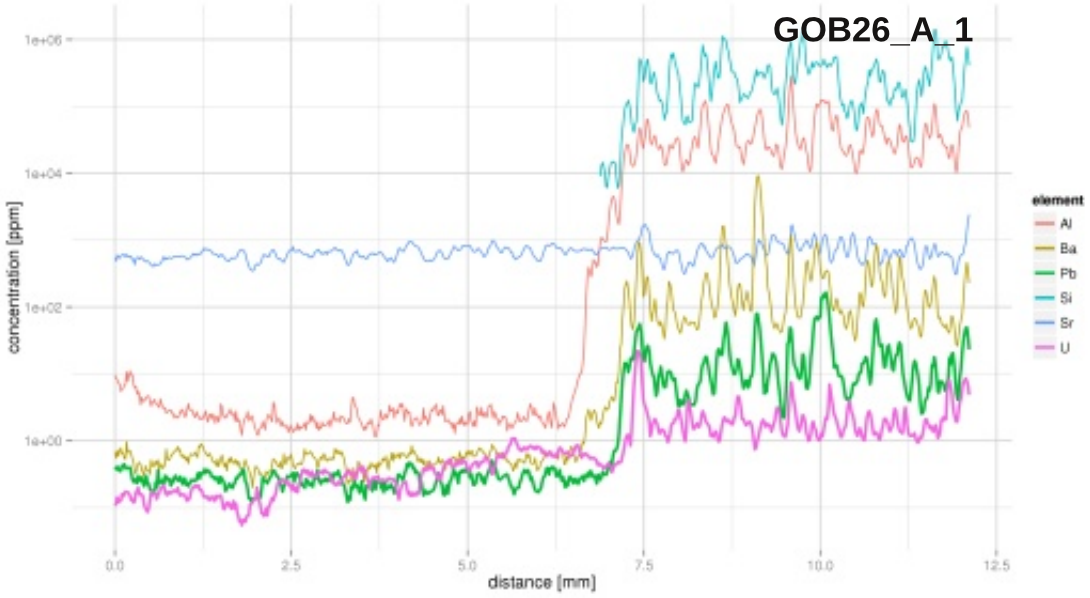
GOB26_A_1
concentration [ppm]
1e+06
1e+04
1e+02
1e+00
0.0
2.5
5.0
7.5
10.0
12.5
distance [mm]
element
Al
Ba
Pb
Si
Sr
U

Lower Inn Valley

Samples KB2 and UAS3 were contributed by Hugo Ortner, University of Innsbruck, Austria.


KB2_B_1
concentration [ppm]
1e+03
1e+01
1e-01
0
10
20
30
distance [mm]
element
Al
Ba
Pb
Si
Sr
U

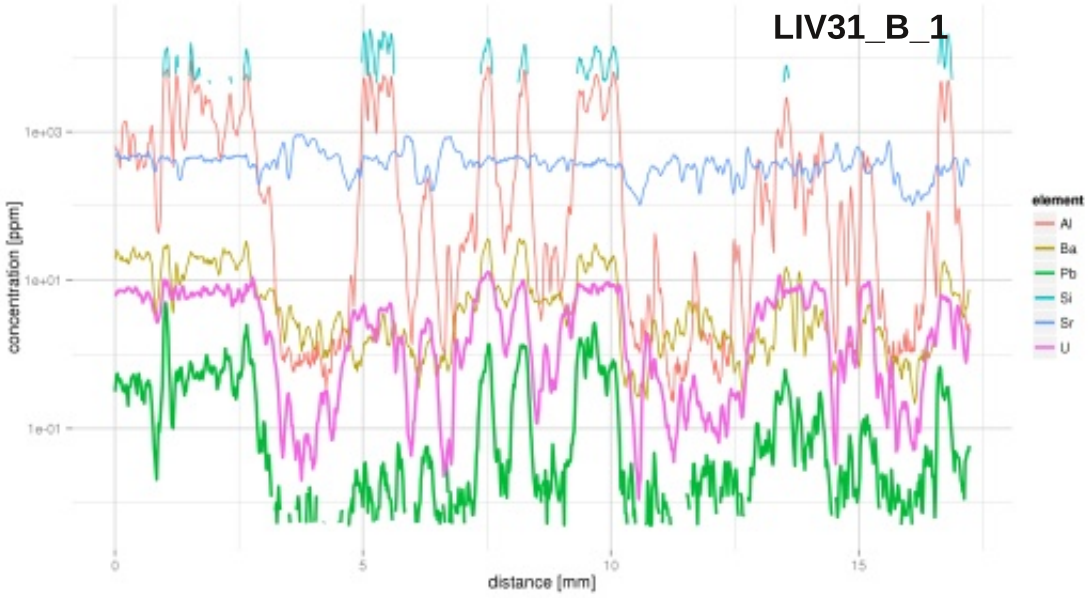
LIV31_B_1
concentration [ppm]
1e+03
1e+01
1e-01
0
5
10
15
distance [mm]
element
Al
Ba
Pb
Si
Sr
U

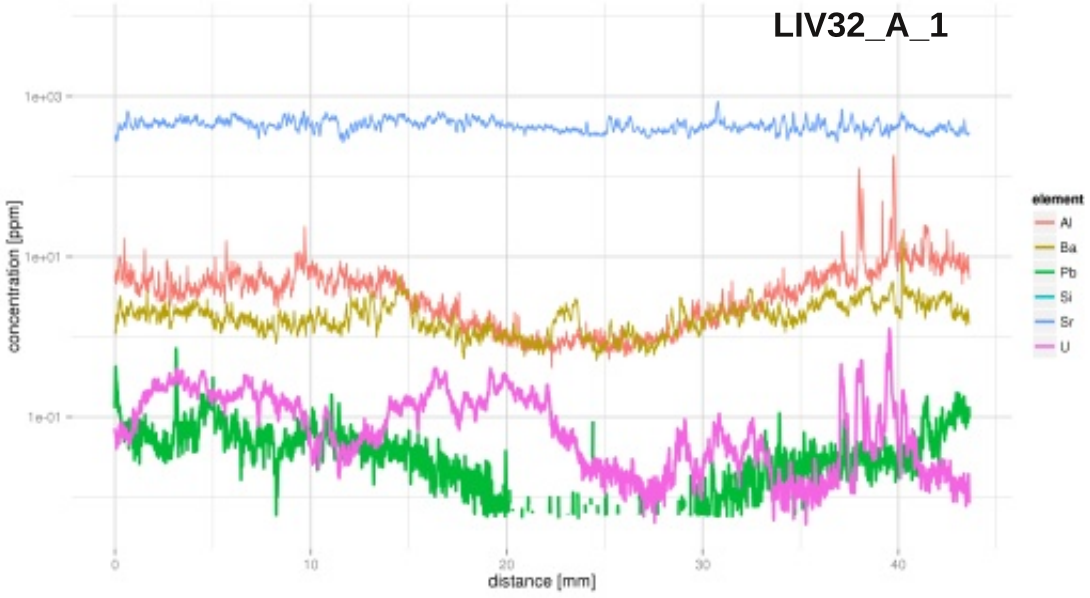
LIV32_A_1
concentration [ppm]
1e+03
1e+01
1e-01
0
10
20
30
40
distance [mm]
element
Al
Ba
Pb
Si
Sr
U

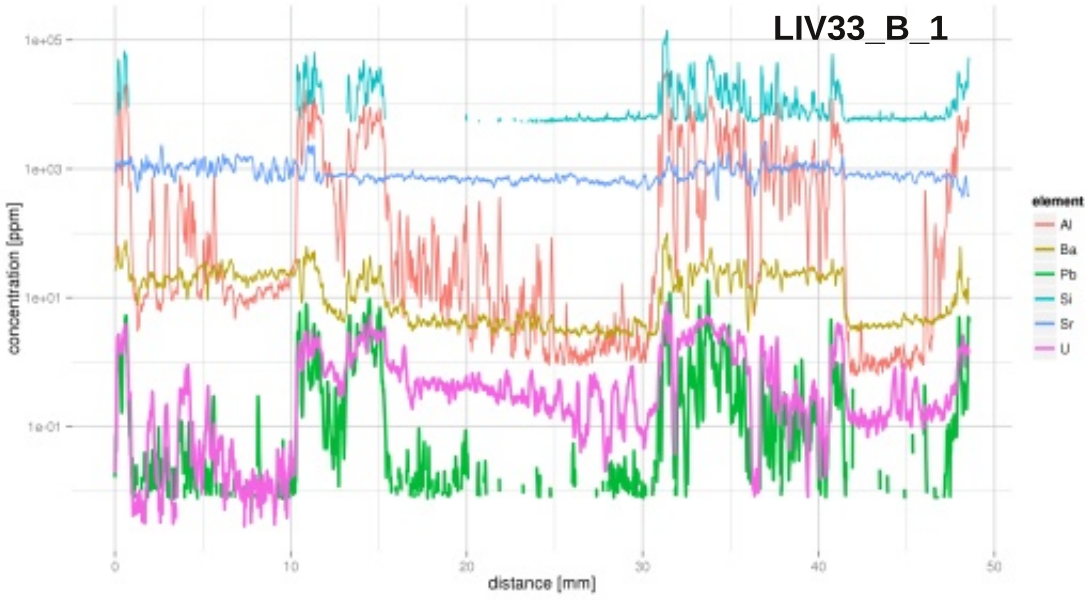
LIV33_B_1
concentration [ppm]
1e+05
1e+03
1e+01
1e-01
0
10
20
30
40
50
distance [mm]
element
Al
Ba
Pb
Si
Sr
U

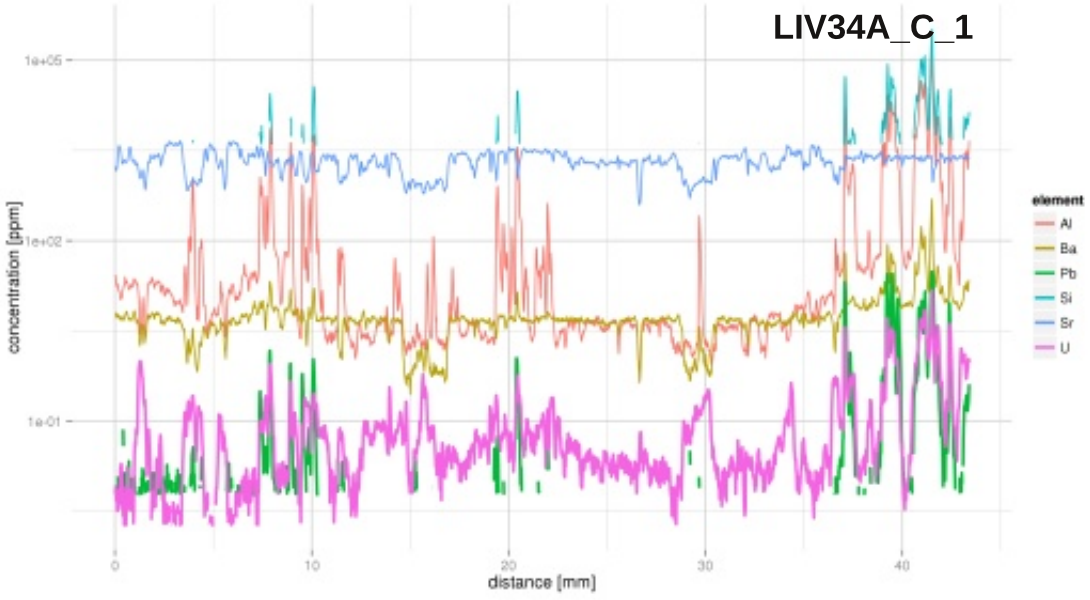
LIV34A_C_1
concentration [ppm]
1e+05
1e+02
1e-01
0
10
20
30
40
distance [mm]
element
Al
Ba
Pb
Si
Sr
U

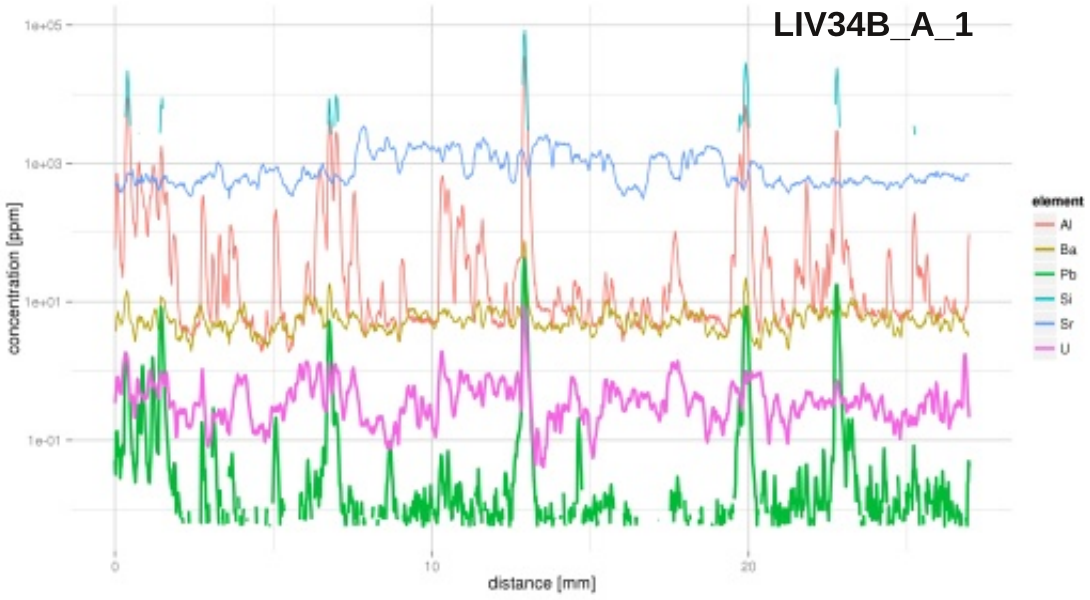
LIV34B_A_1
concentration [ppm]
1e+05
1e+03
1e+01
1e-01
0
10
20
distance [mm]
element
Al
Ba
Pb
Si
Sr
U

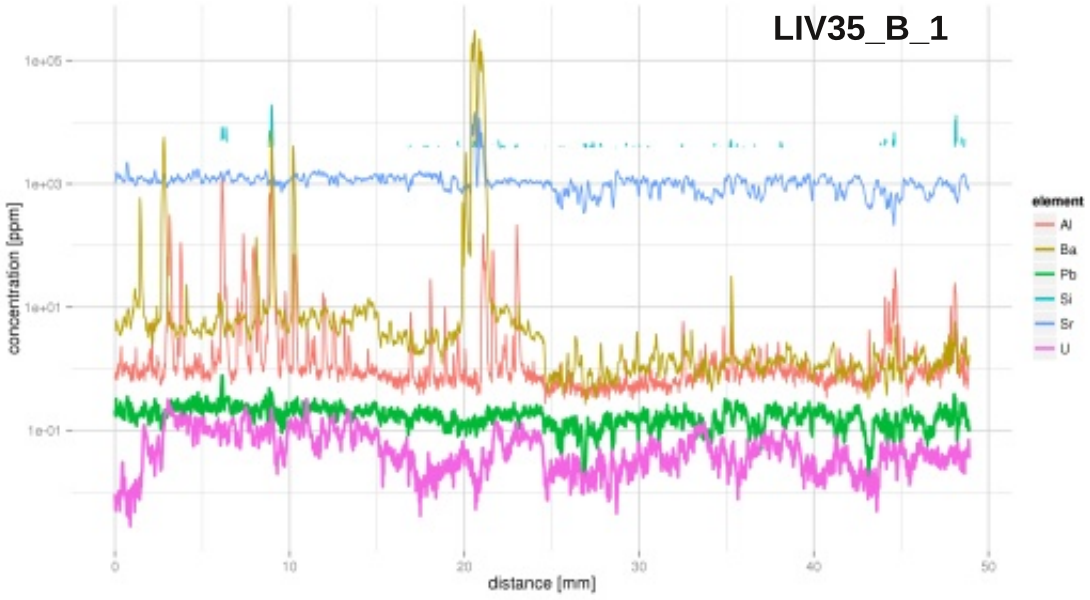
LIV35_B_1
concentration [ppm]
1e+05
1e+03
1e+01
1e-01
0
10
20
30
40
50
distance [mm]
element
Al
Ba
Pb
Si
Sr
U

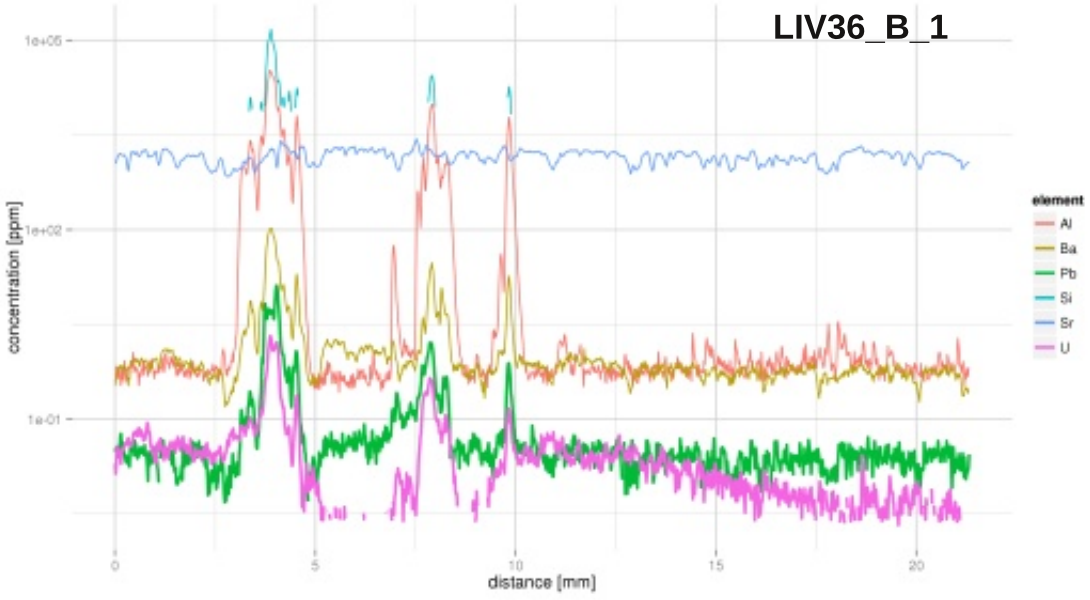
LIV36_B_1
concentration [ppm]
1e+05
1e+02
1e-01
0
5
10
15
20
distance [mm]
element
Al
Ba
Pb
Si
Sr
U

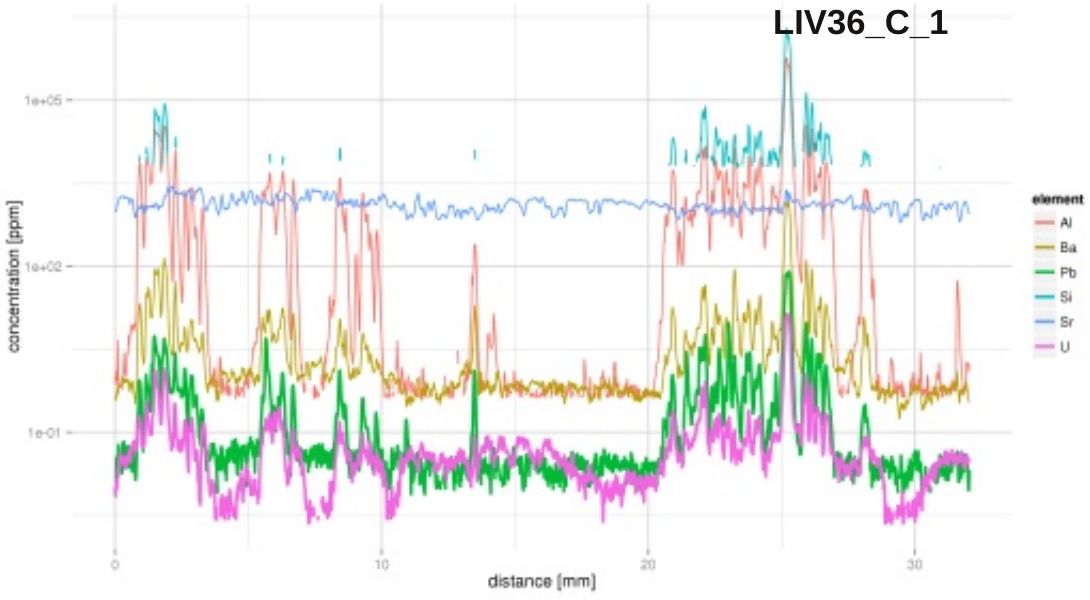
LIV36_C_1
concentration [ppm]
1e+05
1e+02
1e-01
0
10
20
30
distance [mm]
element
Al
Ba
Pb
Si
Sr
U

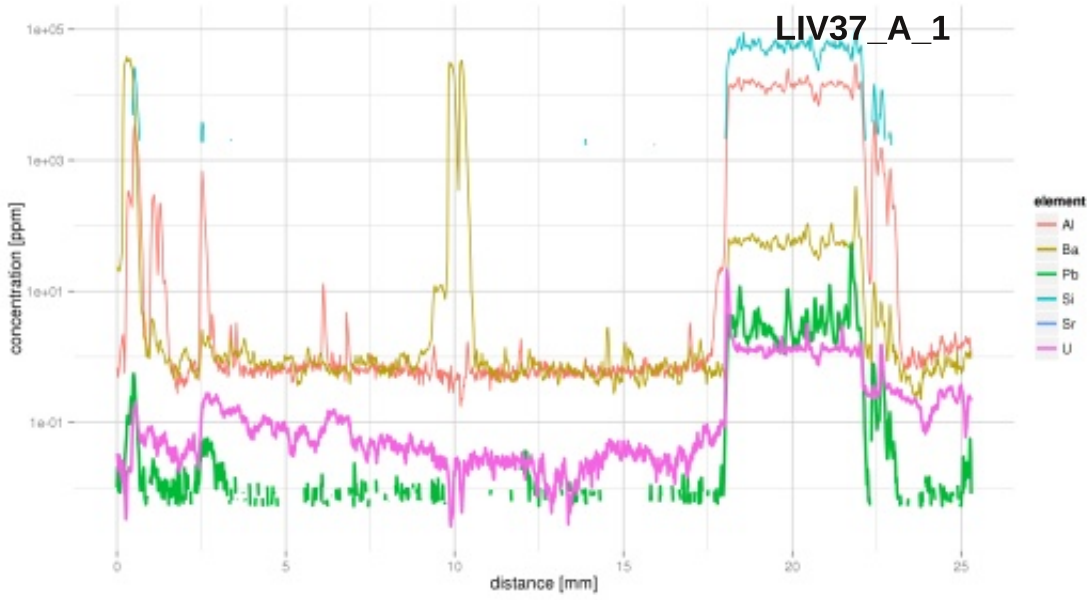
LIV37_A_1
concentration [ppm]
1e+05
1e+03
1e+01
1e-01
0
5
10
15
20
25
distance [mm]
element
Al
Ba
Pb
Si
Sr
U

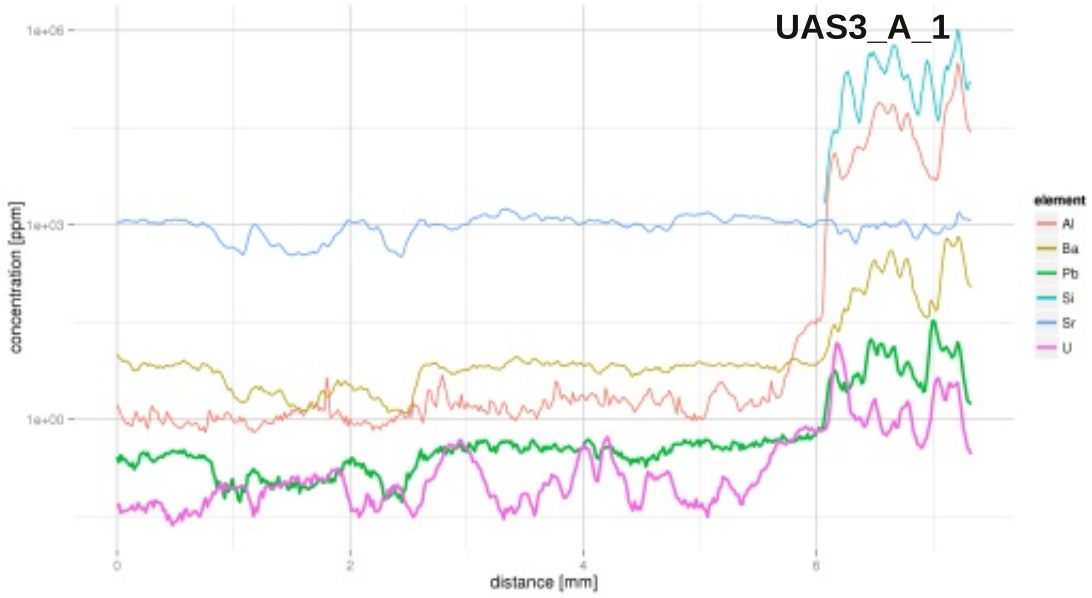
UAS3_A_1
concentration [ppm]
1e+06
1e+03
1e+00
0
2
4
6
distance [mm]
element
Al
Ba
Pb
Si
Sr
U

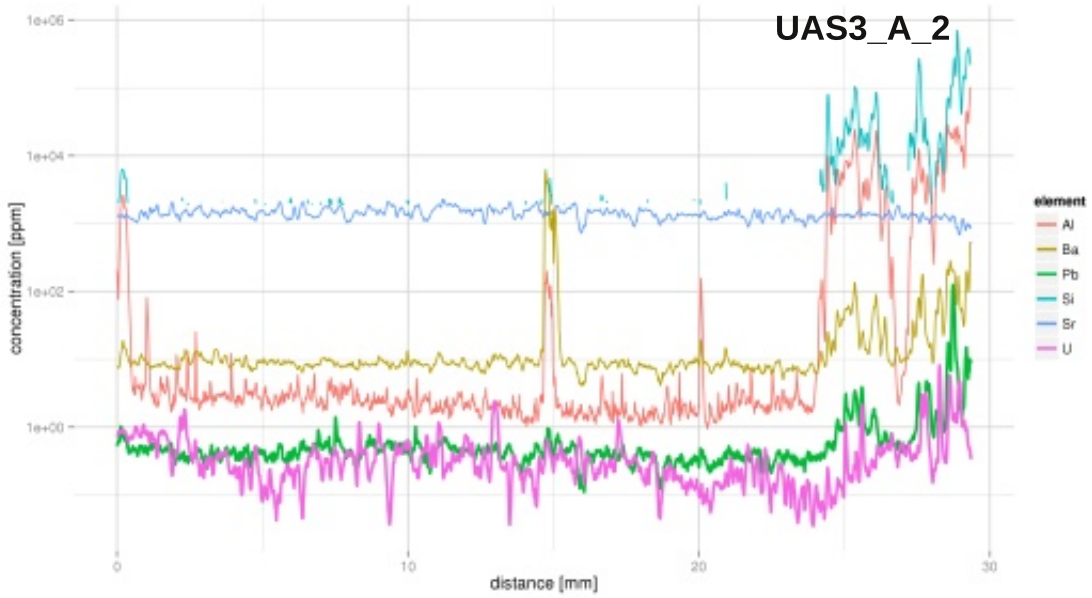
UAS3_A_2
concentration [ppm]
1e+06
1e+04
1e+02
1e+00
0
10
20
30
distance [mm]
element
Al
Ba
Pb
Si
Sr
U

Kilve

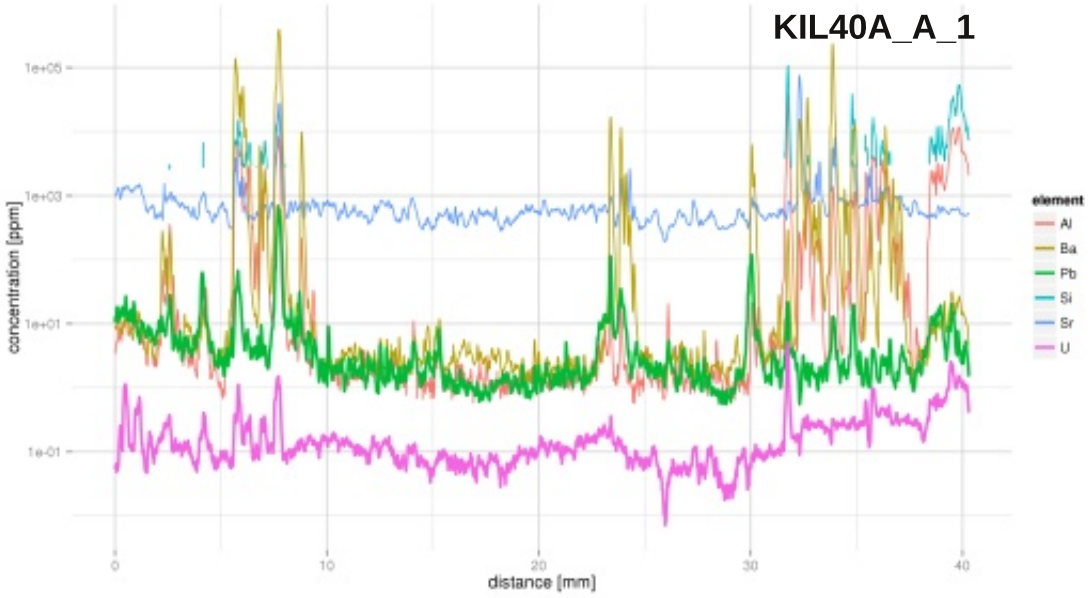
KIL40A_A_1
concentration [ppm]
1e+05
1e+03
1e+01
1e-01
0
10
20
30
40
distance [mm]
element
Al
Ba
Pb
Si
Sr
U

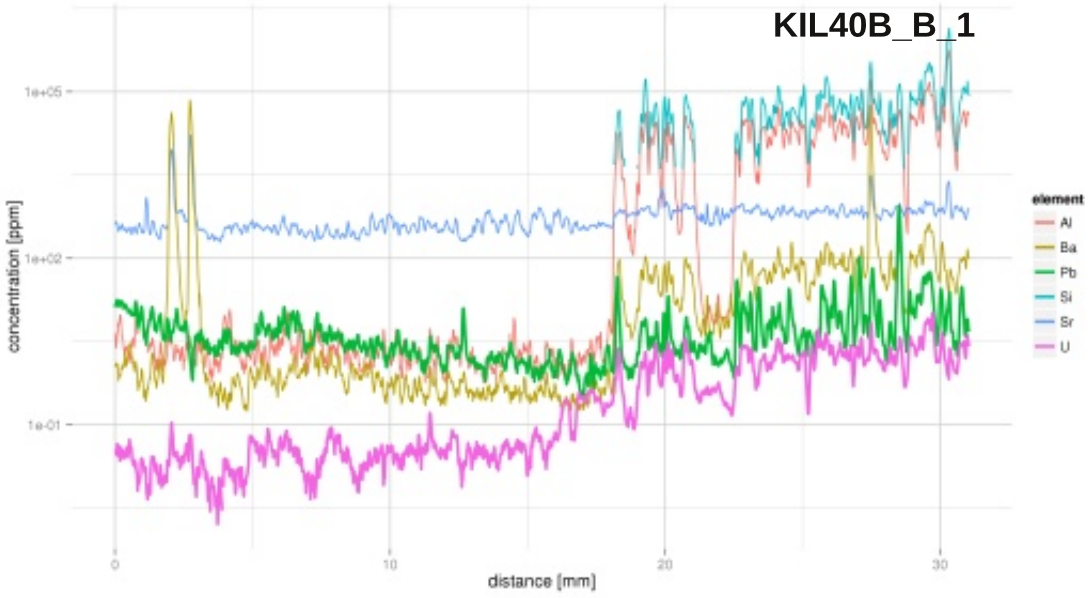
KIL40B_B_1
concentration [ppm]
1e+05
1e+02
1e-01
0
10
20
30
distance [mm]
element
Al
Ba
Pb
Si
Sr
U

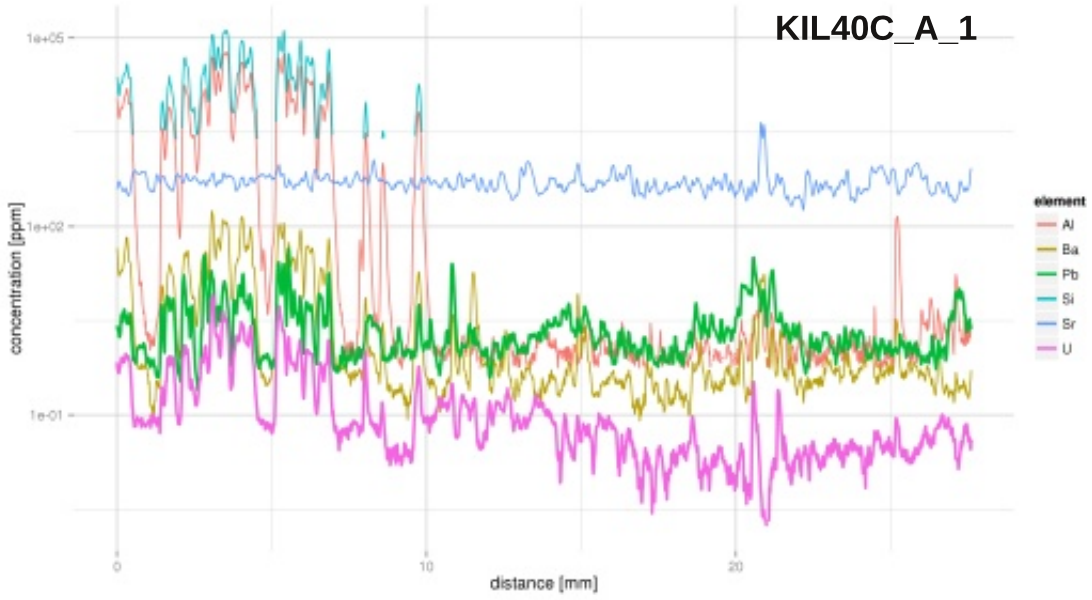
KIL40C_A_1
1e+05
1e+02
1e-01
concentration [ppm]
0
10
20
distance [mm]
element
Al
Ba
Pb
Si
Sr
U


KIL41l1_A_1
10000
100
1
concentration [ppm]
0
5
10
distance [mm]
element
Al
Ba
Pb
Si
Sr
U

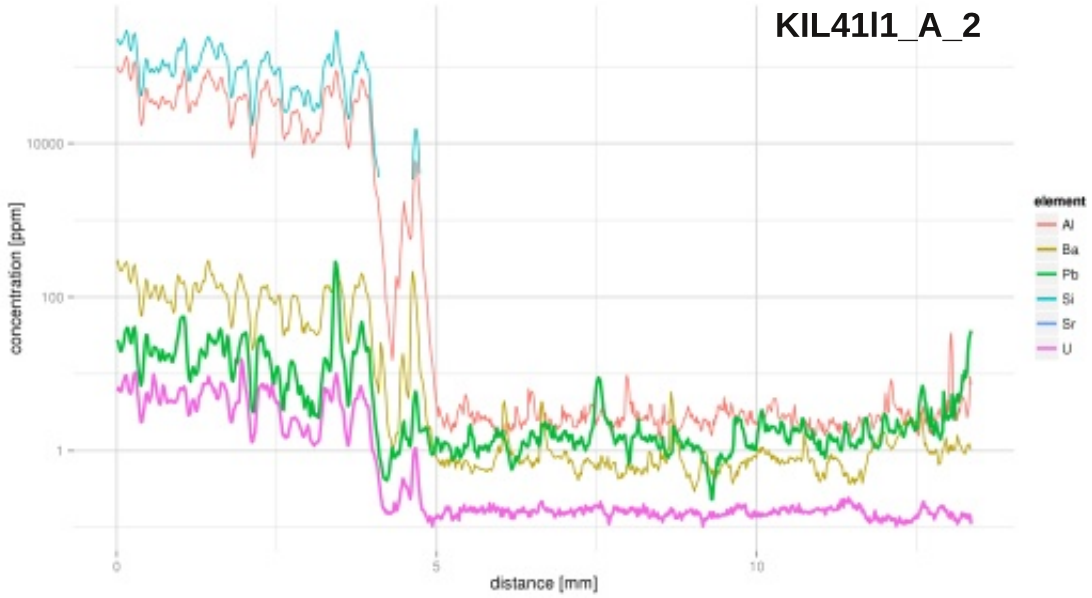
KIL41l1_A_2
10000
100
1
concentration [ppm]
0
5
10
distance [mm]
element
Al
Ba
Pb
Si
Sr
U


KIL41l1_A_3
10000
100
1
concentration [ppm]
0
10
20
30
distance [mm]
element
Al
Ba
Pb
Si
Sr
U

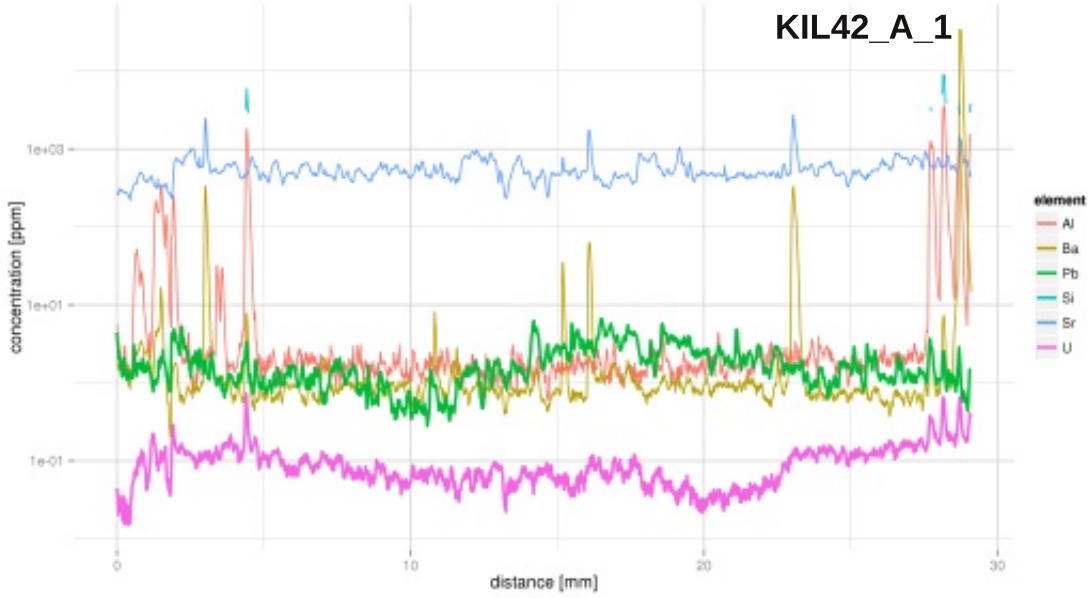
KIL42_A_1
1e+03
1e+01
1e-01
concentration [ppm]
0
10
20
30
distance [mm]
element
Al
Ba
Pb
Si
Sr
U

Leytron

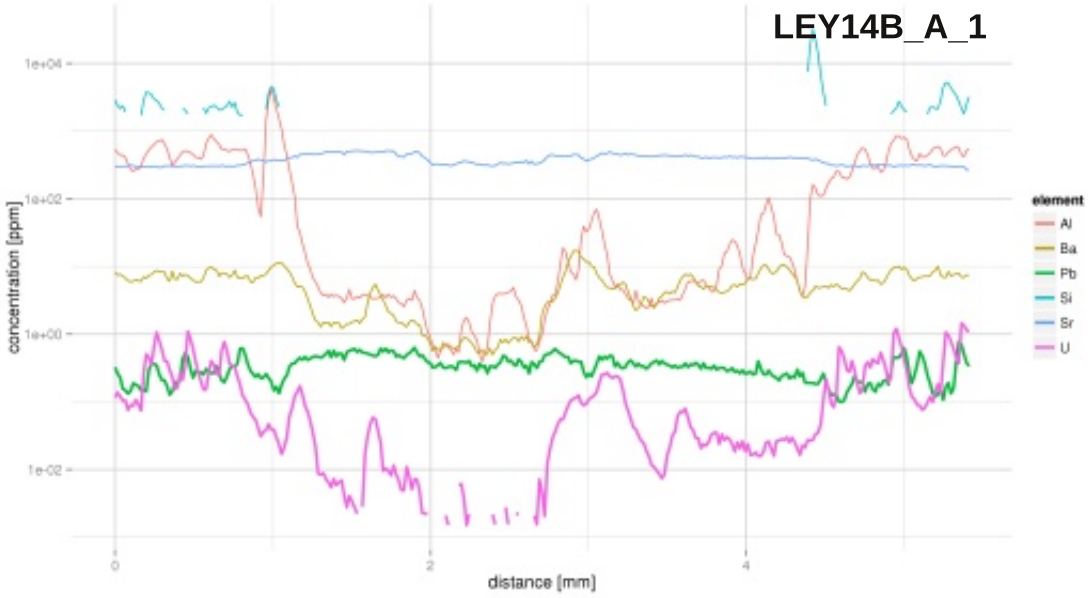
LEY14B_A_1
concentration [ppm]
1e+04
1e+02
1e+00
1e-02
0
2
4
distance [mm]
element
Al
Ba
Pb
Si
Sr
U

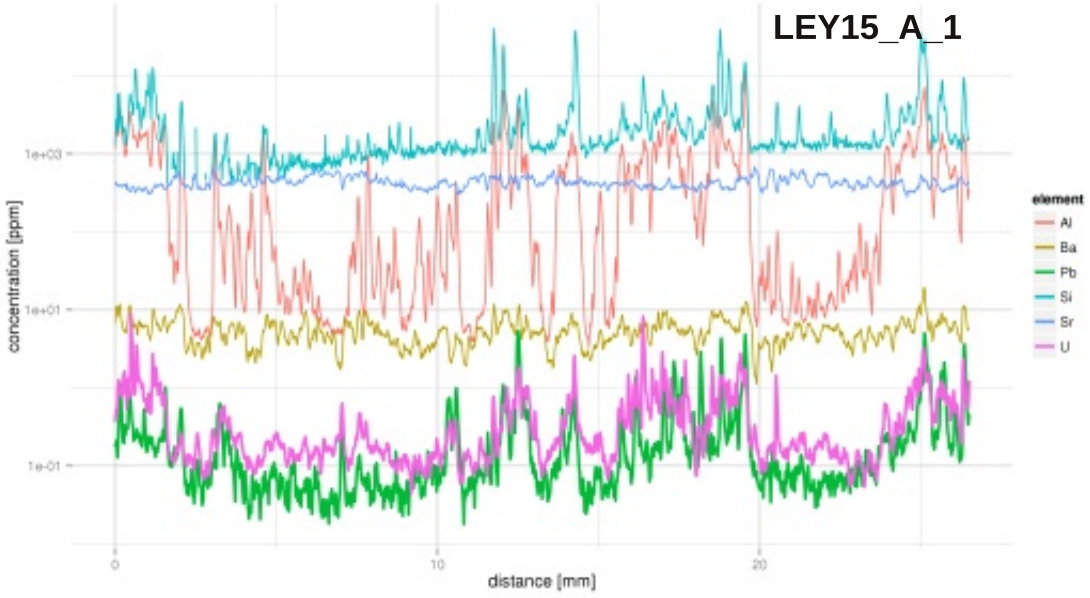
LEY15_A_1
concentration [ppm]
1e+03
1e+01
1e-01
0
10
20
distance [mm]
element
Al
Ba
Pb
Si
Sr
U

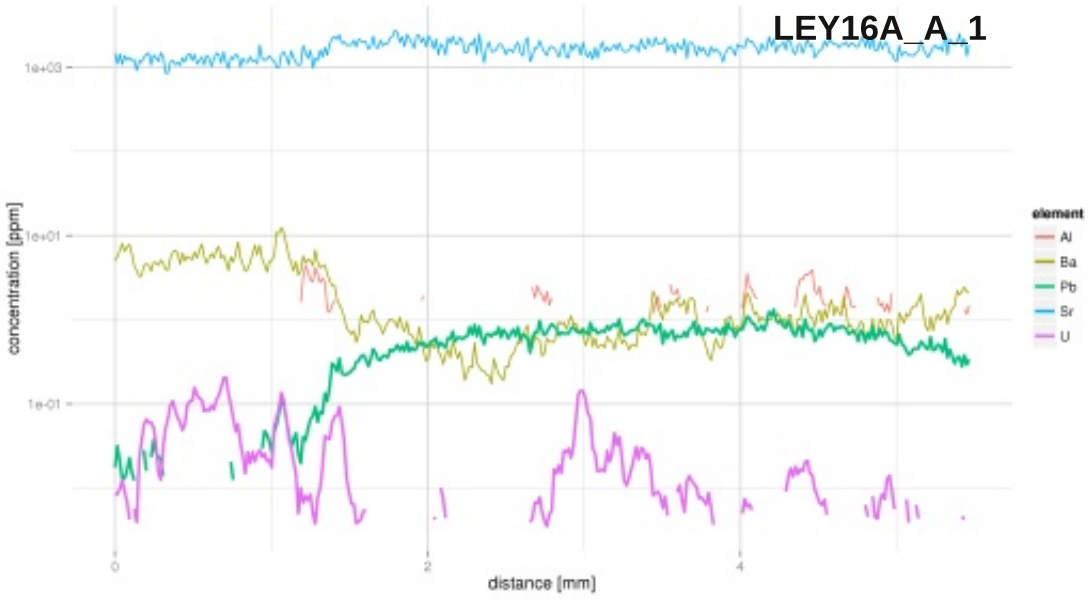
LEY16A_A_1
1e+03
1e+01
1e-01
concentration [ppm]
0
2
4
distance [mm]
element
Al
Ba
Pb
Sr
U

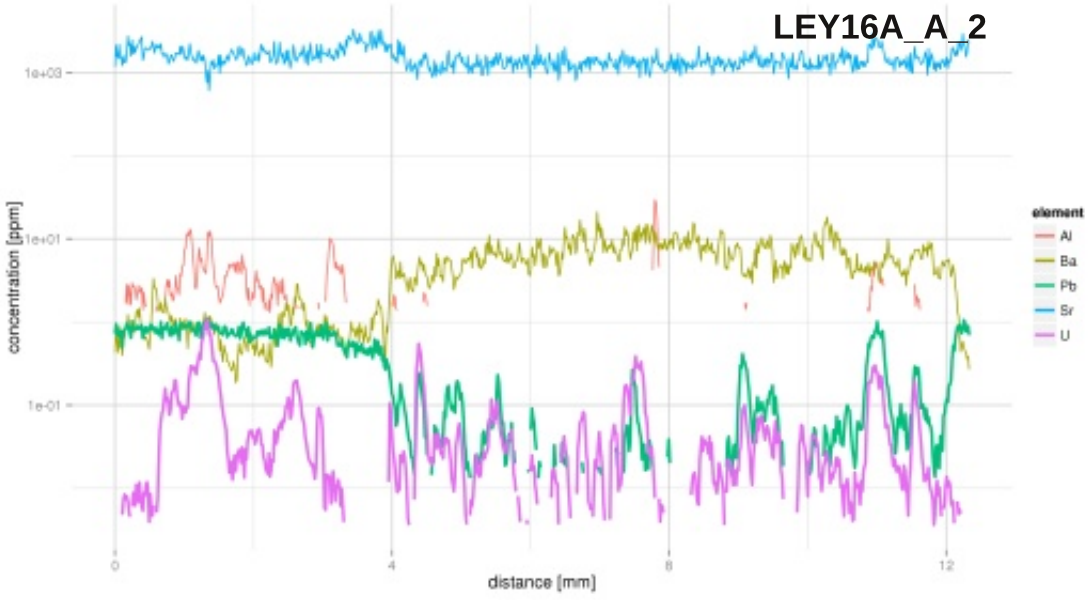
LEY16A_A_2
1e+03
1e+01
1e-01
concentration [ppm]
0
4
8
12
distance [mm]
element
Al
Ba
Pb
Sr
U

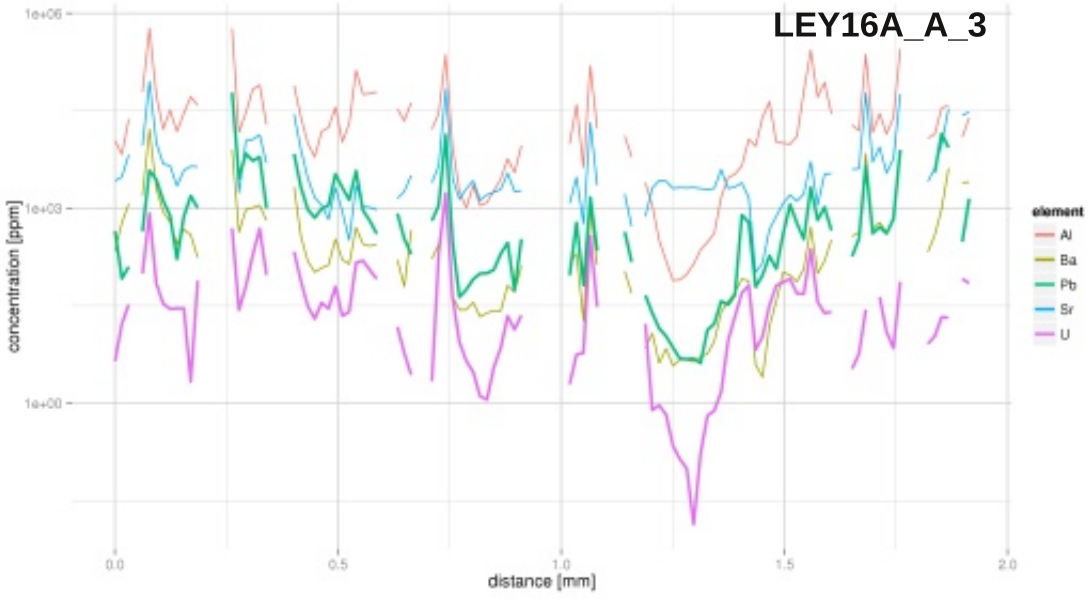
LEY16A_A_3
1e+06
1e+03
1e+00
concentration [ppm]
0.0
0.5
1.0
1.5
2.0
distance [mm]
element
Al
Ba
Pb
Sr
U

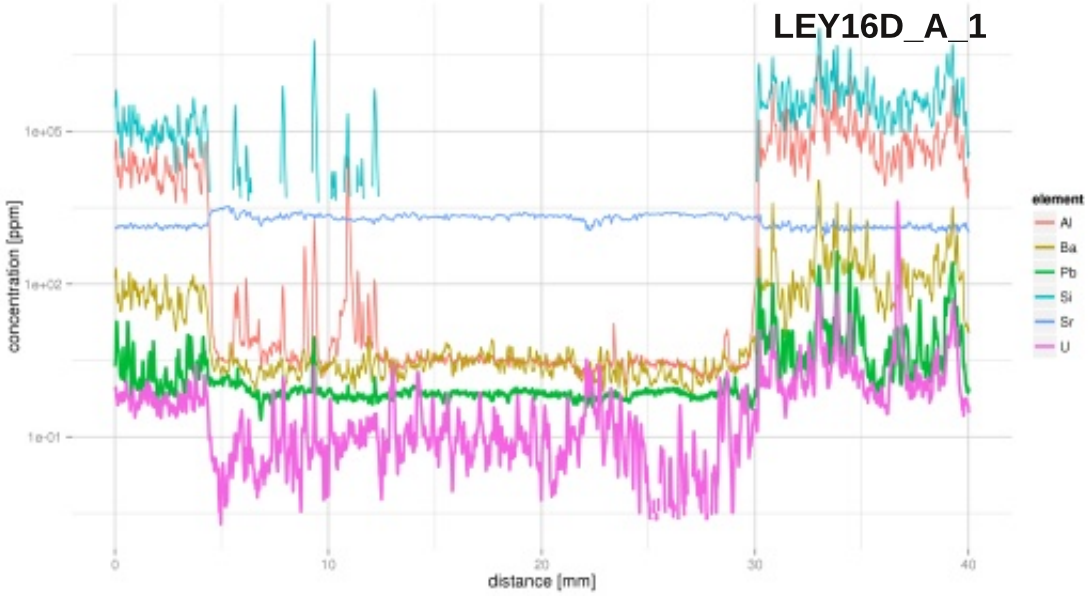
LEY16D_A_1
concentration [ppm]
1e+05
1e+02
1e-01
0
10
20
30
40
distance [mm]
element
Al
Ba
Pb
Si
Sr
U

Seefeld

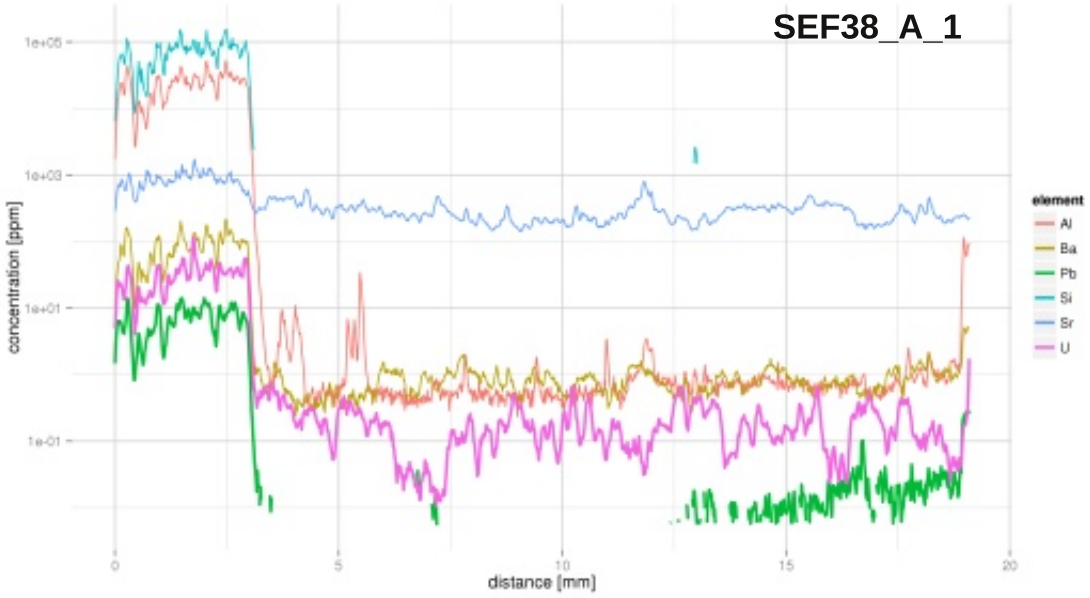
SEF38_A_1
concentration [ppm]
1e+05
1e+03
1e+01
1e-01
0
5
10
15
20
distance [mm]
element
Al
Ba
Pb
Si
Sr
U

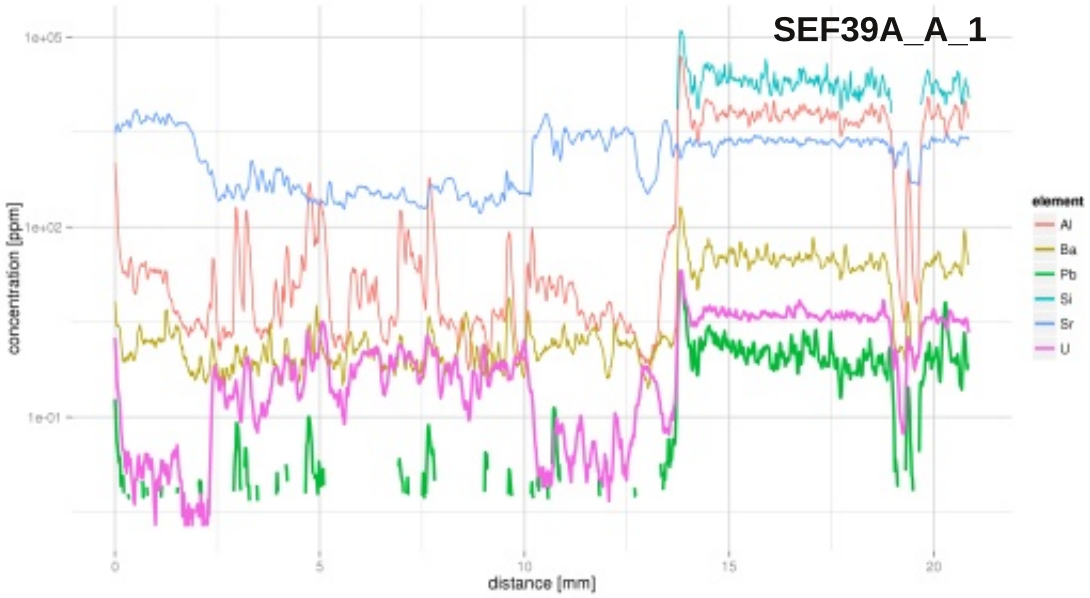
SEF39A_A_1
concentration [ppm]
1e+05
1e+02
1e-01
0
5
10
15
20
distance [mm]
element
Al
Ba
Pb
Si
Sr
U

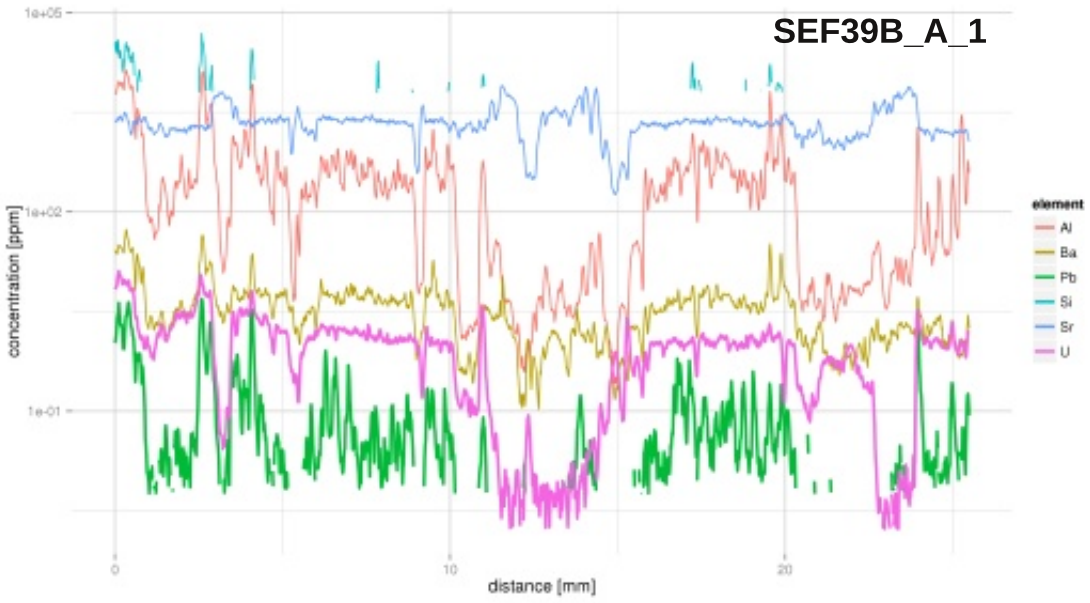
SEF39B_A_1
concentration [ppm]
1e+05
1e+02
1e-01
0
10
20
distance [mm]
element
Al
Ba
Pb
Si
Sr
U

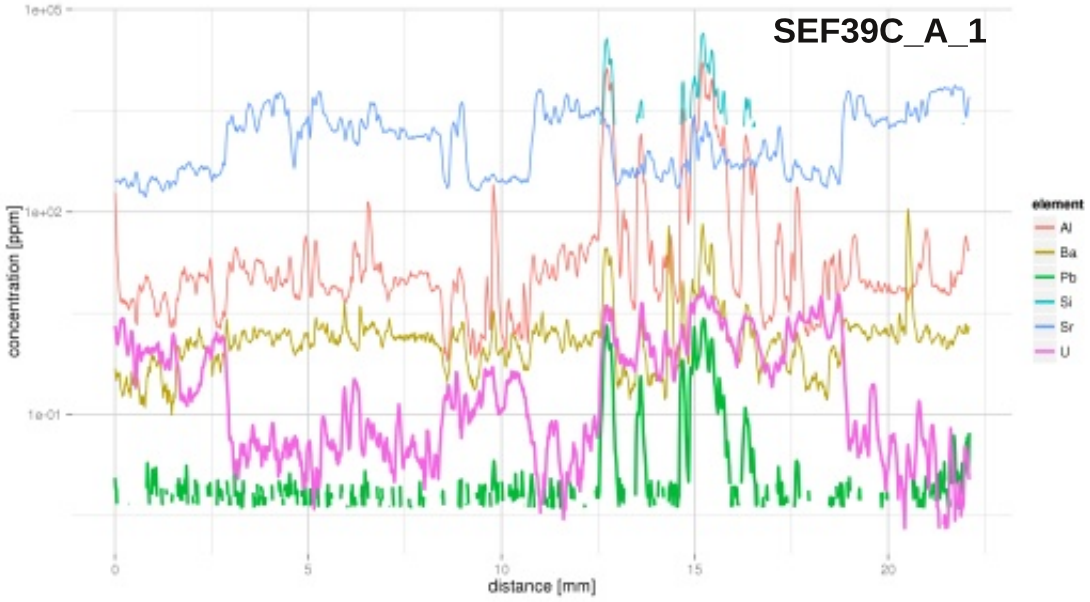
SEF39C_A_1
concentration [ppm]
1e+05
1e+02
1e-01
0
5
10
15
20
distance [mm]
element
Al
Ba
Pb
Si
Sr
U

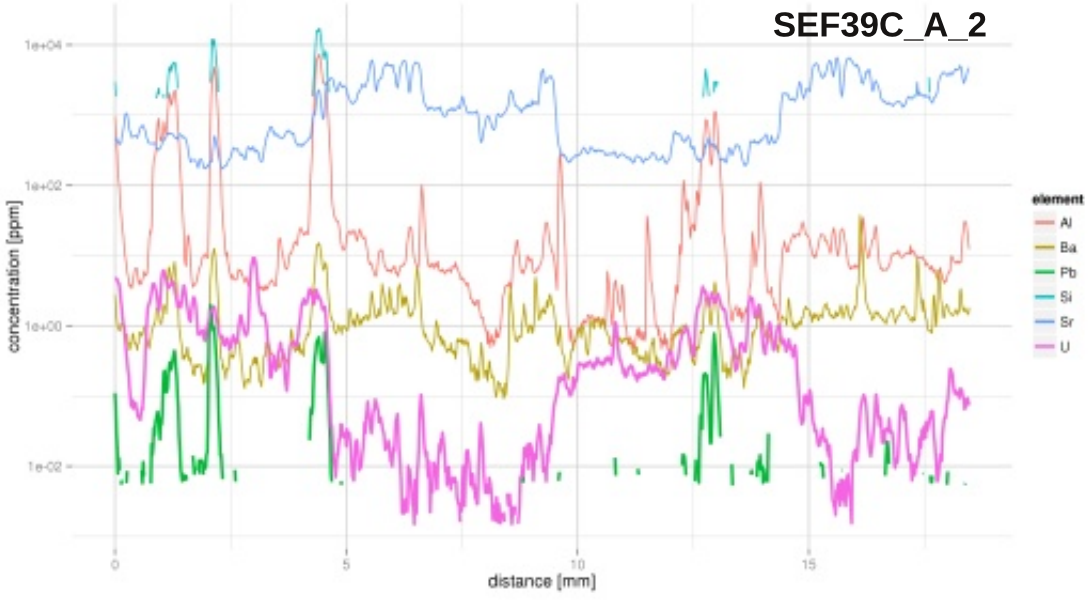
SEF39C_A_2
concentration [ppm]
1e+04
1e+02
1e+00
1e-02
0
5
10
15
distance [mm]
element
Al
Ba
Pb
Si
Sr
U

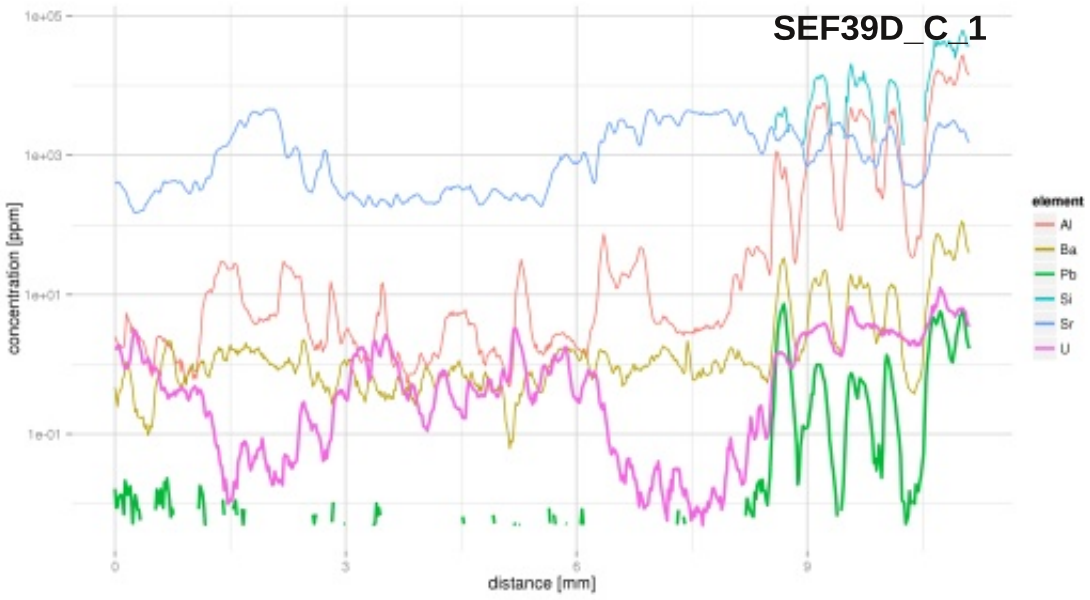
SEF39D_C_1
concentration [ppm]
1e+05
1e+03
1e+01
1e-01
0
3
6
9
distance [mm]
element
Al
Ba
Pb
Si
Sr
U

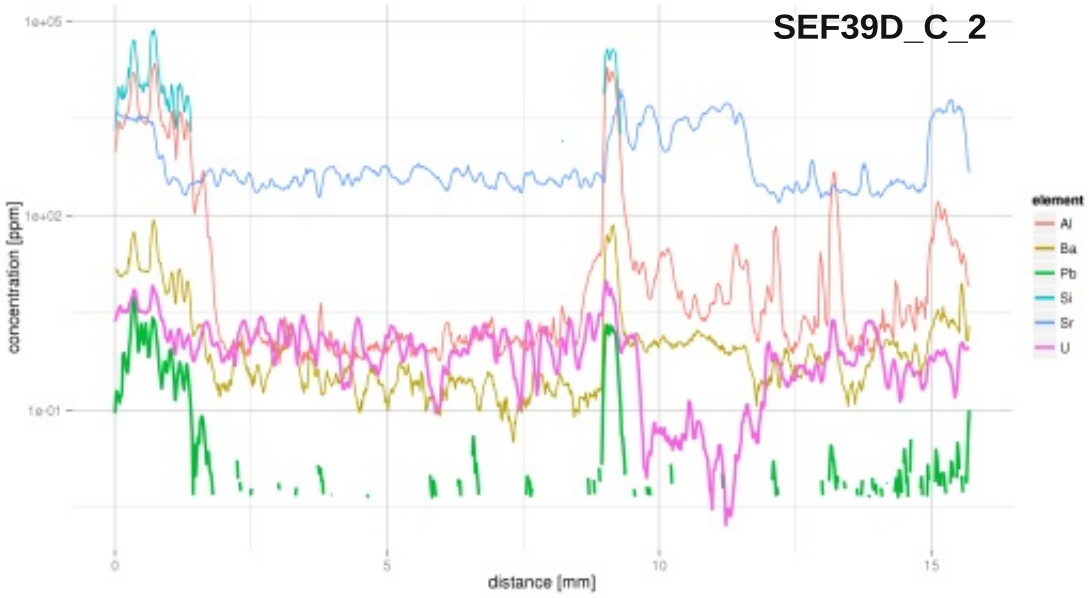
SEF39D_C_2
concentration [ppm]
1e+05
1e+02
1e-01
0
5
10
15
distance [mm]
element
Al
Ba
Pb
Si
Sr
U

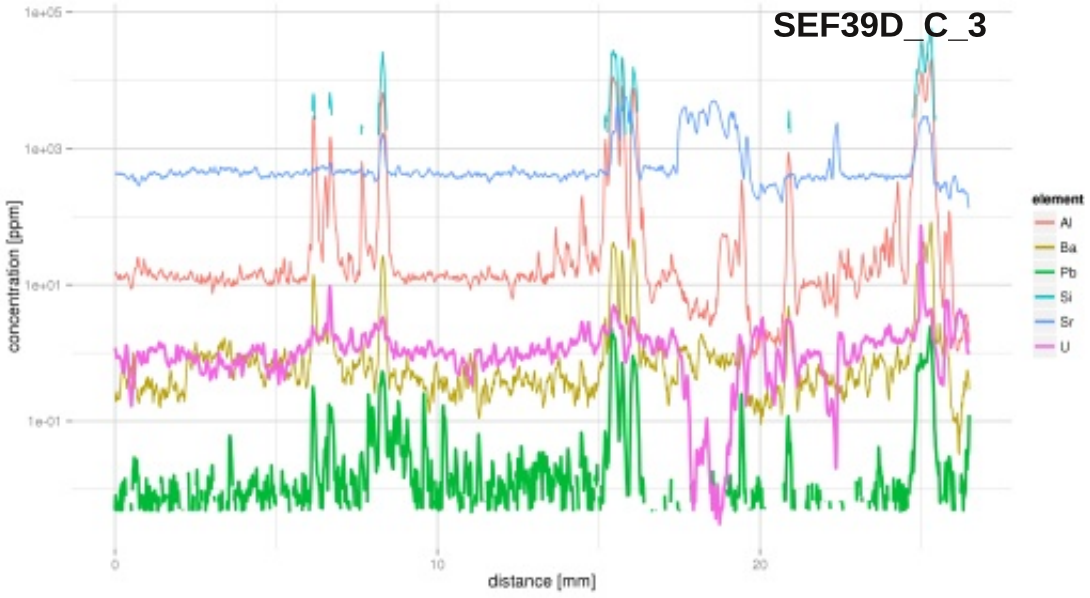
SEF39D_C_3
concentration [ppm]
1e+05
1e+03
1e+01
1e-01
0
10
20
distance [mm]
element
Al
Ba
Pb
Si
Sr
U

Contributed samples

The following samples were contributed by collaborators.

Sample s30 from East Canada was contributed by Simon Craggs, RHUL.

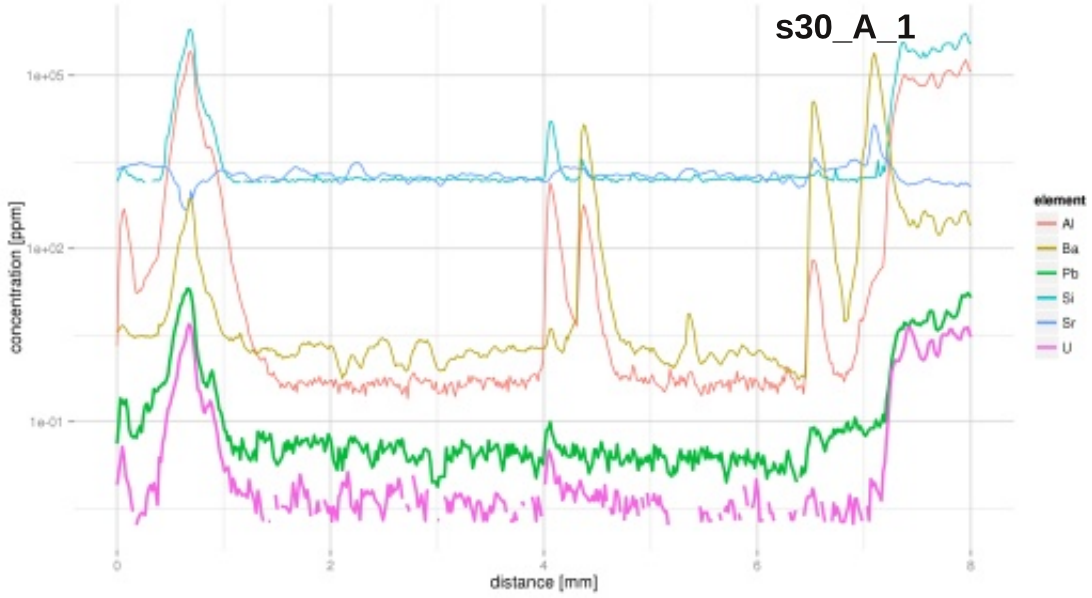

Swiss Helvetic nappes: Samples CF1 - CF15 contributed by Daniel Egli, ETH Zürich, Switzerland.

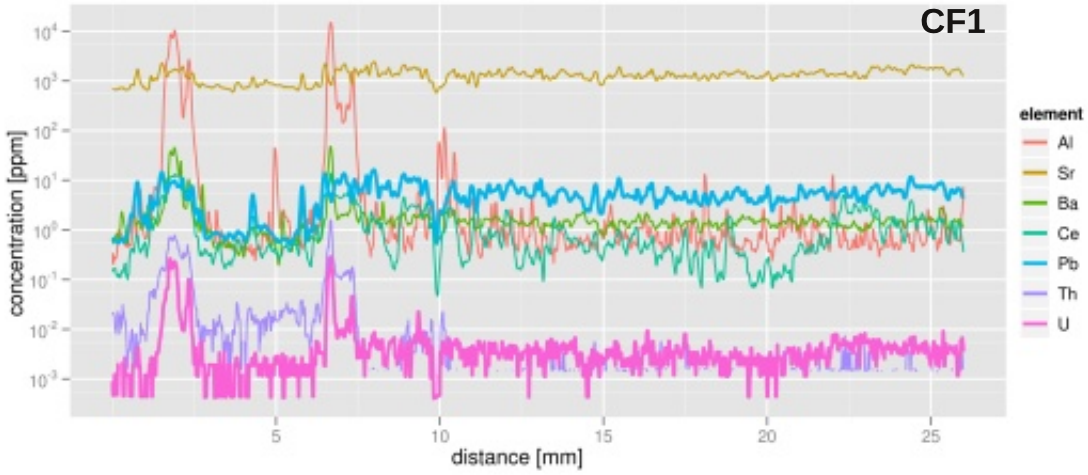

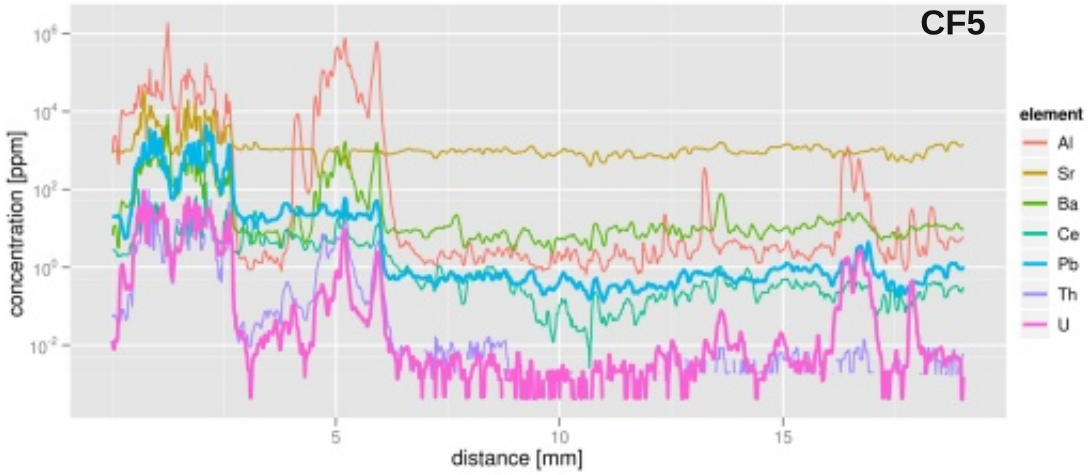

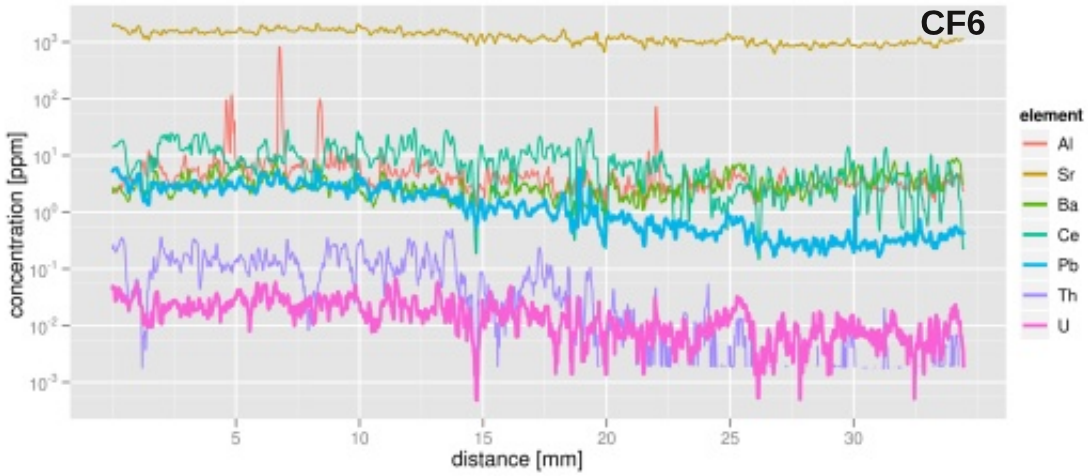

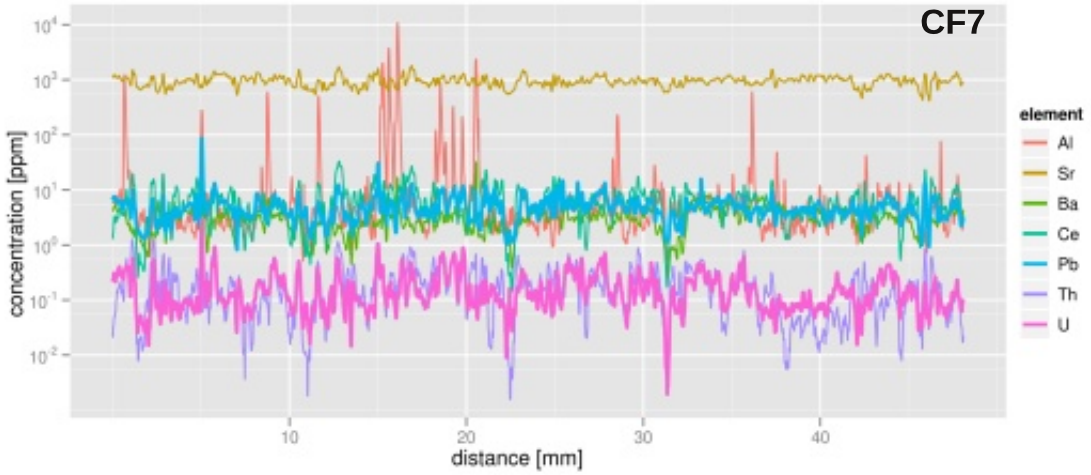
CF7
concentration [ppm]
distance [mm]
element
Al
Sr
Ba
Ce
Pb
Th
U

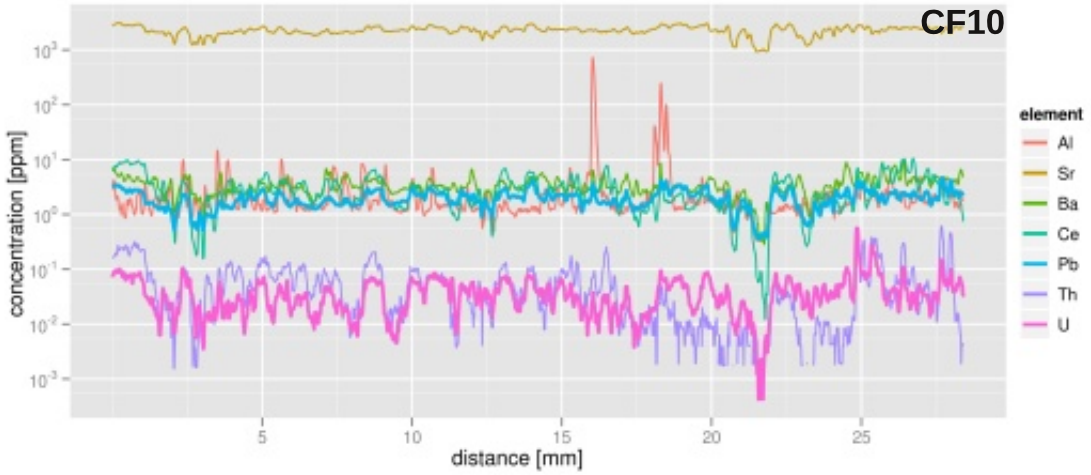
CF10
concentration [ppm]
distance [mm]
element
Al
Sr
Ba
Ce
Pb
Th
U

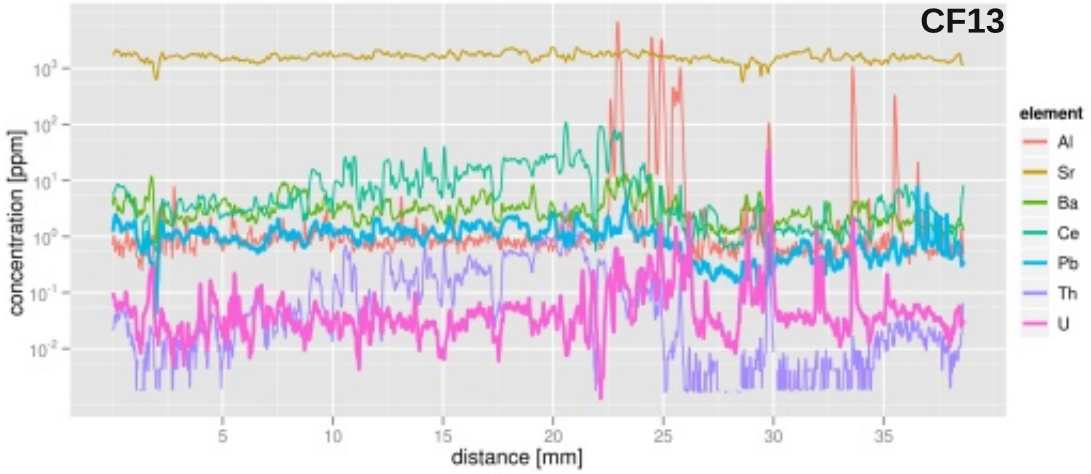
CF13
concentration [ppm]
distance [mm]
element
Al
Sr
Ba
Ce
Pb
Th
U

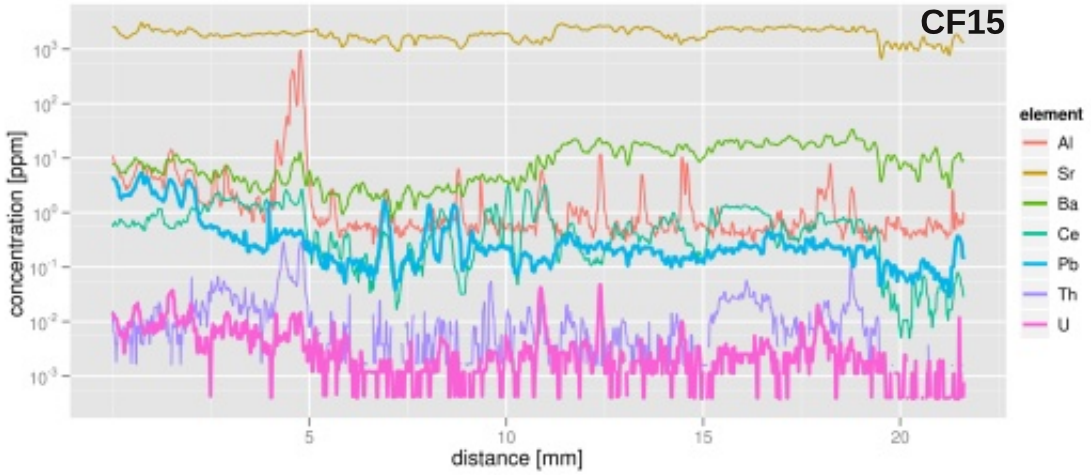
CF15
concentration [ppm]
10^3
10^2
10^1
10^0
10^{-1}
10^{-2}
10^{-3}
5
10
15
20
distance [mm]
element
Al
Sr
Ba
Ce
Pb
Th
U

Swiss Jura samples MHH01 - MHH07 were contributed by Herfried Madritsch, NAGRA, Switzerland.

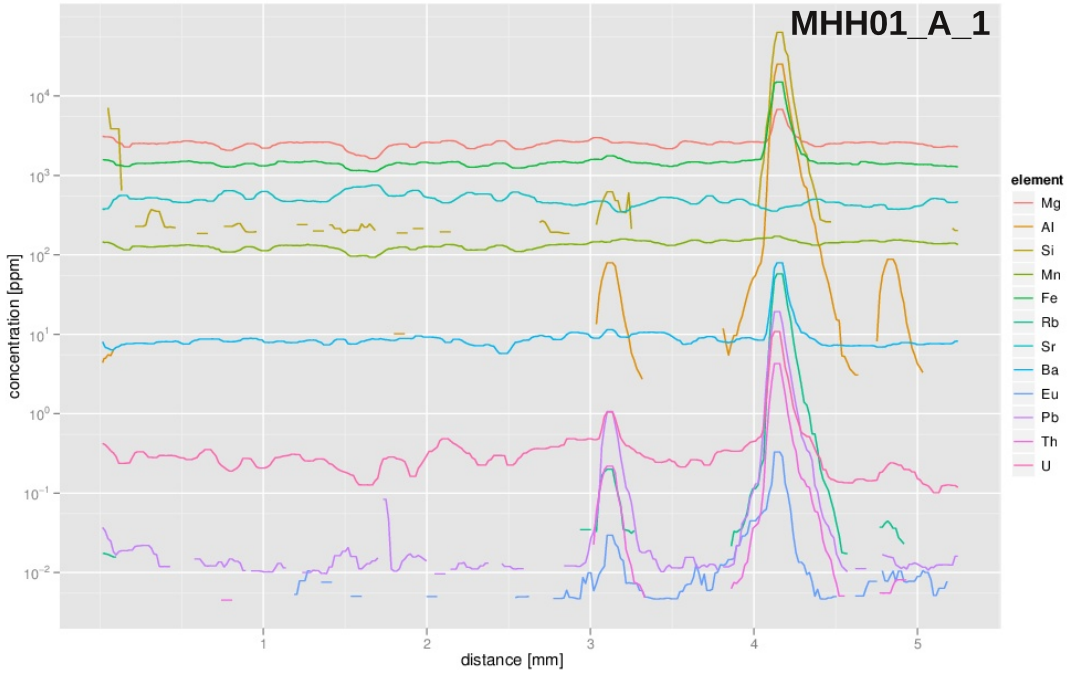

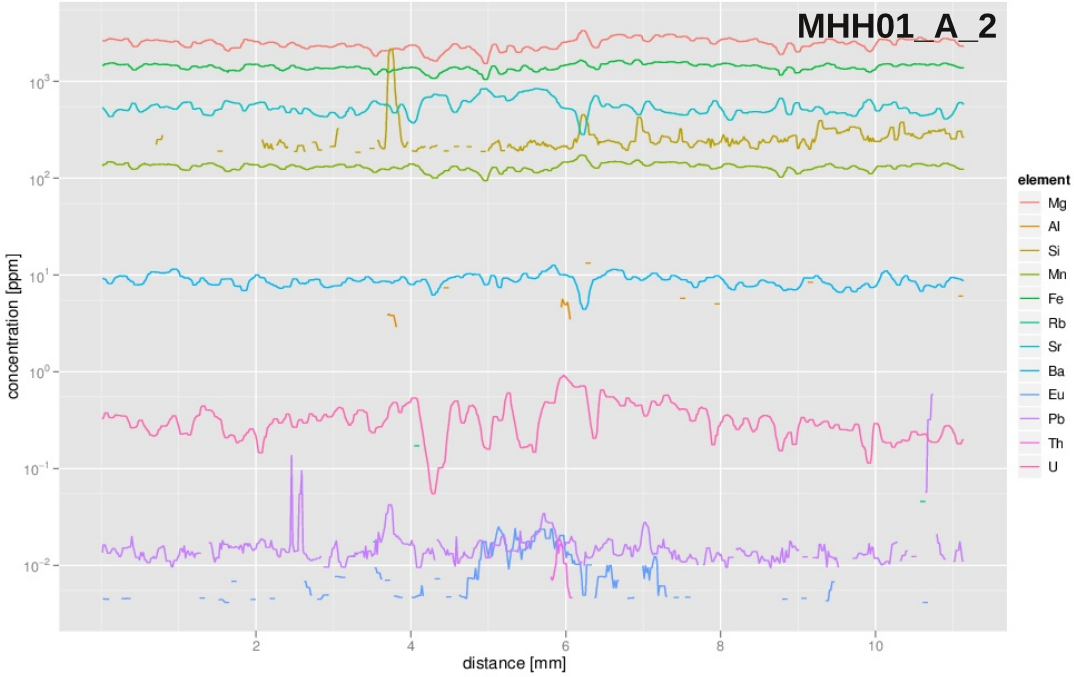

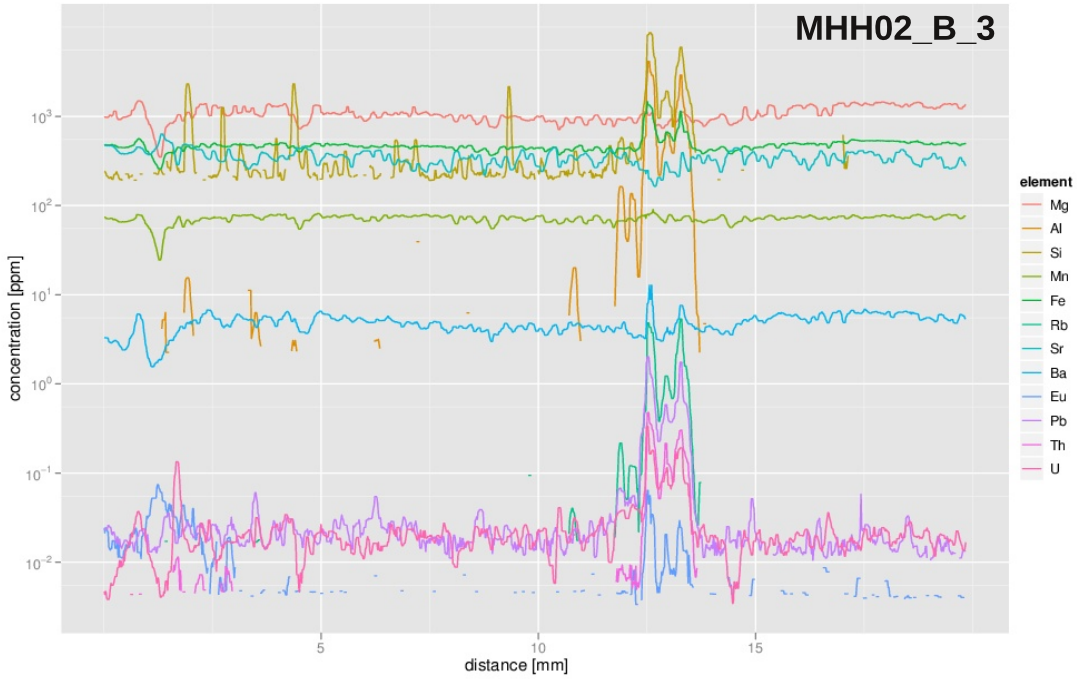
MHH02_B_3
concentration [ppm]
distance [mm]
element
Mg
Al
Si
Mn
Fe
Rb
Sr
Ba
Eu
Pb
Th
U

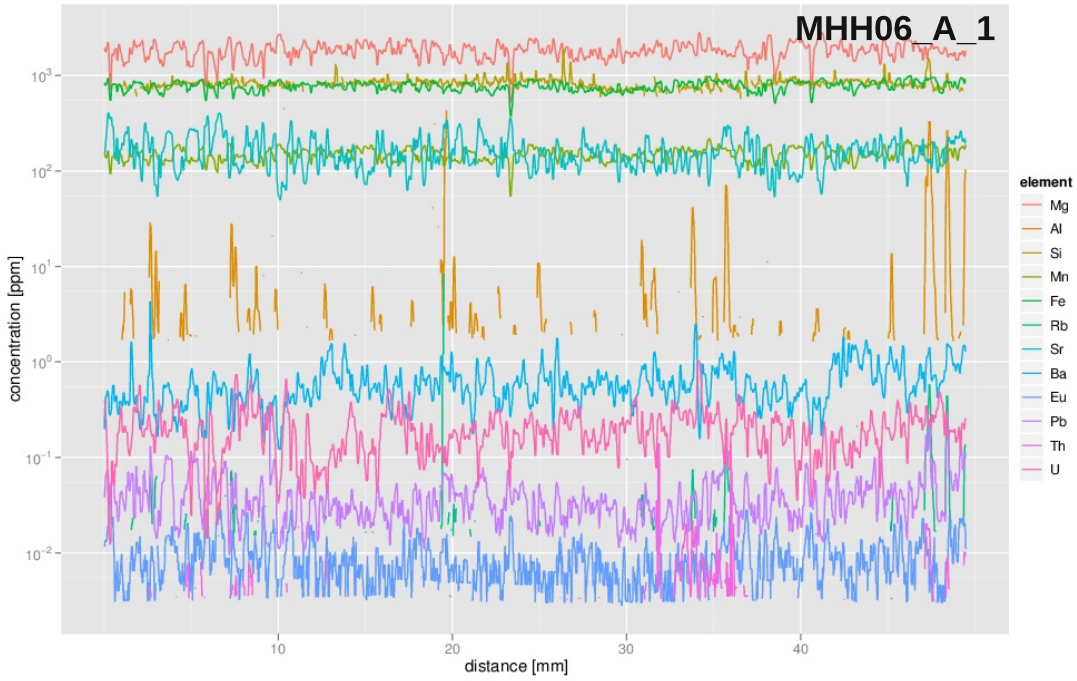
MHH06_A_1
concentration [ppm]
distance [mm]
element
Mg
Al
Si
Mn
Fe
Rb
Sr
Ba
Eu
Pb
Th
U

LA-ICPMS in situ isotope measurements

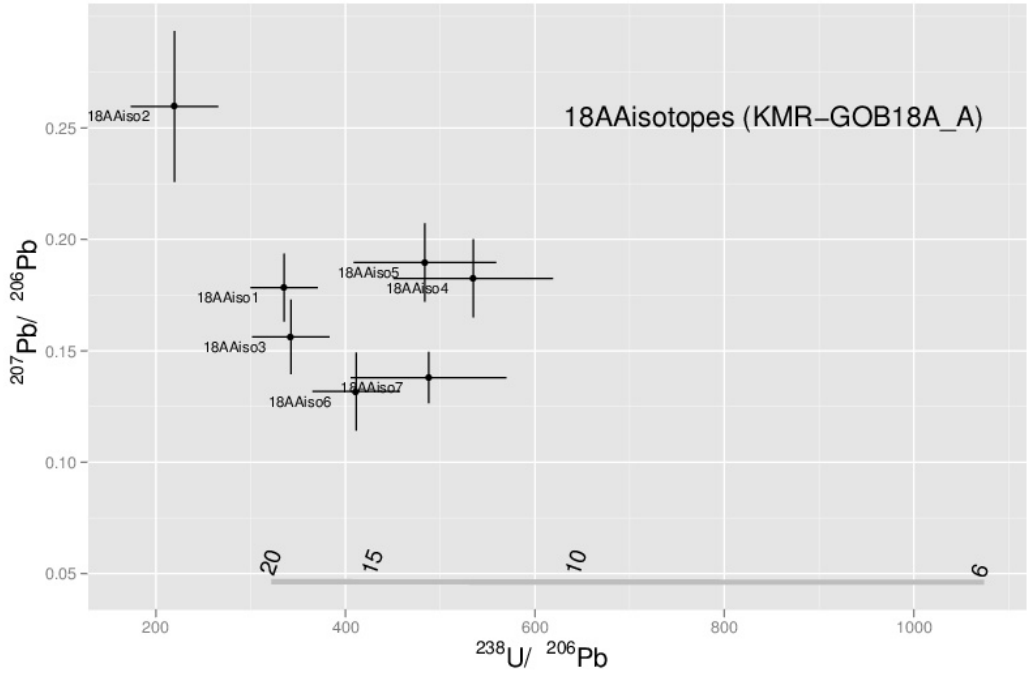

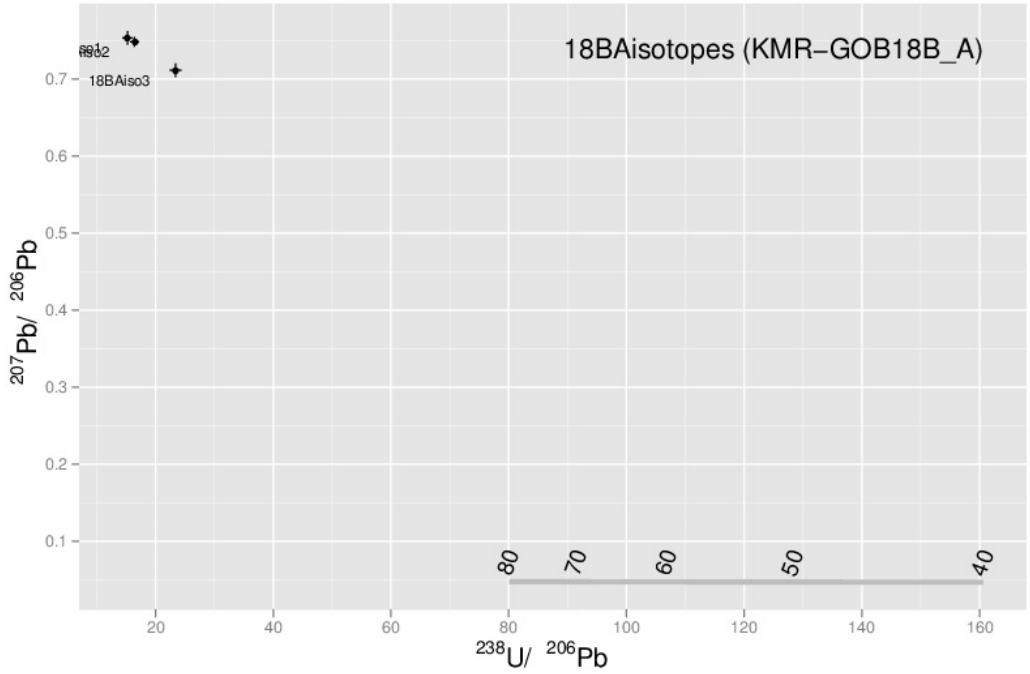

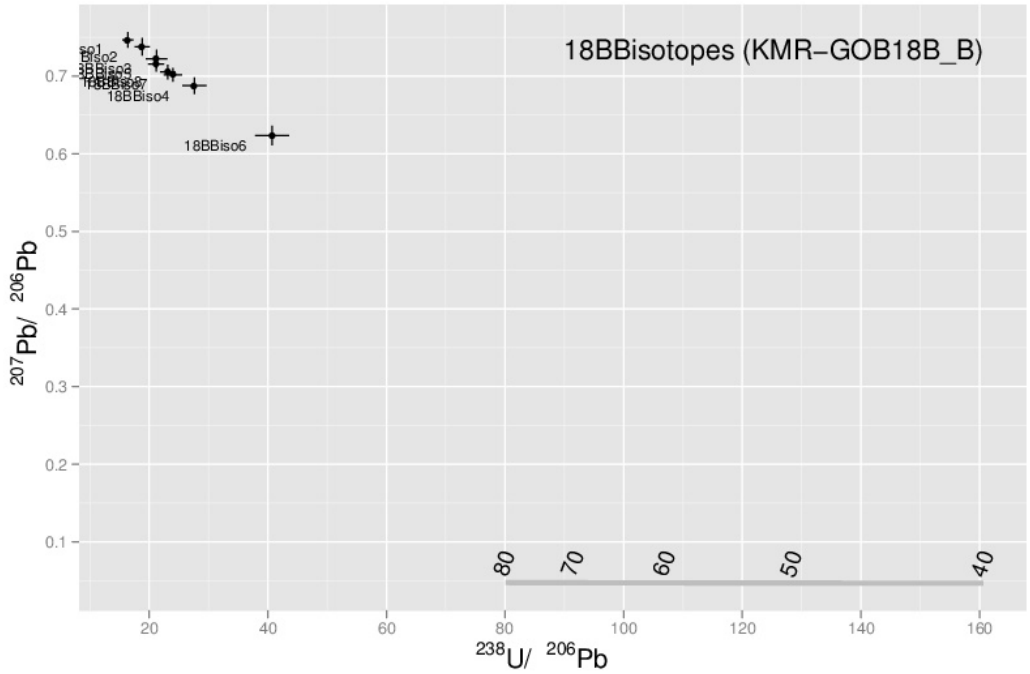
18BBisotopes (KMR−GOB18B_B)
18BBiso4
18BBiso6
80
70
60
50
40
0.7
0.6
0.5
0.4
0.3
0.2
0.1
20
40
60
80
100
120
140
160
^{207}Pb/ ^{206}Pb
^{238}U/ ^{206}Pb

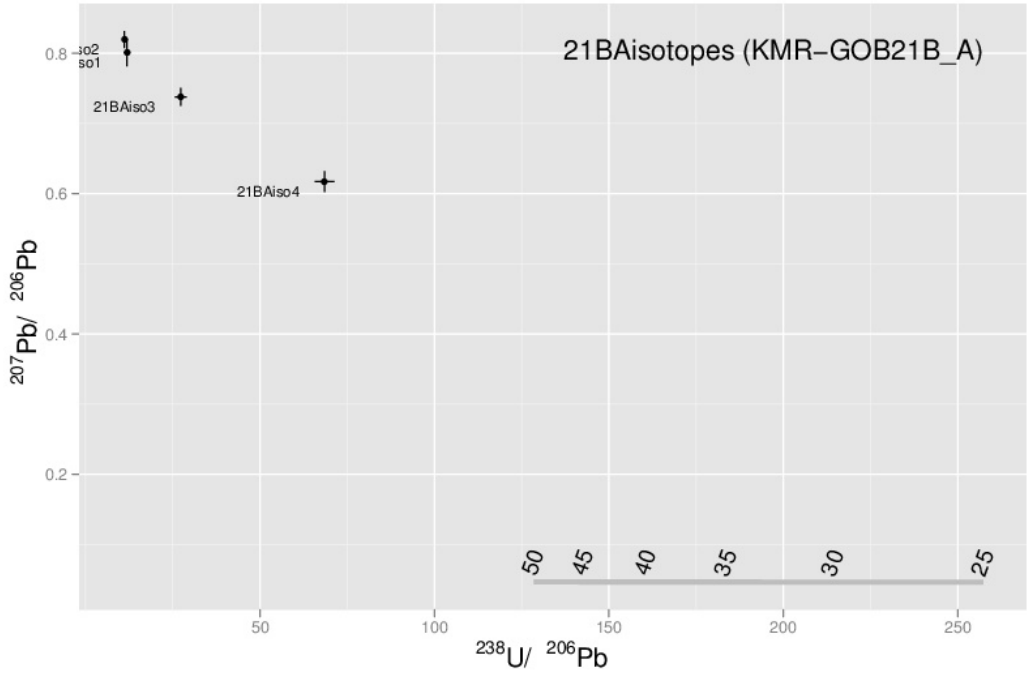
21BAisotopes (KMR−GOB21B_A)
21BAiso3
21BAiso4
50
45
40
35
30
25
0.8
0.6
0.4
0.2
50
100
150
200
250
^{207}Pb/ ^{206}Pb
^{238}U/ ^{206}Pb

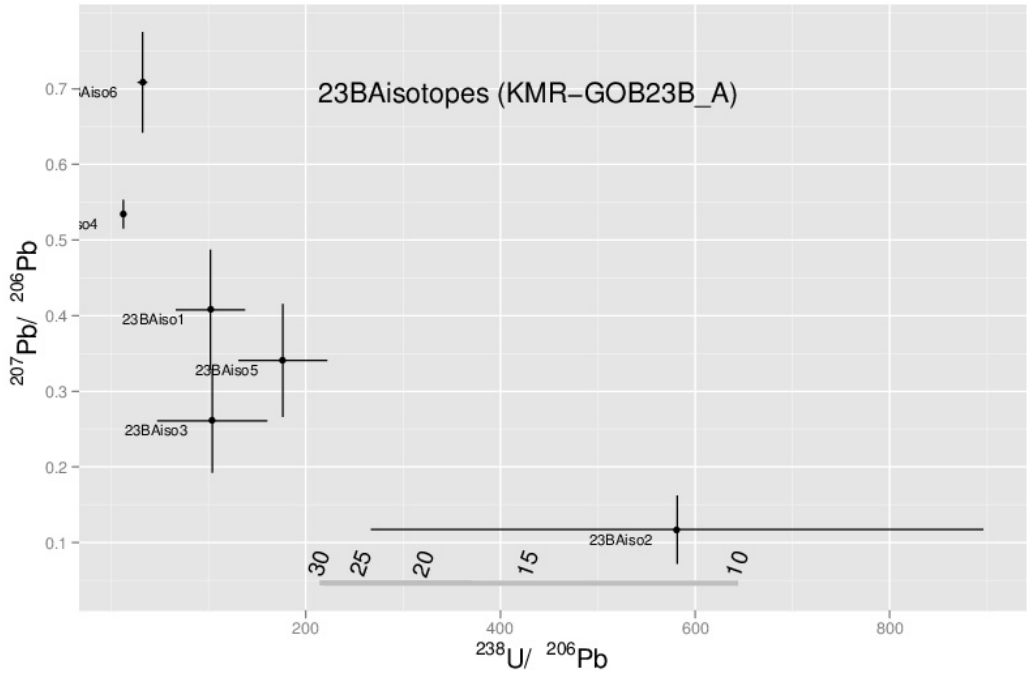
23BAisotopes (KMR−GOB23B_A)
23BAiso1
23BAiso5
23BAiso3
23BAiso2
30
25
20
15
10
0.7
0.6
0.5
0.4
0.3
0.2
0.1
200
400
600
800
$^{207}Pb/^{206}Pb$
$^{238}U/^{206}Pb$

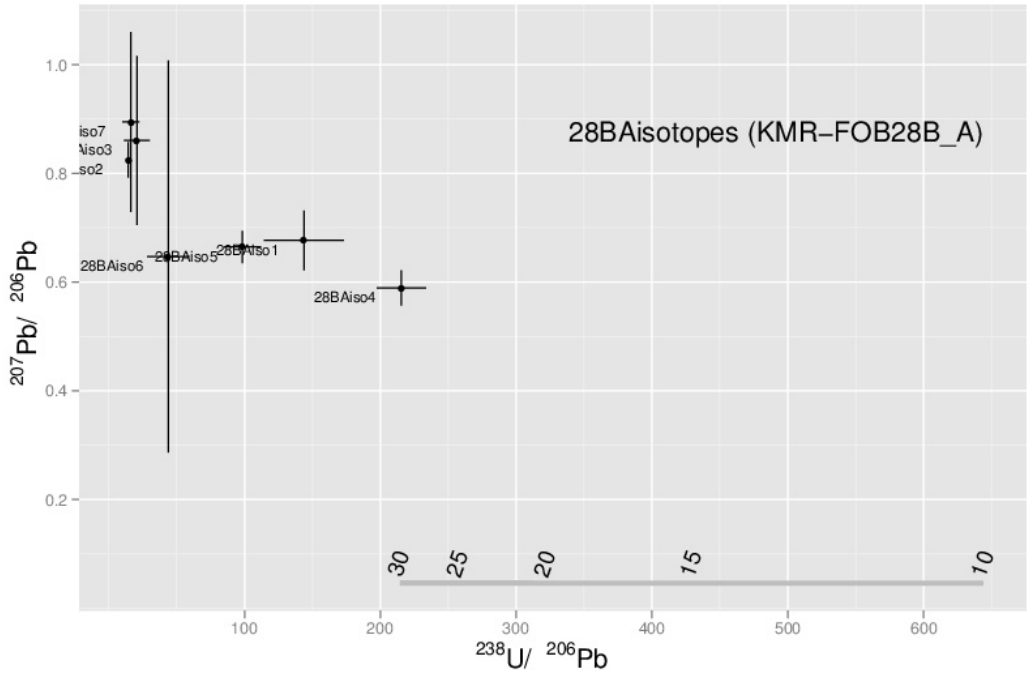
28BAisotopes (KMR−FOB28B_A)
28BAiso6
28BAiso4
30
25
20
15
10
1.0
0.8
0.6
0.4
0.2
100
200
300
400
500
600
$^{207}Pb/^{206}Pb$
$^{238}U/^{206}Pb$

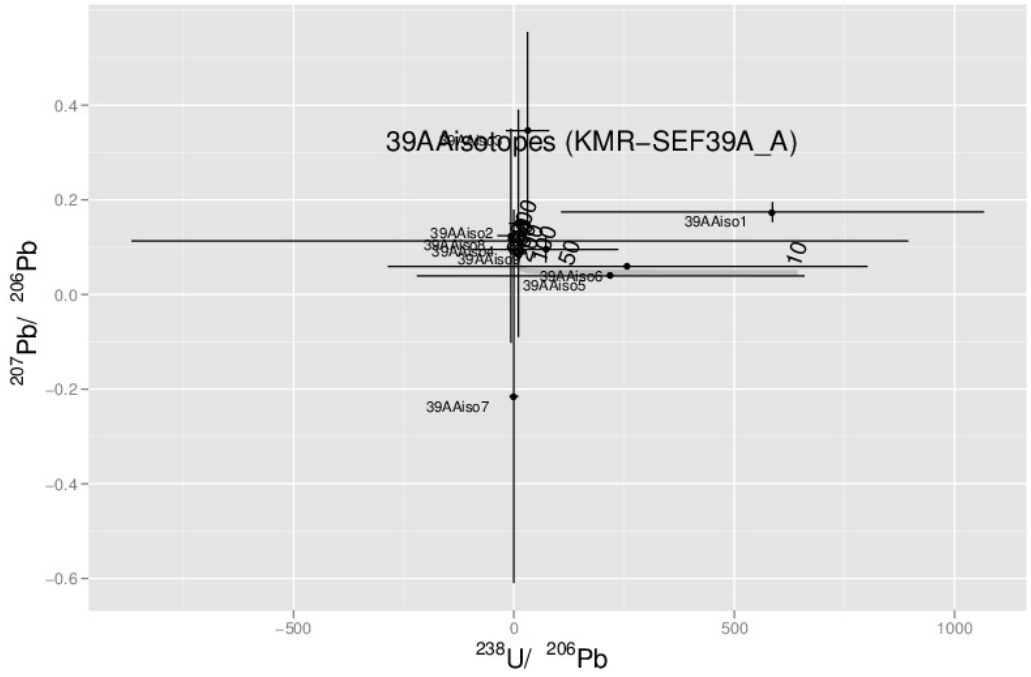
39AAisotopes (KMR−SEF39A_A)
39AAiso1
39AAiso2
39AAiso5
39AAiso6
39AAiso7
0.4
0.2
0.0
−0.2
−0.4
−0.6
−500
0
500
1000
$^{207}Pb/^{206}Pb$
$^{238}U/^{206}Pb$

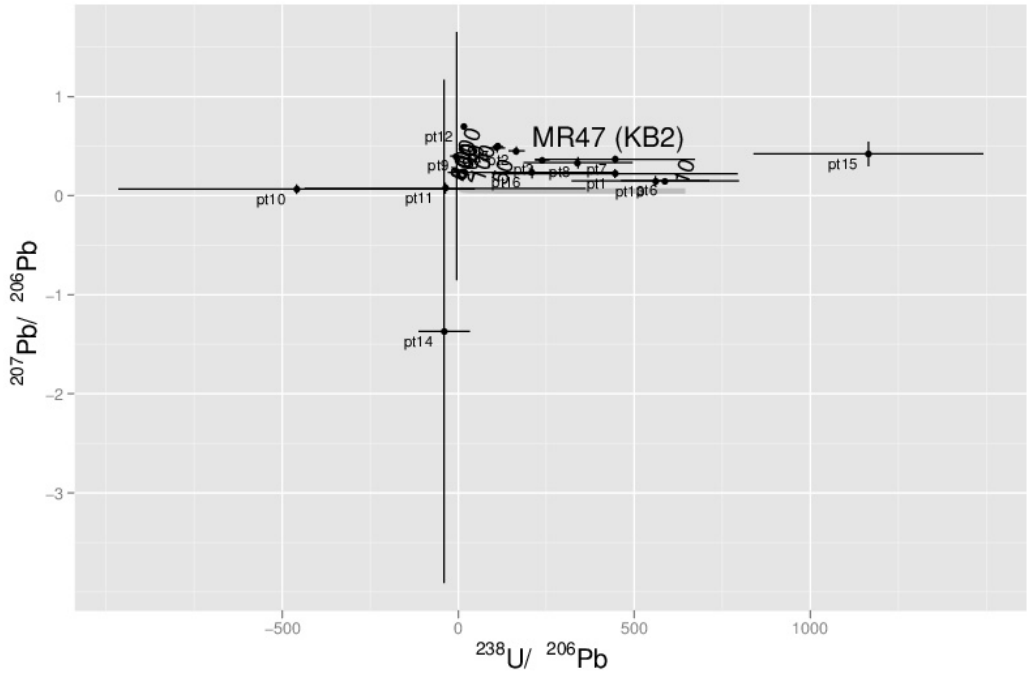
MR47 (KB2)
pt10
pt11
pt12
pt14
pt15
1
0
−1
−2
−3
−500
0
500
1000
$^{207}Pb/^{206}Pb$
$^{238}U/^{206}Pb$

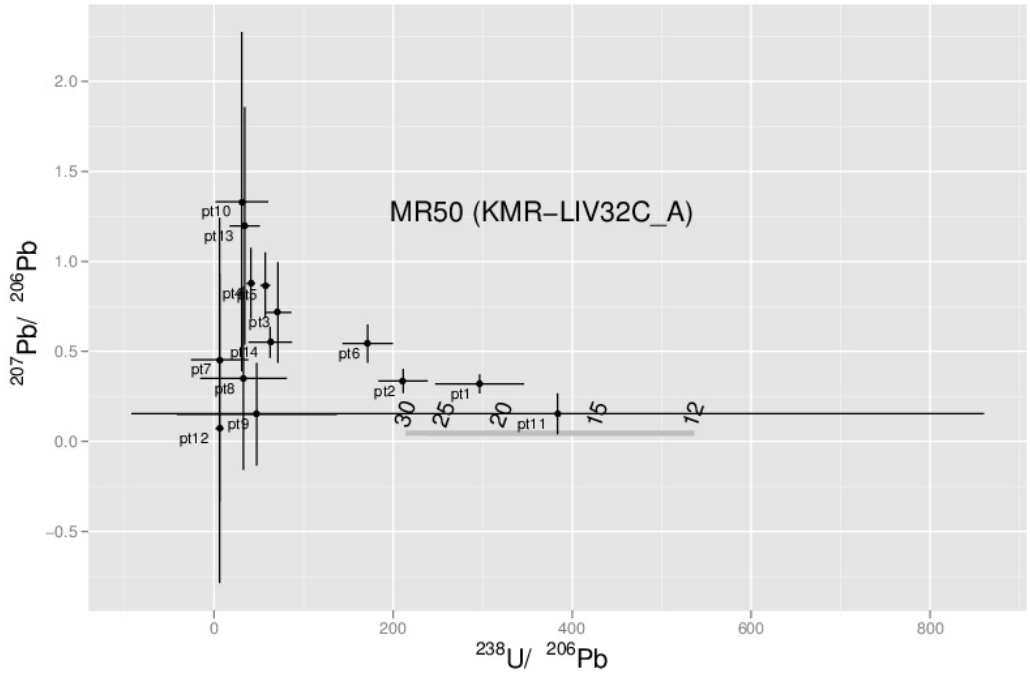
MR50 (KMR−LIV32C_A)
$^{207}Pb/^{206}Pb$
$^{238}U/^{206}Pb$
2.0
1.5
1.0
0.5
0.0
−0.5
0
200
400
600
800
pt10
pt13
pt4
pt5
pt3
pt14
pt7
pt8
pt12
pt9
pt6
pt2
pt1
pt11
30
25
20
15
12

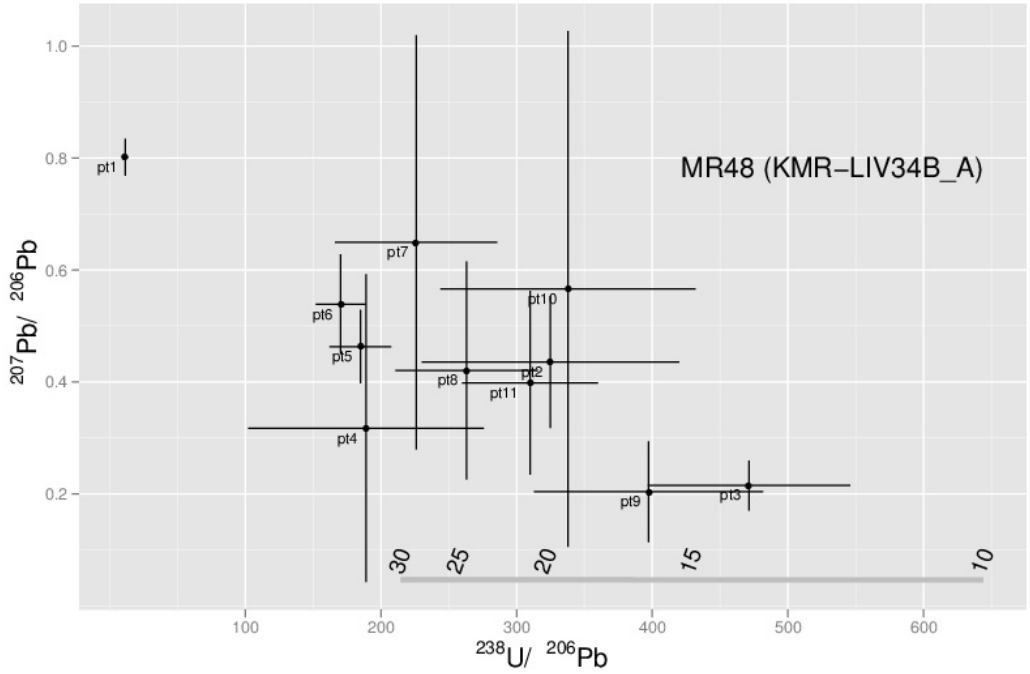
MR48 (KMR−LIV34B_A)
$^{207}Pb/^{206}Pb$
$^{238}U/^{206}Pb$
1.0
0.8
0.6
0.4
0.2
100
200
300
400
500
600
pt1
pt7
pt6
pt5
pt4
pt10
pt2
pt8
pt11
pt9
pt3
30
25
20
15
10

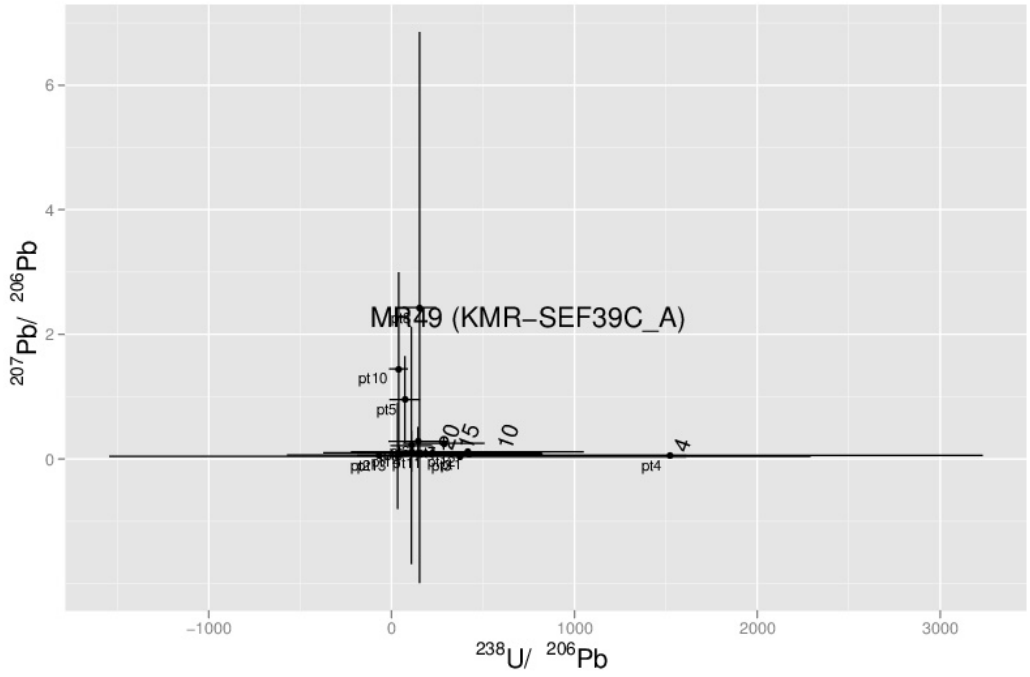
MR49 (KMR−SEF39C_A)
pt10
pt5
pt4
20
15
10
4
6
4
2
0
−1000
0
1000
2000
3000
$^{207}Pb/\ ^{206}Pb$
$^{238}U/\ ^{206}Pb$